

Electrochemical Reduction of Carbon Dioxide

A thesis submitted to the University of Manchester for the degree of

Doctor of Philosophy

in the Faculty of Engineering and Physical Sciences

2013

Briony Setterfield-Price

School of Chemistry

Table of Contents;

List of Figures	7
List of Tables	16
Abstract	17
Declaration	18
Copyright	18
Abbreviations and Symbols and Definitions of Cells	19
1. Introduction	24
1.1. The Trouble with Carbon Dioxide	24
1.2. Electrochemical CO ₂ Reduction	27
1.2.1. Effect of the Electrode Material	28
1.2.2. Effect of the Electrolyte	35
1.2.3. Effect of CO ₂ Concentration	42
1.2.4. Effect of Temperature	43
1.3. Electrocatalytic CO ₂ Reduction	45
1.3.1. Macrocyclic Catalysts	47
1.3.1.1. Cyclam-based Species	48
1.3.1.2. Metallophthalocyanines	50
1.3.1.3. Porphyrins	51
1.3.2. Polypyridyl Catalysts	53
1.3.2.1. Rhenium bipyridyl Systems	53
1.3.2.2. Ruthenium bipyridyl Systems	55
1.3.2.3. Osmium bipyridyl catalyst	57
1.3.2.4. Other Polypyridyl and Similar Catalysts	59
1.3.3. Other Catalysts	61
1.3.3.1. Organic Cations	61
1.3.3.2. Enzymes	63
1.4. M(CO) ₄ αα-diimines	66
1.4.1. Structure	67
1.4.2. Radical Anion Species	69

1.4.3. MLCT and Solvatochromism	70
1.4.4. Electrochemistry of $\text{M}(\text{CO})_4\alpha\alpha$ -diimines	71
1.4.5. $\text{Mo}(\text{CO})_4\text{bpy}$	71
1.5. Diffusion Ordered Spectroscopy as a Complementary Technique	73
1.6. Scope of Present Work	76
2. Electrochemical Methods	80
2.1. Diffusion Limited Electrochemical Techniques	80
2.1.1. Diffusion	80
2.1.2. Cyclic Voltammetry	82
2.1.2.1. Cyclic Voltammetric determination of k^o	87
2.1.2.2. Cyclic Voltammetric determination of k^i	88
2.1.3. Chronoamperometry	90
2.1.3.1. Chronoamperometric determination of k^i	95
2.2. Hydrodynamic Electrochemical Techniques	96
2.2.1. Rotating Disk Electrode	96
2.3. Spectroelectrochemistry	98
2.3.1. In situ Electro Paramagnetic Resonance Spectroscopy	98
2.3.2. In situ Raman Spectroscopy	99
2.3.3. Fourier Transform Infra Red Spectroscopy	101
3. Experimental	103
3.1. Electrodes and Materials	103
3.1.1. Working Electrode	104
3.1.2. Counter Electrode	107
3.1.3. Reference Electrode	108
3.2. Three Electrode Cell Configurations	111
3.2.1. Typical Three Electrode Cell	111
3.2.2. In situ EPR Cell	113
3.2.3. Bulk Electrolysis Cell	115
3.3. Chemicals	117
3.4. Other Equipment	119

4. Molybdenum based Molecular Electrocatalyst for CO₂ Reduction.	121
4.1. Introduction to the catalyst	121
4.2. Mo(CO) ₄ bpy in the absence of CO ₂	122
4.2.1. Stability of monoanionic radical	124
4.2.1.1. Double step chronoamperometry of the first redox process of Mo(CO) ₄ bpy	125
4.2.2. Stability of the dianion	129
4.2.2.1. Tricarbonyl formation	131
4.2.2.2. The lack of reversibility of the second reduction	134
4.2.2.3. Bipyridine comparison	136
4.2.2.4. Alternate explanation	137
4.2.3. Effect of oxygen	139
4.3. Mo(CO) ₄ bpy in the presence of CO ₂	141
4.3.1. Voltammetry of Mo(CO) ₄ bpy in the presence of CO ₂	141
4.3.2. Chronoamperometry of Mo(CO) ₄ bpy in the presence of CO ₂	144
4.3.3. Cross-overs	146
4.3.3.1. Effect of CO ₂ concentration upon crossovers	148
4.3.4. Effect of the addition of H ₂ O to the system	149
4.4. Analysis of Mo(CO) ₄ bpy Voltammetry	155
4.4.1. Diffusion coefficient via voltammetry	155
4.4.2. Calculation of heterogeneous electron transfer rate constant k^o	159
4.4.3. Calculation of the homogeneous electron transfer rate constant k'	161
4.4.3.1. Cyclic voltammetry derived k'	162
4.4.3.2. Chronoamperometric k' determination	164
4.5. Product Detection	166
4.5.1. Gaseous Product Detection	169
4.5.1.1. Gas Chromatography	169
4.5.1.2. Fourier transform infrared spectroscopy	173
4.5.2. Non-gas Phase Product Analysis	180
4.5.2.1. Electrode	180

4.5.2.2. Spectroscopic Measurements of Solution	183
4.6. Conclusion	184
5. System Optimisation and Spectroelectrochemical Investigation	188
5.1. Catalyst Structure Investigation and Optimisation	188
5.1.1. Diimine ligands	188
5.1.2. Effect of the Metal Centre	200
5.1.3. Effect of Additional Substituents on the Bipyridyl Ligand	209
5.1.4. Pyridine and Pyridinium	212
5.1.4.1. Addition of Catalytic Quantities	212
5.1.4.2. Pyridine as a Solvent	216
5.2. <i>In situ</i> EPR Spectroelectrochemistry	223
5.2.1. Mo(CO) ₄ bpy Measurement and Modelling	224
5.2.2. Analogous Complexes	231
5.2.3. Addition of CO ₂ to the System	238
5.2.4. Solvent Effects	240
5.3. The Effect of Working Electrode Material	244
5.3.1. Mo(CO) ₄ bpy Stability at Varied Electrode Materials	247
5.3.2. The Addition of CO ₂ to the Mo(CO) ₄ bpy System at Varied Electrode Materials	266
5.4. Conclusion	276
6. The Influence of Electrolyte Identity upon CO₂ Reduction in NMP	280
6.1. Electrochemical Investigation of M ⁺	282
6.2. Surface Enhanced Raman Spectroscopy	295
6.2.1. <i>In situ</i> Surface Enhanced Raman Spectroscopy	295
6.2.2. <i>Ex situ</i> Surface Enhanced Raman Spectroscopy	305
6.3. Conclusions	312
7. Electrochemistry vs. NMR	314
7.1. Practical considerations in measurement method selection	315
7.1.1. Mutual Diffusion Coefficient	318
7.1.2. Self Diffusion Coefficient	318

7.1.3. Relationship between Mutual and Self Diffusion Coefficients	319
7.2. Diffusion Ordered Spectroscopy (DOSY); Diffusion of Mo(CO) ₄ bpy	322
7.2.1. Diffusion Ordered Spectroscopy; Diffusion of Mo(CO) ₄ bpy in the absence of electrolyte	322
7.2.2. Diffusion Ordered Spectroscopy; Diffusion of Mo(CO) ₄ bpy in the presence of electrolyte	328
7.3. Ferrocene	332
7.3.1. Introduction to Ferrocene	332
7.3.2. Electrochemical Measurement	333
7.3.3. DOSY Measurement	377
7.4. Ferrocene Derivatives; The Effect of Charge	340
7.4.1. Cyclic Voltammetry	345
7.4.2. Chronoamperometry	349
7.4.3. DOSY-NMR	355
7.5. Conclusions	366
8. Conclusions and Further Work	368
8.1. Conclusion	368
8.2. Further Work	371
References	373

Word count: 76,686.

List of figures;

Figure 1.1; Reaction Pathways for Carbon Dioxide Reduction	29
Figure 1.2; A schematic view of the typical electrochemical processes found in Li salt solutions of aprotic solvents at a noble metal electrode (Ag/Au).	41
Figure 1.3; Schematic illustrating the activation barriers for CO ₂ reduction to CO in protic environment in the presence (dashed line) and absence (solid line) of a catalytic species.	45
Figure 1.4: Quasi Redox Reaction Mechanism.of CO ₂ reduction	46
Figure 1.5; Ni(II)-cyclam structure	48
Figure 1.6; Proposed catalytic cycle for the photoreduction of CO ₂ catalysed by Ni(II) cyclam at the sc-CO ₂ :water interface	49
Figure 1.7; Stucture of tetrasulphonated M-phthalocyanine	50
Figure 1.8; Iron 5, 10, 15, 20-tetrakis(2',6'-dihydroxyphenyl)-porphyrin, FeTDHPP	52
Figure 1.9; Proposed catalytic mechanism of CO ₂ reduction to CO by rhenium bipyridyl complexes	54
Figure 1.10; Proposed mechanism for CO ₂ electroreduction by [Ru(bpy) ₂ (CO)H] ⁺	55
Figure 1.11; Tanaka catalyst proposed mechanism	56
Figure 1.12; cis[Os(bpy) ₂ (CO)H][PF ₆] catalyst proposed mechanism	57
Figure 1.13; Structures of the thiazole ligands	59
Figure 1.14; Proposed mechanism of CO ₂ reduction to oxalate by the dinuclear copper complex	60
Figure 1.15; Schematic detailing the proposed pyridinium catalysed CO ₂ reduction to methanol	62
Figure 1.16; Schematic showing the steps of the proposed CO ₂ photoreductive system	65
Figure 1.17; Structure of Mo(CO) ₄ bpy	67
Figure 1.18; MO diagram of Cr(CO) ₄ bpy	68
Figure 2.1; Schematic of Fick's law showing the change in flux with changing concentration and distance.	81
Figure 2.2; Potential scheme as a function of time for cyclic voltammetry	83
Figure 2.3; A typical reversible cyclic voltammogram.	84
Figure 2.4. Ratio of kinetic peak current for the E _r C _i ' reaction scheme to diffusion-controlled peak current as a function of $\lambda^{1/2}$	89
Figure 2.5; Potential scheme for chronoamperometry	91

Figure 2.6; Phase boundary at the electrode-electrolyte interface showing the electrical double layer and diffuse layer.	92
Figure 2.7; A representative chronoamperogram	93
Figure 2.8; Chronoamperometric working curve for the E_rC_i' case for various values of $\lambda^{1/2}$	95
Figure 2.9; A schematic depicting RDE convective flow.	97
Figure 2.10; A schematic depicting Raman scattering.	100
Figure 3.1; Typical acid voltammetric responses for Au (top) and Pt (bottom)	106
Figure 3.2; Typical three electrode cell schematic.	112
Figure 3.3; Schematic of the in-situ EPR cell set up.	114
Figure 3.4; Schematic of the large bulk electrolysis cell.	116
Figure 4.1 DFT calculated ball and stick diagram of $[\text{Mo}(\text{CO})_4\text{bpy}]$ with labelled atoms.	121
Figure 4.2. Voltammetry of $\text{Mo}(\text{CO})_4\text{bpy}$ showing the known 1 st two reductions. $\text{Mo}(\text{CO})_4\text{bpy}$ (0.5 mM) at 200 mV s^{-1} in cell 1.	123
Figure 4.3; Current ratio of the oxidative and reductive current associated with the first redox process of $\text{Mo}(\text{CO})_4\text{bpy}$ as a function of scan rate.	124
Figure 4.4; Double step chronoamperogram of $\text{Mo}(\text{CO})_4\text{bpy}$ (0.5 mM) measured in cell 1 with applied potentials of -1.995 V and -1.846 V vs Fc.	125
Figure 4.5; Density Functional Theory calculated LUMO.	127
Figure 4.6; 2 nd reduction of $\text{Mo}(\text{CO})_4\text{bpy}$ (0.5 mM) at various scan rates in cell 1.	129
Figure 4.7; Current ratio of the oxidative and reductive current associated with the second redox process of $\text{Mo}(\text{CO})_4\text{bpy}$ as a function of scan rate.	130
Figure 4.8; $\text{Mo}(\text{CO})_4\text{bpy}$ (0.5 mM) scanning to various negative vertex potentials at 200 mVs^{-1} in cell 1.	131
Figure 4.9; DFT images showing the calculated singly occupied molecular orbitals (SOMO's) for (a) $[\text{Mo}(\text{CO})_4\text{bpy}]^{\bullet-}$ and (b) $[\text{Mo}(\text{CO})_3\text{bpy}]^{\bullet-}$	133
Figure 4.10; DFT images showing the calculated highest occupied molecular orbitals (HOMO's) for (a) $[\text{Mo}(\text{CO})_4\text{bpy}]^{2-}$ and (b) $[\text{Mo}(\text{CO})_3\text{bpy}]^{2-}$	134
Figure 4.11; Current ratio of oxidative and reductive peak current of the first reduction of $\text{Mo}(\text{CO})_4\text{bpy}$ as a function of negative vertex potential. Scan rate 200 mV s^{-1} .	135
Figure 4.12; (a) Bipyridine (0.5 mM) in cell 2 at 200 mV s^{-1} (b) $\text{Mo}(\text{CO})_4\text{bpy}$ (0.5 mM) in cell 1 at 200 mV s^{-1}	136
Figure 4.13; $\text{Mo}(\text{CO})_4\text{bpy}$ (0.5 mM) in cell 1 at 200 mV s^{-1} . Blue lines show the system under usual conditions, purple show consecutive scans upon bubbling of air through the system.	139

Figure 4.14; Direct CO ₂ reduction and reduction in the presence of Mo(CO) ₄ bpy (0.5 mM) both with and without CO ₂ . Measurements made in cell 2 at 200 mV s ⁻¹ .	142
Figure 4.15; Direct CO ₂ response (pink) compared against CO ₂ catalysed response blue: Mo(CO) ₄ bpy corrected for response in presence of Ar signal.	143
Figure 4.16; Chronoamperomagram: Direct CO ₂ reduction (turquoise) and reduction in the presence of Mo(CO) ₄ bpy (0.5 mM) both with (blue) and without (pink) CO ₂ . Measurements made in cell 1. Potential stepped between -1.0 V, where no reaction observed for 30 s, and -2.1 V for 5 s.	144
Figure 4.17; (above) Mo(CO) ₄ bpy (0.5 mM) scanning to various vertex potentials (E _s) (below) Mo(CO) ₄ bpy (0.5 mM) with (blue) and without (pink) CO ₂ . Measurements made in cell 2 at 200 mV s ⁻¹	147
Figure 4.18; Cyclic Voltammogram of Mo(CO) ₄ bpy (0.5 mM) in CO ₂ saturated cell 2. Scan rate: 200 mVs ⁻¹	148
Figure 4.19. Mo(CO) ₄ bpy CV with and without H ₂ O in the presence and absence of CO ₂ measured in cell 1 at 200 mV s ⁻¹	150
Figure 4.20; Subtracted data to give the response due to (a) water and (b) CO ₂ in all systems (conditions as in figure 4.19)	152
Figure 4.21; Subtracted data to give the response highlighting the extra current response not directly attributable	154
Figure 4.22; Mo(CO) ₄ bpy at various scan rates measured in cell 1	156
Figure 4.23; Plot of Peak current vs. square root of the scan rate for the Mo(CO) ₄ bpy voltammetry given in figure 4.22. Line of best fit (least squares) is shown.	157
Figure 4.24; Plot of ideal and experimental ΔE vs. v ^{1/2} data for Mo(CO) ₄ bpy first redox process in THF system where D _o = 9.9 x 10 ⁻⁶ cm ² s ⁻¹ and k ^o = 2.0 x 10 ⁻³ cms ⁻¹ .	160
Figure 4.25; Current ratio of the 1 st reduction of Mo(CO) ₄ bpy with and without CO ₂ as a function of scan rate measured in cell 1.	161
Figure 4.26; CV of Mo(CO) ₄ bpy (0.5 mM) in CO ₂ saturated as cell 2 except measured at bulk gold mesh electrode (approximately 12.5 cm ²) in bulk electrolysis cell.	170
Figure 4.27; Bulk electrolysis current response when -2.2 V applied to the Mo(CO) ₄ bpy (0.5 mM) in CO ₂ saturated cell 2 except measured at bulk gold mesh electrode (approximately 12.5 cm ²) in bulk electrolysis cell.	170
Figure 4.28; CV of Mo(CO) ₄ bpy (0.5 mM) as cell 1 except measured at bulk gold mesh electrode (approximately 12.5 cm ²) in the presence (blue) and absence (red) of CO ₂ .	174
Figure 4.29; Bulk electrolysis current response when -2.2 V applied to the Mo(CO) ₄ bpy (0.5 mM) as cell 1 except measured at bulk gold mesh electrode (approximately 12.5 cm ²) in the presence (blue) and absence (red) of CO ₂ .	175
Figure 4.30; FTIR spectra of the headspace gas post bulk electrolsis in the presence (blue) and absence (red) of CO ₂ corresponding to the data in Figure 4.29.	176

Figure 4.31; Enlargement of the CO region of the FTIR spectra given in Figure 4.30.	177
Figure 4.32; Cyclic voltammogram of Au working electrode (2 mm d) in 0.1 M H ₂ SO ₄ prior to (black) and post use (red and yellow, two different experimental runs) in Mo(CO) ₄ bpy CO ₂ reduction system cell 1. Scan rate 100 mV s ⁻¹ .	181
Figure 5.1; Structure of Molybdenum tetracarbonyl complexes. (a) = Molybdenum tetracarbonyl dicyclohexylethylthlenediimine (DAB), (b) = Molybdenum tetracarbonyl N-(2-pyridinylmethylene) cyclohexamine (PyCa), (c) = Molybdenum tetracarbonyl 2,2'-bipyridine (bpy), (d) = Molybdenum tetracarbonyl 1,10-phenanthroline (PHEN).	189
Figure 5.2; Cyclic Voltammogram for (a) to (d) . Mo(CO) ₄ (α-LL') at ~0.5 mM, in cell 2 under argon. Scan rate 200 mV s ⁻¹	191
Figure 5.3; Cyclic Voltammogram for (a) Mo(CO) ₄ DAB and (c) Mo(CO) ₄ bpy respectively, ~0.5 mM, cell 2 under argon. Scan rate 200 mV s ⁻¹ .	195
Figure 5.4; Cyclic Voltammogram for (d) . Mo(CO) ₄ (PHEN) at ~0.5 mM, cell 2 under argon (pink) and upon saturation with CO ₂ (blue) and CO ₂ saturated electrolyte solution in the absence of Mo(CO) ₄ (PHEN) (dashed blue). Scan rate of 200 mV s ⁻¹ .	196
Figure 5.5; Voltammetry of W(CO) ₄ bpy (10 mM) both with (blue) and without (pink) CO ₂ and direct CO ₂ reduction in the same system (turquoise dashed). Measurements made in cell 1 at 200 mV s ⁻¹	205
Figure 5.6; Voltammetry of bipyridine (10 mM) both with (blue) and without (pink) CO ₂ and direct CO ₂ reduction in the same system (turquoise dashed). Measurements made cell 1 at 200 mV s ⁻¹	207
Figure 5.7; Molybdenum tetracarbonyl with [a] 5,5'-di-nitro substituted 2,2'-bipyridyl ligand, [b] 4,4'-di-tertiary butyl substituted 2,2'-bipyridyl ligand.	209
Figure 5.8; Cyclic Voltammogram for [a] . Mo(CO) ₄ (4,4'-di- ^t butyl-2,2'-bpy) at ~0.5 mM, in cell 2 under argon (pink) and upon saturation with CO ₂ (blue). Scan rate 200 mV s ⁻¹ .	211
Figure 5.9; Cyclic Voltammogram for pyridine (10 mM), dashed lines and pyridinium (10 mM pyridine + 10 mM trifluoroacetic acid), solid lines, in cell 1 under argon (blue) and CO ₂ (purple). CO ₂ reduction in NMP + 0.1 M TBABF ₄ plotted for comparison (pink long dashed). Scan rate 200 mV s ⁻¹ .	214
Figure 5.10; Direct CO ₂ response (pink) compared against CO ₂ pyridinium 'catalysed' response (purple): Pyridinium corrected for response in presence of Ar signal. Original data given in figure 5.9.	216
Figure 5.11; Cyclic voltammetry employing pyridine as solvent with TBABF ₄ (0.1 M) in the presence (blue) and absence of CO ₂ (purple), with (solid) and without (dashed) 10% H ₂ O. Au WE (2 mm d) employed at a scan rate of 200 mV s ⁻¹ . Pt wire pseudo reference and Fc calibration (as used for cell 1).	218
Figure 5.12; Cyclic voltammetry employing pyridine as solvent with TBABF ₄ (0.1 M) in the presence (blue) and absence of CO ₂ (purple), with (solid) and without (dashed) 10% H ₂ O. Au WE (2 mm d) employed at a scan rate of 200 mV s ⁻¹ . Pt wire pseudo reference and Fc calibration (as used for cell 1).	220
Figure 5.13; EPR spectrum of electrogenerated Mo(CO) ₄ bpy ^{•-} in 0.1 M TBAF in Ar degassed NMP, Mo(CO) ₄ bpy (10 mM) -1.7V (vs Ag wire) applied Pt wire WE at RT. Mod. Freq: 100 kHz, Mod Amp:1.0 G, X-band frequency: 9.878 GHz.	224

Figure 5.14; DFT calculated spin density of $\text{Mo}(\text{CO})_4\text{bpy}^{\bullet-}$	225
Figure 5.15; EPR spectrum of electrogenerated $\text{bpy}^{\bullet-}$ in 0.1 M TBAF in Ar degassed NMP, bpy (10 mM) -1.9 V (vs Ag wire) applied Pt wire WE at RT. Mod. Freq: 10 kHz, Mod Amp:0.1 G, X-band frequency: 9.878 GHz	226
Figure 5.16; EPR spectra of electrogenerated $\text{bpy}^{\bullet-}$ (red) and $\text{Mo}(\text{CO})_4\text{bpy}^{\bullet-}$ (purple) given in Figures 5.13 and 5.15	227
Figure 5.17; EPR spectrum of electrogenerated $\text{Mo}(\text{CO})_4\text{bpy}^{\bullet-}$ (as seen in figure 5.13) in blue and simfonia simulation using the DFT calculated EPR parameters in red. The instrumental parameters were kept consistent with those used experimentally with the following isotropic hyperfine coupling constants; $a_N=3.18$, $a_{H1}=5.7$, $a_{H2}=1.5$, $a_{H3}=1.0$, $a_{Mo}=1.89$ G and g-value= 2.0001.	229
Figure 5.18; EPR spectrum of electrogenerated $\text{Mo}(\text{CO})_4\text{bpy}^{\bullet-}$ (as seen in Figure 5.13) in green and easyspin simulation in blue. The instrumental parameters were kept consistent with those used experimentally with the following isotropic hyperfine coupling constants; $a_N=4.2$, $a_{H1}=4.2$, $a_{H2}=1.1$, $a_{H3}=0.6$, $a_{H4}=0.7$ G and g_{iso} -value= 2.0001.	230
Figure 5.19; EPR spectrum of electrogenerated $\text{W}(\text{CO})_4\text{bpy}^{\bullet-}$ in 0.1 M TBAF in Ar degassed NMP, $\text{W}(\text{CO})_4\text{bpy}$ (10 mM) -1.7 V (vs Ag wire) applied Pt wire WE at RT. Mod. Freq: 10 kHz, Mod Amp:0.1 G, X-band frequency: 9.878 GHz.	232
Figure 5.20; EPR spectra of electrogenerated $\text{W}(\text{CO})_4\text{bpy}^{\bullet-}$ (red) and $\text{Mo}(\text{CO})_4\text{bpy}^{\bullet-}$ (purple) given in figures 5.19 and 5.13	233
Figure 5.21; EPR spectrum of electrogenerated $\text{Mo}(\text{CO})_4[5,5'\text{-dimethylbpy}]^{\bullet-}$ in 0.1 M TBAF in Ar degassed NMP, bpy (10 mM) -2 V (vs Ag wire) applied Pt wire WE at RT. Mod. Freq: 10 kHz, Mod Amp:0.1 G, X-band frequency: 9.878 GHz	234
Figure 5.22; EPR spectra of electrogenerated $\text{W}(\text{CO})_4\text{bpy}^{\bullet-}$ (red) and $\text{Mo}(\text{CO})_4[5,5'\text{-dimethylbpy}]^{\bullet-}$ (purple) given in Figures 5.19 and 5.21	235
Figure 5.23; EPR spectrum of electrogenerated $\text{Mo}(\text{CO})_4\text{bpy}^{\bullet-}$ in 0.1 M TBABF_4 in Ar/ CO_2 saturated NMP, $\text{Mo}(\text{CO})_4\text{bpy}$ (10 mM) -1.7 V (vs Ag wire) applied Pt wire WE at RT. Mod. Freq: 100 kHz, Mod Amp:1.0 G, X-band frequency: 9.878 GHz	239
Figure 5.24; EPR spectrum generated upon application of -2.0 V (vs Ag wire) in 0.1 M TBABF_4 in N_2/CO_2 saturated THF, $\text{Mo}(\text{CO})_4\text{bpy}$ (10 mM) applied Pt wire WE at RT. Mod. Freq: 100 kHz, Mod Amp:0.30 G, X-band frequency: 9.438 GHz	241
Figure 5.25; CV response plotting current density vs. applied potential of 0.5 mM $\text{Mo}(\text{CO})_4\text{bpy}$ in cell 1, measured at Au, Pt (d= 2 mm) and GC WE (d= 3 mm). Scan rate employed was 200 mV s ⁻¹ .	247
Figure 5.26; Schematic depicting possible $\text{Mo}(\text{CO})_4\text{bpy}$ -electrode orientations.	249
Figure 5.27; CV of 0.5 mM $\text{Mo}(\text{CO})_4\text{bpy}$ in cell 1 except measured at GC WE (d= 3 mm). Scan rate employed was 200 mV s ⁻¹ .	250
Figure 5.28; CV of 0.5 mM $\text{Mo}(\text{CO})_4\text{bpy}$ in cell 1 except measured at GC WE (d= 3 mm). Scan rate employed was 200 mV s ⁻¹ . 1 st scan indicated by the dashed line.	252
Figure 5.29; CV of 0.5 mM $\text{Mo}(\text{CO})_4\text{bpy}$ in cell 1 (measured at Au WE (d= 2 mm)). Scan rate employed was 100 mV s ⁻¹ .	253

Figure 5.30; CV of 0.5 mM Mo(CO) ₄ bpy in cell 1 except measured at Pt WE (d= 2 mm). Scan rate employed was 200 mV s ⁻¹ with varied negative vertex potentials. 1 st scan shown by solid lines with subsequent scans shown in dashed and dotted lines.	254
Figure 5.31; Plot showing the ratio of peak currents associated with the first reduction of Mo(CO) ₄ bpy for the first and second scans ($I_{p(\text{scan}\#1)}/I_{p(\text{scan}\#2)}$) as a function of negative vertex potential on Pt. Corresponding voltammetry is given in figure 5.30.	256
Figure 5.32; CV of 0.5 mM Mo(CO) ₄ bpy in cell 1 except measured at Pt WE (d= 2 mm). Scan rate employed was 200 mV s ⁻¹ for 100 consecutive scans with every 5 th plotted.	257
Figure 5.33; Absolute current for the Mo(CO) ₄ bpy reduction (red) and subsequent reoxidation (blue) as a function of scan number. Corresponding CV Figure 5.32.	258
Figure 5.34; CV of 0.5 mM Mo(CO) ₄ bpy in cell 1 (measured at Au WE (d= 2 mm)). Scan rate employed was 200 mV s ⁻¹ for 100 consecutive scans with every 10 th plotted.	260
Figure 5.35; A plot showing the peak separation as a function of scan rate for the first redox peaks of Mo(CO) ₄ bpy measured at GC, Pt and Au electrodes	261
Figure 5.36; A Randles-Sevcik plot showing the current density as a function of the square root of the scan rate for the first redox peaks of Mo(CO) ₄ bpy measured at GC, Pt and Au electrodes.	262
Figure 5.37; The ratio of peak currents (reductive/-oxidative) for the first redox process of Mo(CO) ₄ bpy vs. scan rate at GC, Au and Pt WE. The open circles highlight the current ratio seen at the lowest scan rate sampled, 20 mV s ⁻¹ . First scan.	264
Figure 5.38; CV of 0.5 mM Mo(CO) ₄ bpy in cell 1 except measured at GC WE (d= 3 mm) in the presence (solid lines) and absence (broken lines) of CO ₂ . Scan rate employed was 200 mV s ⁻¹ . 5 subsequent scans shown for each system.	267
Figure 5.39; CV of 1 mM Mo(CO) ₄ bpy in cell 2 except measured at GC WE (d= 3 mm) in the presence (solid lines) and absence (broken lines) of CO ₂ with direct CO ₂ reduction also shown (pale blue) Scan rate employed was 200 mV s ⁻¹ . 1st scans shown for each system.	268
Figure 5.40; CV of 0.5 mM Mo(CO) ₄ bpy in cell 1 except measured at Pt WE (d= 2 mm) in the presence (solid lines) and absence (broken lines) of CO ₂ . Scan rate employed was 200 mV s ⁻¹ . 1 st scan= red, 5 th scan= purple.	271
Figure 5.41; CV of 0.5 mM Mo(CO) ₄ bpy in cell 1 except measured at Pt WE (d= 2 mm) in the presence (solid lines) and absence (broken lines) of CO ₂ . Scan rate employed was 200 mV s ⁻¹ . Scans 1 to 10 shown for CO ₂ saturated solution and 1 to 3 for the corresponding system in the absence of CO ₂ .	273
Figure 5.42; CV of 5 mM Mo(CO) ₄ bpy in cell 2 except measured at Pt WE (d= 2 mm) in CO ₂ saturated solution. Scan rate employed was 200 mV s ⁻¹ . Scans 1 to 5 shown.	274
Figure 6.1; CV of CO ₂ saturated NMP at Au WE (2 mm d) with NaBF ₄ (0.1 M) in red and TBABF ₄ (0.1M) in purple supporting electrolyte. Scans 1 (dashed) and 5 (solid) shown. Scan rate 200 mV s ⁻¹ .	282

Figure 6.2; CV of Ar degassed and CO ₂ saturated NMP at Au WE (2 mm d) with LiBF ₄ (0.1 M) supporting electrolyte. Scans 1 to 3 shown for each. Scan rate 200 mV s ⁻¹ .	283
Figure 6.3; CV of Ar degassed NMP at Au WE (2 mm d) with LiBF ₄ (0.1 M) supporting electrolyte. Scans 1 to 3 shown (solid line #1, dashed line #2 and dotted line #3). Scan rate 200 mV s ⁻¹ .	288
Figure 6.4; CV of CO ₂ saturated NMP at Au WE (2 mm d) with LiBF ₄ (0.1 M) supporting electrolyte. Scans 1 to 3 shown (solid line #1, dashed line #2 and dotted line #3). Scan rate 200 mV s ⁻¹ .	290
Figure 6.5; CV measured at Au WE (2 mm), in 0.1 M H ₂ SO ₄ prior to (black) and after (red) use in LiBF ₄ NMP solution in the absence of CO ₂ . Scan rate 100 mV s ⁻¹ .	293
Figure 6.6; CV of Ar degassed (red) and CO ₂ saturated (blue) NMP at Au WE (2 mm d) with NaBF ₄ (0.1 M) supporting electrolyte. Scan #3 shown. Scan rate 200 mV s ⁻¹	294
Figure 6.7; In situ SERS: LiBF ₄ (0.1 M) in Ar degassed NMP at an electrochemically prepared gold foil working electrode (1 cm ²) at potentials 0.1 V to -4.0 V vs Pt (corresponding E-I response given in figure 6.10)	297
Figure 6.8; An enlargement of the region 800-900 cm ⁻¹ of figure 5. In situ SERS LiBF ₄ (0.1 M) in NMP at an electrochemically prepared gold foil working electrode (1 cm ²) at potentials 0.1 V to -4.0 V vs Pt (corresponding E-I response given in figure 6.10).	298
Figure 6.9; In situ SERS of CO ₂ saturated LiBF ₄ (0.1 M) in NMP at a electrochemically prepared gold foil working electrode (1 cm ²) at potentials 0.2V to -4.0 V vs Pt (corresponding E-I response given in figure 6.10)	300
Figure 6.10; Current response for the initial 30 s of each of the applied potentials corresponding to the in situ SERS gathered. Red points show measurements made in the absence of CO ₂ in the LiBF ₄ -NMP system described above, blue correspond to the CO ₂ saturated system. Left shows the full current-potential range observed with the plot on the right an enlargement to show the processes occurring at less negative potentials more clearly.	301
Figure 6.11; SERS for CO ₂ saturated NMP with TBA ⁺ (blue) and Li ⁺ (red) supporting electrolyte in the absence of applied potential.	302
Figure 6.12; SERS of NMP on electrochemically prepared Au foil in the absence of applied E with varied solvent pathlengths.	304
Figure 6.13; Plot of NMP Raman peak intensity response as a function of volume of NMP, corresponding to Raman spectra in Figure 6.12.	305
Figure 6.14; SERS of Au WE after application of negative potential in CO ₂ saturated NMP with LiBF ₄ (0.1 M). Red and gold lines represent separate results from different areas of the shiny side of the electrode	307
Figure 6.15; SERS of Au WE after application of negative potential in CO ₂ saturated NMP with LiBF ₄ (0.1 M). Blue and purple lines represent separate results from different areas of the darkened side of the electrode	308

Figure 6.16; CV of CO ₂ saturated NMP at Pt foil WE (approx 1 cm ²) with TBABF ₄ (0.1 M), TBABF ₄ :NaBF ₄ 1:1 (0.1 M total supporting electrolyte concentration) and NaBF ₄ (0.1 M) supporting electrolytes. Scan #1 shown. Scan rate 200 mV s ⁻¹ .	310
Figure 6.17; CV of CO ₂ saturated NMP at Pt foil WE (approx 1 cm ²) with TBABF ₄ (0.1 M), TBABF ₄ :NaBF ₄ 1:1 (0.1 M total supporting electrolyte concentration) and NaBF ₄ (0.1 M) supporting electrolytes over different potential ranges. Scan #3 shown. Scan rate 200 mV s ⁻¹ .	311
Figure 7.1; Experimental data from the Mo(CO) ₄ bpy experiments showing the attenuation of NMR signal for the varied gradient amplitudes trialed.	323
Figure 7.2; DOSY-NMR spectrum of Mo(CO) ₄ bpy (0.5 mM) in d ₈ -THF	324
Figure 7.3; Molecular structure of Mo(CO) ₄ bpy illustrating the different proton environments.	326
Figure 7.4; DOSY-NMR spectrum of Mo(CO) ₄ bpy (0.5 mM) in d ₈ -THF with TBABF ₄ (0.1 M).	328
Figure 7.5; Structure of ferrocene	332
Figure 7.6; CV of ferrocene (0.5 mM) in THF + TBABF ₄ (0.1 M) at Au WE (2 mm d) at 20 mV s ⁻¹	333
Figure 7.7; Cyclic Voltammogram of Ferrocene (0.5 mM) measured at a Rotating Disk Electrode (Au 2 mm diameter) in Ar saturated THF with 0.1 M TBA(BF ₄) at room temperature and pressure. 1 st scan shown. Scan rate= 10mVs ⁻¹ . At various rotation speeds. Experimental shown by unbroken lines and calculated ideal data shown by dotted lines.	335
Figure 7.8; Levich plot corresponding to the data shown in figure 7.7. The line represents the linear regression obtained.	337
Figure 7.9; [a] Ferrocene DOSY without electrolyte. [b] Ferrocene DOSY with TBABF ₄ (0.1 M) present.	338
Figure 7.10; Structures of the Ferrocene derivatives; [a] deprotonated ferrocene carboxylic acid (FcCOO ⁻), [b] ferrocene methanol (FcMeOH) and [c] protonated dimethylaminomethyl ferrocene (FcN ⁺).	341
Figure 7.11; Diffusion coefficients obtained for FcN ⁺ in the 'buffered' H ₂ O and D ₂ O systems	345
Figure 7.12; Cyclic Voltammogram of dimethylaminomethyl ferrocene, FcN ⁺ at various scan rates. (0.5 mM) at various scan rates in H ₂ O with KCl (0.16 M) and HCl (0.04 M) measured at 30°C. Gold WE (2 mm diameter), Pt pseudo reference electrode and counter.	346
Figure 7.13; (a) Peak current ratio, I _(ox) /-I _(red) and (b) Peak separation, ΔE, as a function of scan rate from the CV data for FcN ⁺ • seen in figure 7.11 and experimental data from analogous experiments with the stated conditions for FcMeOH • and FcCOO ⁻ •. The solid circles represent the H ₂ O data, hollow ones the equivalent D ₂ O data.	346
Figure 7.14; Randles-Sevcik plot for approximately 0.5 mM ferrocene derivatives (FcMeOH, FcCOO ⁻ , slightly higher 1.2 mM for FcN ⁺) in H ₂ O (solid) and D ₂ O (hollow)	348

Figure 7.15; (a) CV depicting chosen E's for potential steps. (b) Chronoamperogram for FcN^+ where $E_{\text{ox}}=0.1$ V and $E_{\text{r}}=-0.15$ V	350
Figure 7.16; (a) transients for subsequent oxidising potential steps (0.1 V) for FcN^+ data from figure 14 (b) Cottrell plot for approximately 0.5 mM ferrocene derivatives (FcN^+ , FcMeOH , FcCOO^-) in H_2O (solid) and D_2O (hollow)	351
Figure 7.17; DOSY Spectra of dimethylaminomethyl ferrocene, FcN^+ (0.5 mM) in D_2O with KCl (0.1 M) and HCl (1.0 mM) measured at 30°C; ferrocene carboxylic acid, FcCOO^- (0.5 mM) in D_2O with KCl (0.1M) and NaOH (1.0 mM) measured at 28°C; ferrocene methanol, FcMeOH (0.5 mM) in D_2O with KCl (0.1 M) at 28°C.	355
Figure 7.18; Logarithmic analysis of the normalised peak amplitude as a function of the squared magnetic field gradient for FcN^+ , FcMeOH and FcCOO^- data shown in figure 7.16.	357

List of Tables;

Table 1.1 Carbon Dioxide reduction standard potentials at pH 7.0 (in an aqueous system)	27
Table 1.2; Data for benzothiazole and bithiazole complexes	59
Table 1.3; Comparison of reduction potentials reported for Mo(CO) ₄ bpy	72
Table 3.1; Electrodes and electrode materials.	103
Table 3.2; Electrode acid cycling experimental parameters.	105
Table 3.3; Reagents and solvents employed and their purity and supplier.	118
Table 3.4; Specialised equipment employed with model and supplier.	119
Table 4.1; Diffusion co-efficients for Mo(CO) ₄ bpy in THF and NMP for calculated and average experimental results from cyclic voltammetry.	158
Table 4.2. Heterogeneous electron transfer rate constants.	160
Table 5.1; The standard redox potential of the 1 st and 2 nd reductions of complexes (a) to (d) (corresponding to CV Figure 5.1) and the difference in potential between the first and second redox processes.	193
Table 5.2; Relative permittivity and dipole moments of the solvents investigated; tetrahydrofuran (THF), pyridine (Py) and N-methylpyrrolidone (NMP)	202
Table 5.3; Redox potentials of M(CO) ₄ bpy where M=Cr, Mo, W and of uncomplexed bipyridine. All measurements made in cell 2 at 200 mV s ⁻¹ with an analyte concentration of ~0.5 mM.	203
Table 5.4; Experimental g _{iso} -values for the EPR spectra of the radicals investigated.	236
Table 5.5; Diffusion coefficient of Mo(CO) ₄ bpy in NMP calculated from the Randles-Sevcik plot for GC, Pt and Au electrodes.	263
Table 6.1; Literature, predicted and observed M ⁺ reduction potentials	285
Table 7.1; Diffusion coefficients obtained using DOSY at 298.5 K (Mo(CO) ₄ bpy system)	329
Table 7.2; Diffusion coefficients obtained using DOSY at 298.5 K (Ferrocene system)	339
Table 7.3; Diffusion coefficients for ferrocene derivatives measured via cyclic voltammetry for both H ₂ O and D ₂ O systems. R ² obtained from Randles-Sevcik plot analysis (where R is the correlation coefficient).	349
Table 7.4; Diffusion coefficients for ferrocene derivatives measured via chronoamperometry for both H ₂ O and D ₂ O systems. R ² obtained from Cottrell plot analysis (where R is the correlation coefficient).	351
Table 7.5; Diffusion coefficients for ferrocene derivatives measured via DOSY in D ₂ O. R ² obtained from ln(S/S ₀) vs G ² plot analysis (where R is the correlation coefficient).	358
Table 7.6; Diffusion coefficients for the ferrocene derivatives from all methods trialled	361

The University of Manchester

Briony Setterfield-Price

Doctor of Philosophy Thesis; "Electrochemical Reduction of Carbon Dioxide"

Submission Date: 16/07/2013

Abstract;

The work undertaken involved the exploration of CO₂ electroreduction systems, focussing heavily upon electrocatalysis utilising an array of electrochemical, spectroelectrochemical and spectroscopic techniques.

The identification and characterisation of a relatively inexpensive and simple electrocatalyst for CO₂ reduction was achieved, with the optimisation and development undertaken in such a manner that not just the electrocatalytic species, but also the entire electrochemical system was investigated, in order to determine and better understand the roles played by the various components.

The complex of interest, Mo(CO)₄bpy, represents the first molybdenum based molecular electrocatalyst reported to be active toward CO₂ reduction, despite the prominence of Mo in enzymes with analogous function. The electrochemical characterisation of the complex in the both the presence and absence of CO₂ was undertaken, yielding valuable information on the redox behaviour of the complex within the non-aqueous system in which it was employed and highlighting previously unreported features such as a third reduction and new reoxidation attributed to the reoxidation of a tricarbonyl anionic species. Non-aqueous solvents were chosen as they provide greater CO₂ solubility than water with portions of the investigation undertaken in tetrahydrofuran, THF, then moving to the less widely used N-methylpyrrolidone, NMP. NMP is significantly less volatile than THF and has a large negative electrochemical window so is ideal for looking at reduction processes and, importantly, is also used as a commercial CO₂ scrubbing solvent.

Upon addition of CO₂ to the Mo(CO)₄bpy system there was an observable lowering of the overpotential by over 300 mV, and significant increase in CO₂ associated current when compared to that for 'direct' CO₂ reduction within the same system, at the reduction potential associated with the first reduction of the tetracarbonyl bipyridyl species. The confirmation of the anionic radical as the active species was attained through DFT calculation and EPR spectroelectrochemistry. Under inert gas the spectrum rapidly generated upon application of the first reduction potential is consistent with the expected response for the radical anionic [Mo(CO)₄bpy]^{•-}. When the system is saturated with CO₂ this radical is no longer detectable. This supports the idea that the unpaired electron is transferred from the [Mo(CO)₄bpy]^{•-} to the CO₂ molecule and also suggests that this transfer is rapid as no adduct is detectable via EPR even at reduced temperature (240 K). This is in keeping with the rate constants calculated from the voltammetric measurements made. The stability and activity toward CO₂ reduction exhibited by Mo(CO)₄bpy displayed a strong dependence on working electrode material, with gold proving optimal, indicative of adsorption being significant in the process.

Optimisation of both the catalyst structure and the solvent and electrolyte system were also explored, as well as the (somewhat less directly related) comparison of various sources of diffusivity data.

Declaration;

The author declares that no portion of the work referred to in the thesis has been submitted in support of an application for another degree or qualification of this or any other university or other institute of learning.

Copyright;

- i) The author of this thesis (including any appendices and/or schedules to this thesis) owns certain copyright or related rights in it (the “Copyright”) and she has given The University of Manchester certain rights to use such Copyright, including for administrative purposes.
- ii) Copies of this thesis, either in full or in extracts and whether in hard or electronic copy, may be made only in accordance with the Copyright, Designs and Patents Act 1988 (as amended) and regulations issued under it or, where appropriate, in accordance with licensing agreements which the University has from time to time. This page must form part of any such copies made.
- iii) The ownership of certain Copyright, patents, designs, trade marks and other intellectual property (the “Intellectual Property”) and any reproductions of copyright works in the thesis, for example graphs and tables (“Reproductions”), which may be described in this thesis, may not be owned by the author and may be owned by third parties. Such Intellectual Property and Reproductions cannot and must not be made available for use without the prior written permission of the owner(s) of the relevant Intellectual Property and/or Reproductions.
- iv) Further information on the conditions under which disclosure, publication and commercialisation of this thesis, the Copyright and any Intellectual Property and/or Reproductions described in it may take place is available in the University IP Policy (see <http://documents.manchester.ac.uk/DocuInfo.aspx?DocID=487>), in any relevant Thesis restriction declarations deposited in the University Library, The University Library’s regulations (see <http://www.manchester.ac.uk/library/aboutus/regulations>) and in The University’s policy on Presentation of Theses.

Symbols, Abbreviations and Cell Definitions;

Symbols and Abbreviations;

α	transfer coefficient
γ	gyromagnetic ratio/activity coefficient
δ	diffusion layer/duration of gradient pulse
Δ'	effective diffusion encoding delay
ΔE	difference in potential/peak separation/energy gap to excited state
ΔG	free energy change
ϵ	relative permittivity
ϵ_0	vacuum permittivity
η	dynamic viscosity
λ	wavenumber/spin orbit coupling constant/ kinetic parameter
μ_B	Bohr magneton
ν	scan rate/microwave frequency
ρ	density of bulk material
τ	sampling time
ν	kinematic viscosity
Φ_m	potential of electrode surface
Φ_{OHP}	potential of the outer Helmholtz plane
Φ_s	potential of the bulk solution
ψ	dimensionless rate parameter
ω	angular velocity
a	covalency parameter/activity
A	working electrode area
$Ag/AgCl$	silver/silver chloride saturated reference electrode
B_0	magnetic field strength
bpy	2,2'-bipyridine
C	concentration
C_o	concentration of oxidised species
C_r	concentration of reduced species

C_z[*]	bulk concentration of reactant
CA	chronoamperometry
CE	counter electrode
CV	cyclic voltammogram
D	mutual diffusion coefficient
D_o	diffusion coefficient of starting material
D_k	diffusion coefficient of product
D[*]	self diffusion coefficient
DAB	dicyclohexylethylthlenediimine
DFT	density functional theory
DI	de-ionised
DMF	dimethylformamide
DMSO	dimethyl sulfoxide
DOSY	diffusion ordered spectroscopy
e	charge of an electron
E	potential
E^o	standard redox potential
E_r	cathodic peak potential
E_o	anodic peak potential
E_{1/2}	half-wave potential
E_i	initial potential
E_s	step/chosen potential
E_{pa}/E_{pc}	peak anodic/cathodic potential
E_rC_i	reversible electron transfer-irreversible chemical reaction
E_rC_i'	reversible electron transfer-irreversible catalytic reaction
EPR	electron paramagnetic resonance
f	frequency/ $\frac{F}{RT}$
F	Faraday's constant
Fc	ferrocene
Fc⁺	ferricinium
FcCOO⁻	deprotonated ferrocene carboxylic acid
FcMeOH	ferrocene methanol

FcN⁺	protonated dimethylaminomethyl ferrocene
FTIR	Fourier transform infrared spectroscopy
g_e	free electron g-value
g_{iso}	g-factor
G	gradient amplitude
GC	glassy carbon
GCMS	gas chromatography mass spectroscopy
h	Planck's constant
HER	hydrogen evolution reaction
HOMO	highest occupied molecular orbital
I/i	current/quantum spin number
I_p	peak current
I_{pa}/I_{pc}	peak anodic/cathodic current
i_d	diffusion limited current
IR	infrared
J/j	flux of the electroactive species/ current density
k_b	Boltzmann constant
k^o	standard heterogeneous rate constant
k'	electron transfer rate constant
k_f	rate of electron transfer
LUMO	lowest unoccupied molecular orbital
M⁺	alkali metal
MLCT	metal to ligand charge transfer
MO	molecular orbital
MW	molecular weight
n	number of electrons transferred
N_a	Avogadro's number
NHE	normal hydrogen electrode
NMP	N-methylpyrrolidone
NMR	nuclear magnetic resonance
NR₄⁺	tetraalkylammonium cation
OTTLE	optically transparent thin-layer electrochemical
Pa	packing friction

PHEN	1,10-phenanthroline
Py	pyridine
PyCA	N-(2-pyridinylmethylene) cyclohexamine
PyH⁺	pyridinium
Q	charge
r	radius
R	gas constant
RDE	rotating disk electrode
RE	reference electrode
RPM	rotations per minute
S	spin signal amplitude
S₀	spin signal amplitude in the absence of diffusion
SCE	saturated calomel electrode (Hg/HgCl)
SERS	surface enhanced Raman spectroscopy
SHE	standard hydrogen electrode
SLUMO	second lowest molecular orbital
SOMO	singly occupied molecular orbital
T	temperature
t	time
TBA⁺	tetrabutylammonium cation
THF	tetrahydrofuran
TOF	turn over frequency
UME	ultra microelectrode
UPD	under potential deposition
UPS	under potential stripping
UV-vis	ultraviolet-visible
V	molar volume
WE	working electrode
x	mole fraction
z	charge of ion

Cell Definitions;

Throughout the captions cells 1 and 2 are referred to in order to avoid repetition in the specifics of the cell set up and composition, the definitions of which are given below.

Cell 1;

- Standard three electrode cell set up (figure 3.2, volume ~30 ml)
- NMP/0.1 M TBABF₄
- Gold working electrode (2 mm d, freshly prepared)
- Platinum mesh counter electrode
- Platinum pseudo reference electrode. Ferrocene added as an internal calibrant to the solution after measurement to verify the potentials
- Measurements made at room temperature and pressure

Cell 2;

- Standard three electrode cell set up (figure 3.2, volume ~30 ml)
- THF/0.1 M TBABF₄
- Gold working electrode (2 mm d, freshly prepared)
- Platinum mesh counter electrode
- Ferrocene/ferrocinium reference electrode (detailed in 3.13)
- Measurements made at room temperature and pressure

1. Introduction

1.1. The trouble with carbon dioxide;

CO₂ has been long considered a waste product; it is a by-product of combustion and respiration so not only the burning of carbon based fuels but even through the process of exhalation it is released into the atmosphere.

Natural carbon dioxide production is balanced to varying degrees by the existence of CO₂ sinks such as the biosphere and oceans which remove CO₂ from the atmosphere, however due to the ever increasing anthropogenic contribution to CO₂ emission, predominantly from the burning of carbonaceous fuels as well as the loss of sinks from deforestation, the balance has been lost and CO₂ is now left accumulating in the atmosphere.

CO₂ even at its recent heightened concentrations makes up only a tiny fraction of the composition of air but its presence has a pronounced effect on the environment due to its ability to absorb and re-emit infrared radiation in the atmosphere. It is an unreactive molecule therefore relatively long lived when compared to CO or HCl which although possess changeable dipole moments so also absorb IR radiation, have limited detrimental affect due to their reactivity and solubility. The effect of carbon dioxide on global warming has been long known with research as early as 1896 by Arrhenius^[1] entitled '*On the influence of carbonic acid in the air upon the temperature of the ground*' accurately describing the relationship between increased anthropogenic CO₂ emissions from burning fossil fuels and increases in retention of the sun's radiation.

The linear structure of carbon dioxide allows for numerous vibrational and rotational states as the molecule bends and stretches therefore is able to absorb many wavelengths of light with the potential to absorb any of the photons it encounters possessing corresponding quantum energies to each transition between energy states. This absorbed energy can then be re-emitted instead of leaving the atmosphere.

The greenhouse effect is responsible for the habitable temperatures experienced on Earth (14 °c instead of – 19 °c)^[2] but the ever increasing levels of CO₂ and other greenhouse gases have led to concern over the effects and implications of anthropogenic climate change not only for ourselves but for the world around us as well as future generations.

Despite the need for CO₂ for life itself it is with this in mind that CO₂ has been classified as a pollutant,^[3] public awareness raised and action finally taken to reduce its presence in the atmosphere.

The challenge of reducing the CO₂ content of the atmosphere is being tackled on many levels with one of the most important being to lower the emissions of the gas in the first place. Individuals as well as businesses are being encouraged to diminish their own carbon footprint by minimising energy use, driving and air travel as well as larger scale carbon capture programs underway.

Carbon capture and storage is seen as an important global mitigation option involving the capture of CO₂ from large man made emission sources, its transport via a pipeline network and its storage in subsurface geological reservoirs.^[4] These storage sites include depleted oil and gas fields, exhausted coal seams and saline aquifers (water permeable rocks saturated with brine) and

are, particularly for the UK's storage options, off-shore. So, to recap, the best strategy at present is to take CO₂ and inject it into the sea. This plan does have its detractors raising the difficulty in ensuring that the CO₂ stays put for example, the environmental implications such as acidification of the oceans (which has already been observed to be having adverse effects on various ecosystems, particularly corals, oysters and other creatures which form calcium based structures, even without deliberate pumping of CO₂), the availability of sufficient suitable space to make any meaningful impact on global CO₂ levels and the cost and commercial viability of what can only at best be considered buying time to find a real solution to the carbon dioxide problem.

The treatment of CO₂ as waste to be buried is, however, not the only option with more and more alternative uses arising as the recycling of this abundant gas is explored. The addition of extra CO₂ in greenhouses to help plants grow and the cleaning of waste gases to replace the manufactured CO₂ used in the vast majority of industrial processes in which CO₂ is commonly employed, such as food and beverage manufacture, would allow for CO₂ to be beneficially exploited without chemical alteration. The energy efficient mineralisation of CO₂ to yield sodium bicarbonate and many useful building products is already known and the process can be operated with flue gases making the relatively costly CO₂ capture and purification steps superfluous. CO₂ can be implemented as a chemical feedstock in the synthesis of many useful bulk and fine chemicals and polymers including urea, aspirin and plastics.^[5] The only problem with this utilisation is the quantity of carbon dioxide for which practical and constructive employment can be found does not necessarily match up with the vast quantities needing disposal.

1.2. Electrochemical CO₂ Reduction;

The energy efficient reduction of carbon dioxide to form a useful fuel source has become the alchemy of the late 20th and early 21st century, with the earliest report of its electrochemical reduction dating back to 1870.^[6]

Although carbon dioxide recycling is blatantly obvious in principle and from a thermodynamic view point is not too unfavourable, as can be seen from table 1.1, with the 8 electron reduction of CO₂ to methane by protons having a standard potential of just -0.24V, the process proves much more difficult due to the formation of high energy intermediates with large kinetic barriers.

	E°/ V (vs. NHE)
$2\text{CO}_{2(\text{g})} + 2\text{H}^+_{(\text{aq})} + 2\text{e}^- \rightarrow \text{H}_2\text{C}_2\text{O}_{4(\text{aq})}$	-0.90
$\text{CO}_{2(\text{g})} + 2\text{H}^+_{(\text{aq})} + 2\text{e}^- \rightarrow \text{HCOOH}_{(\text{aq})}$	-0.61
$\text{CO}_{2(\text{g})} + 2\text{H}^+_{(\text{aq})} + 2\text{e}^- \rightarrow \text{CO}_{(\text{g})} + \text{H}_2\text{O}_{(\text{l})}$	-0.52
$\text{CO}_{2(\text{g})} + 4\text{H}^+_{(\text{aq})} + 4\text{e}^- \rightarrow \text{HCHO}_{(\text{aq})} + \text{H}_2\text{O}_{(\text{l})}$	-0.48
$\text{CO}_{2(\text{g})} + 6\text{H}^+_{(\text{aq})} + 6\text{e}^- \rightarrow \text{CH}_3\text{OH}_{(\text{aq})} + \text{H}_2\text{O}_{(\text{l})}$	-0.38
$\text{CO}_{2(\text{g})} + 8\text{H}^+_{(\text{aq})} + 8\text{e}^- \rightarrow \text{CH}_{4(\text{aq})} + 2\text{H}_2\text{O}_{(\text{l})}$	-0.24

Table 1.1 Carbon Dioxide reduction standard potentials at pH 7.0 (in an aqueous system) Data from ref [7]

Before discussion of electrocatalysis the direct or ‘uncatalysed’ electroreduction of CO₂ should be considered. This can be taken to mean the reduction of CO₂ at an electrode surface, without the introduction of additional molecular catalyst to the system. The process is not necessarily ‘uncatalysed’ as from the investigation

of many materials employed as the working electrode, electrolyte and solvents for CO₂ reduction, it has been seen that some systems are significantly more efficient than others, allowing reduction at lower potentials and influence the products formed, i.e. the surface acts as a catalyst.^[8]

1.2.1. Effect of Electrode material;

Overall electrocatalytic performance and product distribution on different metals and other electrode surfaces has been investigated by Ikeda, Hori and various other groups.^{[9][10][11][12]} The work has reviewed by Jitaru et al^[6] who developed a classification with systems being split into four distinct groups from which products could be predicted; metal highest occupied molecular orbital sp or d (with metals with full outer d-orbital, d¹⁰ configuration, such as Zn, Cd, Hg, Cu, Ag and Au falling into sp group) and whether the electrolyte used is aqueous or non-aqueous.

Jitaru appears to over-simplify the situation as no visible attempt is made to take pH, surface conditions or any of the other variables highlighted later into consideration with these factors having been shown to have a dramatic effect on product formation, but the classification does give an indication of some general trends.

Hori wrote a later, very thorough review^[8] which highlighted many practical issues associated with CO₂ reduction experimental technique as well as mechanistic ideas. The grouping adopted in this work was simply aqueous or non-aqueous and then based upon product distribution of the reduction process with much data tabulated and experimental conditions more fully described.

The electrode material is considered, alongside proton availability, to be the most significant contributor in the determination of the overpotential of and product distribution associated with CO₂ electroreduction.

The mechanisms of electrochemical and photochemical reduction of CO₂ via various methods are still unclear despite many efforts to define them^[13] with the major pathways depicted in the scheme figure 1, covering most of those proposed which seem plausible.^[9]

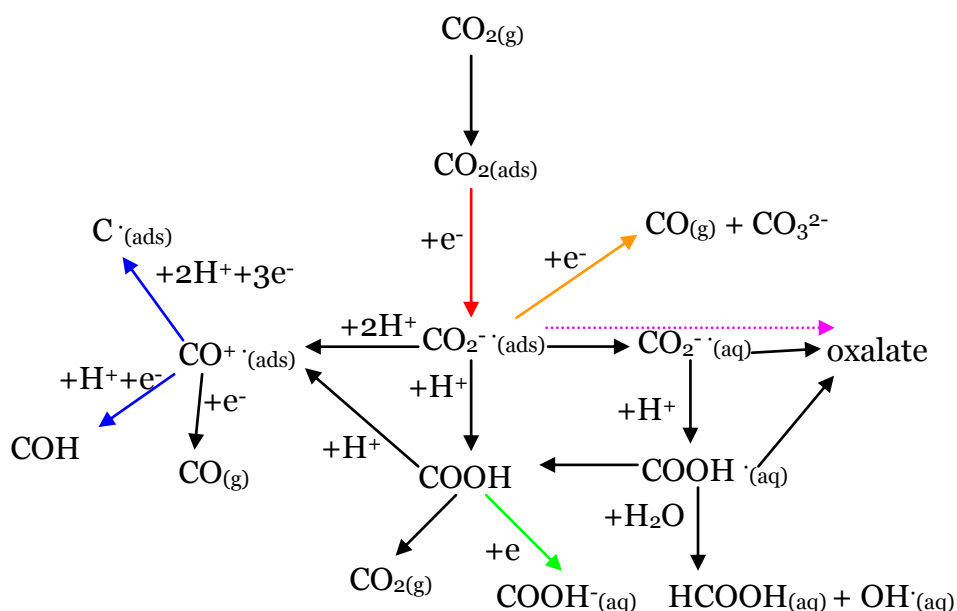


Figure 1.1; Reaction Pathways for Carbon Dioxide Reduction. *Adapted from* [9].

The major pathways shown are;

- The formation of CO₂^{•-}(aq)
- The disproportionation of CO₂^{•-}(ads) and CO₂(g) to give CO and CO₃²⁻
- The reduction of COOH[•] to formate (which is considered among the most useful products)

→ The formation of a range of adsorbed, reduced CO_x^Y species giving CO, hydrocarbons and alcohols.

→ The formation of oxalate without desorption.^[14]

The LUMO of CO_2 is found predominantly on the carbon atom and it is generally accepted that both uncatalysed aqueous and non-aqueous, and many suggested catalysed reduction mechanisms proceed via the high energy intermediate $\text{CO}_2^{\cdot -}$; found in the centre of figure 1.1. The transition between $\text{CO}_{2(\text{ads})}$ and $\text{CO}_2^{\cdot -}(\text{ads})$ has been suggested to be a common critical limiting step seen by the elbow in plots of E vs. I common to most reactions regardless of the end product produced.^[9] This high energy intermediate is associated with the changing geometry of the linear CO_2 molecule to the bent $\text{CO}_2^{\cdot -}$ radical ion, resulting in the observed high overpotential for CO_2 reduction.^[15]

The CO_2 coordinates to the metal via either a η^1 or η^2 bond depending upon the identity of the metal and its surface conditions,^{[6][15]} to give adsorbed carbon dioxide. The $\text{CO}_{2(\text{ads})}$ then accepts an electron to form the adsorbed radical species, $\text{CO}_2^{\cdot -}(\text{ads})$, from which a number of reaction pathways are possible.

In non-protic solvents, from this one electron reduced intermediate the different possible products are seen on the right hand branch of the scheme and limited to CO and carbonate or oxalate.^[16] As will be discussed subsequently, this ideal non-protic system is rare, with the availability of protons from trace water, supporting electrolyte or other sources common.^[8]

The uncatalysed reaction pathways do show a fairly strong correlation with the affinity of CO_2 towards the metal, specifically its adsorption and desorption

properties; the longer the carbon atom of the CO₂ is held complexed to the metal, the more highly reduced the products formed tend to be.^{[6][8][13]}

The metals reported to be most effective for direct CO₂ reduction commonly have small numbers of electrons in sp orbitals and/or full d-orbitals, (e.g.; copper, palladium). Transition metal electrodes have been reported to dramatically reduce the overpotential of reduction to at least 500 mV anodic of E⁰ for CO₂ → CO₂^{-•}. Sullivan et al^[17] find E⁰=+0.1 V vs. SHE for CO₂ + 2H⁺ + 2e⁻ → HCOOH on copper, which is much more positive than that calculated from Gibbs energy of formation. Coordination of the CO₂ to M can activate the CO₂ - and promote its reductive disproportionation shown by the yellow arrow on figure 1.1 and equation 1.1 below;



Upon addition of even trace quantities of water to non-aqueous solvent, the radical can undergo protonation either by substitution, where the CO₂^{-•} (ads) is added across a M-H bond, or reaction with a co-adsorbed water or hydrogen atom to give MOCOH.

CO₂^{-•} (ads) may be released into the electrolyte where it can react with water (or other proton source) to give COOH[•], which can then be readsorbed, react further to give COOH + OH[•] or may dimerise to give C₂H₂O₄.

Oxalate formation is traditionally, although not exclusively, associated with non-aqueous systems. It has been observed in basic aqueous solution at carbon based electrodes with tetramethylammonium cations at relatively positive potentials (-0.74 V (vs. SCE) at pH 10).^[18] This was thought to be a result of the stabilising effect of the adsorbed cations on CO₂^{-•}.

Oxygen can be removed from the $-M-CO_2^-$ species via electrophilic attack by water or other electrophile. This route is favoured by metals of a basic nature like copper.

Adsorbed COOH species formed by the protonation reaction in carboxylic form, unless stabilised, will tend to revert back to $M-H + CO_2$ or undergo nucleophilic attack to give $M-CO^+$ (i.e.; $M-C=O$). This reactive intermediate is thought to be commonly formed for Cu, Ru and some other d-block metals and is believed to be present in the pathways resulting in highly reduced products.

Copper has been found to stand out from the majority of metals and been much investigated, primarily in aqueous and methanol solutions, as it catalyses the cleavage of the C-O bonds of CO_2 and allows the formation of highly reduced products such as methane, ethane and ethanol thought to be due to the co-adsorption of CO_2 and H_2O on different sites of the copper surface or the presence of other pre-adsorbed species.^{[19]-[22]} As well as reduction of CO_2 from solution gas diffusion electrodes (GDE) and solid polymer electrolyte (SPE) incorporating Cu have been reported to form hydrocarbons from gas phase CO_2 .^{[23]-[25]} The current density obtainable at these electrodes is considerably higher than the aqueous or methanol systems employing standard electrodes due to the more effective mass transport and high electrode working area, however, with respect to the overpotentials required and durability, they require further development.

A molybdenum electrode was reported to yield methane with reasonable Faradaic efficiencies (50-100%) at -0.8V (vs. SCE) but unfortunately with low current density, and the mechanism for the process is not known.^[26] Methane

formation has been found to be blocked by increased pH and operating pressure,^{[10] [27] [28][29]} which would tend to leave the formate pathway unaffected therefore allowing selectivity of product.

The addition of a proton and an electron to the intermediate CO^{+*} species can occur to give the further reduced M-CHO , an excellent starting material for formation of alkanes, alkenes, alcohols and aldehydes.^[9] If C^\bullet is formed and subsequently reacts with protons and electrons ethene and methane can be formed.

Some groups investigating this route however reported deactivation through carbide build up on the electrode surface. This deterioration was noted on copper by a number of researchers^{[9] [27] [30-35]} but was minimised by modulating applied potential or pulsing or the use of ultrasonic equipment.^[35] One group found their copper electrodes suffered a loss of activity due to graphite deposition (XPS analysis confirmed) therefore the electrodes were etched in nitric acid before each measurement or had a potential of -150 mV vs. SCE applied for no longer than 1 minute.^[34] Bard et al^[36] found that the Faradaic efficiency of CO_2 reduction was optimum after 20 minutes of experimentation, dropping to almost zero after 120 minutes on copper in 0.5 M KHCO_3 with a CO_2 flow of $45 \text{ cm}^3 \text{ min}^{-1}$. This deactivation was not however observed by Hori and his associates who showed that with careful preparation and pre-electrolysis (application of a potential slightly more negative than the potentials to be applied during the experiment for ~60s) of electrolyte used, no deactivation was observed. They instead suggested that solution phase impurities were a more likely cause of the deactivation than product build up.^[8]

Higher pH solution increases the presence of 'H' on the electrode and the amount of carbon dioxide in solution, therefore electrodes with low affinity for hydrogen adsorption such as aluminium will exhibit optimum CO₂ reduction kinetics at high pH but for others (eg. Palladium) the stronger M-H bonds will mean that H_(ads) will dominate the electrode surface, inhibiting CO₂ reduction.

Different surface preparation of electrodes will also dictate the type of bonding of CO₂, its strength and therefore its reaction products and efficiency. This has led to a notable variation in findings in experiments under conditions which are otherwise very similar.^{[37][38]}

From work done by Hori *et al*^[39] it is seen that although CO-species are recognised as an intermediate in many routes to CO₂ reduction, as illustrated in figure 1.1, if employed as the starting material CO is less reactive with less reduction taking place on the copper electrode implemented in his work. This is suggestive of a difference in the binding of carbon dioxide compared to carbon monoxide; possibly less CO is adsorbed or the M-CO bond, as opposed to the M-CO₂ bonds is too strong for catalysis.

These findings were supported by overall lower yield of products with CO as a reactant compared to CO₂ more recently.^[40] This was attributed to strong M-CO adsorption blocking the initial hydrogen reaction sites.

As should be now quite evident carbon dioxide reduction and the final product distribution depends on many factors as well as the electrode material including; proton availability, presence of catalyst, identity of electrolyte, applied potential, mass transport, carbon dioxide concentration, pH and temperature as well as more subtle effects such as the physical structure of the

electrode. This is illustrated by the variety of possible product distributions obtained utilising various pathway steps, each of which having a preference toward different conditions, where small changes can lead to competitive reactions and different routes, making generalisations based on individual studies very dubious and grouping difficult.

1.2.2. Effect of the Electrolyte;

The effect of electrolyte upon CO₂ reduction is, compared to the extensive research conducted into electrode material, a relatively understudied area riddled with ambiguity. In much of the CO₂ reduction literature the supporting electrolyte is assumed to act as simply a charge carrier, despite the significant effects that the ion identity can have on not only the electrical double layer, a region with influence over all electrode processes (see figure 2.6), solvent properties (such as viscosity and solvating parameters), but also ion pairing stabilisation of radicals and ions generated as well as prospective specific interactions with species of interest and the electrode surface.

Due to the unique properties of Cu toward CO₂ reduction, systems in which this is employed as the electrode material have received the greatest degree of academic interest with respect to the effects of electrolyte, particularly in aqueous^{[41][42][43][44]} and methanol systems.^{[45][46][47]} The use of methanol as a solvent for CO₂ electroreduction is industrially pertinent as along with N-methylpyrrolidone (NMP) and the Purisol process, MeOH is used as a CO₂ scrubbing solvent under the process name Rectisol.^[48]

From the comparison of these studies, and the limited studies available in non-protic systems (DMF)^{[49][50]}, reports are often completely contradictory, e.g. NH_4^+ is reported as an effective electron mediator, enhancing CO_2 reduction in the photochemical CdTe DMF system^{[49][50]} however reportedly yielding only hydrogen in MeOH and aqueous systems with Cu WE.^{[43][46]} This suggests that the electrolyte behaviour is very much dependent upon its environment.

Electrolyte is likely to show an effect upon CO_2 reduction through the following;

- Adsorption at the electrode surface
- Alteration in the hydrophilicity of the solution near the electrode
- Alteration of the pH of solution near the electrode
- Specific or ion-pairing interaction with the species of interest
(resulting in significantly different stabilisation to that offered by the solvent)

Each of these factors is dictated by the electrode material and/or the nature of the solvent employed.

For non-aqueous solvents, such as those employed for much of this work, the correlation with reported data measured in aqueous systems is, as such, fairly improbable.

Some broad trends recurred throughout the studies;

- CO₂ reduction rates can be significantly affected within the system by electrolyte size and charge.
 - Rates increased $\text{Cl}^- < \text{Br}^- < \text{I}^-$ for CO₂ reduction in MeOH/H₂O on Cu.^{[41][44]}
 - Rates increased upon moving from Na⁺ to La³⁺ in an aqueous Cu system.^[41]
- The product distribution and current efficiencies can be altered by cationic and anionic nature.
 - Formation of CH₄ was found with increasing current efficiencies $\text{Li}^+ < \text{Na}^+ < \text{Cs}^+ \approx \text{K}^+$ in an aqueous Cu system.^[43]

Of particular relevance to the research reported here is the influence of tetraalkylammonium salts on CO₂ reduction and electrolyte in non-protic media. Although, as mentioned, many of the effects seen are very much system specific, some of the behaviour reportedly associated with NR₄⁺ cations are now discussed.

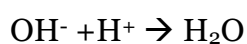
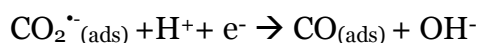
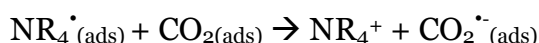
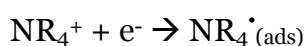
A study of the effects of these electrolytes on CO₂ reduction, again on a copper electrode, found that a subtle change in the cation gave a drastic change in the product formed.^{[51][52]}

The electrolytes used in the study were tetrabutylammonium tetrafluoroborate (TBAT), tetrabutylammonium perchlorate (TBAP) and tetraethylammonium perchlorate (TEAP). The CO₂ was used at very high concentrations; its mole fraction (χ) was 0.34 at 4.0 MPa and 0.94 at 5.8 MPa. The copper electrode was etched in concentrated H₃PO₄ before use.

The TBAT and TBAP systems gave CO and HCOOCH₃ as products whereas the TEAP produced methane and ethene. Note, the only (minor) difference between the TBAP and TEAP systems is the chain length of the cation. The total Faradaic efficiency was >90% for all electrolyte systems, but CO production decreased and hydrocarbon production increased when TBAP was swapped for TEAP.

Large NR₄⁺ cations have been reported as shifting CO₂ reduction to more negative potentials and decreasing the associated rate constant as their size increases, hypothesised to be due to the blocking effect of the compact layer of adsorbed cations.^[53]

This effect is perhaps linked to the reported catalysis seen by tetraalkylammonium cations in the direct CO₂ photo-electroreduction on CdTe in DMF and acetonitrile.^{[49][50]} The catalysis was reportedly most greatly enhanced by the shorter alkyl chain length with NH₄⁺ optimal. The supposed mechanism through which the enhancement was obtained was given as;^[50]



The hypothesised adsorption and electron transfer through the cation was further supported through experiments employing crown ether catalysts in the solution. It was reported that upon addition of these ring structures, the tetraalkylammonium species best able to fit within the cavity now yielded the higher catalytic activity. The additional lowering of the overpotential in this case

was thought to be a result of a similar mechanism, with the crown ether allowing the ammonium ion to get closer to the electrode surface (specific adsorption in the inner Helmholtz plane, rather than outer Helmholtz), increasing the rate of electron transfer to the NR_4^+ species.^[50]

A study comparing CO_2 reduction in the presence of TBA^+ and Li^+ in MeOH at a Cu electrode again reported TBA^+ to catalyse the process through electron transfer and possible ion pair stabilisation of the CO_2 radical anion, to yield CO.^[46] Where Li^+ was employed the overpotential associated with the reduction was higher with the primary product being methyl formate. The anions were found to have little impact upon the product distribution or potentials.

The difference in product distribution seen when employing tetraalkylammonium salts compared to lithium salts was rationalised in terms of the difference in hydrophilicity of the cations. TBA^+ is a hydrophobic species therefore a route requiring less protons is preferential, whereas Li^+ offers a hydrophilic environment promoting the incorporation of protons. The formation of methyl formate (the CO_2 reduction product in the presence of Li^+) was however observable in the absence of CO_2 .

The differing overpotentials required for the respective systems was attributed to the ion pairing stabilising effects of the cations on the $\text{CO}_2^{\cdot-}$. Formation of $\{\text{TBA}^+-\text{CO}_2^{\cdot-}\}$ would be expected to stabilise the radical to a lesser extent than $\{\text{Li}^+-\text{CO}_2^{\cdot-}\}$ due to the size disparity of the species. The higher stability offered by the formation of $\{\text{Li}^+-\text{CO}_2^{\cdot-}\}$ is proposed to result in the second electron transfer to the CO_2 becoming more difficult and requiring a higher applied bias.

In experiments where both Li^+ and TBA^+ were present higher overpotentials were required and lower current efficiency was reported than in the solely TBA^+ case leading to the conclusion that Li^+ suppresses CO_2 reduction.

The paper reports that no deactivating film was observed upon the electrode surface in the presence of Li^+ due to the voltammetry measured before and after electrolysis being identical.

This is somewhat surprising as the formation of lithium related films at the electrode surface of noble metals (such as copper, gold and platinum) when applying negative potentials is fairly well documented, due to this being a significant challenge faced by developers of the lithium ion battery.^{[54]-[59]} The nature of the films and potential at which they are formed is strongly dependent upon the electrode material, solvent and in some cases, impurities present in solution.^{[54][56]}

In solvents similar to the ones employed within this research, aprotic organic solvents, at noble metal surfaces in the absence of CO_2 the variation in products with applied potential is well documented with the summation of the findings, supported by research from several different groups, presented in figure

1.2.^{[54][55][56]}

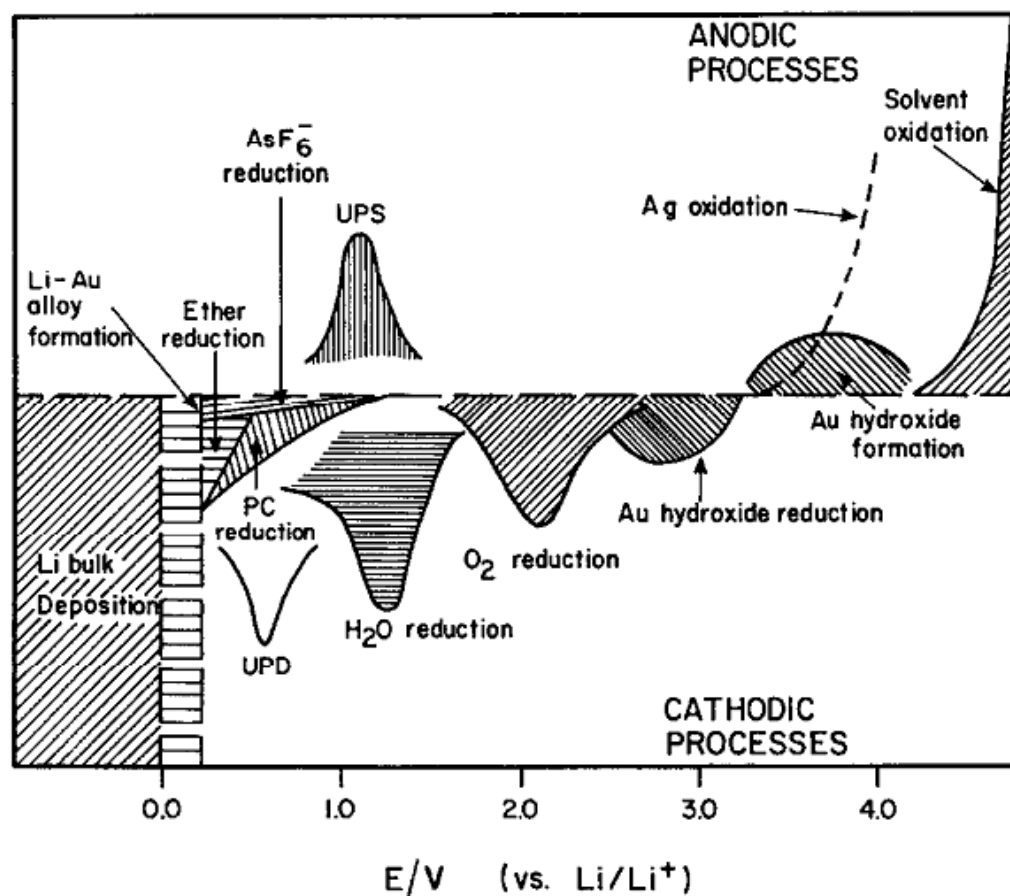


Figure 1.2; A schematic view of the typical electrochemical processes found in Li salt solutions of aprotic solvents at a noble metal electrode (Ag/Au). Reproduced from [54]

As evident from figure 1.2, prior to the bulk reduction of the Li^+ to Li metal on the electrode several other reductions are reached including that of trace oxygen and water as well as the underpotential deposition region. Each of these processes is reported to result in significant changes to the electrode surface. Upon reduction of O_2 the products rapidly react with Li^+ forming a LiO_2 and Li_2O_2 layer at the electrode surface, passivating the surface toward further O_2 reduction but showing little effect toward other reductions. Upon reduction of H_2O a LiOH and Li_2O solid layer is formed, with evidence of this layer being further reduced to LiH . More negative still, the UPD of Li can occur.

A similar situation is found for all alkali metal salts.^[58] This metal based layer formation results in the previously noble metal being significantly altered and in some situations passivated toward further electron transfer with surface specific processes (such as CO₂ reduction) likely to be greatly affected.

1.2.3. Effect of CO₂ Concentration;

CO₂ reduction to give hydrocarbon products in aqueous solution is reportedly less efficient at high CO₂ concentrations as excess CO₂ at the electrode surface is thought to prevent the inclusion of hydrogen atoms to the products by preventing access by water and adsorption sites for H.^[29] When the reactants were stirred, CO was reported as the main product yet CH₄ is reported without stirring.

In non-protic solvent if the local CO₂ concentration is low, due to either low solubility or slow mass transport (lack of stirring), oxalate is reportedly formed from the dimerisation of two CO₂^{•-}. If the CO₂ concentration is higher the anionic radical is more likely to combine with a CO₂ molecule to give OCOCO₂^{•-} which then undergoes a further one electron reduction yielding carbon monoxide and carbonate.^[60] If even a few percent of water is added to the solvent the CO₂^{•-} is often found to react with this instead and undergo a second reduction to yield formate shown by the green arrow on figure 1.1.^{[9][60]} This is analogous to the oxalate/CO formation seen upon some surfaces in non-protic solvent.

The reduction of CO₂ on rotating electrodes has been studied allowing for the removal of any possible mass transfer limitations, from what is, suggested by Wasmus, a diffusion controlled process.^[34]

1.2.4. Effect of Temperature;

Higher temperature should favour reaction products of higher activation energy but as well as reducing overpotentials and increasing rate, the solubility of carbon dioxide is reduced, which in aqueous solution is not very high (0.033 mol dm⁻³ at standard temperature and atmospheric pressure at pH 7)^[9] and the lifetime of species adsorbed is also lowered.

The use of organic solvent allows for this limited solubility to be overcome with the ability to dissolve substantially more CO₂ (equilibrium solubility of CO₂ in THF is 0.205 mol dm⁻³ at 25 °C and atmospheric pressure).^{[61][62]} Against this advantage, it should be noted that non-aqueous solvents tend to have low electrolytic conductivity, which can lead to high ohmic losses.^[63]

The lowered conductivity of non-aqueous compared to aqueous electrolyte solutions is due to a number of factors;

- The solubility of ions tends to be lower in non-aqueous solvents.
- Ions employed in non-aqueous systems are larger therefore typically possess lower mobility.
- The electrolytes do not completely dissociate in non-aqueous solvent, with a portion left as ion pairs.

In non-protic solvents, increase in temperature reportedly leads to a change in the products of CO₂ reduction with CO favoured over oxalate formation at higher temperature.^[14]

The reduction of CO₂ to CO has received enormous attention as it is possible to carry out this two electron reduction without formation of the free CO₂ radical anion, in doing so lowering the overpotential therefore current efficiencies and rates tend to be fairly high. Carbon monoxide is the feedstock for various synthetic processes, such as the d-metal catalyzed Fischer-Tropsch (production of hydrocarbons), Monsanto, and Cativa (both acetic acid) processes. Carbon monoxide also has significant fuel value ($\Delta_c H^\circ$)-283.0 kJ mol⁻¹) and can readily be converted into methanol (e.g., by the CuO/ZnO/Al₂O₃-catalyzed ICI-process) for use as a liquid fuel.^[64]

1.3. Electrocatalytic CO₂ Reduction;

Carbon dioxide transformation into more complex molecules via chemical catalysis is done on a massive scale by photosynthesis in organisms all over the planet using enzymes and electromagnetic radiation to carry out the photosynthetic reaction. This efficient process has inspired much work into the creation of catalysts to act as enzyme mimics (and investigation of actual enzymes in electrochemical systems).^{[65][66][67]}

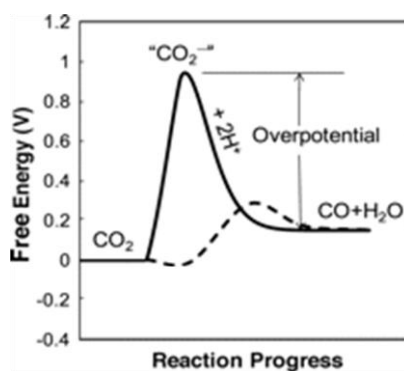


Figure 1.3; Schematic illustrating the activation barriers for CO₂ reduction to CO in protic environment in the presence (dashed line) and absence (solid line) of a catalytic species. Adapted from ref [68]

An ideal catalyst would allow for a lowering of the overpotential needed for CO₂ reduction as suggested by figure 1.3, but also allow for selective product formation at high efficiencies, with reasonable stability and rate, which can be easily separated from the products formed. Many of these requirements have been met in various forms but to date no research has managed to combine all of these prerequisites.

There have been catalysts developed or discovered for use in both aqueous and non-aqueous environments where the function of the catalytic species within the system is dependent upon an array of factors (as may be predicted from the

already complicated direct reduction!). The electron transfer between the catalytic species and the CO_2 can be divided into inner sphere (chemical catalysis) or outer sphere (redox or quasi redox catalysis). In his review of molecular catalysis in electrochemical reactions, Sav  ant dedicates several pages to the reduction of carbon dioxide and addresses the distinction between the catalytic processes.^[60] Redox and “Quasi Redox” catalysis is illustrated in Figure 1.4.

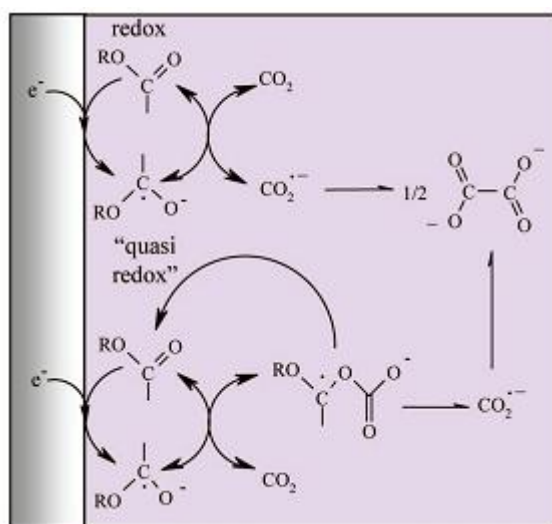


Figure 1.4: Quasi Redox Reaction Mechanism of CO_2 reduction reproduced from [60]

This reactivity is illustrated in figure 1.4 by aromatic esters and nitriles^{[60][69]} but is also reported to be exhibited by some nickel macrocycles and 1-electron reduced Ag^{II} and Pd^{II} complexes.^{[60][15]} The CO_2 radicals are produced via a two step process seen in the diagram above with the rate determining step the cleavage of the adduct of the carbon dioxide and the catalytic anion radical (in figure 1.4, an ester or nitrile species).

The product of CO_2 reduction via a redox catalyst in non-protic media at a non-catalytically active electrode surface (such as mercury) is reported to be exclusively oxalate.^[16] When the catalytic efficiency decreases as the standard

potential of the catalyst couple becomes more positive, this is suggestive of a redox catalysis mechanism which proceeds through the generation of the high energy intermediate $\text{CO}_2^{\cdot-}$.

Chemical catalysts involve more complex interaction between the active form of the catalyst and the substrate (CO_2), either inner-sphere electron transfer where bonding in the transition state lowers the activation energy compared with the outer-sphere, or an adduct between CO_2 and the catalyst allowing for easier reduction. An inner sphere mechanism allows the bypass of the $\text{CO}_2^{\cdot-}$ intermediate formation.

A multitude of catalytically active species for CO_2 reduction have been reported. An overview of these catalysts is presented in this section, focussing upon homogeneous electrocatalysts split into three sections; macrocyclic species, transition metal carbonyl complexes and other catalysts of interest including enzyme mediated and proposed simple molecular catalysts with an example from each group examined more thoroughly.

1.3.1. Macrocyclic Catalysts;

From the very first CO_2 electroreduction catalyst, a metallophthalocyanine, reported by Meshitsuka *et al* in 1974,^[70] macrocyclic species have featured highly in the discovery and development of CO_2 electrocatalysis, yielding some of the most efficient and promising examples to date.^[16] A wide range of different macrocyclic species have been found to exhibit catalytic ability in both aqueous and non aqueous systems, the species including; cyclams and similar

aza-macrocyclic structures (e.g. fig 1.5), M-phthalocyanines (e.g. fig 1.6) and porphyrins (e.g. fig 1.8).

1.3.1.1. Cyclam-based Species;

The metals incorporated into the structures reported were generally Co and Ni with the catalyst adsorbed on an electrode surface (generally Hg),^{[71]-[76]} in supported polymer films or electropolymerised^[77] and most recently, adsorbed at a supercritical CO₂-water interface.^[78] Both the aqueous and non aqueous systems were found to yield CO however with varied efficiency, turnover number and overpotential.

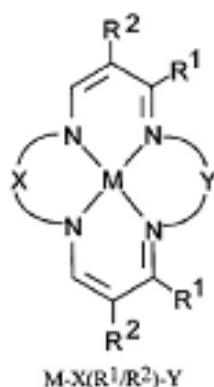


Figure 1.5; Ni(II)-cyclam structure where M=Ni

A very selective electrocatalyst for CO₂ reduction to CO is [Ni(II)-cyclam], which was studied extensively by Sauvage^[72] and found to catalyse carbon dioxide reduction on mercury electrodes at ca. 0.5 V below the calculated thermodynamic value ($E^0 = -0.41$ V vs. NHE at pH5) at a “remarkable” velocity (to quote the authors) of ca. 32 h⁻¹ with 95% CO formation current efficiency. The catalyst was reported to cycle more than 1000 times with no notable deactivation. The system was found to be pH dependent, anion specific, prone

to deactivation through CO build up (resulting in Ni(cyclam)(CO) precipitation if solution is not stirred) and reported to require a Hg surface for appreciable rates and turn over.^{[7][72]}

This system was, however, further developed more recently (2011) with Ni(cyclam) successfully employed as an aqueous molecular catalyst in the absence of Hg in the interfacial photoreduction of CO₂ to give CO and H₂.^[78] The proposed mechanism is reproduced in figure 1.6.

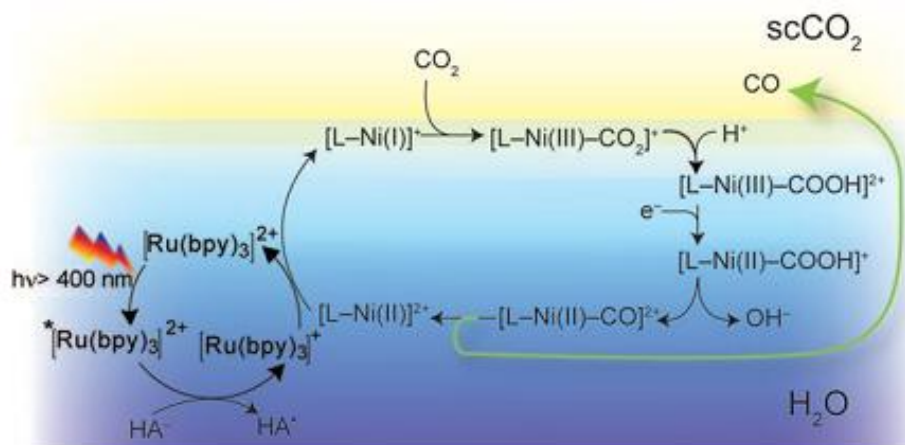


Figure 1.6; Proposed catalytic cycle for the photoreduction of CO₂ catalysed by Ni(II) cyclam at the sc-CO₂:water interface reproduced from ref [78]

Mechanistically the source of energy for the catalyst activation, whether from direct electroreduction or photoactivation, is unimportant for the CO₂ reduction.

The work was conducted at high pressure (up to 144 bar) which was reported to enhance CO₂ reduction by Ni(cyclam) at the interface, with the apparent rate limiting step in their system reported to be the photosensitisation.

The planar ligand geometry of the Ni(cyclam), allowing access to the metal centre, has been suggested to be of significance with respect to the catalytic ability exhibited.

1.3.1.2. Metallophthalocyanines;

The very first reported CO₂ electrocatalysis states that when the electrode was coated with cobalt phthalocyanine, the cyclic voltammetry measured in aqueous solution showed a reduction current peak with height proportional to the concentration of CO₂ at a less negative potential than previously found.^[70] The efficiency, products and mechanism were not considered. The potentials were later found to correspond to the potentials at which the metallophthalocyanine catalyst is found in its di-negative state with its dz² orbital occupied and an excess of ligand π electrons.^[27]

The Co phthalocyanine was developed further to give water soluble tetrasulphonated Co and Ni phthalocyanines of the structure shown in Figure 1.7.

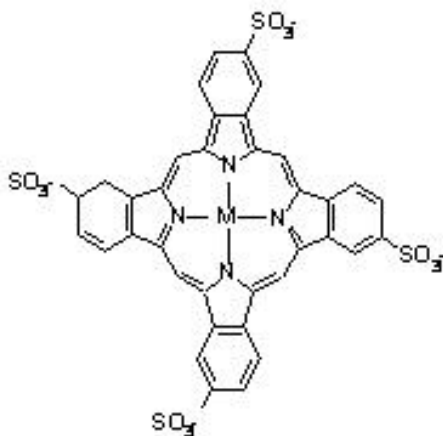
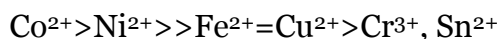


Figure 1.7; Stucture of tetrasulphonated M-phthalocyanine

The tetrasulphonated compounds were reported to lower the reduction potential by about 0.3 V at 1 mA cm⁻² compared to the uncatalysed systems. The metal centre found in the phthalocyanines has a strong influence on their catalytic activity with the relative order;^[67]



The current efficiency and product distribution of these species are reported to be heavily influenced by pH; At -1.2 to -1.4 V (vs. SCE) at pH > 5 the main product is formic acid, formed with a current efficiency of ca. 60%. At lower pH methanol is also produced, but with a current efficiency of < 5%.

1.3.1.3. Porphyrins;

Porphyrins, the final group of macrocyclic complexes to be addressed, with metal centres of Fe and Co have been thoroughly investigated as homogeneous molecular catalysts in non-aqueous systems.^{[79]-[82]} Polymer films incorporating the supported porphyrins with a wide array of different transition metal centres have also been reported as CO₂ reduction electrocatalysts, with Co and Ni found to be significantly more efficient.^[83] All of the porphyrin systems were found to yield primarily CO.

Savéant *et al* first reported the activity of Fe-porphyrins toward CO₂ reduction in the early 90's finding that CO was formed with high efficiency at -1.8 V (vs SCE) in DMF.^[82] The initial porphyrins were found to be unstable and degraded rapidly however upon further experimental investigation it was discovered that

the addition of Mg^{2+} , a hard electrophile, led to significant stabilisation of the system through the formation of MgCO_3 .^[7]

More recent development of the Fe-porphyrin system led to the inclusion of phenolic groups in all ortho and ortho' positions on the phenyl groups^[84] as depicted in figure 1.8.

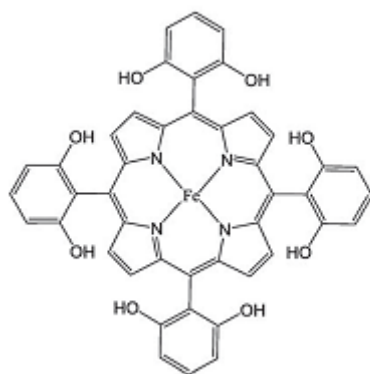


Figure 1.8; Iron 5, 10, 15, 20-tetrakis(2',6'-dihydroxyphenyl)-porphyrin, FeTDHPP.
Reproduced from [16]

This modified Fe-porphyrin catalyst was reported to give CO in Faradaic yields >90% through 5×10^7 turnovers over 4 hours at an overpotential of just 0.465 V in DMF with 0.2 M water added causing no observable degradation. The enhancement in activity was attributed to the higher local concentration of protons associated with the phenolic hydroxyl groups.

From a recent review (2013) and comparison of the catalytic activity and efficiency of CO_2 electroreduction catalysts for which the data is available, through a series of benchmark evaluations this modified Fe-porphyrin catalyst was reported as being the most efficient catalyst developed to date with a lower overpotential and turnover number higher than the other catalytic species analysed (albeit evaluated by the Fe-porphyrin group).^[16]

1.3.2. Polypyridyl Catalysts;

Some of the most well recognised CO₂ reduction electrocatalysts are polypyridyl complexes, incorporating a transition metal centre and often CO ligands. A vast array of predominantly ruthenium and rhenium (but also rhodium, osmium, nickel, cobalt, iron, copper and more recently manganese) metal centred structures containing bipyridine, or closely related ligands, are reported as showing activity toward CO₂ reduction.^{[85]-[89]} Those reported pre-2007 are tabulated, along with the ligand structures and system details in a comprehensive review,^[60] numbering well over 50, employed both as homogeneous catalysts and within polymer films. A selection of the most prominent are addressed below.

1.3.2.1. Rhenium bipyridyl Systems;

The Lehn group reported the electrocatalysis of CO₂ reduction by Re(bpy)CO₃Cl in 1984 forming CO at -1.49 V vs SCE in DMF-H₂O (9:1) solution.^{[85]-[88]} The associated current efficiencies were 98% with the complex exhibiting excellent selectivity for CO over H₂ production. Despite the relatively low turn-over frequency of 21.4 h⁻¹ this remains to date one of the best and most well studied CO₂ electrocatalysts with research into this system still underway almost 30 years on.^[90] The development of this system led to inclusion of tertiary butyl groups at the 4,4' positions of the bipyridyl ligand^[91] and protic additives to the system^[92] increasing the previously limited TOF to >250 s⁻¹.

The mechanistic details of the catalysis by $\text{Re}(\text{bpy})\text{CO}_3\text{Cl}$ and the derived species is, at present, considered incomplete however the currently accepted mechanism involves the two electron reduction resulting in the loss of the labile chloride (or similar) ligand to form the tricarbonyl anion species, reported to be the active form of the catalyst. The subsequent mechanistic steps are depicted in figure 1.9, although the order of the electron transfer and protonation steps remain undetermined, however the ligand loss and subsequent transfer of electron density to the metal centre have been reported as essential steps in the process.^[93]

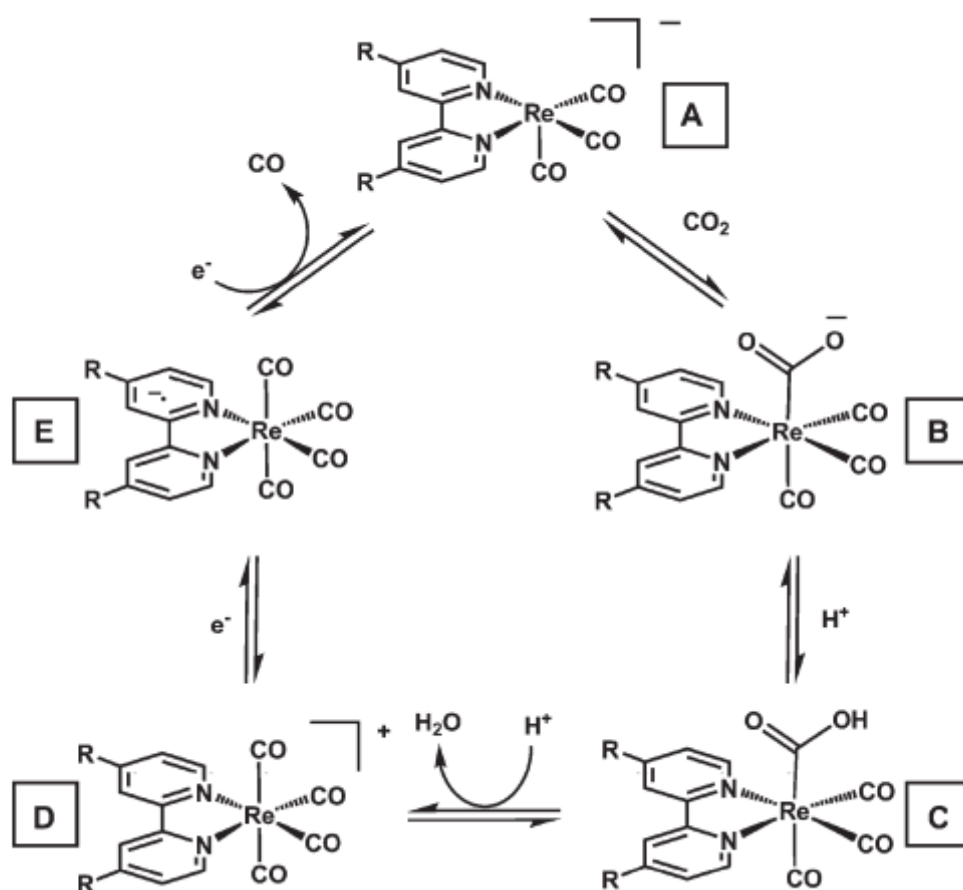


Figure 1.9; Proposed catalytic mechanism of CO_2 reduction to CO by rhenium bipyridyl complexes reproduced from [90]

1.3.2.2. Ruthenium bipyridyl Systems;

In the study of $[\text{Ru}(\text{bpy})_2(\text{CO})\text{H}]^+$ in CO_2 saturated CH_3CN with added H_2O ^[51], CO_2 was reported as being reduced to formate anion and CO with proposed key steps for formate production being 1) Reductively induced insertion of CO_2 into Ru-H and 2) Reformation of Ru-H by reduction of H_2O as seen in figure 1.10.

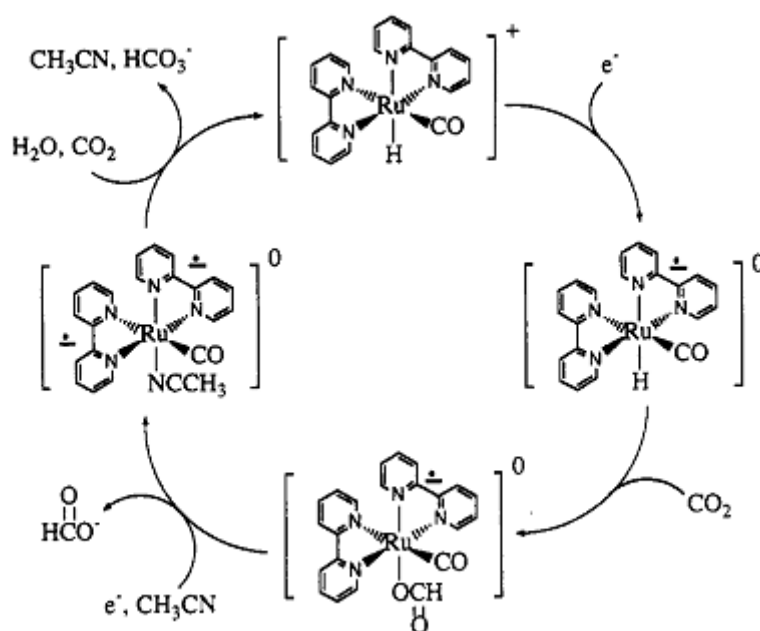


Figure 1.10; Proposed mechanism for CO_2 electroreduction by $[\text{Ru}(\text{bpy})_2(\text{CO})\text{H}]^+$ reproduced from [94]

The insertion and two electron attack rely on interactions between the reduced complexes and CO_2 as the electrophile. In this case both are activated by the occupation of the π^* orbitals of bipyridine. The ligand based reduction exerts a strong influence on reactivity as electron density at the metal centre and in the metal hydride bond is reported as increased making them more susceptible to CO_2 attack. For $[\text{Ru}(\text{bpy})_2(\text{CO})\text{H}]^+$ in the absence of CO_2 reversible processes were observed at $E_{1/2} = -1.45 \text{ V}$ and -1.65 V (vs. SSCE) attributed to reduction of

bipyridine ligand. Upon saturation of the solution with carbon dioxide there was a large increase reported in current at both potentials.

Tanaka *et al* developed a series of very similar electrocatalysts of the formulae $\text{Ru}(\text{bpy})_2(\text{CO})\text{Cl}^+$ and $\text{Ru}(\text{bpy})_2(\text{CO})_2^{2+}$, however, in contrast to the work above reported their mechanistic processes as in keeping with that observed for the $\text{Rebpy}(\text{CO})_3\text{Cl}$ (see figure 1.11).

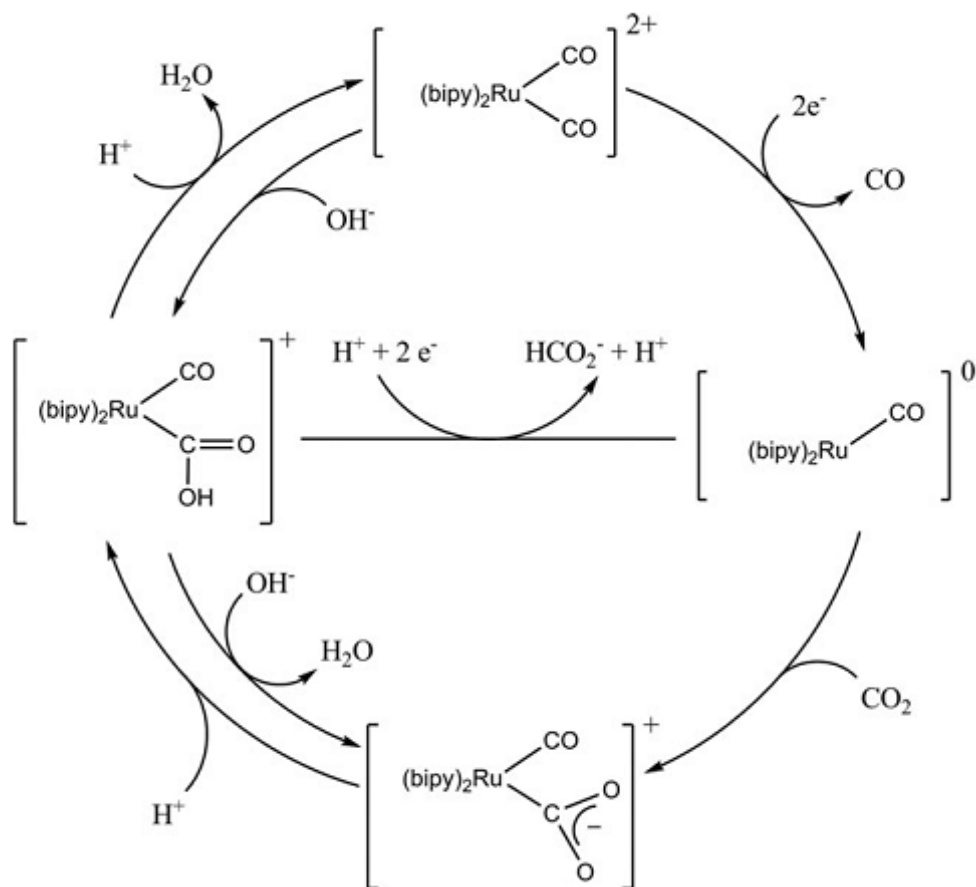


Figure 1.11; Tanaka catalyst proposed mechanism reproduced from ref [7]

The product of CO_2 reduction was found to be pH dependant with acidic conditions favouring CO production and basic solution resulting in formate as the primary product.

Both of the Ru systems were however only reported to be active with respect to CO₂ reduction in systems where water was present.^[95]

1.3.2.3. Osmium bipyridyl Catalyst;

Another similarly structured complex based around an osmium metal centre, *cis*[Os(bpy)₂(CO)H][PF₆] was reported by Sullivan et al^[17] to lead to associative activation of CO₂ in non-aqueous solution. At a platinum electrode the reduction took place at −1.4 to −1.6 V (vs. a NaCl saturated calomel electrode). The proposed mechanism in this case is again different with the complex accepting 2 electrons to give the active species which, instead of CO loss or insertion, then reacts with CO₂, binding as an extra ligand (coordination sphere expansion). The proposed reaction mechanism is reproduced in figure 1.12.

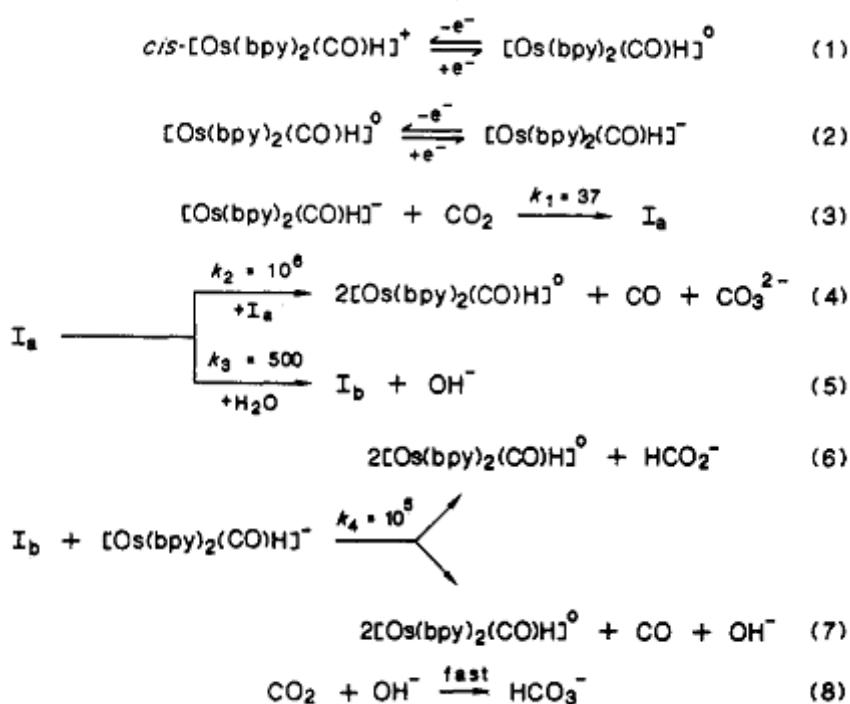


Figure 1.12; *cis*[Os(bpy)₂(CO)H][PF₆] catalyst proposed mechanism reproduced from ref [17]

As seen from the scheme in figure 1.12, there are different routes proposed where either the initial interaction with the catalyst results in the disproportionation or two of the di-reduced molecules may combine to give an uncharged complex and disproportionation products, CO and carbonate.

In the experiments where water was present (including trace water of less than 10 mM,) they reported the incorporation of a proton into the intermediate di-reduced species, followed by combination to give formate or CO and hydroxide.

The complex structure was investigated with the H found cis to the carbonyl being swapped for ligands of different sizes, $H \rightarrow CH_3 \rightarrow CH_2-C_6H_5 \rightarrow C_6H_5$. It was seen that the rate constant for the reaction decreased with increasing size of this ligand. The trans structure was also trialled as a catalyst but the less sterically demanding configuration was less active. This highlighted the impact of relatively small differences in the molecular structure of the catalyst with a pronounced effect upon catalytic ability seen.

As highlighted by the range of different mechanistic ideas published for seemingly similar polypyridyl complexes, often under similar conditions, the role of the pyridyl species is decidedly unclear. The observed trend appears to suggest that Re complexes tend to produce carbon monoxide with Ru producing formate or carbon monoxide presumably due to the differing affinity of the metals for CO₂ and H₂O as observed for the product profiles for direct reduction on different metal electrodes, or possibly as a result of different interactions and mechanism of catalysis.

It is tempting to assume that any complex with a bipyridyl ligand will be active toward CO₂ reduction as so many are with a high proportion of these having the bipyridine intimately involved in the suggested mechanism. This is, however, not the case as demonstrated by Ru(bpy)₃²⁺ which shows no activity toward CO₂ reduction.^[96]

1.3.2.4. Other Polypyridyl and Similar Catalysts;

A family of CO₂ electrocatalytic complexes containing bipyridyls reported as not directly involved in their catalytic interactions are the ruthenium benzothiozoles and thiozoles.^[96] A series of different thiazole containing ligands (see figure 1.13) were investigated with the results indicating that the number of electrons required before the complexes become active is dependent upon the number of sulphur atoms present in the complex as shown in table 1.2.

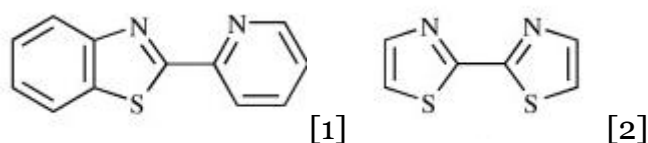


Figure 1.13; Structures of the thiazole ligands

E_{red}/V vs SCE	Complex	# of S atoms in complex	# of e⁻ needed to be transferred before activity observed
-1.06	[Ru(bpy) ₂ (1)] ²⁺	1	1
-1.45	[Ru(bpy) ₂ (2)] ²⁺	2	2
-1.51	[Ru(2) ₃] ²⁺	6	3

Table 1.2; Data for benzothiazole and bithiazole complexes

The data presented in table 1.2 led to the reported conclusion that CO₂ reduction occurred at the S atom of the ligand, not the bipyridyl or metal centre, and a threshold electron density was needed on the atom before the reaction could occur, therefore another mechanism different to those previously described is proposed.

An interesting dinuclear copper complex which incorporated pyridyl-like groups (the structure of which can be seen in figure 1.14), was reported to transform CO₂ into oxalate with only a very small applied potential, around 2V less negative than that required for CO₂ reduction to the anion radical (ie -0.03V vs NHE) in acetonitrile on a glassy carbon electrode.^[97] This was found to proceed via a very different mechanism again to that commonly observed as seen in figure 1.14.

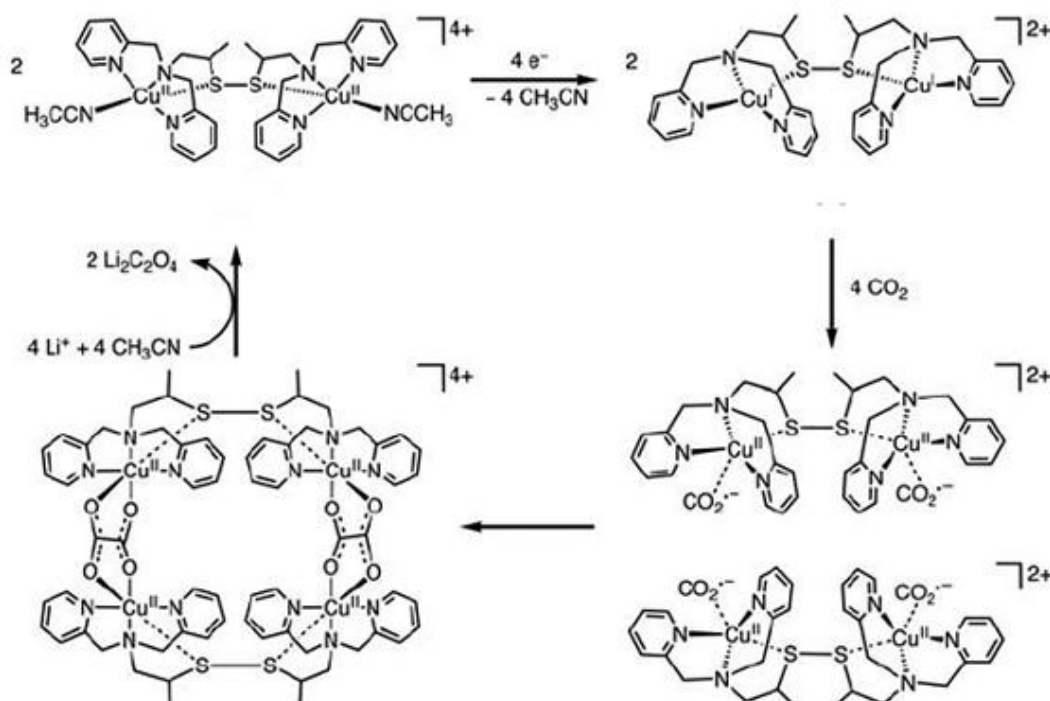


Figure 1.14; Proposed mechanism of CO₂ reduction to oxalate by the dinuclear copper complex reproduced from ref [16]

Two dinuclear direduced copper complexes are thought to form a tetranuclear complex with two bridging CO₂ derived oxalates which are subsequently released as Li₂C₂O₄ precipitate. The reduction of CO₂ in this system is found at a significantly less negative potential than that of dioxygen allowing the selective reduction of CO₂ from air. Unfortunately this catalyst only completed 6 turnovers (forming 12 equivalents of oxalate) in 7 hours so cannot be considered suitable as a realistic catalyst yet however is the most efficient route to oxalate in terms of overpotential reported to date.^[16]

1.3.3. Other catalysts;

1.3.3.1. Organic cations;

One of the most well publicised reduction catalysts reported over recent years has been that of Bocarsly where the multi-electron reduction of CO₂ to methanol is reportedly catalysed by the simple pyridyl radical.^{[98]-[102]}

The mechanism proposed for the aqueous reduction is via a series of single electron transfers rather than the typical multielectron charge transfer. The rate determining step of the aqueous system was reportedly determined as being the initial step, formation of the pyridinium-CO₂ radical, as seen in the scheme given in figure 1.15;

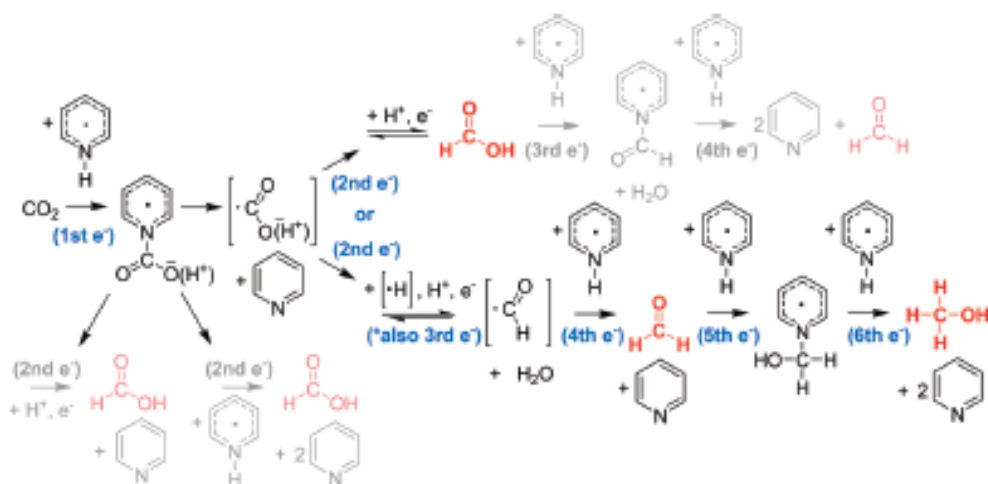


Figure 1.15; Schematic detailing the proposed pyridinium catalysed CO₂ reduction to methanol reproduced from [101]

The overpotential required has varied throughout the publications, dependent upon various experimental factors, but has been reportedly as low as 300 mV below the standard reduction potential of CO₂ reduction.^[100] The evaluation of this proposed mechanism by other researchers was suggested to be somewhat over simplified neglecting to consider the significant role played by the working electrode material and the employment of very low scan rates as a means of mechanistic determination disparaged.^[16]

A similarly starting recent report of CO₂ electrocatalysis is by the ‘ionic liquid’ 1-ethyl-3-methylimidazolium tetrafluoroborate^[68] The term ‘ionic liquid’ is applied loosely throughout this paper as the salt was employed dissolved (albeit it at relatively high concentration of 18 mol%) in water, however the reported yield of CO from the system was almost 100% with an overpotential of just 270 mV. The stabilisation of the CO₂ radical formation through ion pairing interaction with the cation (1-ethyl-3-methylimidazolium) is reported as the proposed mechanism through which the overpotential is lowered so

significantly. The likelihood of this assertion being correct has been deemed doubtful in a recent review by Savéant^[16] where his evaluation of the energies associated with ion pairing led to the conclusion that the working electrode materials (Pt and Ag) were more likely responsible or at least significantly influenced the observed catalysis.

1.3.3.2. Enzymes;

In nature sequential two electron CO₂ reduction steps each have different catalysts with the involvement of two enzymes in the Calvin cycle transformation of CO₂ into four electron reduced sugar. With the incorporation of enzymes able to reduce CO₂ into electro and photoelectro- systems, the overpotential required can be lowered significantly. The adsorption of enzymes onto an electrode is not always prudent as the active site is often found inside the enzyme, which upon adsorption can be made inaccessible to the electrode surface and substrate, however there have been some systems reported which have successfully achieved enzyme electrocatalysis.^{[65]-[67]}

An account of efficient enzymatic CO₂ electrocatalysis involved the adsorption of a tungsten containing enzyme, formate dehydrogenase (FDH1) , onto the surface of a graphite electrode.^{[65][66]} FDH1 contains Fe-S clusters, metal centres, nitrogen and bears similarity to NADH reductases therefore sharing properties with many known molecular catalysts. This enzyme system is reported as being two orders of magnitude faster than any known catalyst for the reaction, CO₂ → formate, and gave a thermodynamically reversible electrocatalysis at very small overpotentials. Carbon dioxide reduction was

reported as starting at just -0.4 V (vs. SHE) and reached 0.08 mA cm⁻² at -0.8 V at pH 5.9 with formate oxidation increasing to 0.5 mA cm⁻² at +0.2 V at pH 8.

From the constantly changing current seen in the cyclic voltammograms produced, the smallest change in potential drives turnover with the system found to interconvert electrical and chemical bond energies efficiently.

(Faradaic efficiencies were reported as $97.3 \pm 1.1\%$, decreasing at higher overpotentials.) The tungsten hydride bond has been previously reported to allow CO₂ insertion to form a stable formate adduct^[103] so the selectivity for this product seems easily rationalised despite the complexity of the enzyme.

Unfortunately the enzyme is not only large and complex but also oxygen sensitive so in common with the tetranuclear copper complex described above it is not realistic for large scale exploitation but the work's findings offer a starting point for further development.^[65]

A more recent report of the employment of enzymes was in a photoreductive system where TiO₂ nanoparticles were modified with a photosensitiser and the CO₂ reducing enzyme COD I from the anaerobic microbe *Carboxydotherrmus hydrogenoformans*.^[104] This was reported as bypassing the one-electron radical pathway, instead catalysing a controlled two electron reduction to generate exclusively CO at -0.46 V vs SHE at pH 6, the given scheme reproduced in figure 1.16.

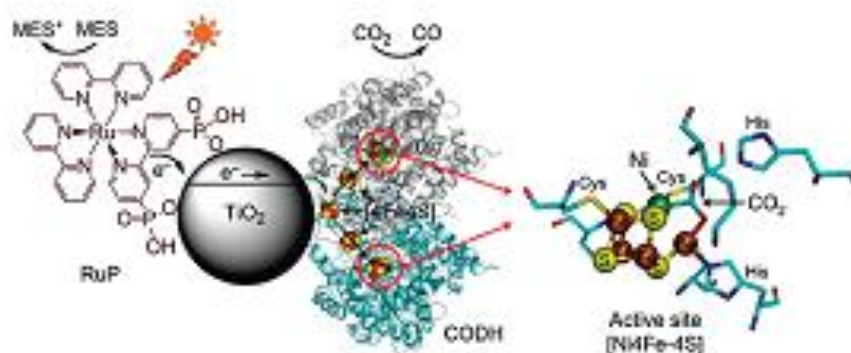


Figure 1.16; Schematic showing the steps of the proposed CO₂ photoreductive system reproduced from ref [104].

The active site of the enzyme was reported to be at a nickel-iron-sulphur cluster.

A related study investigating one of the constituents of many enzymes, including the above, this time in non aqueous solution (DMF) looked at CO₂ reduction in the presence of iron-sulphur clusters, [Fe₄S₄(SR)₄]²⁻ where R= CH₂C₆H₅ and C₆H₅.^[105]

Fe-S proteins are used within living systems for redox electron transfer reactions with the ones investigated containing 15 transferable electrons per molecule.

When used as catalysts in CO₂ reduction they are reported as resulting in a potential shift ~0.7 V, with the major product found to be formate (CHOO⁻). The formate results from electron transfer from the reduced clusters to the CO₂ in bulk solution, as opposed to adsorbed CO₂, therefore radicals formed are not in close proximity to each other and undergo protonation not self coupling (to form oxalate). This is presumed to be due to the presence of trace amounts of water which, as mentioned previously, only a few % of which is needed to alter

the reaction mechanism from non-aqueous to aqueous. The clusters showed a two step reduction to a trianion and tetraion with the tetraion reported as active towards CO₂ reduction.

Molybdenum and tungsten centres with chelated Fe-S ligands with the structure [M₂Fe₆S₈(SEt)₉]³⁻ in excess PhCH₃ have also been reported to catalyse CO₂ reduction,^[27] although this time to phenyl acetate with faradaic efficiencies of 5-15% in the reaction 1.2;



Fe-Mo clusters, [(C₂H₅)₄N]₃[Fe₆Mo₂S₈(SC₂H₅)₉] used in the electrochemical reduction of CO₂ in the presence of thioethers were reported to yield α-ketoacids, a process involving a C-C bond formation, from the two electron reduction.^[27]

1.4. M(CO)₄αα-diimines;

A significant portion of the work presented involves the investigation and application of group 6 M(CO)₄αα-diimine complexes as CO₂ reduction electrocatalysts, with particular attention paid to Mo(CO)₄bpy. M(CO)₄αα-diimines, (where M= Cr, Mo, W): their properties have been studied by various groups for over 65 years with the earliest reported synthesis of Mo(CO)₄bpy dating back to 1959.^[106] Two of the most prominent researchers in this field are Vlček and Stufkins, both having produced reviews detailing the area.^{[107][108]} The most recent literature on Mo(CO)₄bpy addresses the crystal structure,^[109] new

synthetic routes to^[110] and the molecule as a starting material for catalyst synthesis^[111] with no direct applications evident.

An overview of the pertinent literature and documented behaviour to date is now given with respect to this group of organometallic complexes which uniquely combine an electron rich low valent d⁶ metal centre, stabilising carbonyl groups and an electron accepting, non-innocent $\alpha\alpha$ -diimine ligand.

1.4.1. Structure;

The structure of $M(\text{CO})_4\alpha\alpha$ -diimines, established through DFT calculations^{[108][112]} and more recently crystallographic determination,^[109] is reported as pseudooctahedral as depicted in figure 1.17.

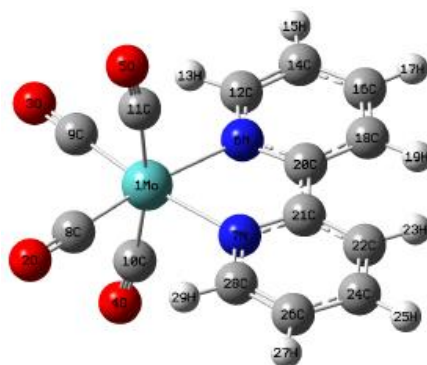


Figure 1.17; Structure of $\text{Mo}(\text{CO})_4\text{bpy}$ (from DFT calculations, see section 4.1 for details)

The complexes may be considered as two moieties, $M(\text{CO})_4$ and $\alpha\alpha$ -diimine. The symmetry of the complexes is dependent upon the bidentate ligand, however in the case of $\text{Mo}(\text{CO})_4\text{bpy}$ is C_{2v} . $M(\text{CO})_4\alpha\alpha$ -diimines have many common electronic features with a generally representative MO diagram given in figure 1.18.

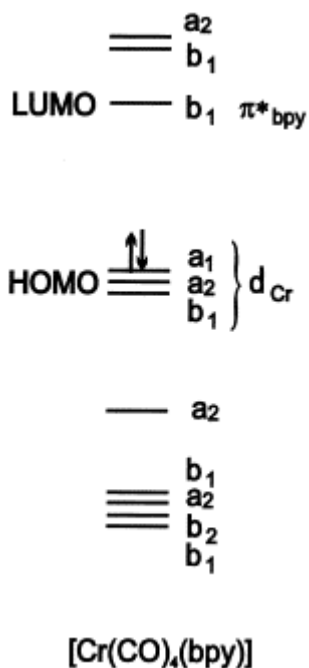
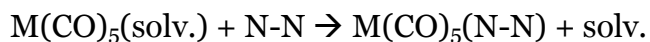
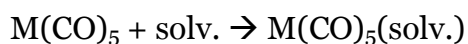
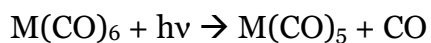


Figure 1.18; MO diagram of Cr(CO)₄bpy reproduced from [112]

The synthesis of M(CO)₄αα-diimines generally proceeds via direct, thermal, photochemical or more recently microwave assisted reaction of the αα-diimine and hexacarbonyl.^{[107][110]} In THF the following process has been reported;^{[113][114]}



The complex incorporating the monodentate coordination of the αα-diimine, M(CO)₅(N-N), has been reported as stable at low temperature for αα-diimine= DAB, PyCa and bpy.^{[107][115][116]}

1.4.2. Radical Anionic Species;

The DFT calculated lowest molecular orbital (LUMO) for several $M(\text{CO})_4\alpha\alpha$ -diimines have been reported^{[112][117]} including that of $\text{Cr}(\text{CO})_4\text{bpy}$. For this species, with the same trend followed for all $M(\text{CO})_4\alpha\alpha$ -diimines, the LUMO was found to be 76% bpy localised, 24% on CO groups (14.2% on equatorial and 9.6% on the axial) and just 0.8% on the Cr metal centre. The M contribution has been reported as between 1-10% depending upon the metal ($W > \text{Cr}$) and ligand ($\text{DAB} > \text{Phen}$). For bpy and phen containing species the DFT predicts the second lowest molecular orbital (SLUMO) is entirely $\alpha\alpha$ -diimine localised.^[108]

The DFT predicted localisation of the LUMO on the $\alpha\alpha$ -diimine is supported by experimental observations;

- The electrochemical reduction of $M(\text{CO})_4\alpha\alpha$ -diimine follows the same reduction pattern with correlating potentials (although shifted positive by 0.5 to 0.8 V) as the $\alpha\alpha$ -diimine with relatively little influence held by the M.^[108]
- EPR spectra of $[M(\text{CO})_4\alpha\alpha\text{-diimine}]^{\cdot-}$ are almost identical when compared to that of the $[\alpha\alpha\text{-diimine}]^{\cdot-}$.^{[108][118]}
- UV-vis spectra show evidence of a clear $\alpha\alpha$ -diimine chromophore (i.e. A broad structured band in the red/NIR region (>600 nm) and a strong sharp band at 360-390 nm).^[107]

1.4.3. MLCT and Solvatochromism;

$M(CO)_4$ $\alpha\alpha$ -diimines are strongly coloured as a result of $M \rightarrow$ diimine metal-to-ligand-charge-transfer (MLCT).^[108] The electron density expected at the $\alpha\alpha$ -diimine ligand upon MLCT excitation for $Cr(CO)_4bpy$ is reportedly approximately equal to that expected upon the one electron reduction,^[108] however the two states are not completely analogous but are reported to show distinct similarities in electron distribution and behaviour.^[119]

$M(CO)_4\alpha\alpha$ -diimines are known to experience negative solvatochromatic shifts, therefore the MLCT absorbance moves to higher energy (lower wavelengths) upon increasing solvent polarity.^{[107][108]} Many theories have been put forward to explain this with the supposed difference in stabilisation offered by the solvent of the ground and MLCT excited states (and polarisability differences between the two) through dipole-dipole interactions thought responsible.^[108]

The ground state is reportedly more polar than the MLCT excited state due to diimine $\rightarrow M$ σ donation resulting in $M^{\delta-}(\text{diimine}^{\delta+})$ charge distribution in the ground state, with the negative charge transferred to the $\alpha\alpha$ -diimine upon excitation decreasing the dipole moment.^[108]

The energy gap between the ground and excited state is reportedly increased upon increasing the polarity of the solvent employed, with the degree of solvatochromism experienced dependent upon the ligand;

$\text{phen} \approx \text{bpy} > \text{PyCa} > \text{DAB}$.^{[108][120]}

1.4.4. Electrochemistry of $M(CO)_4\alpha\alpha$ -diimines;

$M(CO)_4\alpha\alpha$ -diimines undergo a single oxidation and two or more reductions, depending upon the ligand. The oxidation of the tetracarbonyl complexes has been reported as reversible for $M=Cr$ yet irreversible for $M=W, Mo$,^[108] the reasoning for this is unclear.

The first reduction of $M(CO)_4\alpha\alpha$ -diimines is reported to be both electrochemically and chemically reversible, generating the radical anion with the potential dependent most strongly upon the nature of the diimine ligand. Altering the metal results in only slight potential shifts; $M(CO)_4bpy$ for $W = -1.84$ V, $Mo = -1.91$ V and $Cr = -1.99$ V (vs Fc) in the same system.^[121]

The second reduction, where $\alpha\alpha$ -diimine is *bpy* or *phen*, is thought to be completely localised upon this ligand and reportedly occurs approximately 600 mV more negative than the first.^{[108][121]} This second reduction is reported to result in the loss of a carbonyl group to form a tricarbonyl species.^[108] This assertion does not however appear to take into consideration the solvent, already established to have an important role in the stabilisation during MLCT excitation, or electrode material into consideration.

1.4.5. $Mo(CO)_4bpy$;

Of $M(CO)_4\alpha\alpha$ -diimines, although not unmentioned, this complex features in relatively little literature with no existing DFT studies and although it has been subject to characterisation by several groups,^{[119]-[128]} the available voltammetry and other electrochemical data showed a high degree of inconsistency.

The exact reduction potentials are not known due to the variety of solvents, electrolytes, reference electrodes and other experimental differences between groups giving an array of different values as seen in Table 1.3.

$E_{red1}/$ V vs Fc	$E_{red2}/$ V vs Fc	Solvent	Electrolyte	WE	RE*	Ref #
-2.12^a	-2.69 ^a	THF	[Bu ₄ N][PF ₆]	Dropping mercury	SCE	[119]
-1.94^a	-2.69 ^a	DMF	[Bu ₄ N][PF ₆]	Glassy carbon	Ag/AgCl	[126]
-2.28^b	-2.88 ^b	1,2-dimethoxy ethane	[Et ₄ N][OH]	Mercury pool	AgClO ₄ /Ag (APE)	[124]

* reference electrode employed for the measurement ^a potentials translated using Fc/Fc⁺ data from [129][130] and ^b[131]

Table 1.3; Comparison of reduction potentials reported for Mo(CO)₄bpy

It has been reported that the first reduction is chemically and electrochemically reversible but the second reduction, although electrochemically reversible, is chemically irreversible, determined using Kalousek polarography and cyclic voltammetry at low temperature and high scan rates.^[119]

In a separate study the extra electron density upon reduction of the complex, is reported as localised on bipyridine and the first reduction thought to lead to labilisation of the coordination sphere, specifically the carbonyl group found cis to the bipyridine, through the previously mentioned intramolecular transmission of the influence of the extra charge.^[119]

Infrared, ultraviolet-visible and Raman spectra have been recorded for this complex, as well as the EPR spectrum of the anion radical.^{[108][118][119][121]}

Given the limited and inconclusive nature of the reports regarding Mo(CO)₄bpy and the general understanding of the significant influence of the system, particularly the solvent employed, gleaned from the consideration of M(CO)₄αα-

diimines as a whole, the behaviour, reactivity and perhaps catalytic ability of $\text{Mo(CO)}_4\text{bpy}$ in differing systems is likely to show considerable variation. The available interpretations of previous studies offer a starting point for investigation and development of mechanistic ideas yet may not hold true upon significant deviation from the published restricted experimental parameters.

1.5. Diffusion Ordered Spectroscopy as a Complementary Technique;

Electrochemical analysis can be supported and enhanced through employment of complementary techniques, such as the spectroelectrochemistry discussed in the experimental section. Diffusion Ordered Spectroscopy (DOSY), is a comparatively recent technique^[132] allowing access to diffusivity data within a solution, albeit the self-diffusion coefficient rather than mutual parameter (the distinction addressed in chapter 7), prospectively offering an additional experimentally unrelated source of the diffusion coefficient. This could be applied as a means of confirmation of electrochemically determined values.

Despite the reliance of a vast array of research on the different techniques to establish what is considered by many to be the same parameter over the usual concentrations associated with electrochemical analysis, papers offering a direct comparison of the values obtained by the two methodologies are scarce. To date, although several publications have reported the use of both techniques in analysis of a system as a whole, the specific comparison of the diffusion coefficients obtained has been limited to just three papers^{[133]-[135]} with none of these having the system investigated of the same composition for both

techniques. The limited scope of these reports, although in agreement, leads to a degree of uncertainty as to the validity of the assumption that the same value is determinable.

The first reported comparison was from 2011^[134] where the diffusion coefficients of SeCN⁻ both in, and as a component of, ionic liquids were determined by use of DOSY, rotating disk voltammetry and a RAM electrode (Random Assemblies of Microelectrode). Despite the claims of “*The solutions for NMR measurements were exactly the same as those used in the electrochemical investigations*”, the only data given with respect to D , and indeed directly compared in the conclusions, was for significantly different concentrations of analyte (500 mM and 5.3 M) despite earlier evidence in the paper of clear concentration dependence.

By far the most comprehensive and exacting study in this area compared the electrochemical and DOSY derived diffusivity data for ferrocene in a variety of non-aqueous solvents and was published just 7 days later.^[133] This appears to be the first report in which the electrolyte was added to the system during the DOSY measurement although different ferrocene concentrations were employed in the DOSY and electrochemistry (10 to 23 mM and 5 to 10 mM respectively), however ferrocene is a well studied species by both methodologies and as such this moderate change in concentration was not expected to affect the results. This group showed, much more convincingly, that the diffusion coefficients were, for the systems investigated (Fc in CH₃CN, CH₂Cl₂, DMF and DMSO and their fully deuterated counterparts with TBAPF₄ supporting electrolyte) were consistent and yielded values generally within, or very close to the margin of, the errors associated with the measurements.

The final study addressing the comparison of methodologies investigated streptocyanine dyes in acetonitrile and its deuterated counterpart.^[135] This group reported that the diffusion coefficients obtained via DOSY were ‘similar’ with and without the addition of TBAP electrolyte so decided not to add it to the NMR solutions. This is surprising as the effect of electrolyte upon solvent properties is often significant affecting viscosity etc^[136] and in the case of self diffusion measurements is highly likely to give at least obstructive effects due to its bulky size and high concentration (which although was given as 0.1 mM throughout the document, communication with the author established that a typographical error meant the employed concentration was actually 0.1 M). The concentrations of the analyte were again significantly altered between the two systems employing 0.2 M for the NMR experiments and 1 mM for the electrochemistry. The DOSY was calibrated against the known tracer diffusion coefficient of the acetonitrile, yet yielded a surprisingly high degree of variation in the diffusivity of ferrocene present in the system compared to that seen in the study focused upon ferrocene.^[136] Despite the presence of Fc in the electrochemical system, no attempt was made to assess the diffusion coefficient electrochemically for additional comparison.

The publication concluded that the methods were in good agreement having obtained values which correlated. Although whether the systems can be considered as fully comparable is a difficult judgement.

1.6. Scope of the Present Work;

The primary aim of the work undertaken was the exploration of CO₂ electroreduction systems. Research into the area of CO₂ reduction and electrocatalysis of this process is plentiful however the complexity and limited understanding of the array of prospective mechanisms involved and the subtle experimental parameters which influence them means that direct comparison and evaluation is challenging.

The identification and characterisation of a relatively inexpensive and simple electrocatalyst for CO₂ reduction was achieved with the optimisation and development undertaken in such a manner that not just the electrocatalytic species, but also the entire electrochemical system, was investigated in order to determine and better understand the roles played by the various components.

The bulk of the work relied heavily upon electrochemical techniques for the analysis, however, spectroelectrochemical measurements and complementary non-electrochemical techniques were also employed to both validate conclusions tentatively drawn from electrochemical results and allow exploration of electrochemically inaccessible information with regard to aspects of the system.

Chapters 2 and 3 describe, in some detail, the electrochemical techniques and analysis as well as the specifics relating to the materials, chemicals and equipment employed throughout the research.

Chapter 4, the first of the results chapters, focuses heavily upon the electrochemical characterisation of the molybdenum based tetracarbonyl, Mo(CO)₄bpy and its behaviour toward CO₂ reduction catalysis. The first sections

address the structure and electrochemistry of $\text{Mo(CO)}_4\text{bpy}$ in the employed electrochemical system, which as the solvent, electrode material and electrolyte differ from those previously reported, was expected to result in deviation from the small quantity of prior literature documenting the electrochemical behaviour of $\text{Mo(CO)}_4\text{bpy}$. This section explores the processes undergone upon reduction of the complex, the degree of reversibility and the stability of the mono and dianions formed.

The utilisation of $\text{Mo(CO)}_4\text{bpy}$, or in fact any molybdenum based organometallic complex, as a CO_2 reduction catalyst has yet to be reported and was explored in section 4.3. The incorporation of CO_2 into the $\text{Mo(CO)}_4\text{bpy}$ system and the comparison with direct CO_2 reduction within the same system (as well as the system in the absence of CO_2) via cyclic voltammetry and chronoamperometry yielded evidence of catalytic current enhancement and lowering of the overpotential compared to that observed for direct CO_2 reduction.

The quantitative evaluation of the diffusion coefficients and rate constants associated with the electron transfer steps is then presented, based upon the data and mechanisms yielded in sections 4.2 and 4.3.

The final section of this chapter (4.5) presents the experimental data associated with the CO_2 detection and its analysis.

Chapter 5 explores the further investigation and optimisation of the electrocatalyst, $\text{Mo(CO)}_4\text{bpy}$, system studied in chapter 4. The influence of the structural components of the M-tetracarbonyl $\alpha\alpha$ -diimine is assessed, with respect to both reactivity and CO_2 reduction. Voltammograms and *in situ* EPR

spectra highlighted the effect upon alteration of the identity of the α -diimine ligand, the metal centre and inclusion of additional substituents on the bipyridyl ligand. The evaluation of the effects of pyridine and pyridinium, both as additives to the NMP electrolyte system in catalytic quantities and with pyridine employed as a solvent, upon CO_2 reduction was undertaken in an extension of the well publicised pyridinium catalyst reported for aqueous systems.

The effect of working electrode material upon the stability and catalytic ability of $\text{Mo}(\text{CO})_4\text{bpy}$ is also addressed in this chapter as this has been reported to be an important, yet frequently neglected, aspect of CO_2 electrocatalysis.

Chapter 6 explores CO_2 reduction in the absence of the additional molecular catalyst and instead explores the role of electrolyte upon CO_2 reduction within the employed NMP system. NMP, despite being employed industrially for CO_2 scrubbing and as an electrochemical solvent for investigation into carbon nanostructures has rarely been employed as a solvent for CO_2 reduction, and as such its behaviour in this role is not well understood. Catalytic effects of tetraalkylammonium cations toward CO_2 reduction within some non-aqueous systems have been previously reported, with this chapter addressing whether a similar catalytic process is undergone in the employed electrochemical system. This was investigated through the comparison of the typically employed tetrabutylammonium tetrafluoroborate (TBABF_4) with analogous alkali metal salts. Differences between voltammetric responses for the M^+ and TBA^+ electrolytes confirmed the existence of differences between the systems. The effects of M^+ upon the electrode surface, in the presence and absence of CO_2 as a function of potential, were investigated through Raman spectroscopic measurements made both *in situ* and *ex situ*.

The final results chapter is not directly related to CO₂ reduction or catalysis but instead presents a comparative study of electrochemical and DOSY-NMR methods of diffusivity measurement although the work grew out of a need for an accurate determination of the diffusion coefficient of the Mo(CO)₄bpy catalyst. The validity of the assumption that the two unrelated techniques provide access to the same value is tested with the experimental conditions such as concentration and addition of electrolyte kept consistent between the techniques, offering directly comparable data. The verification of the interchangeability of the DOSY derived self diffusion coefficient, D^* , and electrochemically determined mutual diffusion coefficient, D , would allow for the independent verification of data gathered by either technique and allow mechanistic details, such as number of electrons transferred, in voltammetric analysis to be more readily accessed.

Finally, overall conclusions are presented in chapter 8, and also some of the important areas where further work would be immensely beneficial are highlighted.

2. Electrochemical Techniques

2.1. Diffusion limited electrochemical techniques;

2.1.1. Diffusion;

Diffusion is one of the fundamental processes by which material moves, the macroscopic result of random molecular motion describing the spread of particles, and is an important factor controlling the rate at which many interactions occur.

The diffusion coefficient (D) is a parameter indicative of the diffusional mobility of species and encountered most famously in Fick's laws (2.1) and (2.2) but also in numerous other equations throughout physics and chemistry.

Fick's 1st law of diffusion states^[137];

$$J = -D \frac{\partial C(x)}{\partial x} \quad (2.1)$$

where J is the diffusion flux, D is the diffusion coefficient, C is concentration and x is the position in the one dimensional system. This proportionality of flux of matter to the concentration gradient (2.1) shows that the flux of matter is dependent upon the variation in concentration with position. From this relationship it is suggested that without a concentration gradient there is no net

flux and the diffusive flux would be zero. This 1st law describes mathematically diffusion within steady state systems where the concentration is time-invariant however this is not always the case, which leads to the less specific 2nd law.

Fick's 2nd law of diffusion^[137];

$$\frac{\partial C(x, t)}{\partial t} = -\frac{\partial J}{\partial x} = D \frac{\partial^2 C}{\partial x^2} \quad (2.2.)$$

Fick's 2nd law of diffusion (2.2) predicts the change in concentration (accumulation or depletion) with time as a result of diffusion with t denoting the time. The concentration change is proportional to the diffusivity (diffusion coefficient, D) and the second derivative (or curvature) of the concentration as illustrated in Figure 2.1. This equation assumes that the diffusion coefficient is independent of composition or the range of compositions is small.

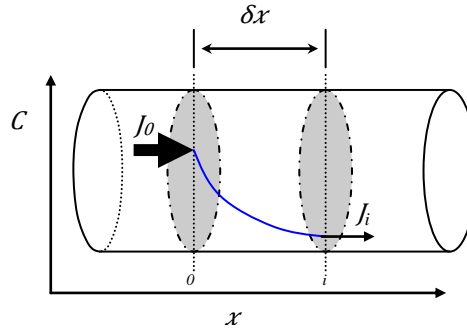


Figure 2.1; Picture of Fick's law showing the change in flux with changing concentration and distance.

The diffusion coefficient of a species in a given system can be evaluated using the Stokes-Einstein (2.3) and Wilke-Chang (2.4) relations given below ^{[138][139]}.

$$D = \frac{k_B T}{6\pi\eta r} \quad (2.3)$$

$$D = \frac{7.4 \times 10^{-8} (xM)^{1/2} T}{\eta V^{0.6}} \quad (2.4)$$

In the Stokes-Einstein equation (2.3), k_B is the Boltzmann constant, T is the temperature in K, η is the dynamic viscosity (SI units of Pa•s), r is the molecular radius of the analyte in m to give D in m² s⁻¹.

In the Wilke-Chang relationship (2.4), x is the association parameter of the solvent, M is the molecular mass of the solvent in u, T is the temperature in K, η is the dynamic viscosity in cP (or mPa•s) and V is the molar volume of analyte (at boiling point under standard conditions) in cm³ mol⁻¹ to give the diffusion coefficient in cm² s⁻¹.

Some of the most well utilised electrochemical techniques have diffusion as the primary form of mass transport and as such D is a useful parameter to define and can be measured experimentally.

2.1.2. Cyclic Voltammetry;

Cyclic voltammetry is possibly the most widely recognised and utilised electrochemical method due to its versatility, non-destructive nature and rich information that can be extracted relatively quickly, with wide ranging applications in organic and inorganic chemistry as well as materials development.

The technique is often employed for initial investigations into prospective catalysts as it is quick and effective at providing useful data regarding electron transfers and allows identification of potentials required for various

transformations. It is non-destructive as cyclic voltammetry only involves electrolysis of a small portion of the solution. The current is measured as a potential sweep is applied from an initial potential (E_i), generally where no net reaction, therefore minimal current, is expected and the composition of the analyte solution is not affected, to a chosen potential (E_s), relevant to the species being investigated. This overpotential can be oxidative or reductive depending upon the nature of the species under examination but is scanned so that the concentration of the redox active analyte concentration at the electrode surface is close to zero, passing through the standard potentials of redox couples studied, E^o , where $E^i < E^o < E^s$. Once E_s is reached the potential sweep direction is reversed and returned to E_i , with any reverse reactions taking place observable in the current response obtained on the reverse sweep. A schematic of the potential waveform used in a typical CV is given in Figure 2.2.

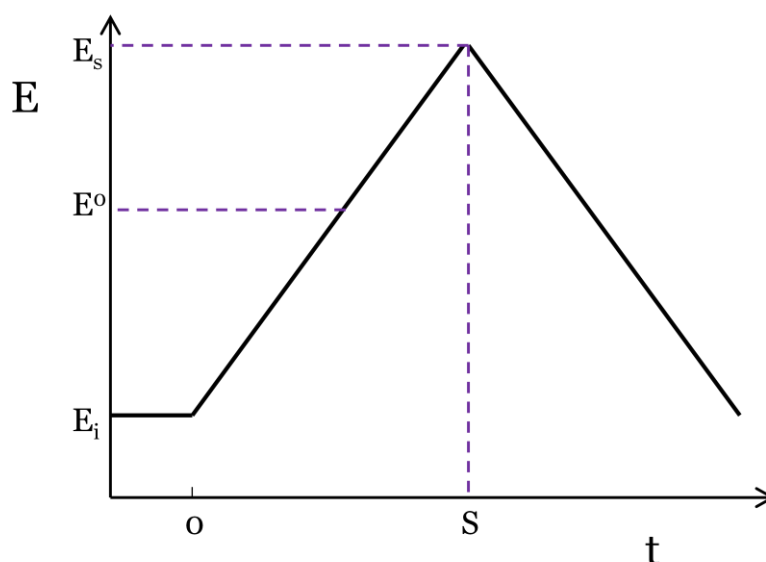


Figure 2.2; Potential scheme as a function of time for cyclic voltammetry

The current response recorded is plotted against the potential to give a cyclic voltammogram (CV), which shows current enhancements and peaks where

electrochemical oxidation and reduction have taken place, an example of which is given in figure 2.3.

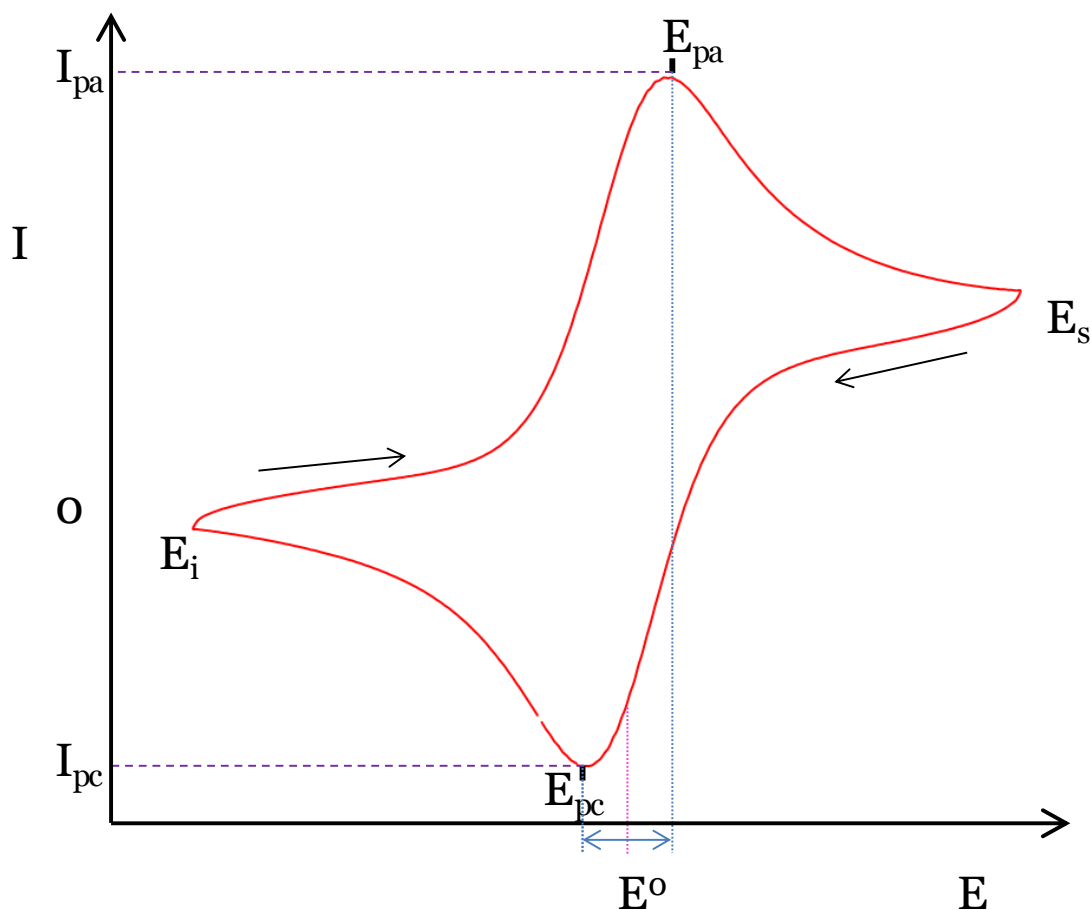


Figure 2.3; A typical reversible cyclic voltammogram. Arrows indicate the direction of the potential sweep

As can be seen in figure 2.3, initially, due to the careful selection of E_i , no current flows however as the potential is scanned closer to the standard potential of the electrochemical reaction (in this case the oxidation of ferrocene), a current is produced which increases with potential to give a peak where maximum current is observed (E_{pa} , I_{pa}) and upon passing E_{pa} the current response drops.

The appearance of the peak is due to mass transport effects; as cyclic voltammetry is undertaken in non-stirred homogenous solution containing excess background electrolyte both convection and migration are avoided so the movement of analyte to the electrode surface is limited by the rate of diffusion. As this is usually slow compared with the electron transfer step, once high enough overpotentials are reached for the redox process, the analyte concentration at the electrode drops to zero and diffusion of replacement analyte becomes the limiting step with current response decaying as the depletion layer grows. The diffusion layer thickness depends upon experimental timescale but is usually of the order of μm to mm in width, and is the region of solution where the concentration varies from that of the bulk solution.^[140]

The voltammetric behaviour prior to the diffusion limitation is described by the Nernst equation (2.5)^[141].

$$E = E^0 + \frac{RT}{nF} \ln \left(\frac{C_o}{C_r} \right) \quad (2.5)$$

This equation describes the concentration changes near the electrode, with C_o the concentration of oxidised and C_r the concentration of reduced redox species. E is the applied potential, E^0 is the standard redox potential and R , T , n and F are the ideal gas constant, temperature, number of electrons transferred per molecule and Faraday's constant respectively. The logarithmic relationship between the concentration change and potential is responsible for the initial rapid exponential growth in current.

Upon reversal of the scan, for an electrochemically reversible system, the opposite processes occur with the product of the forward scan being reduced or

oxidised back to the starting material as E^o is reached and exceeded, giving a similar form of current response but of the opposite sign. For a completely reversible process the ratio of the oxidative and reductive peak currents, $I_{pa}/-I_{pc}$ equals unity.

The peak current for diffusion limited processes are described by the Randles-Sevcik equation (2.6) below, where the peak current (I_p) of a reversible system is dependent on: the number of electrons transferred (n), the area of the electrode (A), the diffusion coefficient (D), the concentration of the redox species in solution (C) and the scan rate (ν).^[141]

$$I_p = 0.4463 \left(\frac{n^3 F^3}{RT} \right)^{1/2} A D^{1/2} C \nu^{1/2} \quad (2.6)$$

When standard electrochemical units (area in cm^2 , ν in V s^{-1} , D in cm^2s^{-1} and C in mol cm^{-3}) are used at 25 °C the Randles-Sevcik equation can be expressed as:

$$I_p = 2.69 \times 10^5 n^{3/2} A D^{1/2} C \nu^{1/2} \quad (2.7)$$

The degree of reversibility can be assessed using CV through evaluation of the potentials as well as currents observed. If the peak separations of a redox couple increase with scan rate, this is indicative of quasi reversible kinetics. If however the peaks associated with the forward and backward processes have no overlap on the potential axis or, as found for chemically irreversible processes there is a complete absence of a back-peak, the electron transfer is irreversible.

The peak separation of a reversible one electron process at 25 °C is approximately 59 mV and independent of scan rate. If n electrons are transferred the separation is described by equation 2.8^[142];

$$\Delta E = E_{pa} - E_{pc} = 2.218 \frac{RT}{nF} \quad (2.8)$$

The rate of electron transfer between the electrode and analyte, k_f , can be evaluated via voltammetry as it also shows a potential dependence, as described by the Butler-Volmer relation, equation 2.9.^[143]

$$k_f = k^0 e^{\left[-\frac{\alpha n F}{RT}(E-E^0)\right]} \quad (2.9)$$

where k^0 is the standard heterogeneous rate constant and α is the transfer coefficient. The transfer coefficient represents the sensitivity of the transition state to the shift in potential upon moving from the electrode reactant to product with possible values 0 to 1. In electron transfers without significant structural changes or alteration in solvation this value is approximately 0.5.^[143]

2.1.2.1. Calculation of heterogeneous rate constant k^0 ;

The standard rate constant for the heterogeneous electron transfer between the electrode and the redox species can be determined for voltammetric data using the dimensionless rate parameter Ψ defined by equation 2.10.^[141]

$$\Psi = \frac{\left(D_0/D_k\right)^{\alpha/2} k^0}{(\pi D_0 f \nu)^{1/2}} \quad (2.10)$$

f is a constant defined by $f = \frac{F}{RT}$

$\left(D_0/D_k\right)^{\alpha/2}$ is the ratio of the diffusion coefficient of the starting material (D_0)

and the diffusion coefficient of the reduced species formed by the electron transfer (D_k) to the power of $\alpha/2$. When the D_k value is not expected to change compared to that of D_0 giving $\left(D_0/D_k\right) = 1$. This means that the transfer coefficient term, α , does not need to be considered and the equation can be simplified to give equation 2.11;

$$\Psi = \frac{k^0}{(\pi D_0 f \nu)^{1/2}} \quad (2.11)$$

By comparison of this with ideal data generated from numerical simulation of the electrochemical problem, k^0 can be determined for experimental data.^[141]

2.1.2.2. Homogeneous electron transfer rate constant k' ;

The homogeneous rate constant can be determined if the reaction mechanism is known. For the E_rC_i' mechanism, which is relevant for the work presented as discussed in chapter 4, the plot reproduced below can be employed, along with voltammetric data to gather $\lambda^{1/2}$ values;

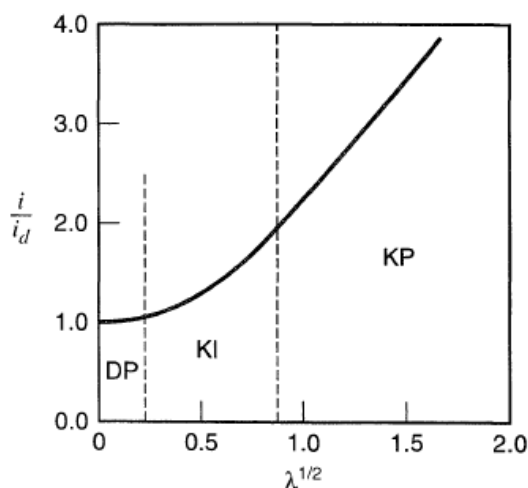


Figure 2.4. Ratio of kinetic peak current for the E_rC_i' reaction scheme to diffusion-controlled peak current as a function of $\lambda^{1/2}$. Reproduced from ref. [141]

where the kinetic parameter λ is defined by the following equation 2.12.

$$\lambda = \frac{k' C_z^*}{\nu} \left(\frac{RT}{nF} \right) \quad (2.12)$$

C_z^* is the bulk concentration of the species present in excess which undergoes electron transfer from the redox species, (in this work $[CO_2]$), so with the experimental scan rates employed a value of k' can be established.

In figure 2.4 the DP zone is where there is pure diffusion control of the peak current. The peak current here is proportional to the square root of scan rate and reversible.

The KP region is purely kinetically controlled with no diffusion contribution therefore the peak current is independent of scan rate. Complete kinetic control would be expected to result in the voltammogram shifting from peak-shaped toward a sigmoidal form with a steady state current being reached.^{[16][141]}

The KI region is the transitional region where both diffusion and kinetics play a part in the control of the limiting current and therefore current ratio.

Cyclic voltammetry is not always particularly well suited for quantitative analysis of a system although it is easily employed for qualitative studies and the evaluation of potentials associated with electron transfer etc as discussed in more depth in chapter 4.

2.1.3. Chronoamperometry;

Chronoamperometry involves the application of a fixed potential at a stationary electrode in an unstirred solution with the working electrode area kept small compared to the volume of solution under investigation. The current produced is measured as a function of time to give current transients or chronoamperograms. Chronoamperometry, like cyclic voltammetry, usually involves an initial potential at which no reaction is anticipated therefore minimal current flows, E_i , which is then stepped to a set potential where the electron transfer of interest (either oxidation or reduction) takes place, E_s . The potential scheme is given in figure 2.5.

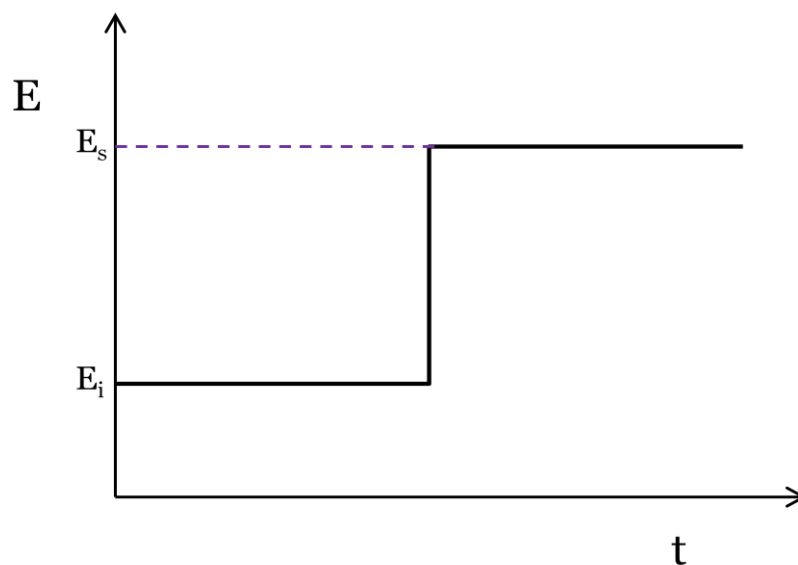


Figure 2.5; Potential scheme for chronoamperometry

The overpotential applied (E_s) is generally set to be high enough for the electroactive analyte near the electrode surface to react immediately and, assuming this electron transfer is fast, the associated current response is limited by mass transport; in the presence of migration-mitigating supporting electrolyte and absence of convection, this is diffusion controlled.

The concentration of the analyte at the electrode surface during the application of E_s is constantly approaching zero as it reacts to form a new species, creating a diffusion layer or depletion zone, and as such a concentration gradient to produce diffusion of the analyte from bulk solution to the electrode surface and of the new species accumulating at the electrode toward the bulk phase. The diffusion layer increases with time as the electroactive analyte is depleted resulting in lowering current responses.^[142]

The diffuse layer, is the region over which the potential varies. This, as well as the electrical double layer (found in the solution immediately adjacent to the electrode), are depicted in figure 2.6.

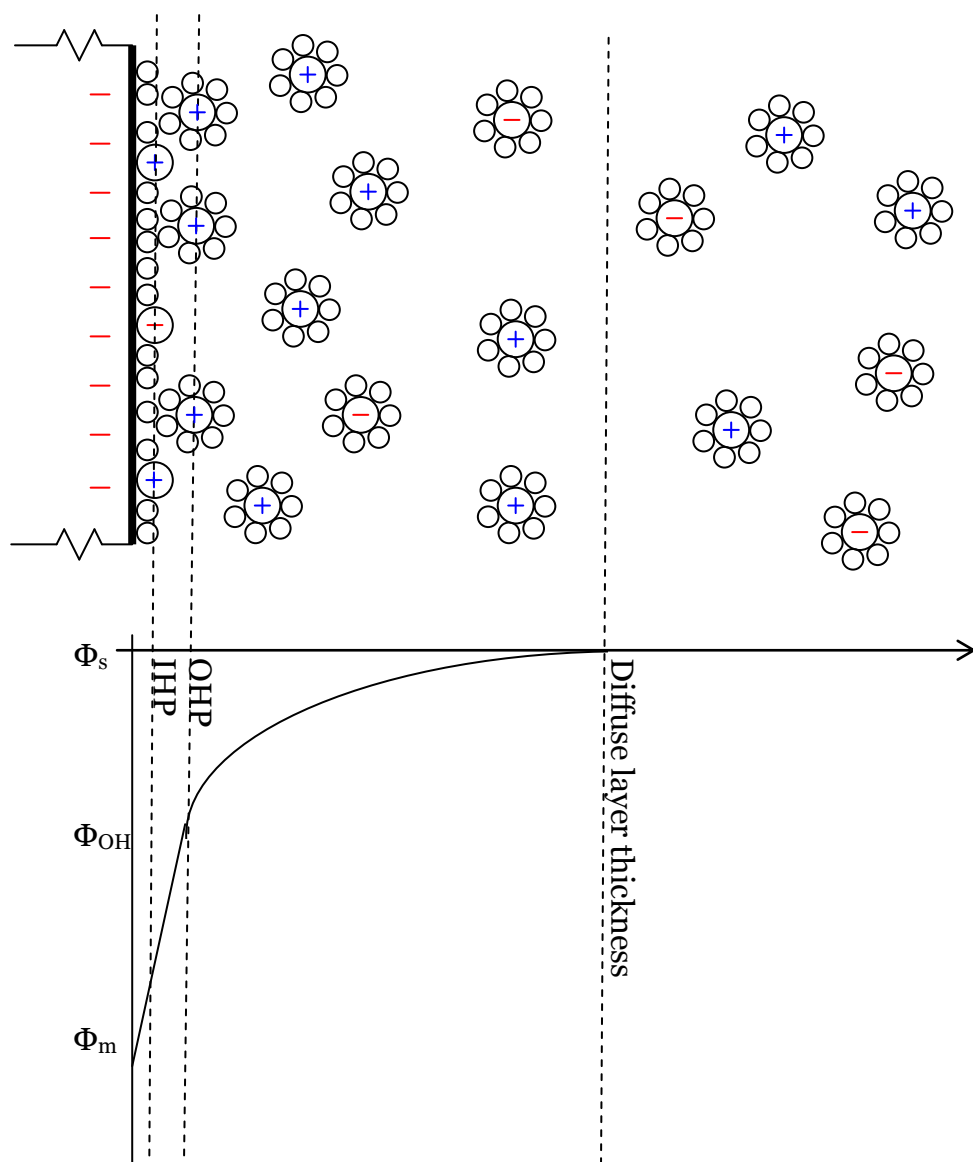


Figure 2.6; Phase boundary at the electrode-electrolyte interface showing the electrical double layer and diffuse layer.

Figure 2.6 shows the change in potential between the electrode surface (Φ_m) and the bulk solution (Φ_s) with distance from the electrode. Upon moving from the electrode surface the first layer reached is the Inner Helmholtz Plane (IHP), which is defined as running through the centre of the specifically adsorbed species at the electrode surface. This specific adsorption is not necessarily charge dependant and is made up of non-solvated species. The Outer Helmholtz Plane (OHP) marks the minimum distance of approach of solvated ions. The

ions here are predominantly of the opposite charge to that of the electrode and are responsible for the sharp drop in potential as the charge difference between the electrode and bulk solution is balanced. These two layers make up what is termed the double layer. Beyond this point the potential drop is more gradual as the concentration of excess counter ions decreases until the potential of bulk solution is matched marking the end of the diffuse layer.^[141]

A typical current transient can be seen in figure 2.7.

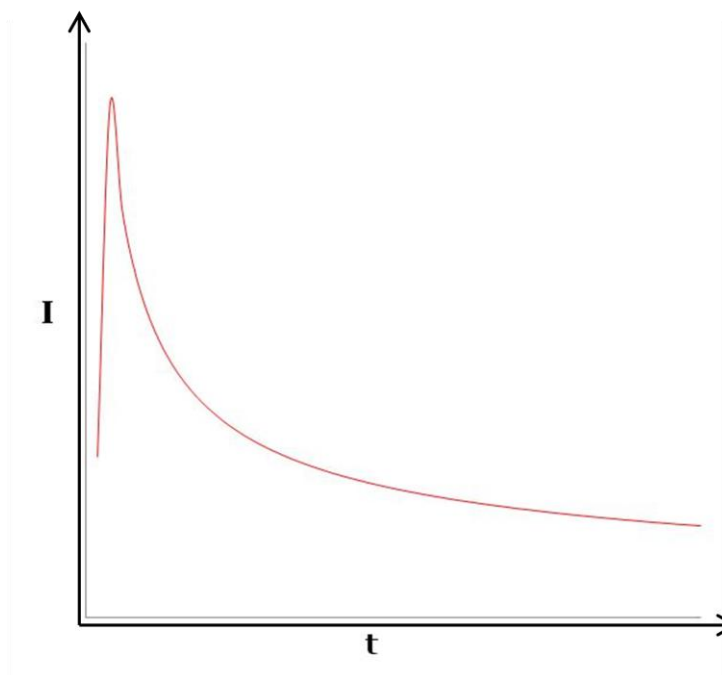


Figure 2.7; A representative chronoamperogram

At very short times, very high currents are usually produced due to the charging of the double layer (depicted in figure 2.7). After this the current drops as electrolysis occurs. The shape of the current transients is a result of the concentration gradients and Faraday's law (equation 2.13)^[144];

$$Q = nFN \quad (2.13)$$

where the charge transferred, Q , corresponding to the integral of the current transient, is proportional to the number of electrons transferred per molecule n , and the moles of reactant N .

The current observed is proportional to the flux of the electroactive species (J) using Fick's diffusion laws (equations 2.1 and 2.2), as can be seen from equation 2.14.

$$I = nFAJ = nFAD \left(\frac{\partial C(x)}{\partial x} \right)_{x=0} \quad (2.14)$$

At a planar electrode of working area A the Cottrell equation (2.15) describes the instantaneous current.^[141]

$$I = \frac{nFACD^{1/2}}{(\pi t)^{1/2}} \quad (2.15)$$

where the symbols are defined as previously with the addition of t which is time.

This relationship allows reproducible quantitative evaluation of the currents and diffusion coefficient of a system at high overpotentials where the diffusion to the electrode is the limiting mode of mass transport. At very short times, deviation due to the aforementioned charging and instrumental error are anticipated and over prolonged application of potential (>10-20 s) convection may become significant, however Cottrell plots, where current is plotted as a function of $t^{1/2}$, show clearly the period where the diffusion control is limiting with a linear region, an example of which can be seen in figure 7.15 b.

2.1.3.1. Chronoamperometric k' determination;

In a similar manner to the voltammetric k' determination the homogeneous rate constant can be evaluated using chronoamperometric data and the working curve reproduced in figure 2.8;

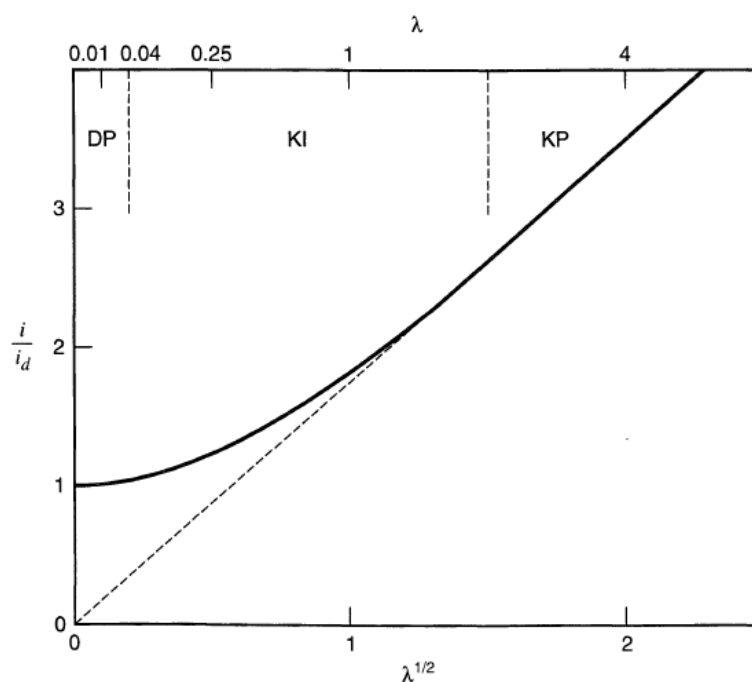


Figure 2.8; Chronoamperometric working curve for the E_rC_i case for various values of $\lambda^{1/2}$ reproduced from [141]

The λ values are related to k' for chronoamperometric experiments through equation 2.16;

$$\lambda = k' C_z^* t \quad (2.16)$$

The plot is again split into the three zones described above for voltammetry but with the dashed line from the origin showing the KP region limiting line.

2.2. Hydrodynamic electrochemical techniques;

2.2.1. Rotating Disk Electrode (RDE);

The rotating disk electrode (RDE), is a hydrodynamic technique which, unlike those discussed so far where diffusion limitation plays a vital role, forced convection is the dominant form of mass transport. Convection, which implies movement of the solution (in this case with respect to the electrode surface) is a much more effective form of transport than diffusion and when controlled allows for excellent reproducibility and increased sensitivity in electrochemical measurements.

The RDE consists of a standard macro-electrode encased in insulating material which can be set to rotate about its own axis at selected specific frequencies, f (revolutions per second) which can be easily transformed to angular velocity, ω through equation 2.17.

$$\omega = 2\pi f \quad (2.17)$$

The convective flow of electrolyte to the electrode surface produced by the rotation is shown in the schematic figure 2.9.

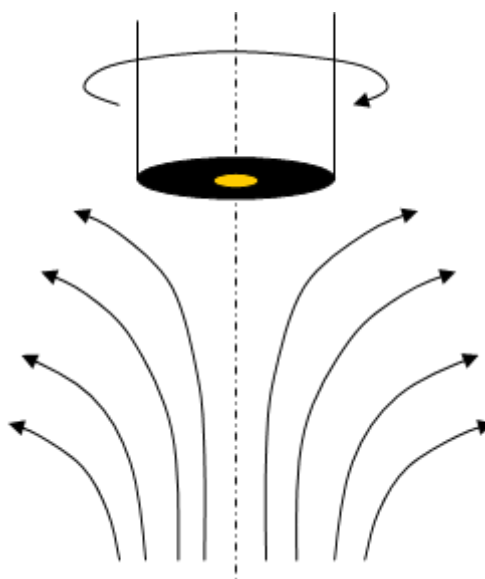


Figure 2.9; A schematic depicting RDE convective flow

Rather than the diffusion related peaks seen in CV, RDE gives a steady state limiting current response dependent upon the fixed angular velocity employed as illustrated in the Levich equation^[141] for the RDE (2.18).

$$I_l = 0.62nFAD^{2/3}\nu^{-1/6}C\omega^{1/2} \quad (2.18)$$

In equation (2.18) ν is the kinematic viscosity of the electrolyte solution.

The presence of the diffusion coefficient D , in the equation describing a convection controlled system may seem contradictory, however although convection is dominant in the bulk solution there is still a thin layer close to the electrode surface where diffusion plays an important role.

The thickness of this layer (δ) is dependent upon rotational velocity as shown by equation 2.19.^[142]

$$\delta = \frac{1.61D^{1/3}v^{1/6}}{\omega^{1/2}} \quad (2.19)$$

2.3. Spectroelectrochemistry;

Spectroelectrochemical techniques, as the name suggests, involve the combination of spectroscopic and electrochemical methods, either ex-situ where samples taken from the electrochemical cell are studied, or in-situ with spectroscopic measurements made during the electrochemical procedure. This can provide more direct characterisation than electrochemistry alone, relating to identification of homogeneous or heterogeneous phase molecules, investigation of adsorbed species at the electrode and electrode surface characterisation.

Various combinations of techniques are possible both in- and ex-situ, some examples of which are given below.

2.3.1. In-situ EPR Spectroelectrochemistry;

EPR or electron paramagnetic resonance spectroscopy investigates exclusively species with unpaired electrons, which when combined with a technique which selectively transfers electrons makes for a judicious pairing as any reversible one electron transfer will mean that either the starting material or product is paramagnetic and therefore EPR active. An unpaired electron has two possible spin states which, when placed in a magnetic field are no longer degenerate,

making it possible to excite the electron with the energy gap corresponding to microwave frequencies.

The basis of a standard EPR measurement involves the employment of a fixed microwave frequency and sweeping of the magnetic field, ensuring that when the energy gap between the spin states matches the energy of the microwaves, the photon absorption is detected as its first derivative due to Zeeman modulation. The spectra provides a g-value along with hyperfine and superhyperfine coupling, which can yield information regarding the specific site of the redox processes within the molecule and the contribution of various nuclei to the singly occupied molecular orbital (SOMO).^[145]

Generally the species investigated using EPR spectroelectrochemistry are diamagnetic in the starting redox state and an EPR signal forms upon electrogeneration of the reduced or oxidised species at the electrode. Depending upon the nature of the solvent and stability of the radical generated, different cell types, electrode assembly, electrolyte concentration and lowered temperatures may be required in order to obtain a well resolved spectrum.^[145]

2.3.2. In-situ Raman spectroscopy;

Raman spectroscopy is a form of vibrational spectroscopy, experimentally the detection of inelastic scattering of incident radiation. The majority of the light is not absorbed or inelastically scattered but instead passes through the sample or is elastically scattered due to the Rayleigh effect, R' (illustrated in figure 10). The photons, E , which interact and exchange energy with the sample are scattered inelastically R_1 and R_2 , with the altered wavelength of the scattered light

reflecting the decrease or increase in energy giving Stokes or anti-Stokes lines respectively. As a result of the quantised vibrational modes of the sample the energy changes experienced by the photons, relative to the incident light, are discrete.

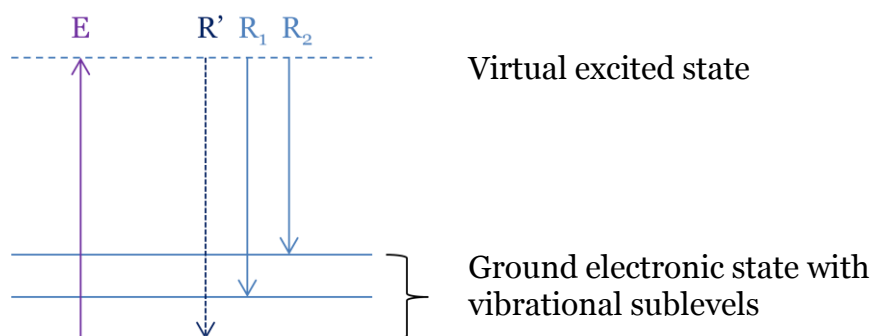


Figure 2.10; A schematic depicting Raman scattering

As mentioned the probability of Raman scattering is low therefore, as a result high concentrations tend to be employed and a high intensity monochromatic light source is required (LASER). The resultant Raman spectra provide molecular vibrational information and can be used for fingerprinting, identification of functional groups and structural information based upon the polarisability of the bonds.^[137]

When employed as a spectroelectrochemical technique, the selection and preparation of an electrode of specific material which possesses a surface plasmon frequency resonant with the incident radiation can lead to a huge enhancement in Raman intensity (10^5 - 10^6), an effect which when utilised is termed surface enhanced raman spectroscopy or SERS^[146]. SERS active metals, including roughened gold, silver, copper and nanostructures of platinum and palladium, when employed as an electrode offer a dramatic enhancement of

species found at the electrode surface which can be easily investigated as a function of potential.^[141]

Despite the enhancement in signal, the interpretation of SERS spectra is not always straightforward due to the adsorption processes and their effects upon molecular symmetry and orientation of molecules, the selection rules associated with Raman activity can change. For example there can be differences in the number of modes present in spectra compared to non-surface enhanced Raman, where the mutual exclusion rule applies. This rule states that no normal mode (bend or stretch of a bond) can be infra-red and Raman active in a molecule possessing a centre of symmetry, however a centre of symmetry may be introduced or lost upon specific adsorption of a species.^[147]

2.3.3. FTIR (Fourier Transform Infrared Spectroscopy);

FTIR is a very well established absorption spectroscopic technique which is complementary to Raman, as it too investigates vibrational modes of a molecule. When incident IR radiation reaches resonance with the frequency of the molecular vibrations (10^{13} - 10^{14} Hz), absorption can occur leading to a vibrationally excited state, particularly if the excitation results in a change in the dipole moment. As IR spectra tend to be well documented and catalogued, spectra can be used as 'fingerprints' to identify substances or functional groups by their characteristic bands.^[137]

The in-situ employment of IR has been well developed with optically-transparent thin-layer electrochemical (OTTLE) cells commercially available for the monitoring of electrochemical reactions. The cells are thin layer due to the

tendency of the solvent to have a significant absorption bands in the IR region of the electromagnetic spectrum, the results of which should be minimised in order to avoid this dominating and potentially obscuring the response of interest.^[141]

3. Experimental;

3.1. Electrodes and materials;

A variety of electrodes were employed throughout this work, some of which were commercially available, others customised or made in house, the details of which are given in table 3.1.

Electrode/ Material	Specifications	Supplier
Glass Tubes	4 mm d	Alfa/ glass blower
Glassy Carbon Disk	3 mm d, Kel-F enclosure	CH Instruments Inc.
Gold Disk	2 mm d, Kel-F enclosure	CH Instruments Inc.
Gold Foil	Various, thickness 0.25 and 0.5 mm	Advent Research Materials
Gold Mesh	82 mesh per inch	Advent Research Materials
Gold Microdisk	10, 25 μm d encapsulated in glass	CH Instruments Inc.
Gold Wire	Various, 0.5 - 0.05 mm d	Advent Research Materials
Graphite Rod	6.3 mm d	Alfa
Heat shrink Teflon	-	SciMed Ltd
Parafilm	-	Swastik Scientific Co.
Platinum Disk	2 mm d, Kel-F enclosure	CH Instruments Inc.
Platinum Foil	0.25 mm thickness	Advent Research Materials

Platinum Mesh	~81 mesh per inch	Advent Research Materials
Platinum Microdisk	10, 25 μm d encapsulated in glass	CH Instruments Inc.
Platinum Wire	Various, 0.5- 0.05 mm d	Advent Research Materials
PTFE Tape	-	Fluorocarbon
Silver Wire	0.5 mm d	Advent Research Materials
Teflon coated Pt wire	0.05 mm d	Advent Research Materials
Teflon coated Ag wire	0.075 mm d	Advent Research Materials
Vycor frits	-	SciMed Ltd.

Table 3.1; Electrodes and electrode materials

3.1.1. Working electrodes (WE);

The working electrode, where the electron transfer of interest takes place, is very important. The rates and even potentials associated with electron transfer and adsorption and reaction mechanisms undergone can be significantly affected by not only the WE material but also its mode of preparation. As such a well defined starting surface is vital for gathering consistent and reproducible data.

The standard preparation for the disk working electrodes varied slightly dependent upon the WE material however all macro disk electrodes were polished with diamond suspensions, initially 1.0 μm grade, rinsed with de-ionised (DI) water, then 0.25 μm diamond, on a polishing cloth. They were then

thoroughly rinsed in DI water. The Au and Pt WE were sonicated and submerged in a water-acetone mixture for one minute. The GC WE was immersed in an ethanol-water mixture and put in the ultrasonic bath for one minute: contact with acetone was avoided.

Post sonication the Au and Pt WE were further cleaned and characterised by cycling in 0.1 M H₂SO₄ in the electrochemical cell. Cyclic voltammetric scans were performed, initially at high scan rate (500 mV s⁻¹), then more slowly (100 mV s⁻¹) until reproducible scans, showing only the anticipated features, were obtained. The potentials employed for the differing conditions are given in Table 3.2;

WE	Gold		Platinum	
	500 mV s⁻¹	100 mV s⁻¹	500 mV s⁻¹	100 mV s⁻¹
Starting E	0.0	0.25	0.1	0.1
Positive Vertex E	1.7	1.6	1.3	1.25
Negative Vertex E	0.0	0.25	-0.3	-0.25

Table 3.2; Electrode acid cycling experimental parameters. (E values given in V vs Ag/AgCl)

Typically 10 to 30 scans were performed in total with potential steps employed when necessary to form bubbles and aid mechanical exfoliation of the surface. (1.80 V and -0.1 V vs Ag/AgCl for Au and 1.6 V and -0.3 V vs Ag/AgCl for Pt).

Typical CVs for the freshly cleaned surfaces can be found in figure 3.1.^{[148]-[150]}

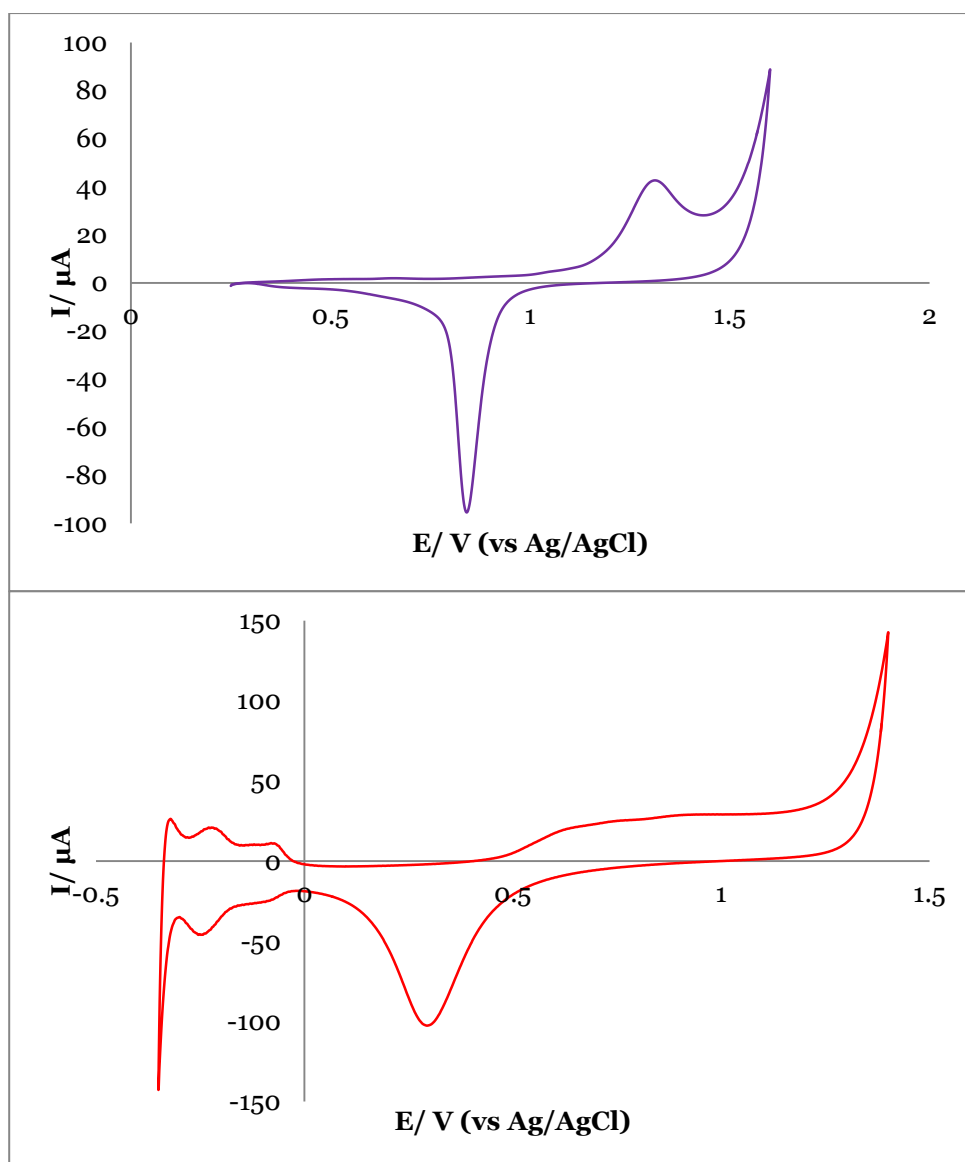


Figure 3.1; Typical acid responses for Au (top) and Pt (bottom) (H_2SO_4 , 0.1 M, scan rates 100 mV s^{-1} and 500 mV s^{-1} respectively)

Where microelectrodes were employed as the WE, the cleaning and preparatory regime was the same as that for the corresponding macroelectrodes except that the diamond suspensions were of smaller particle size (0.25 μm and 0.10 μm) more appropriate to the smaller exposed area of metal.

Where foil, mesh and non insulated wires were employed as WEs they were flame cleaned using the Bunsen burner or smaller blow torch rather than mechanically polished prior to acid cycling.

Where Teflon coated wire WEs were necessitated, such as the *in situ* EPR cell, rather than attempting vigorous cleaning, a fresh section of wire was exposed for each set of measurements undertaken.

3.1.2. Counter electrodes (CE);

The counter or auxiliary electrode is included in the cell setup to allow the current to flow between the WE and CE, avoiding the reference electrode. This is of vital importance as current flowing through the reference electrode would result in destabilisation and without a stable reference electrode the potentials applied across the cell would not be measurable. Although the potential of the working electrode is under potentiostatic control relative to the stable reference, the same is not true of the CE which can experience any potential necessary for the generation of the correct potential at the WE, not equal and opposite as may be expected. This means that at the CE unobservable reactions occur at unmonitored potentials. For this reason it is sensible to place the CE a reasonable distance from the WE and enclose it within a partially permeable frit, therefore avoiding the contamination of the solution near the working electrode with any of the products formed by reaction at the CE. This is not always possible in non-aqueous solution due to the higher resistivity compared to water, where the extension of pathlength and inclusion of an extra resistive frit component can hinder the flow of current making the measurements

impossible however, where practical the segregation allows for more reliable data.

Throughout the electrochemical measurements platinum counter electrodes were utilised. The CE to WE surface area ratio was maintained throughout the various set ups and the scale of the electrodes ensured that the CE was always substantially higher therefore preventing the flow between the WE and CE from becoming limiting. For the most part the CE consisted of a platinum mesh folded and spot welded onto a platinum wire.

The choice of platinum as the CE material was related to the ease of preparation and maintenance, with flame cleaning in a Bunsen flame well suited to removing any surface impurities quickly and effectively.

3.1.3. Reference electrodes (RE);

A stable and reliable reference electrode is extremely important for the measurement and application of potentials and proved a challenging practical aspect of the experimental design. A number of different referencing systems were employed, dependent upon the solvent being used for the measurement in question.

All aqueous voltammetry (predominantly electrode preparation etc) was conducted via a Ag/AgCl reference electrode. Ag/AgCl reference electrodes are one of the most widely used reference electrodes and although commercially available, were prepared in house using the following method; A silver wire and graphite rod were immersed in 0.1 M KCl solution and connected to either the

anode and cathode, respectively, of a 9 V battery or in a two electrode set up to the potentiostat with the Ag as the WE, a piece of Pt connected as the CE/RE and 4 mA applied between them (chronopotentiometry). After between 5 and 15 minutes the Ag wire, now coated in brown AgCl, was disconnected and placed inside a glass tube with a porous tip containing 3.0 M KCl and then sealed using parafilm with a portion of clean silver protruding for connection. When not in use the electrode was stored in 3.0 M KCl solution. The Ag/AgCl electrode was frequently remade to ensure stability by stripping the AgCl from the wire, by submerging in concentrated ammonium hydroxide and the frit and tube emptied and cleaned by sonication in nitric acid then DI water.

The bulk of the electrochemical measurements made were, however, in non-aqueous solvents for which simple and reliable reference electrodes are less widely available.

For the measurements made in THF a ferrocene-ferrocenium (Fc/Fc⁺) reference electrode was developed and tested based upon a similar Fc/Fc⁺ electrode developed by Compton.^{[151][152]} The Fc/Fc⁺ electrode employed the same glass tube and frit as the Ag/AgCl electrode but with a freshly flame cleaned Pt wire submerged in 'reference solution'. The 'reference solution' consisted of 0.1 M TBABF₄ in THF (the same solvent and electrolyte at the same concentration as found in the bulk solution) with equimolar quantities (0.4 mM) of ferrocene (Fc) and ferrocenium tetrafluoroborate (FcBF₄, the same counter ion as the electrolyte). Oxygen and water were excluded from the electrode by oven drying the components where appropriate and using dried, degassed solvent. The tube was evacuated and flushed with Ar as the solution was added and sealed promptly with PTFE tape. When the electrode was not in use it was stored in a

degassed vial of 0.1 M TBABF₄ in THF with Ar flushed headspace. The potential of the Fc/Fc⁺ electrode was checked prior to and post use by measuring a CV of Fc in THF with 0.1 M TBABF₄, with the Fc redox potential consistently at, or very close to zero volts and stable over the duration of measurements made.

This electrode did require renewal more regularly than the Ag/AgCl and although it was found to be stable for up to a month, it was generally disassembled, its components cleaned and dried and freshly made daily (or for each set of measurements). Oxygen contamination of the solution resulted in a positive potential drift away from zero and given the working environment (not a glovebox!) it was found impossible to exclude completely over long time periods.

A similar electrode was trialled for the NMP system but met with limited success as the ferrocenium did not appear stable in NMP, with significant potential drift seen with regularity even over the relatively short experimental timescale. For most of the electrochemical measurements in NMP, a platinum wire pseudo reference electrode was employed. Once the data from the system was gathered, ferrocene was added and a full CV covering the Fc and previous analyte processes was recorded, allowing the calibration of potentials vs Fc.

The ferrocene/ferrocenium ion (Fc/Fc⁺) redox couple is recommended by IUPAC ^[153] as a potential reference in non-aqueous solvents with the process often used as a solvent-independent potential reference for comparison of potentials in different solvents.^[154]

The merits of this are often disputed as although the structure of ferrocene is such that the neutral and oxidised forms are very similar size and the presence

of the bulky cyclopentatrienyl ligands shield the charge of the cation from its surroundings (therefore very little influence is expected from the solvent), a shift in potential of up to 500 mV with varying solvent electro-donating properties has been reported.^[155]

The one electron oxidation of ferrocene to form the ferricinium cation (reaction 3.1) is undergone in non-aqueous systems with a half wave potential in the range of 0.8 to 1.3 V vs. Ag/AgCl, dependent upon the precise nature of the solvent and temperature at which the measurement is made.^{[156][157]}



In THF, the solvent employed in much of the work presented, the potential is reported to be 1.209 V vs. Ag/AgCl^[158] however a corresponding value for NMP measured under the same exacting conditions is not given. The two solvents have similar properties, both being fairly electrodonating,^[154] therefore could be expected to have similar effects upon the ferrocene redox potential.

3.2. Three Electrode Cell Configuration;

3.2.1. Typical Three Electrode Cell;

The electrodes described above were typically employed in a cell similar to that depicted in figure 3.2.

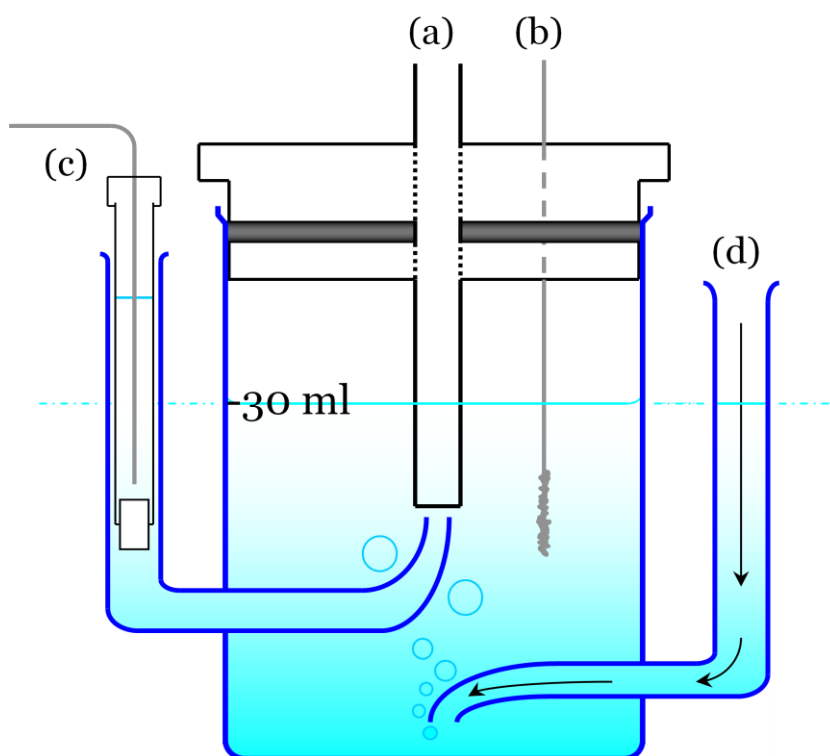


Figure 3.2; Typical three electrode cell schematic. For discussion of the labels, see the main text. Cell made in-house by the glass blower, Mr David Gordon.

The volume of the cell depicted is approximately 50 cm³ with typically 30 cm³ of electrolyte employed. The WE (a) can be seen in the middle of the cell, entering through a tight fit hole in the PTFE cell lid. The lid was sealed with an O-ring protected from the organic solvents by a layer of PTFE tape. There are two other small holes in the lid, one allowing the counter electrode (b) access to solution and one small, easily sealable hole to allow gas flow through the cell and sampling of solution or the headspace. Directly under the WE is the ‘outlet’ of the Luggin capillary homing the RE (c) connecting it to the solution closest to the WE. On the opposite side of the cell to the RE is a gas inlet (d) for de-aeration of solution in the cell or saturation with CO₂.

Prior to use the cells were washed with acetone and DI water and oven dried with periodic, more thorough cleansing in nitric acid or piranha solution

(sulphuric acid and hydrogen peroxide) to remove any potential build up of residue.

Variations upon this set up were used when necessary, for example the segregation of the CE, as discussed above but also for the in-situ EPR and experiments where analysis of products was investigated.

3.2.2. In-situ EPR Cell;

In order to measure the EPR spectra of radicals formed electrochemically there are several possible cell setups available including thin layer cells with a large flat window.^[141] These allow the employment of large electrodes in a thin layer of solvent so large quantities of paramagnetic species can be generated whilst ensuring the solvent pathway is kept minimal. The cell found, not only to be the simplest to construct, but also the most efficient was however based on a sealed standard EPR tube (a) using thin wire electrodes (b) as depicted in figure 3.3.

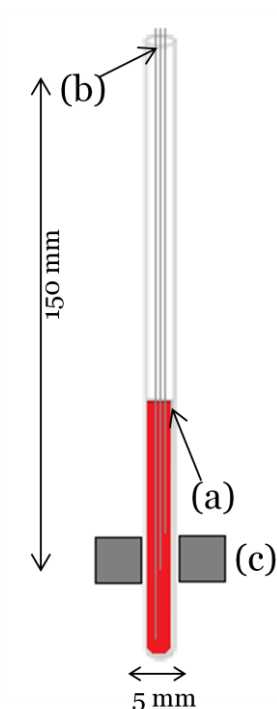


Figure 3.3; Schematic of the in-situ EPR cell set up.

The wire electrodes (b) were Teflon coated platinum for the WE and CE and silver for the pseudo reference electrode, with approximately 0.2 cm of the respective metals exposed. The electrodes were carefully positioned so as the WE was situated within the microwave cavity (c), the RE was found close to, but not in contact with the WE and the CE was positioned as far as was possible from the WE and microwave cavity whilst maintaining voltammetry which was not entirely dominated by resistivity (with peaks still observable). The cavity itself was a TE₁₀₂ mode resonator, specifically an ER 4123SHQE. The headspace (or space in the EPR tube not occupied by solution) was flushed with the gas appropriate for the experiment and the cell sealed using PTFE and parafilm.

The use of the standard EPR tube cell meant that the tuning of the EPR spectrometer and critical coupling of the cavity was as standard (albeit for a

solvent with a high dielectric constant) and the set up compatible with the various spectrometers available as well as the additional optional hardware such as the thermostatic control for low temperature measurements.

3.1.3. Bulk electrolysis Cell;

In order to investigate product formation bulk electrolysis was employed. This uses a held potential (chronoamperometry) for significant time periods and unlike the electroanalytical method described previously is aimed at creating a significant change in the composition of the starting solution. As such a large WE (and corresponding CE) were employed (Au foil, 5 cm² and Au mesh, 5 cm²) and where appropriate the solution was stirred to avoid diffusion limitation of the currents and product formation. Different cell set ups were used depending upon whether the gas phase or solution phase were being investigated.

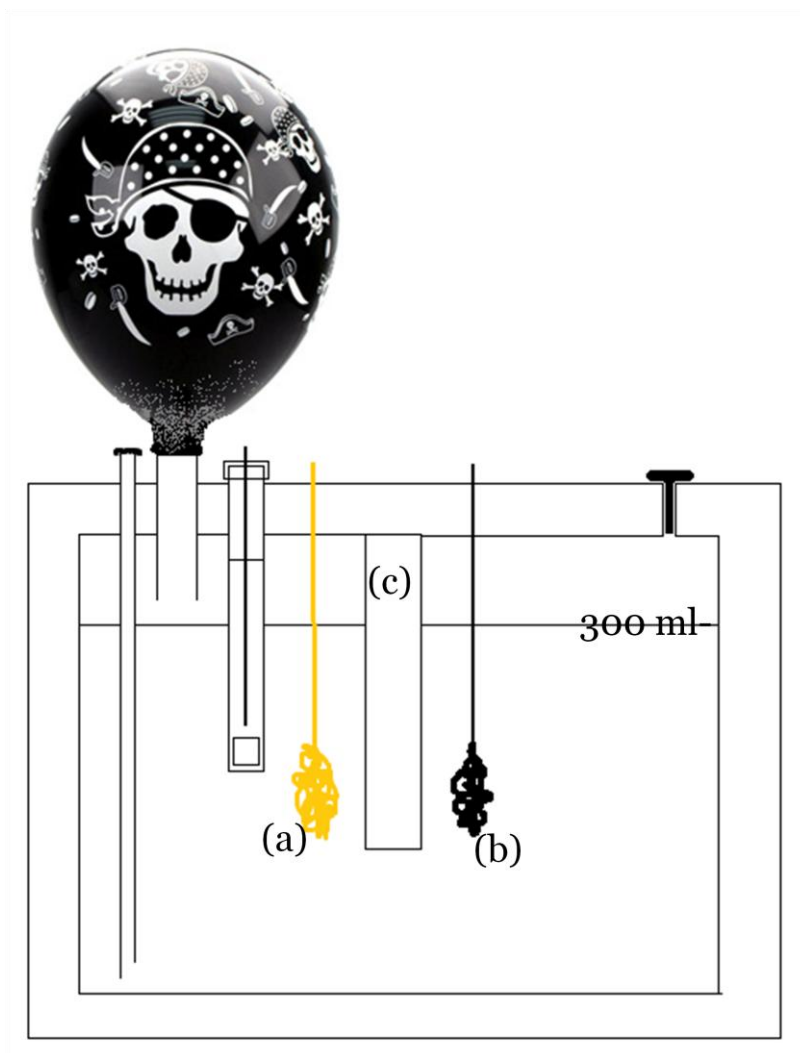


Figure 3.4; Schematic of the large bulk electrolysis cell employed for collection of gaseous samples. Cell made in-house by Mr Christopher Slann (mechanical workshop).

Figure 3.4 shows a schematic of the large Teflon cell employed for the bulk electrolysis where gaseous product generation and collection were the primary aim. This cell allows the bulk solution to remain in contact, avoiding the resistivity issues associated with the separation of the WE (a) and CE (b), however any gases generated at the respective electrodes are kept separate by the divided headspace (c). The volume of this cell was significantly higher than that of the typical three electrode cell depicted in figure 3.2, with 300 cm³ of solution used for the experiments. This allowed for the generation of larger

quantities of gases making the sampling and detection less challenging. The cell was constructed with strong seals and held together with a series of bolts allowing it to be used above ambient pressure.

Where attempts to investigate the solution phase products were made the counter electrode was enclosed within a glass tube and contacted the solution through a Vycor frit. In these experiments such a large volume of analyte was no longer useful so the typical glass three electrode cell (figure 3.2) was employed with the larger electrodes. Addition of a stirrer bar, magnetic stirrer and gas bubbled over (or on occasion through) the solution whilst the bulk electrolysis was performed allowed greater current flow and therefore a higher rate of product formation.

3.3. Chemicals;

The reagents which were procured commercially for this work are presented in Table 3.3. They were, for the most part, used without further purification with the exception of drying and deaeration where exclusion of water and oxygen were deemed necessary. THF was available dried on a still having been distilled from Na/benzophenone under an atmosphere of nitrogen for experiments where particularly dry solvent was required. NMP was found to give the cleanest solvent background when it was syringed directly from the suba sealed container in which it was supplied using a dried gas tight syringe into the cell. The aqueous solutions employed were all made using DI water ($>18\text{ M}\Omega\text{ cm}$ resistivity), prepared using a Millipore reverse osmosis unit coupled to an Elga “Purelab Ultra” purification system (Veolia Water Systems).

The deaeration and saturation of solutions with various gases took differing lengths of time dependent upon the solvent nature and the volumes employed. The effects of the gases were assessed through CV to determine the appropriate durations. For the general 3 electrode cell (30 ml) organic solvent saturation with CO₂ typically took 20 minutes of gentle bubbling, so 30 minutes was typically employed to ensure saturation was reached.

Name	Details	Supplier
Acetone	99+%	Fisher
Ammonium Hydroxide	ACS	Sigma-Aldrich
Argon	99.998%	BOC
Bipyridine	99+%	Sigma-Aldrich
Carbon dioxide	>99.990%	BOC CO ₂
Carbon monoxide	99.9 %	BOC
Diamond Suspension	1.0, 0.25, 0.10 µm	Kemet
Deuterium oxide	99.9% atoms D	Sigma-Aldrich
Dimethyl amminomethyl ferrocene	96%	Sigma-Aldrich
Ethanol	99.99%	Fisher
Ferrocene	99%	Alfa Aesar
Ferrocene methanol	97%	Sigma-Aldrich
Ferrocene carboxylic acid	98%	Lancaster
Ferrocenium tetrafluoroborate	Technical grade	Aldrich
Hydrochloric acid	37% aq. solution	Sigma-Aldrich
Hydrogen peroxide	30% aq. Solution	Sigma-Aldrich
Lithium oxalate	99+%	Avocado
Lithium tetrafluoroborate	98%	Sigma-Aldrich
Nitric acid	69% aq. solution	BHD Chemicals
N-Methylpyrrolidone	99.5% anhydrous	Sigma-Aldrich
Potassium chloride	99.5%	Sigma-Aldrich
Potassium tetrafluoroborate	96%	Sigma-Aldrich
Pyridine	99.8%	Sigma-Aldrich
Rubidium tetrafluoroborate	98%	Alfa Aesar
Sodium hydroxide	99.99%	Sigma-Aldrich

Sodium tetrafluoroborate	98%	Janssen Chimica
Sulphuric acid	95+%	Fisher
Tetrahydrofuran	≥99.9%	Sigma Aldrich
Tetrahydrofuran-d₈	99.5% atoms D	Sigma-Aldrich
Tetrabutylammonium tetrafluoroborate	≥99.0%	Fluka Analytical

Table 3.3; Reagents and solvents employed and their purity and supplier.

Many of the organometallic species investigated were not commercially available and were synthesised in house by myself, Dr Mark Whiteley and Mr Logan Barr using pre-existing routes. ^{[107][108]}(and refs within). The recrystallised complexes were characterised using IR, UV-vis, NMR and microanalysis prior to use in the electrochemical systems by Mark Whiteley's group to ensure purity and the desired product formation.

3.4. Other Equipment;

Standard glassware and other laboratory materials were employed for much of the work with the specialised equipment detailed in table 3.4.

Equipment	Model	Company
Analytical Balance	Explorer	Ohaus
Autolab Potentiostat	(a) PGSTAT 100	Eco-Chemie
	(b) μAUTOLABIII	Eco-Chemie
Battery	Silver (9 V)	Eveready
EPR Spectrometer	E580X (X-band)	Bruker
FTIR Spectrometer	(c) Vertex 80v	Bruker
	(d) 8300 (SpecacT5, 5 m)	Shimadzu
GC	7890A	Agilent
Ivium Potentiostat	(e) CompactStat	Ivium
Micropipettes	0.2 – 2.0 μL	Eppendorf Reaseach
NMR Spectrometer	VMS 500 MHz	Varian
pH meter	HI 991300	Hanna
Purification unit	Purelab Ultra	Elga Labwater
Raman Spectrometer	Renishaw system 1000 (632 nm HeNe)	Renishaw

Rotating Disk Motor	EG&G PAR model 616	Princeton Applied Reasearch
Ultrasound Bath	-	Clifton
Syringe	1050TLL	Hamilton
ThermostaticWater Bath	GD100	Grant Scientific

Table 3.4; Specialised equipment employed with model and supplier. (a) employed for non in-situ experiments, (b) EPR in-situ experiments, (c) for analysis of solution, (d) for gas phase analysis, (e) for Raman in-situ experiments

4. Molybdenum based Molecular Electrocatalyst for CO₂ Reduction

4.1. Introduction to the catalyst;

The use of catalysis to surmount the high overpotential associated with direct CO₂ reduction has, as discussed in the introduction, been much investigated. This chapter addresses the study of a relatively inexpensive molybdenum complex, [Mo(CO)₄bpy], employed as a CO₂ reduction electrocatalyst. This species is shown to lower the overpotential of CO₂ reduction and enhance the associated current observed. The intermediates have been explored using various techniques including in-situ EPR spectroscopy.

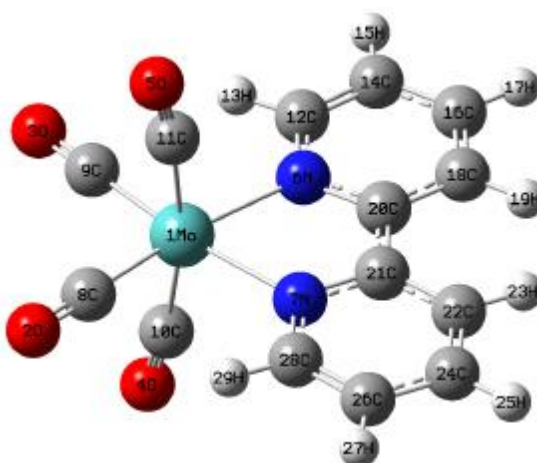


Figure 4.1 DFT calculated ball and stick diagram of [Mo(CO)₄bpy] with labelled atoms.

Mo(CO)₄bpy, the structure of which can be seen above in figure 4.1, shares features with many known CO₂ reduction catalysts, with several previously described polypyridyl complexes (see section 1.32) and also pyridinium itself having been shown to be successful electro- and photoelectrocatalysts.^[99-102]

Many of the most promising electrocatalysts developed are metal based but tend to incorporate group 7 & 8 metal centres meaning costs and limited availability automatically preclude practical large scale application; a molybdenum carbonyl bipyridyl system however could prove a more economically viable and sustainable CO₂ reduction electrocatalyst. Molybdenum is a group 6 transition metal and is stable in many different oxidation states giving it a rich chemistry and is more abundant and less costly than traditional catalytic metals such as ruthenium and platinum. This is the first investigation, to our knowledge, of a molybdenum based CO₂ reducing molecular catalyst despite the importance of Mo in analogous enzyme reductive processes. CO₂ reduction to methane (and subsequent catalysed propylene formation) has recently been reported at molybdenum centred nitrogenase based enzyme^[159].

[Mo(CO)₄bpy] has been previously investigated, and some of its physical and electrochemical properties documented as found in the introduction section 1.4., but no reports have described its application toward electrocatalysis of CO₂ reduction. The complex is readily prepared from inexpensive metal carbonyl precursors by existing published methods.^[107]

4.2. Mo(CO)₄bpy in the absence of CO₂;

Although some voltammetry of [Mo(CO)₄bpy] has been reported elsewhere there are a great deal of variables which can affect the stability of a complex in an electrochemical set up (such as solvent, electrode material, electrolyte etc). Also without a particularly well defined and reliable reference electrode for measurements in non-aqueous solvents the potentials quoted tend to vary

somewhat, therefore it was important to gather all the useful voltammetric measurements for the $[\text{Mo}(\text{CO})_4\text{bpy}]$ species in the systems to be employed in the absence of CO_2 .

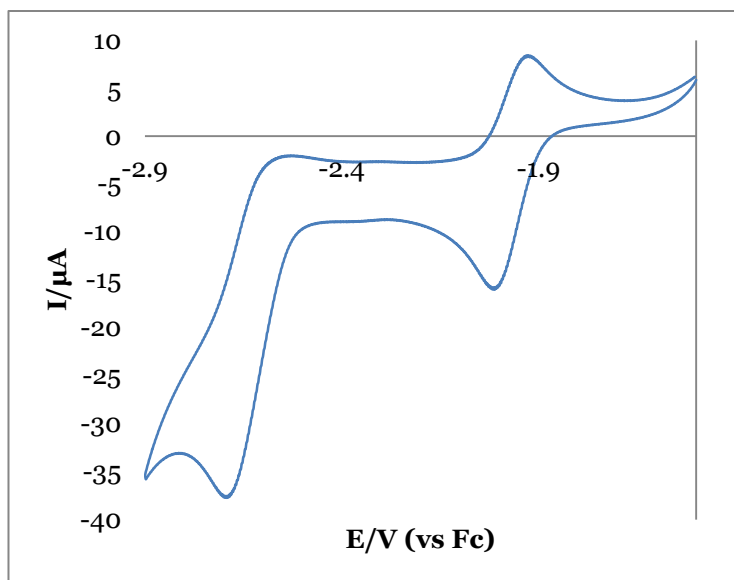


Figure 4.2. Voltammetry of $\text{Mo}(\text{CO})_4\text{bpy}$ showing the known 1st two reductions. $\text{Mo}(\text{CO})_4\text{bpy}$ (0.5 mM) at 200 mV s^{-1} in cell 1.

Figure 4.2 shows the CV measured when reductive potentials are applied, scanning from -0.5 V to -1.9 V vs Pt wire pseudo reference in N-methyl-2-pyrrolidone (NMP). This shows the successive one-electron reductions of $[\text{Mo}(\text{CO})_4\text{bpy}]$ to the 19-electron radical monoanion $[\text{Mo}(\text{CO})_4\text{bpy}]^{\bullet-}$ and then to the 20-electron dianion $[\text{Mo}(\text{CO})_4\text{bpy}]^{2-}$. The first redox process with peaks at -1.995 V and -1.846 V (vs Fc/Fc⁺) corresponds to the reversible reduction and re-oxidation as an electron is added to and removed from the lowest unoccupied molecular orbital (LUMO) of the molecule.

4.2.1. Stability of monoanionic radical;

The monoanion formed is stable over the experimental timescale down to scan rates as low as 5 mV s^{-1} at room temperature as seen by the reversibility of the peaks with A consistent reductive:oxidative current ratio of approximately 1 as shown in figure 4.3.

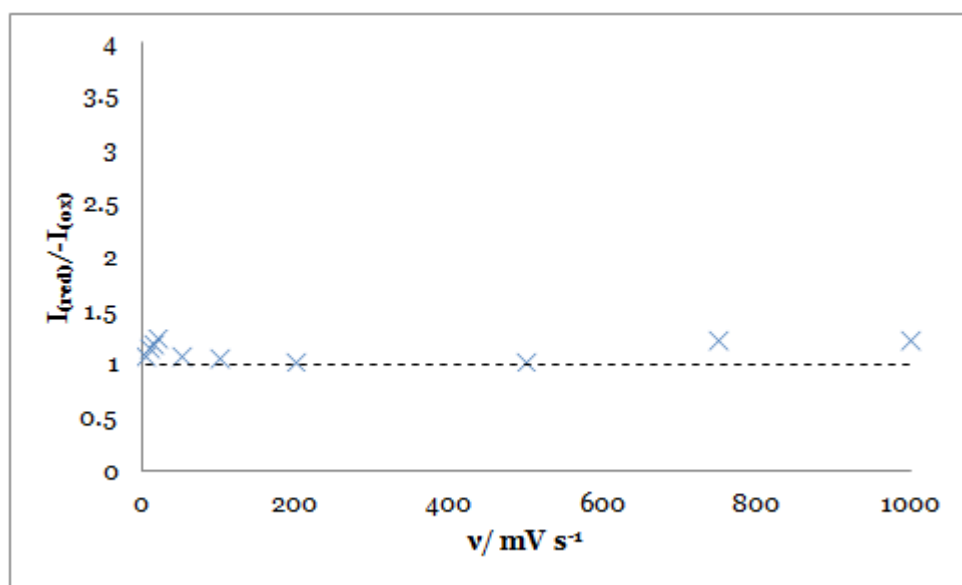


Figure 4.3; Current ratio of the oxidative and reductive current associated with the first redox process of $\text{Mo}(\text{CO})_4\text{bpy}$ as a function of scan rate.

The stability observed in the voltammetry can also be seen by the reversibility of the response in potential step experimental observations.

4.2.1.1. Double step chronoamperometry of first redox process of Mo(CO)₄bpy;

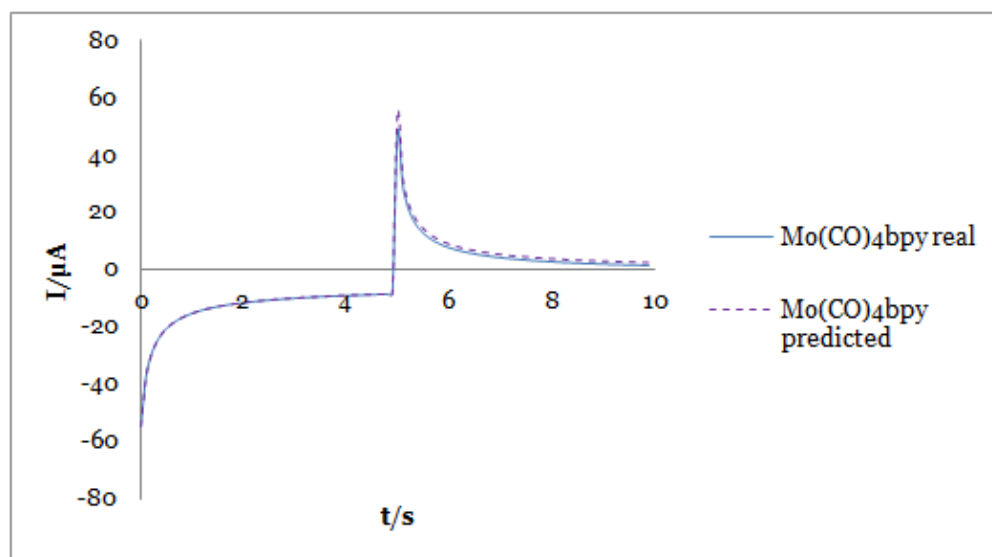


Figure 4.4; Double step chronoamperogram of Mo(CO)₄bpy (0.5 mM) measured in cell 1 with applied potentials of -1.995 V and -1.846 V vs Fc.

Figure 4.4 shows the double step chronoamperometry current response where the potential has been stepped from the potential corresponding to the voltammetric peak of the Mo(CO)₄bpy first reduction, -1.995 V, and the potential of the peak re-oxidation, -1.846 V, spending 5 seconds held at each.

The initial spike observed close to 0 s at very short times (<0.1 s) is due to double layer charging and reduction of material at the electrode surface as the potential is applied. The decay seen subsequently is due to the thickening of the diffusion layer with time and lowering of the analyte concentration at the electrode. The current response declines less steeply after 2 s due to mass transport effects.

At 5 s another sharp spike is observed as the polarity of the electrode is switched and the double layer re-orders with the associated current again levelling off

rapidly. The current at which this levelling is seen is not equal to a mirror image of the reductive peak along the time axis as may be expected. This lack of symmetry is due to a lower availability of the mono-reduced complex available for re-oxidation compared to that of the neutral complex to be reduced.

This is expressed in the following relationships which assume a diffusion limited system. The initial reduction of $\text{Mo}(\text{CO})_4\text{bpy}$ to $[\text{Mo}(\text{CO})_4\text{bpy}]^{\bullet-}$, in this case the forward step of the double step chronoamperometry, has a current response (i_f) described by equation 4.1^[141];

$$i_f(t) = \frac{nFAD_0^{1/2}C_0^*}{\pi^{1/2}t^{1/2}(1 + \xi\theta')} \quad (4.1)$$

Equation 4.1 is an adaptation of the Cottrell equation (2.15) where n is the number of electrons transferred, F is the Faraday constant, D_0 is the diffusion coefficient, in this case of $\text{Mo}(\text{CO})_4\text{bpy}$, C_0^* is the concentration of the analyte ($\text{Mo}(\text{CO})_4\text{bpy}$), t is time and $\xi\theta'$ can be defined by (4.2);

$$\xi\theta' = \frac{i_d(\tau) - i(\tau)}{i(\tau)} \quad (4.2)$$

where τ is the fixed sampling time, i_d is the diffusion limited current and i is the instantaneous current.

The subsequent re-oxidative process, or reverse step where $[\text{Mo}(\text{CO})_4\text{bpy}]^{\bullet-} \rightarrow \text{Mo}(\text{CO})_4\text{bpy}$ is described by equation 4.3;

$$-i_r(t) = \frac{nFAD_0^{1/2}C_0^*}{\pi^{1/2}} \left[\frac{1}{(t - \tau)^{1/2}} - \frac{1}{t^{1/2}} \right] \quad (4.3)$$

These equations both require the knowledge of the diffusion coefficient and working electrode area which if not accurate can introduce significant error into the prediction. To eliminate this factor the reversal current i_r can be divided by the forward current i_f at known time values where t_f and t_r are the times at which the current measurements are made and τ is the current reversal time (in this case 5 s) as seen in equation 4.4;

$$\frac{-i_r}{i_f} = \left(\frac{t_f}{t_r - \tau} \right)^{1/2} - \left(\frac{t_f}{t_r} \right)^{1/2} \quad (4.4)$$

Using this equation the experimental data for the i_f step was used to generate the predicted reversible current response (dotted line on figure 4.4).

As seen the predicted and experimental reverse step currents overlay very well showing that the peak current is indeed diffusion controlled and also that the process is reversible.

The stability of this mono-reduced radical species is due primarily to the extensive delocalisation of the extra electron density over both of the rings of the bipyridyl ligand as illustrated by the image of the LUMO given in figure 4.5.

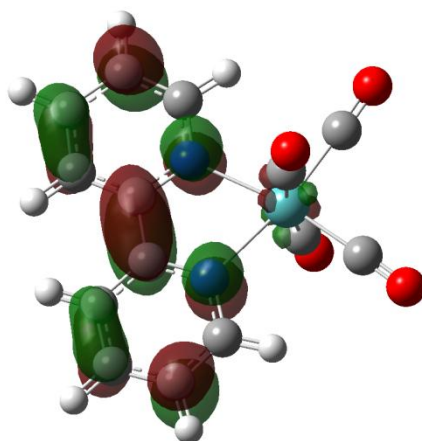


Figure 4.5; Density Functional Theory calculated LUMO. See text for details of the method used.

Density functional theory (DFT) calculations undertaken show the LUMO of the complex is predominantly found on the bipyridyl ligand with a relatively low metal contribution and an additional very small contribution arising from the σ and π^* orbital overlap of the CO ligands in the same plane as the bipyridyl, which is in agreement with existing literature.^[108] DFT calculations were performed by Dr J McDouall using the Gaussian suite of programs.^[160] Geometries were fully optimised using the B3LYP exchange-correlation functional^[161] and the TZVP basis set.^[162] For the Mo atom, the TZVP basis includes an effective core-potential (ECP) which replaces 28 core electrons.^[163] All geometry optimisations and vibrational frequencies used this ECP specification.

The second reduction, observed at -2.619 V, corresponds to the addition of an electron to the second lowest unoccupied molecular orbital, SLUMO, (also thought to be localised predominantly on the bipyridyl ligand). This reduction is only partly reversible with the degree of reversibility observed dependent upon the scan rate employed in the measurement as illustrated in figure 4.6.

4.2.2. Stability of the dianion;

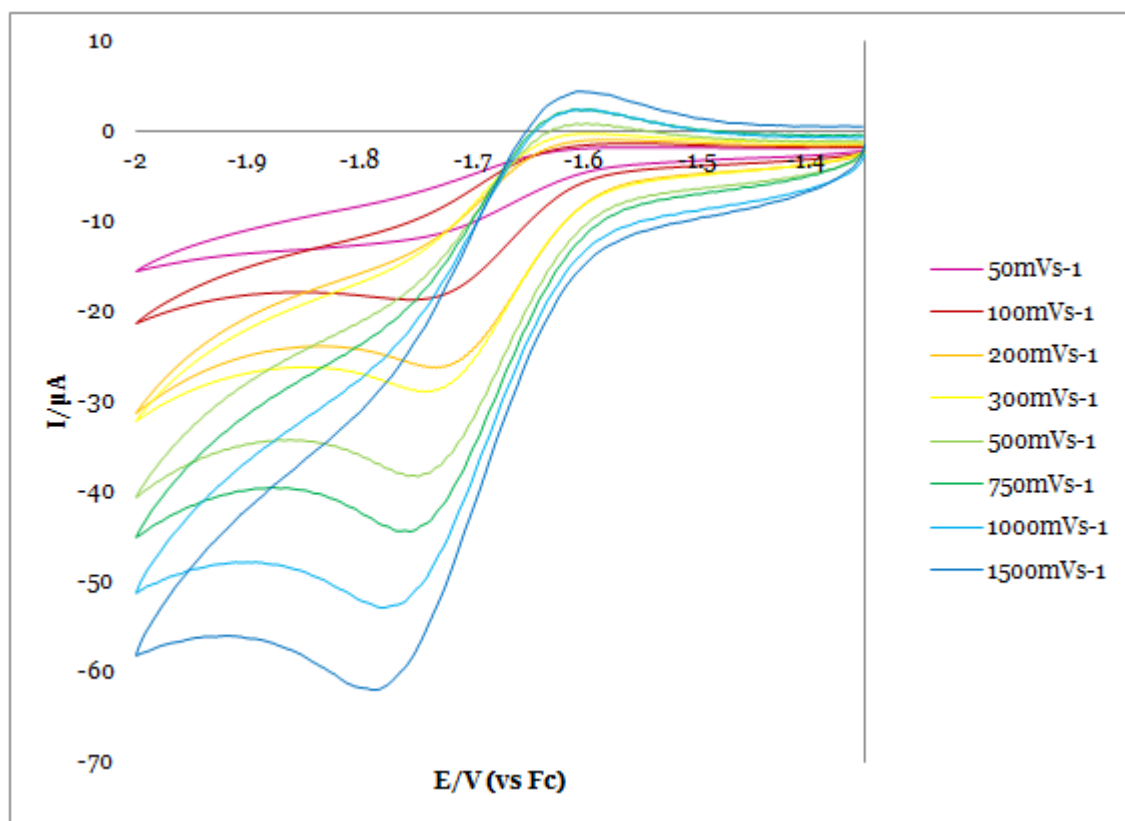


Figure 4.6; 2nd reduction of Mo(CO)₄bpy (0.5 mM) at various scan rates in cell 1

The re-oxidation peak is completely absent at 50 mV s⁻¹ but is quite clearly observed when the scan rate is increased with the current ratio of the oxidative and reductive processes nearing 1 at scan rates greater than ~1000 mV s⁻¹ as shown in figure 4.7.

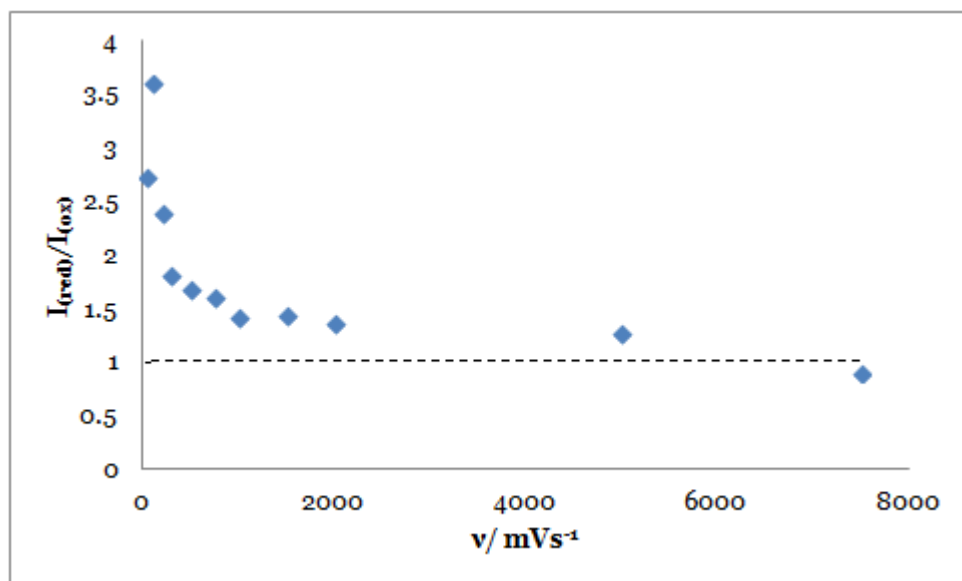


Figure 4.7; Current ratio of the oxidative and reductive current associated with the second redox process of $\text{Mo}(\text{CO})_4\text{bpy}$ as a function of scan rate. The dashed line highlights the expected current ratio for a reversible electron transfer.

From figure 4.7 upon investigation of the degree of reversibility observed in the voltammetry of the second redox process, $[\text{Mo}(\text{CO})_4\text{bpy}]^{\bullet-} + e^- \leftrightarrow [\text{Mo}(\text{CO})_4\text{bpy}]^{2-}$, the fastest scan rates trialled can be seen to give the current ratio closest to unity, therefore possessing the greatest extent of reversibility.

The second reduction, although electrochemically reversible under certain conditions has been reported as being ‘chemically irreversible due to the loss of a CO ligand’.^[119] Throughout the voltammetric measurements made this was not necessarily observed to be the case, as illustrated in section 5.3 where the examination of the effects of differing experimental parameters leads to discovery of a degree of control over this dissociation.

The instability of the dianions may be, in part, due to lability of the CO ligands however the peak thought to be associated with the re-oxidation of the resultant tricarbonyl anionic species^[89] occurs at a different potential to that of the

reoxidation of the tetracarbonyl complex and is not detectable via voltammetry until more negative potentials have been applied as seen in figure 4.8.

4.2.3. Tricarbonyl formation;

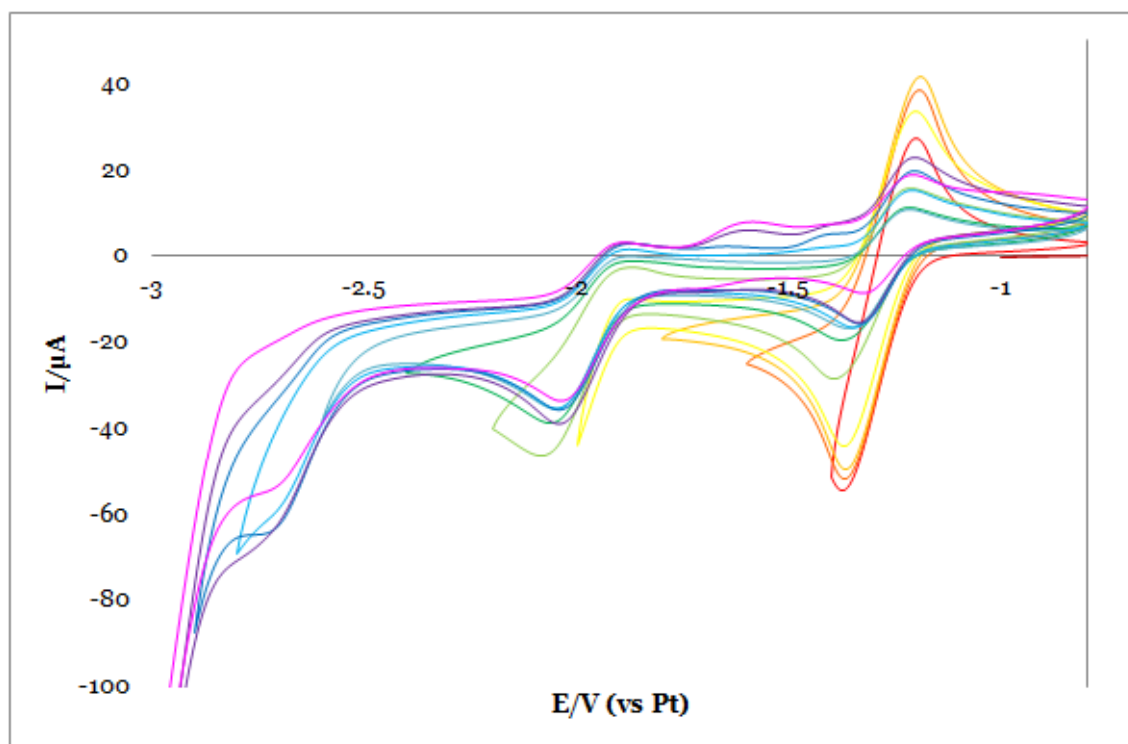


Figure 4.8; $\text{Mo(CO)}_4\text{bpy}$ (0.5 mM) scanning to various negative vertex potentials at 200 mVs^{-1} in cell 1

The two previously observed reductions (see figure 4.2) are evident in the forward (negative) scan, however the potential in figure 4.8 is stepped to increasingly negative vertexes before the sweep direction is changed. Once the potential was scanned to values at or below -2.9 V , a new reductive peak at -2.7 V and a strikingly clear new re-oxidation peak emerged on the back (positive) scan at ca. -1.6 V , directly between the peaks associated with dianion to anionic radical oxidation and the reformation of the neutral species $[\text{Mo(CO)}_4\text{bpy}]$.

Unlike the other processes mentioned so far these peaks have not been described in any of the literature pertaining to $[\text{Mo}(\text{CO})_4\text{bpy}]$ and could be attributed to the formation and re-oxidation of a tricarbonyl anionic species, formed from the dissociation of CO from $[\text{Mo}(\text{CO})_4\text{bpy}]^{2-}$ at sufficiently negative potentials.

The second reduction potential is not sufficiently negative to form the new species with no new oxidative peak emergence even if this potential is held for prolonged periods of several minutes before scanning in the positive direction.

The carbonyl groups of the complex are electron withdrawing so help to stabilise negative charge on the molecule to some extent. The loss of one of these stabilising ligands might be expected to result in a shift toward more negative potentials however the loss of a ligand would result in a change in geometry of the complex. The previously pseudooctahedral $[\text{Mo}(\text{CO})_4\text{bpy}]$ had a limited degree of CO-bpy orbital overlap as shown by almost complete absence of electron density on these groups in the DFT LUMO in figure 4.5.

Figure 4.9 depicting the calculated singly occupied molecular orbital (SOMO) of $[\text{Mo}(\text{CO})_4\text{bpy}]^{\bullet-}$ (a) and $[\text{Mo}(\text{CO})_3\text{bpy}]^{\bullet-}$ (b) shows the predicted orbital structure of the radical anion for the tetracarbonyl and tricarbonyl species.

From comparison of these, upon loss of a carbonyl group the rearranged ligand positions shown allow for greater orbital overlap, observable by the presence of significantly more electron density found upon the remaining CO groups and metal centre. This extra delocalisation found in the tricarbonyl species offers additional, more effective stabilisation of the negative charge found when

compared to the tetracarbonyl where the extra electron density is shown to be more localised on the bipyridyl group.

Figure 4.10 shows the highest occupied molecular orbital (HOMO) for the dianion species for both the tetracarbonyl (a) and tricarbonyl (b) situation. This suggests that upon the formation of the di-reduced species, when a second electron was added to the complex, the tetracarbonyl has an even lower degree of charge delocalisation than seen for the tetracarbonyl radical anion. Conversely the tricarbonyl dianionic complex shows enhanced delocalisation with more charge spread more evenly when compared with the radical anionic species, and even more palpably when compared with the tetracarbonyl dianion.

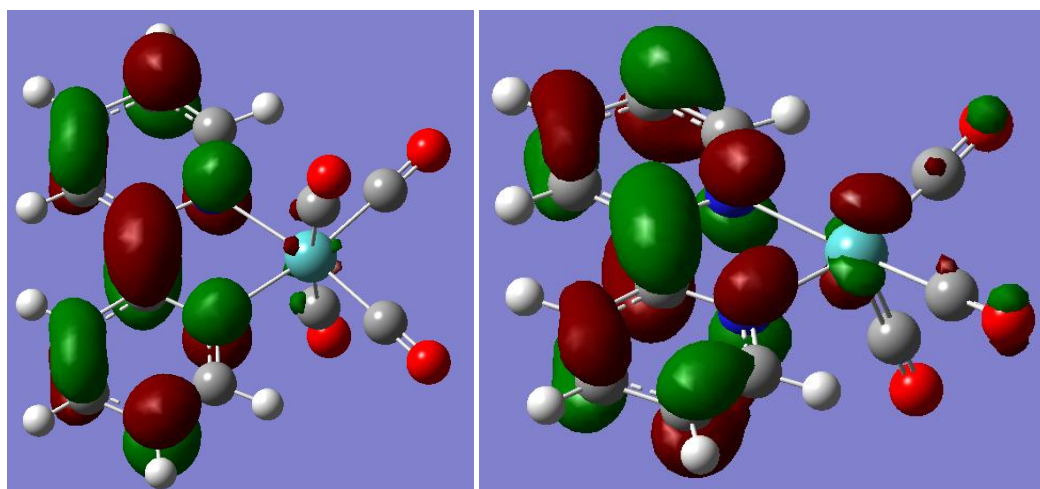


Figure 4.9; DFT images showing the calculated singly occupied molecular orbitals (SOMO's) for (a) $[\text{Mo}(\text{CO})_4\text{bpy}]^{\bullet-}$ and (b) $[\text{Mo}(\text{CO})_3\text{bpy}]^{\bullet-}$

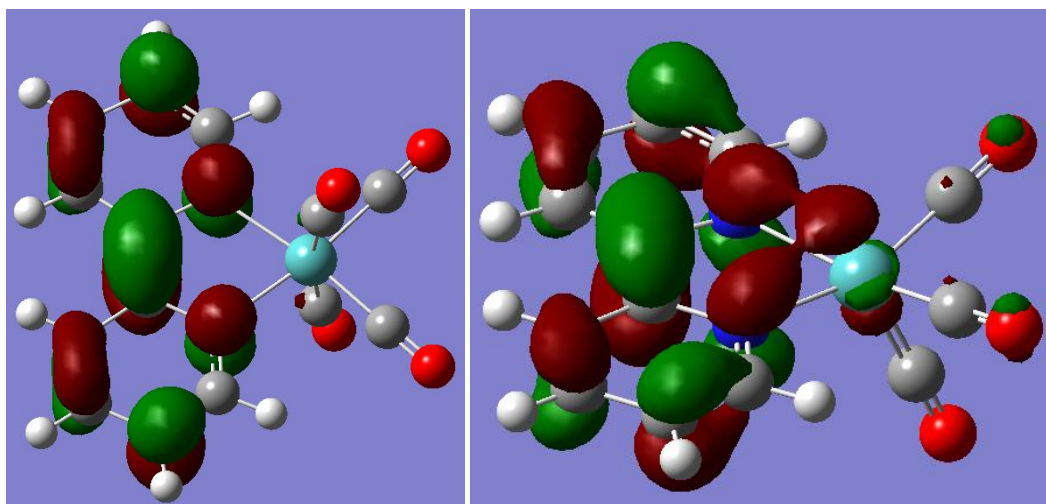


Figure 4.10; DFT images showing the calculated highest occupied molecular orbitals (HOMO's) for (a) $[\text{Mo}(\text{CO})_4\text{bpy}]^{2-}$ and (b) $[\text{Mo}(\text{CO})_3\text{bpy}]^{2-}$

This extra delocalisation, therefore stabilisation, would be expected to shift the tricarbonyl re-oxidation process to more positive potentials than the analogous tetracarbonyl process, thus rationalising the position of the new peak and also the tendency of the tetracarbonyl to lose a relatively strongly bound carbonyl group and form the tricarbonyl upon application of very negative potentials. Something similar has been observed in an analogous manganese complex^[89].

4.2.2.2. The lack of reversibility of the second reduction;

When the potential applied is not so negative as to generate the proposed tricarbonyl species (greater than -2.9 V) the lack of reversibility of the voltammetry does strongly suggest that there is an undetected electron transfer to regenerate the monoanion or possibly a secondary chemical reaction to give electro-inactive, therefore voltammetrically unobservable, products. The first redox process shows a clear drop in peak current upon reaching the second reduction when compared to the case when only the potentials required for the

first redox process are investigated. Prior to the second reduction the CV remains fairly reversible, with the charge associated with the monoanion reoxidation staying approximately equal in magnitude to the charge consumed in its formation. This tends to support the former explanation or suggests an easily reversible chemical reaction as a dramatic change in the quantity of the mono-reduced species available would be expected to alter the reoxidative peak with respect to the reductive.

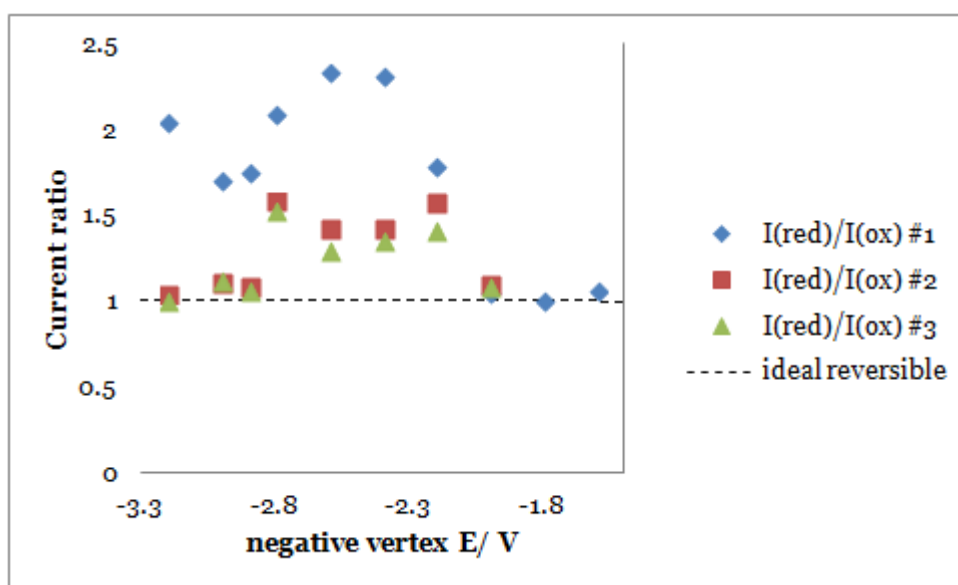


Figure 4.11; Current ratio of oxidative and reductive peak current of the first reduction of $\text{Mo}(\text{CO})_4\text{bpy}$ as a function of negative vertex potential. Scan rate 200 mV s^{-1}

From figure 4.11 it can be seen that the 1st scan (blue) of the set of measurements has a higher current ratio, particularly after the potential has been scanned negative enough to reach the second reduction, than the later scans (#2 and #3 shown in red and green). This could be in part due to the reduction of residual oxygen and other impurities in the system being reduced and overlapping to give an apparent enhancement of the reductive current of $\text{Mo}(\text{CO})_4\text{bpy}$ compared with the re-oxidation. However from the plot it can be seen that the system retains a high degree of reversibility over all of the

potential ranges irrespective of the later reductions the complex undergoes with the majority of points in this data set found close to 1.

4.2.2.3. Bipyridine comparison;

The second partially reversible reduction appears to be bipyridyl based rather than delocalised over the whole complex, as can be seen by comparing the voltammetry of $[\text{Mo}(\text{CO})_4\text{bpy}]$ and uncomplexed bipyridine. The reduction potentials become less negative when moving from the free ligand to the complex but the appearance of the CVs with the two clear 1-electron steps, the first of which is reversible and second less so, is strikingly similar as seen in figure 4.12.

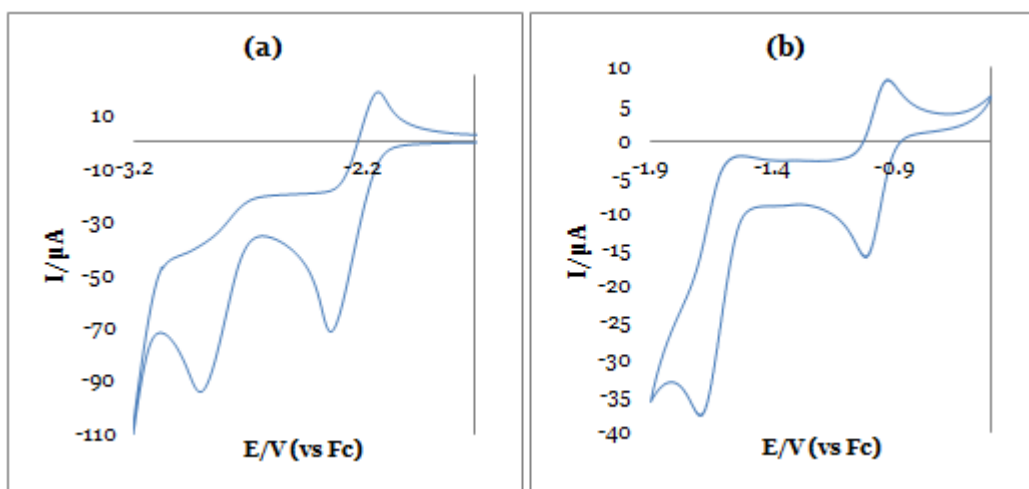


Figure 4.12; (a) Bipyridine (0.5 mM) in cell 2 at 200 mV s⁻¹ **(b)** $[\text{Mo}(\text{CO})_4\text{bpy}]$ (0.5 mM) in cell 1 at 200 mV s⁻¹

The bipyridine is harder to reduce when it is uncomplexed as it does not have the extra stabilising effects of the metal and other ligands. The strong similarity between the voltammetry of $[\text{Mo}(\text{CO})_4\text{bpy}]$ (b) and bipyridine (a) also offers

further confirmation of the evidence for the bipyridyl localised LUMO provided by the DFT.

The quasi-reversibility of the second reduction of bipyridine is obviously not due to carbonyl loss and is attributed in the literature to the protonation of the dianionic species and is reversible as the original bipyridine is regenerated upon application of a more positive potential.^[164]

A similar protonation of the bipyridyl ligand of the complex may be occurring at the second reduction of $\text{Mo(CO)}_4\text{bpy}$ and explain its lack of reversibility.

4.2.2.4. Alternate explanation;

An alternative explanation could be that this oxidative peak emerging at -1.6 V after application of potentials more negative than -2.9 V is, in fact, not tricarbonyl related. The tricarbonyl species may not be detectable via voltammetry, perhaps due to the insignificance of the carbonyl groups' effect upon the reductive processes, the reoxidation of the tricarbonyl species could be found at the same potential as the tetracarbonyl or the CO group lost could recombine with the complex (perhaps if weakly adsorbed on the electrode surface). Supporting this idea the experiment in which $\text{Mo(CO)}_4\text{bpy}$ solution was saturated with carbon monoxide did not lead to loss of (or any particularly pronounced effect on) the oxidative process at -1.6 V, which would be anticipated if tricarbonyl oxidation and the tricarbonyl reforming the tetracarbonyl species were to occur.

Also if the plot showing the current ratios for the first reduction and re-oxidation process as a function of vertex potential (figure 4.11) is examined closely, it does in fact suggest that the second process seen, before the re-oxidative peak emerges, does lead to a slight lessening in reversibility compared to both before the second reduction is reached and also the potentials after the third reduction and re-oxidation are undergone.

This could perhaps make sense if the loss and re-complexation of a carbonyl group were happening it may be expected to be inefficient and some CO lost to solution so some of the $[\text{Mo}(\text{CO})_4\text{bpy}]^{\cdot-}$ would not be reformed to be re-oxidised.

The extra oxidation could in fact be due to a deprotonation. If the bipyridyl of $\text{Mo}(\text{CO})_4\text{bpy}$ acted in a similar way to the uncomplexed bipyridine dianion at negative enough applied potentials it could abstract a proton from the electrolyte or solvent molecules (3rd reduction) and the extra oxidation (-1.6 V) could be attributed to the loss of this proton to give the $[\text{Mo}(\text{CO})_4\text{bpy}]^{\cdot-}$ species ready to be re-oxidised to $\text{Mo}(\text{CO})_4\text{bpy}$.

If this were the case it could explain why the reversibility is increased as protonation and deprotonation would not affect the molecule much and could be expected to be fully reversible.

However if there was the tricarbonyl formation first (as in this scenario CO loss would be expected to happen at a less negative potential than the protonation), the same slightly lessened degree of reversibility would be expected, so somehow both seemingly do not occur or the protonation assists the re-complexation of the carbonyl group.

4.2.3. Effect of oxygen;

A debilitating feature seen particularly with enzyme catalysed CO_2 reduction is sensitivity to oxygen and very specific working conditions, which this complex does not appear to exhibit with the 1st redox process remaining stable enough to be reversible over all the experimental time scales trialled. The presence of oxygen in the system can however make the voltammetry more difficult to interpret as oxygen undergoes several reductions and a reoxidation in aprotic solvent and has also been reported to interact with CO_2 when in its reduced superoxide state^[165] so although the work was not carried out in an inert atmosphere the solutions used were degassed with argon prior to experimentation (not always to fully satisfactory effect).

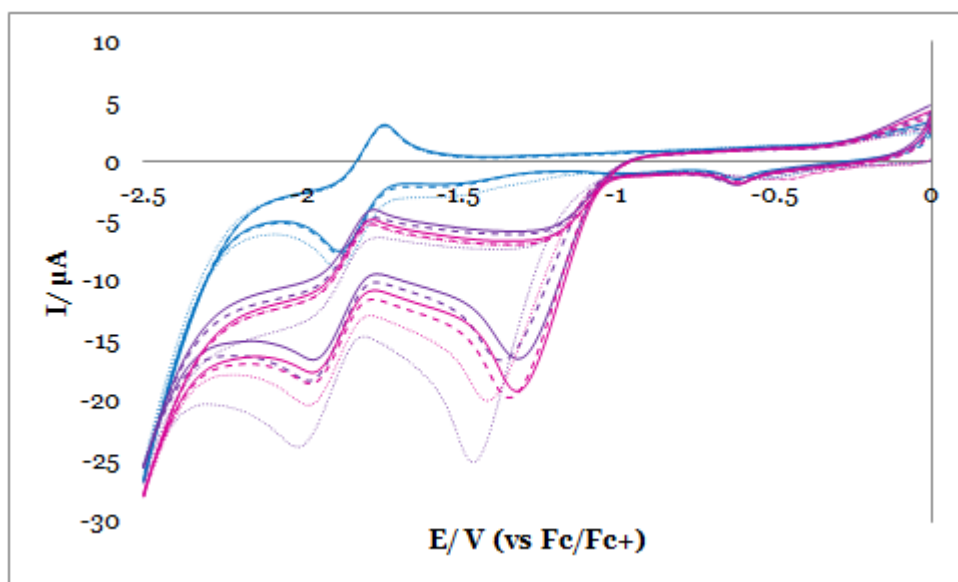


Figure 4.13; $\text{Mo}(\text{CO})_4\text{bpy}$ (0.5 mM) in cell 2 at 200 mV s^{-1} . Blue lines show the system under usual conditions, purple show consecutive scans upon bubbling of air through the system.

As can be seen in figure 4.13, upon addition of air to the $\text{Mo(CO)}_4\text{bpy}$ system the voltammetry shows clear evidence of oxygen reduction exhibiting a peak just after -1 V. The CV at applied potentials more negative than this region is 'sunk' when compared to the CV seen in the usual, relatively air free system (blue), due to the higher reductive current background. Over the six consecutive scans run the $\text{Mo(CO)}_4\text{bpy}$ redox features not only remain present, but also retain reversibility highlighting their stability in the presence of oxygen.

4.3. Mo(CO)₄bpy in the presence of CO₂;

4.3.1. Voltammetry of Mo(CO)₄bpy in the presence of CO₂;

With an understanding of the processes undergone by the complex in the absence of carbon dioxide the same experiments were repeated in CO₂ saturated [Mo(CO)₄bpy] solution. An important additional measurement also made is the response of CO₂ saturated electrolyte solution in the absence of [Mo(CO)₄bpy] for comparison. The direct reduction of CO₂ at metal electrodes is far from well defined and the use of varied solvent, supporting electrolyte, electrode materials, electrode preparation as well as other factors can have a pronounced effect on the reduction potential and current response, so in order to reach a useful assessment of the catalytic behaviour of any additional elements added to the system it should be compared with the CO₂ response in the same system without the Mo(CO)₄bpy complex. (This is a concept not universally accepted or even regularly undertaken but integral to the fair evaluation).

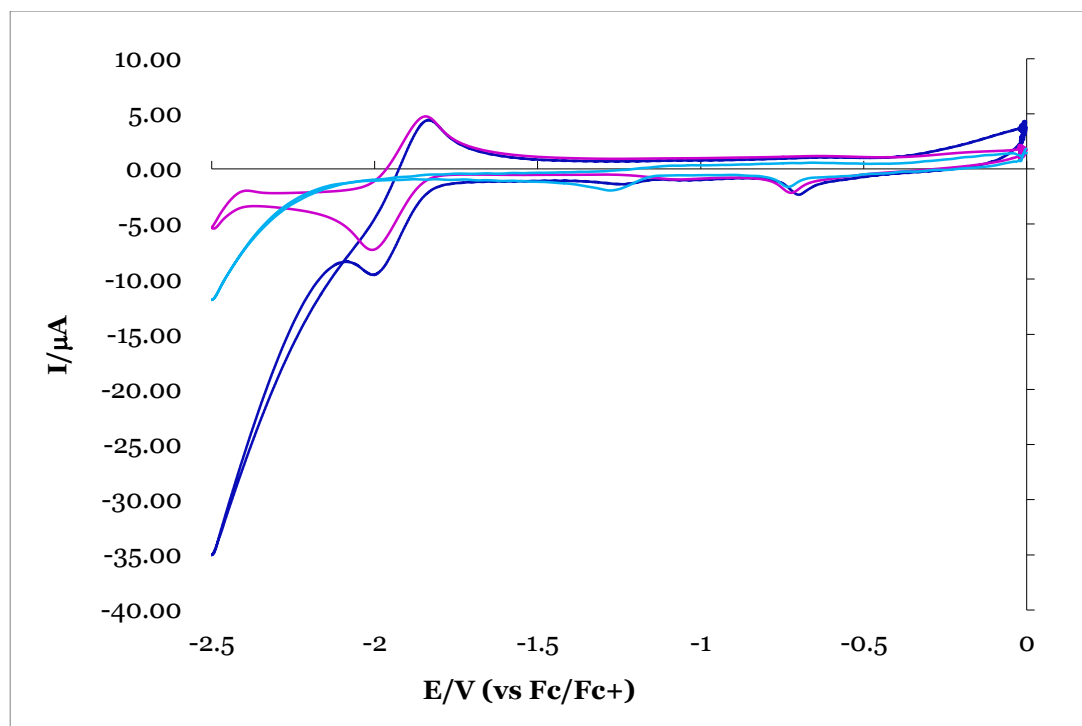


Figure 4.14; Direct CO₂ reduction (turquoise) and reduction in the presence of Mo(CO)₄bpy (0.5 mM) both with (blue) and without (pink) CO₂. Measurements made in cell 2 at 200 mV s⁻¹.

The reversible first reduction and reoxidation of [Mo(CO)₄bpy] in the absence of CO₂ can once again be seen in figure 4.14 depicted in pink, where the beginning of the second reduction is just discernible before the -2.5 V vertex. Upon addition of CO₂ to the system a different response is observed (dark blue line of figure 4.14). At the formation potential of the monoanion, shortly before -2.0 V, there is a clear current enhancement due to the reduction of CO₂. When compared with the direct CO₂ reduction in this system (turquoise line) the CO₂ reductive current starts at a less negative overpotential with much larger currents measured in the potential range -2.0 V to -2.5 V.

The current enhancement described above can be seen clearly in figure 4.15, which shows the current response attributed solely to carbon dioxide reduction, by plotting direct CO₂ reduction as seen above and the CO₂ response for the CO₂ and [Mo(CO)₄bpy] system. The latter is found by plotting the CV found for the

catalysed system in the presence of CO₂ with the current response seen for the complex in an argon environment subtracted.

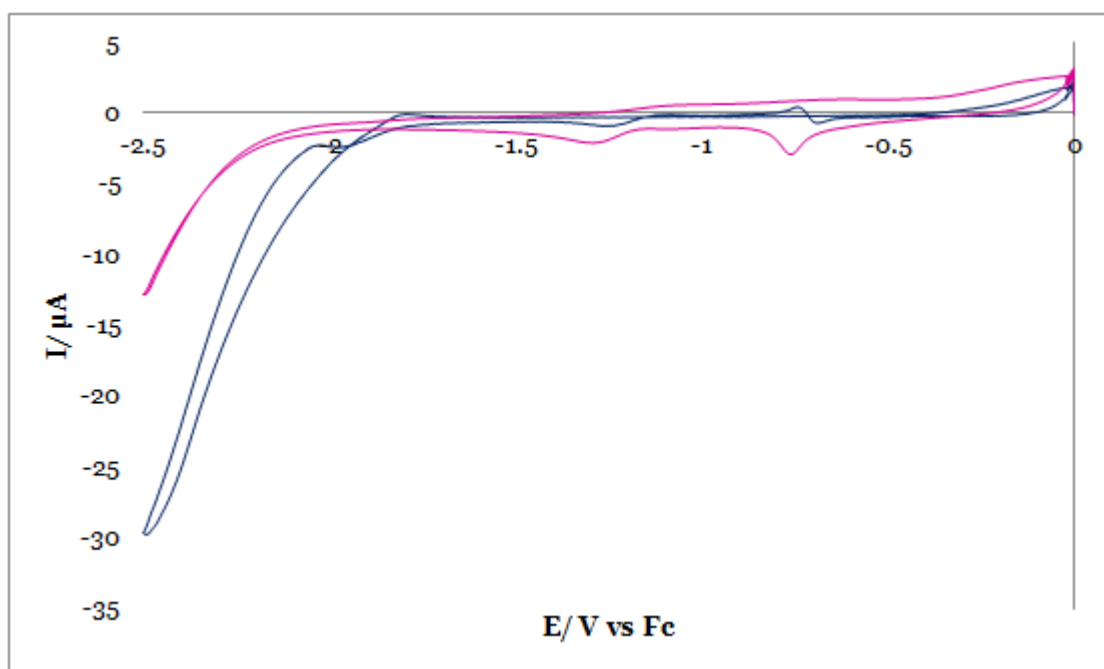


Figure 4.15; Direct CO₂ response (pink) compared against CO₂ catalysed response (blue): Mo(CO)₄bpy corrected for response in presence of Ar signal

With the [Mo(CO)₄bpy] response separated the extra current can be seen more clearly with the CO₂ reduction overpotential lowered by ca. 300 mV compared to the direct reduction system (onset of reduction at – 1.8 V rather than – 2.1 V) and almost three times as much current observed at – 2.5V. The current observations are more qualitative as, despite having had the solutions saturated with CO₂ for the same length of time, these experiments were not completely airtight and the measurements made in THF suffered from solvent evaporation and oxygen contamination so although the trend is representative, the exact CO₂ concentrations for both experiments may not have been equal.

4.3.2. Chronoamperometry of $\text{Mo}(\text{CO})_4\text{bpy}$ in the presence of CO_2 ;

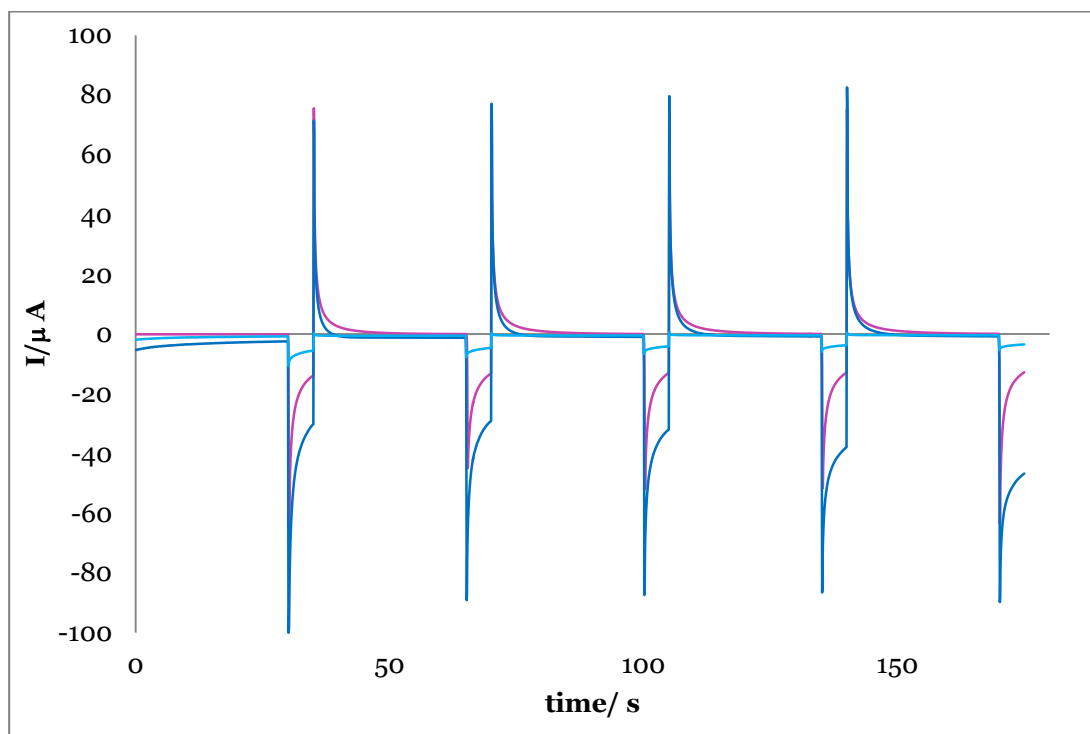


Figure 4.16; Chronoamperogram: Direct CO_2 reduction (turquoise) and reduction in the presence of $\text{Mo}(\text{CO})_4\text{bpy}$ (0.5 mM) both with (blue) and without (pink) CO_2 . Measurements made in cell 1. Potential stepped between -1.0 V, where no reaction observed for 30 s, and -2.1 V for 5 s.

In the chronoamperometry shown in figure 4.16, the potential was stepped between the first reduction potential but then back, past the point at which the re-oxidation occurs, to -1.0 V. At -1.0 V there was no current response associated through the study of the voltammetry of all of the systems investigated so was chosen to be a 'blank' or background step. Also, unlike the double step voltammetry seen earlier (figure 4.4), the step potentials were not applied for equal amounts of time instead spending 30 s at the 'blank' potential, then 5 s at the reductive potential of -2.1 V.

When the potential applied corresponds to the first reduction potential (-2.1 V) of $[\text{Mo}(\text{CO})_4\text{bpy}]$ for the uncatalysed CO_2 reduction, very little current is observed. For the molybdenum complex in the absence of CO_2 a moderate current is observed after the double layer charging (ca. $-20 \mu\text{A}$, $t = 1$ s after E step) which is in keeping with the reduction of $\text{Mo}(\text{CO})_4\text{bpy}$ to give $[\text{Mo}(\text{CO})_4\text{bpy}]^{\bullet-}$ as seen earlier. There is a significant backpeak observable for the $\text{Mo}(\text{CO})_4\text{bpy}$ in the absence of CO_2 as before, associated with the re-oxidation of the radical anion formed. This re-oxidative current is higher with the complex in the absence of CO_2 than in the CO_2 saturated system. This is consistent with the electron transfer between the $[\text{Mo}(\text{CO})_4\text{bpy}]^{\bullet-}$ and CO_2 molecules, which means there is less of the radical anionic species present to transfer the electron back to the electrode upon switching of the polarity. The fact that some re-oxidation is observed perhaps suggests that the electron transfer between the radical anion and CO_2 is slow compared to $[\text{Mo}(\text{CO})_4\text{bpy}]^{\bullet-}$ formation.

From figure 4.16, it is clear that when the reductive potential is applied, significantly more current is seen with the complex and CO_2 present than with the complex in Ar saturated solution or CO_2 in the absence of the complex. Even if the reductive responses of the two are added together, there is still more reduction seen in the experiment where they are both present in solution. This is evidence of the catalytic effect of $\text{Mo}(\text{CO})_4\text{bpy}$ upon CO_2 reduction.

4.3.3. Cross-overs;

The cross-overs seen in the voltammetry, an example of which can be seen at -2.2 V in figure 4.14 and here in figure 4.17, are unusual but can be explained. At potentials lower than -2.0 V a catalytic radical species is formed on the forward scan, which once present results in enhancement of the CO₂ reduction therefore more CO₂ reduction is seen at the same potential on the backward scan.

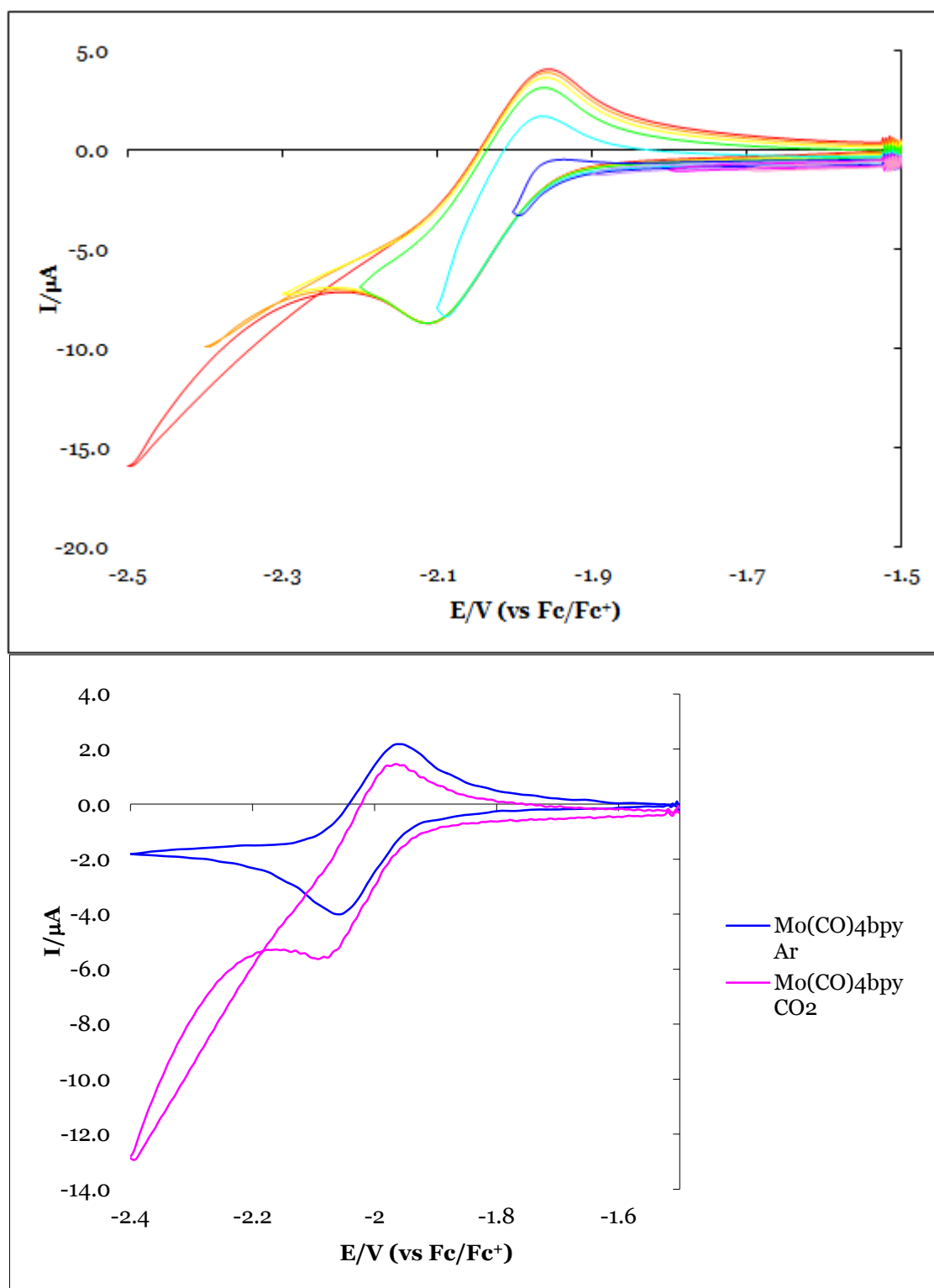


Figure 4.17; (above) $\text{Mo(CO)}_4\text{bpy}$ (0.5 mM) scanning to various vertex potentials (E_s) **(below)** $\text{Mo(CO)}_4\text{bpy}$ (0.5 mM) with (blue) and without (pink) CO_2 . Measurements made in cell 2 at 200 mV s^{-1}

Figure 4.17 (above) shows the voltammetry of $\text{Mo(CO)}_4\text{bpy}$ in CO_2 saturated solution with increasingly negative vertex potential. From this set of data the

cross over mentioned earlier can be seen to occur once the potential is scanned more negative than -2.3 V. The potential at which this cross over occurs is not invariable and has been observed to be dependent on experimental conditions. Figure 4.17 shows a clear cross over in the CO₂ saturated Mo(CO)₄bpy solution which is absent in same experiment with argon saturated solution. For the argon saturated Mo(CO)₄bpy solution the cross over is not observed until very negative potentials (in the region of -5 V vs. Fc, although dependent upon water content and solvent purity), where any crossovers are likely to be due to the decomposition of the electrolyte and solvent and unrelated to Mo(CO)₄bpy or any catalytic effects. In the Mo(CO)₄bpy solution in the presence of CO₂ the potential at which the crossover is first observed is dependent upon CO₂ concentration.

4.3.3.1. Effect of CO₂ concentration upon crossovers;

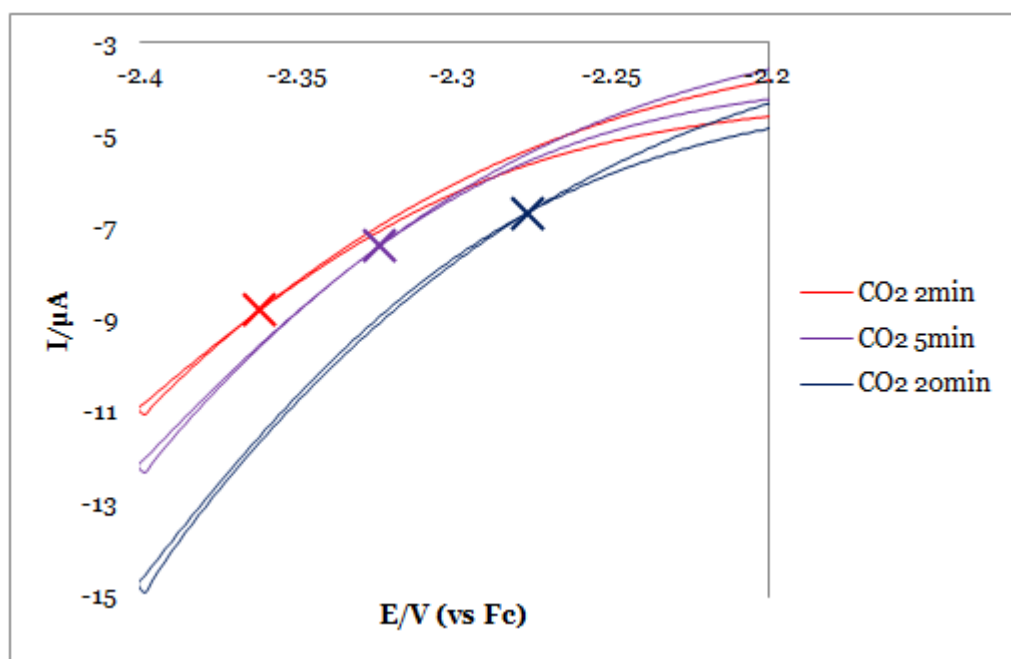


Figure 4.18; Cyclic Voltammogram of Mo(CO)₄bpy (0.5 mM) in CO₂ saturated cell 2. Scan rate: 200 mVs⁻¹. Cross over potential indicated by x

Figure 4.18 shows the section of the CV where the crossover is seen to occur for the same $\text{Mo}(\text{CO})_4\text{bpy}$ solution with different CO_2 partial pressures. The proportion of CO_2 present was controlled by altering the lengths of time that CO_2 was bubbled through the solution. Crude as the technique may be, from these qualitative results the point is illustrated; increasing CO_2 concentration lessens the negative potential at which the crossover occurs.

The fact that the CO_2 concentration has a positive effect on this crossover potential is not surprising as the availability of more CO_2 for reduction would be expected to result in the production of higher CO_2 reductive currents. The crossover position shifting more positive is indicative of the increased current difference between the forward (negative) and back (positive) scan and the variation with concentration confirming that whatever the nature of the catalytic species formed, it is interacting with CO_2 .

The identity of the active catalytic material formed by the reduction is not known as although it would be tempting to assume that it is wholly due to the $[\text{Mo}(\text{CO})_4\text{bpy}]^\bullet-$ a similar crossover feature can be observed in some of the direct CO_2 reduction CVs measured on a gold working electrode at high CO_2 concentrations.

4.3.4. Effect of the addition of H_2O to the system;

Another factor found to influence the formation of crossover regions within the voltammetry was the presence or absence of water in the system. The solvents used for the electrochemical measurements were of high purity and glassware

dried in the oven before use however due to the open nature of the cell and experimental technique trace amounts of water were consistently present in the system. Molecular sieves, although excellent at drying the solvents in question were found to be unsuitable due to the appreciable amount of impurities their presence introduced. Although distillation could be employed to lower the water content for the organic solvents, the expected results would be similar to the water content of the freshly pipetted liquid. NMP has a very high boiling point (204.3 °C at atmospheric pressure) so distillation would be particularly energy intensive.

The addition of extra water to the $\text{Mo}(\text{CO})_4\text{bpy}$ -NMP system was investigated. There have been reports published of the addition of water lowering the overpotential associated with catalysed CO_2 reduction by over a volt.^[89] and some research suggests CO_2 electroreduction in the absence of water, or other proton source, is simply not energetically viable.^{[11][16]}

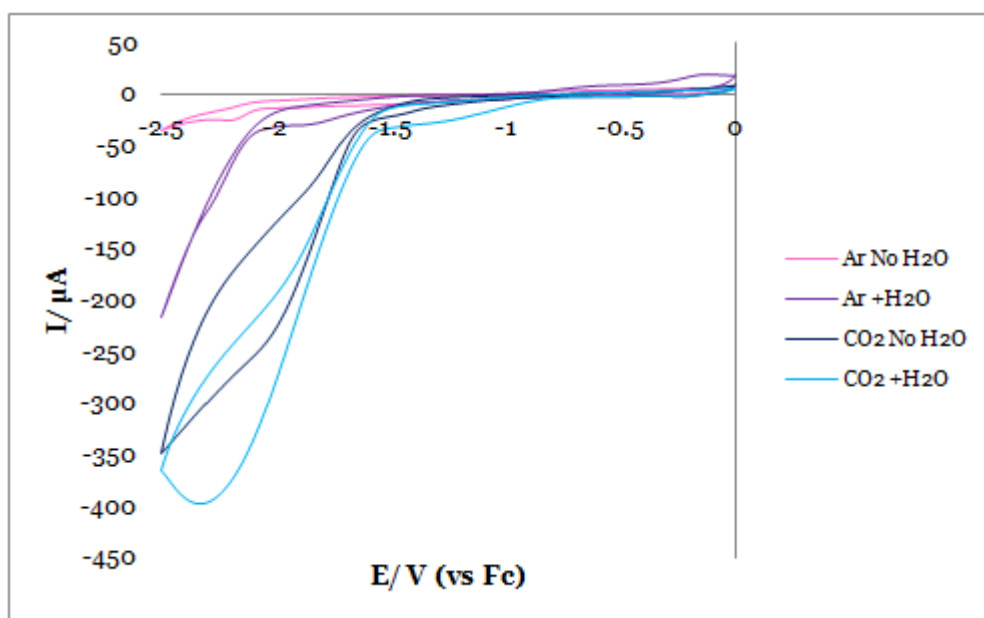


Figure 4.19. $\text{Mo}(\text{CO})_4\text{bpy}$ CV with and without H_2O in the presence and absence of CO_2 measured in cell 1 at 200 mV s^{-1}

Figure 4.19 shows the effect of the addition of 10% H₂O (by volume) to Mo(CO)₄bpy solution in the presence of CO₂ (blue). The CO₂ free system (pink) is also shown. Both the Mo(CO)₄bpy systems show extra current in the presence of H₂O. This is as expected as H₂O tends to be reduced in the same potential range as CO₂ to form hydrogen. This hydrogen evolution reaction (HER) is often found to be a competing reaction with CO₂ reduction in aqueous electrolyte solution and can have limiting effects on the faradaic efficiency possible for such systems.^[8]

The potential shift observed in this system for CO₂ reduction upon addition of water is much less significant than that seen in some other catalytic systems with the bulk reductive current shifted by just ~100 mV.

When the CVs obtained in the absence of CO₂ with and without water added are compared, the presence of extra water leads to a new broad reductive peak between -1.5 V and -1.9 V, a much greater oxidative current on the scan between -1 V and 0 V then most notably a shortening of the potential window with the reduction starting prior to the complex's 2nd reduction. This di-reduction peak can be seen in the tail (pink line in figure 4.19) at ~ -2.3 V.

When the potential range was extended to more negative potentials there was clearly observable solvent destruction seen with bubble formation after ~ -2.6 V for both the systems where water was added, with no such breakdown observed in the absence of water.

The CO₂ saturated system in the presence of additional water shows more current for the region -0.7 V to ~ -1.4 V with the bulk of the reduction occurring

almost 100 mV earlier than in the solution without at -1.56 V (ca. -1.64 V) and higher current densities observed.

The data was analysed so the response theoretically due to the presence of H₂O and CO₂ respectively and is presented in figure 4.20.

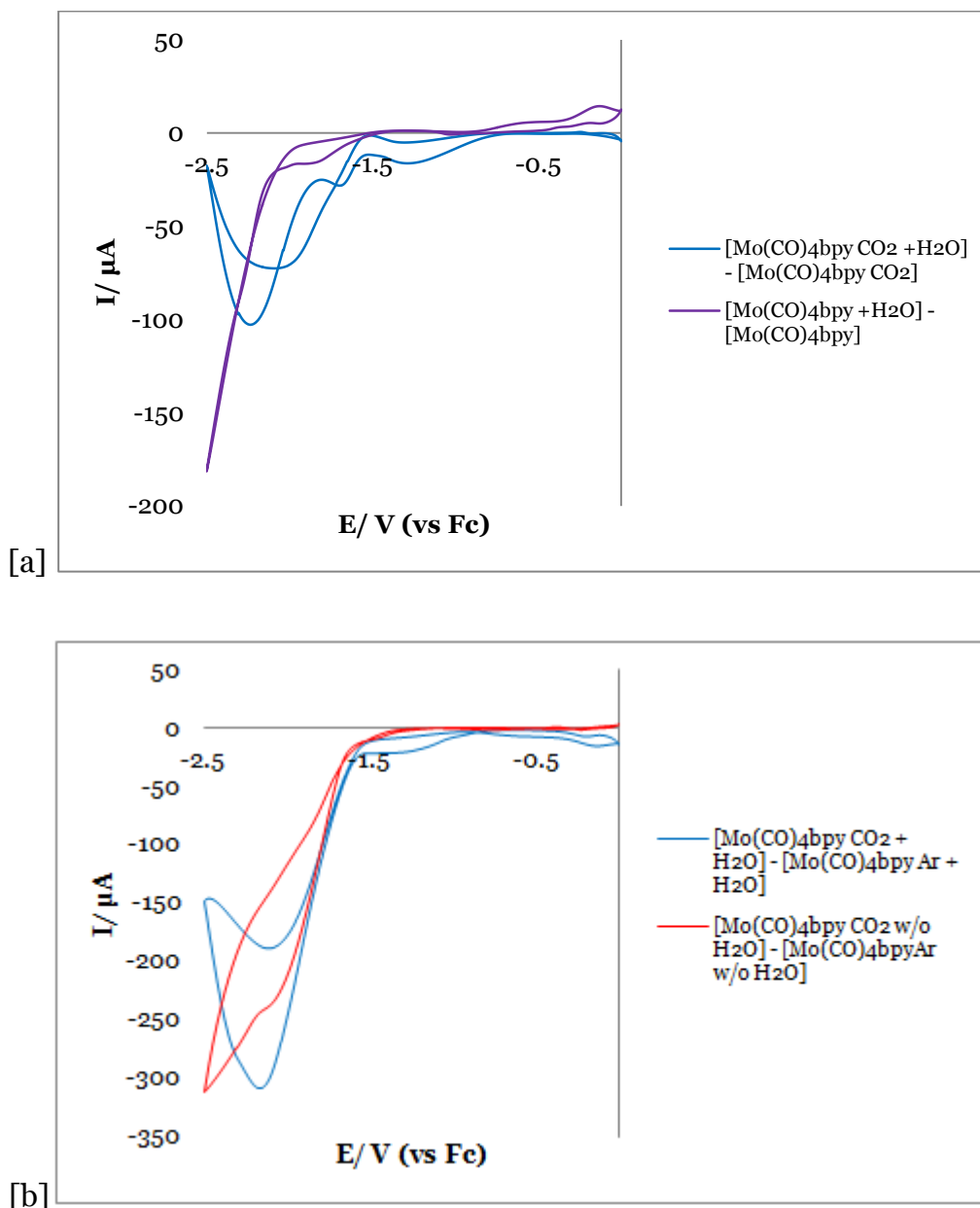


Figure 4.20; Subtracted data to give the response due to (a) water and (b) CO₂ in all systems (conditions as in figure 4.19)

From the plot showing the response due to water in the Argon saturated solution, the extra current just after the 1st reduction of Mo(CO)₄bpy then the shortening of the potential window are more clearly observable. The current seen after the formation of the radical anion may be due to the reaction of this with water but is not wholly clear as the reoxidation although not observable may be masked by the water related oxidative processes. The H₂O related response in the presence of CO₂ is much more interesting! There is observable extra current due to H₂O reduction in 3 different regions on the forward scan (in the negative direction), one prior to Mo(CO)₄bpy reduction, one just after [Mo(CO)₄bpy]^{•-} formation then a large enhancement at the approximate potential where the dianion is formed. As seen in figure 4.19 the current at -2.5 V is approximately the same for the carbon dioxide saturated solutions with and without water, however the backscan of the H₂O response again shows a peak of extra negative current due to H₂O when CO₂ is present. This is one broad peak as opposed to corresponding to the complex reduction potentials as seen on the forward but still clearly extra current.

When the response of CO₂ is analysed in the presence and absence of water the currents are fairly similar to each other with the effect of the complex less pronounced in the voltammetry. The shape of the subtracted data voltammograms do differ quite substantially but a large portion of that is due to the shift in the potential window in the Ar H₂O data, so is not necessarily a meaningful contribution to the CO₂ reduction response. It does suggest that the presence of CO₂ stops this solvent breakdown at such a positive potential, possibly as it reacts preferentially although the presence of solvated CO₂ could affect the solvent intermolecular bonding too. The solvent break down with H₂O

present, presumably the H₂O reduction, is still observed earlier than in its absence but outside the range presented above with CO₂ saturation.

Figure 4.21 shows the unaccounted-for current found by subtracting the response for [Mo(CO)₄bpy with H₂O – Mo(CO)₄bpy] and [Mo(CO)₄bpy with CO₂] from [Mo(CO)₄bpy with H₂O and CO₂].

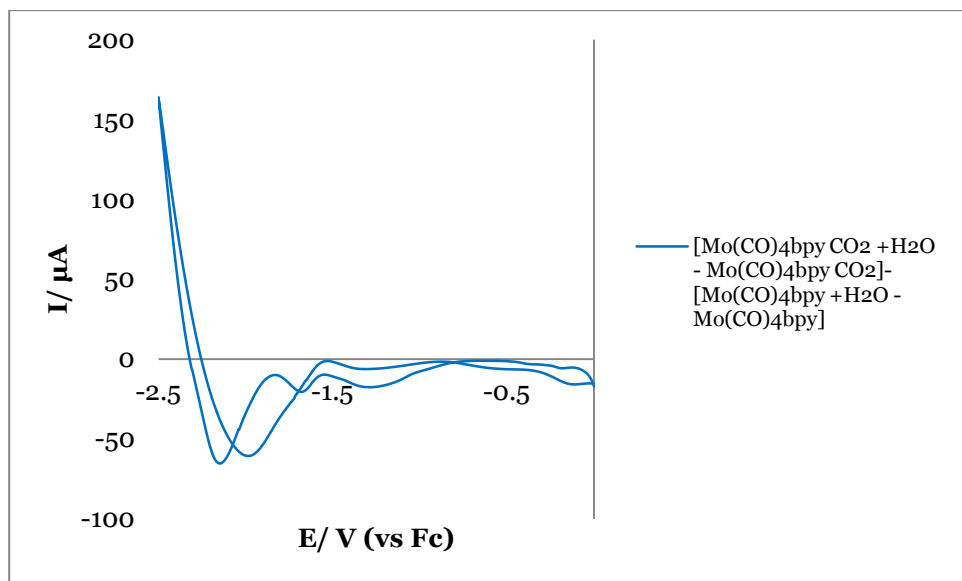


Figure 4.21; Subtracted data to give the response highlighting the extra current response not directly attributable

The addition of water to the catalysed CO₂ reduction can be seen to increase the current by about 20% with 4 regions of extra current enhancement, 3 of which coincide with the reduction potentials of the complex. This could be due to the reduced CO₂ reacting with the water molecules to form a potentially wide array of products, rather than with other CO₂ or CO₂^{•-} molecules in the vicinity to give the non-protonated products expected in the absence of water.

The inclusion of water although shown to have an effect on the potentials and currents of CO₂ reduction, the impact is limited and makes the mechanism through which the system operates much more complicated by introducing

many more variables to what is already an intricate system with an array of experimental features on which the response is dependant. With this in mind it was decided that the investigation would focus on the $\text{Mo(CO)}_4\text{bpy}$ system without deliberately added water.

4.4. Analysis of $\text{Mo(CO)}_4\text{bpy}$ Voltammetry;

4.4.1. Diffusion coefficient via voltammetry;

The voltammetric measurements have provided a wealth of information as to the electronic structure and stability of the mono and di-reduced molybdenum complex and using these simple measurements it is possible to investigate further the behaviour of the complex in solution.

One parameter required for the study of the kinetics and mechanism through which the complex interacts with CO_2 is the diffusion coefficient, D , which it is possible to evaluate from the voltammetric peak current responses when a selection of different scan rates are implemented.

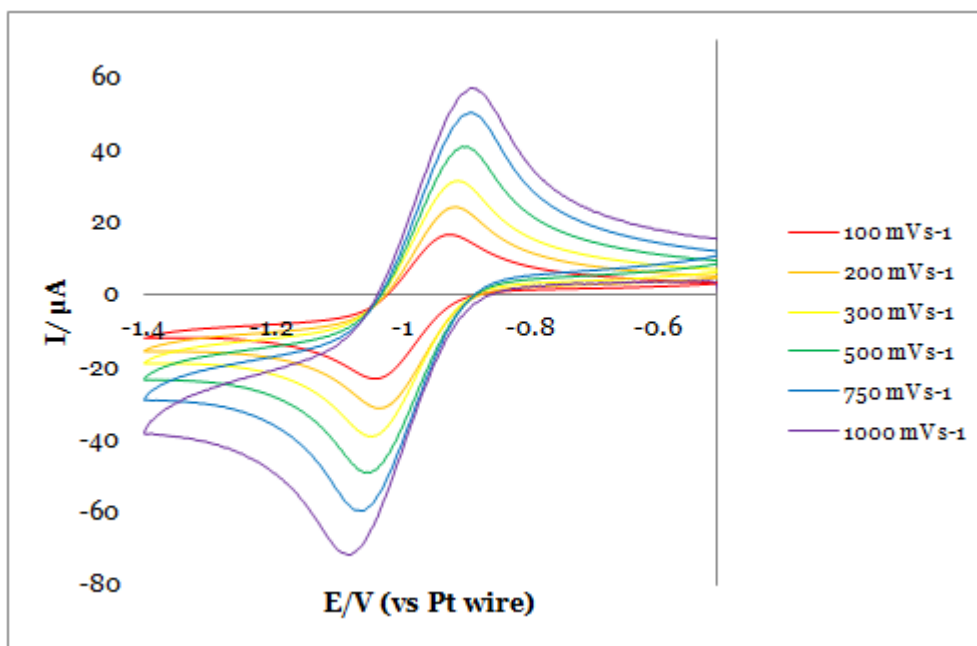


Figure 4.22; Mo(CO)₄bpy at various scan rates measured in cell 1

From figure 4.22 the voltammetric response of the first reduction of Mo(CO)₄bpy in the absence of CO₂ can be seen to remain reversible and shows an increase in peak current with scan rate as anticipated from the thinner diffusion layer associated with higher scan rates.^[142]

A plot of the peak current vs. the square root of scan rate as seen below in Figure 4.23 allows a diffusion coefficient to be calculated using the Randles-Sevcik equation, (equation 2.6 or equivalently equation 2.7).

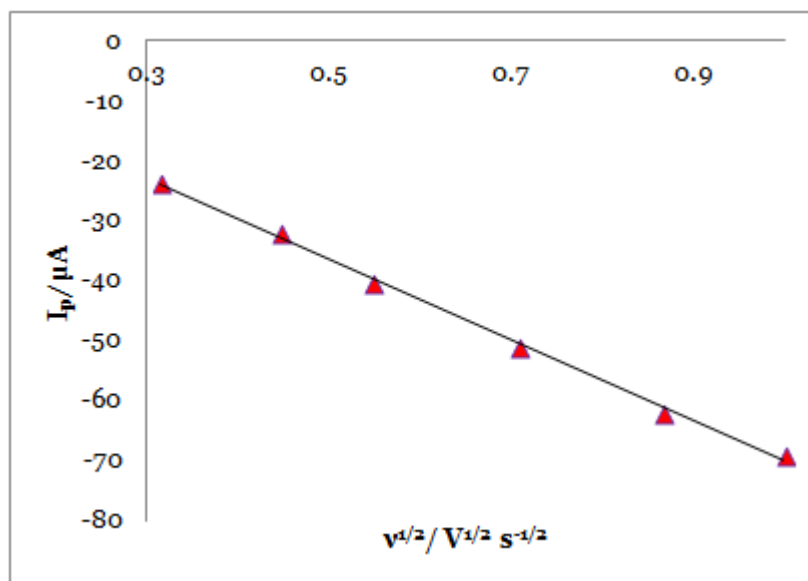


Figure 4.23; Plot of Peak current vs. square root of the scan rate for the $\text{Mo}(\text{CO})_4\text{bpy}$ voltammetry given in figure 4.22. Line of best fit (least squares) is shown.

For the experiments where data was collected in THF there is a fairly wide dispersion of results with the D value found to range from $6.8 \times 10^{-6} \text{ cm}^2 \text{ s}^{-1}$ to $1.4 \times 10^{-5} \text{ cm}^2 \text{ s}^{-1}$. This variation is due largely to the nature of the solvent. THF is volatile so significant quantities of solvent can be lost as vapour if the cell is open, particularly in the gas bubbling process but also noticeably through lengthy experiments, which leads to the concentration of solution (needed for the calculation) being altered from that of the starting system.

Another problem associated with the quantitative analysis of the reductive CVs measured in THF is oxygen contamination as the introduction of oxygen into the solution can lead to an overestimation of the reductive peak current associated with the $\text{Mo}(\text{CO})_4\text{bpy}$.

The D values obtained from the experiments run in NMP showed much less variation with a D equal to $2.6 (\pm 0.3) \times 10^{-6} \text{ cm}^2 \text{ s}^{-1}$ being consistently obtained.

NMP is less volatile and throughout the experiments undertaken was found to be less prone to oxygen contamination when compared to THF.

The values of diffusion co-efficient obtained for the two systems differ due to the difference in the viscosities of the solvents, which can be related to D by the Stokes-Einstein equation (2.3), and Wilke-Chang relationship (2.4).

Both the radius and molar volume were calculated from the DFT calculations data and also using published crystallographic data^[109] and were found to be in agreement. The method for this estimation was checked using data for ferrocene, where the radius and molar volume are known.

	$D_{\text{THF}} / \text{cm}^2 \text{ s}^{-1}$	$D_{\text{NMP}} / \text{cm}^2 \text{ s}^{-1}$
Stokes-Einstein	9.84×10^{-6}	2.78×10^{-6}
Wilke-Chang	1.05×10^{-5}	2.68×10^{-6}
Cyclic Voltammetry	9.9×10^{-6}	2.6×10^{-6}

Table 4.1; Diffusion co-efficients for $\text{Mo}(\text{CO})_4\text{bpy}$ in THF and NMP for calculated and average experimental results from cyclic voltammetry.

As seen above in table 4.1 the diffusion co-efficients calculated using both equations (2.3) and (2.4) are close to those found using the experimental data. The Wilke-Chang relationship is considered to offer the better estimate and has been analysed to give a degree of accuracy within 10%^[139] so the experimental values for both solvents fall within the given range. This was further confirmed by DOSY-NMR experiments run in d^8 -THF (the DOSY spectrum and analysis for which can be found in chapter 7, figure 7.2), yielding $D = 1.06 \times 10^{-5} \text{ cm}^2 \text{ s}^{-1}$ which is in keeping with the other measured and predicted D values.

4.4.2. Calculation of heterogeneous electron transfer rate constant k^o ;

The rate constant for the heterogeneous electron transfer between the electrode and the $\text{Mo(CO)}_4\text{bpy}$ complex can be determined using the dimensionless rate parameter Ψ defined by equation 2.10.^[141]

The incorporation of the extra electron into $\text{Mo(CO)}_4\text{bpy}$ to form $[\text{Mo(CO)}_4\text{bpy}]^{\bullet-}$ does not change the structure of the species significantly and no chemical reaction is undergone in the absence of CO_2 therefore the D_k value is not expected to change compared to that of D_0 meaning $\left(D_0/D_k\right)$ can be approximated as 1. This means that the transfer co-efficient term, α , describing the reversibility of the voltammetry does not need to be considered and the simplified equation 2.11 can be employed.

Using ideal data for the peak separation of a one electron, one step reversible redox process for corresponding Ψ values given by Bard^[141] a plot of ΔE vs $v^{1/2}$ was constructed, denoted as “ ΔE ideal” in figure 2.24.

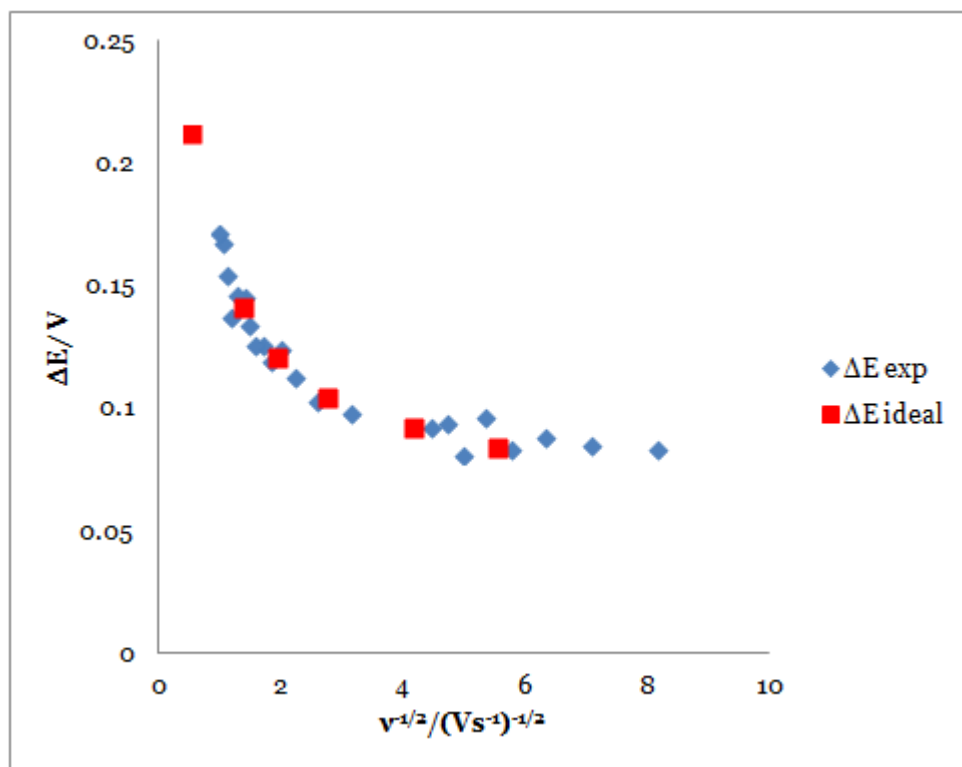


Figure 4.24; Plot of ideal and experimental ΔE vs. $v^{1/2}$ data for $Mo(CO)_4bpy$ first redox process in THF system where $D_o = 9.9 \times 10^{-6} \text{ cm}^2 \text{ s}^{-1}$ and $k^o = 2.0 \times 10^{-3} \text{ cm s}^{-1}$. Experimental data from CV and ideal data from ref [141]

Using this technique the rate constants for the electron transfers observed in NMP were also analysed and the values gathered in table 4.2.

	Solvent	$k^o / \text{cm s}^{-1}$
$Mo(CO)_4bpy \rightarrow [Mo(CO)_4bpy]^{\bullet-}$	THF	2.0×10^{-3}
$Mo(CO)_4bpy \rightarrow [Mo(CO)_4bpy]^{\bullet-}$	NMP	9.5×10^{-4}

Table 4.2. Heterogeneous electron transfer rate constants.

Using the voltammetric data presented in figures 4.6 and 4.7 and assumed E_rC_i mechanism, the heterogeneous rate constant associated with the second reduction of $Mo(CO)_4bpy$ in NMP was also investigated. The peak separations were found to be too great for the available model, presumed due to the resistive effects and possible interaction with the electrode surface. Instead the ratio of

peak currents for the anodic and cathodic scans were compared with the available ideal data^[141] yielding an average rate constant of 2.2 s^{-1} . The data showed a high degree of variation with k^o ranging between 0.4 s^{-1} and 10.1 s^{-1} over the scan rates investigated, particularly at the fastest ($>1500 \text{ mV s}^{-1}$) and slowest ($<200 \text{ mV s}^{-1}$), perhaps indicative of the mechanism employed in the model failing to be entirely representative of the process undergone.

4.4.3. Calculation of the homogeneous electron transfer rate constant k' ;

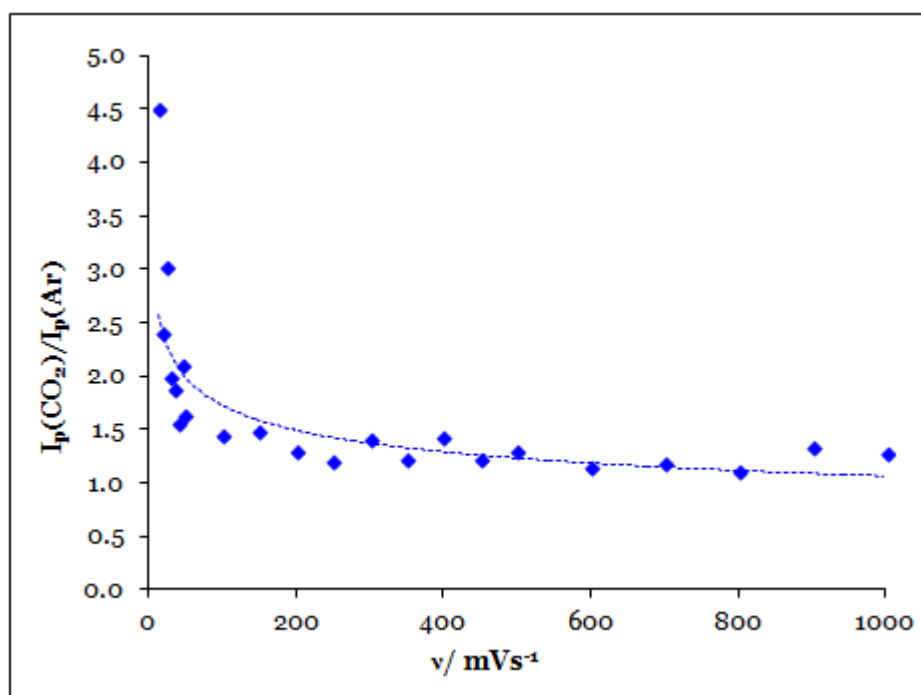
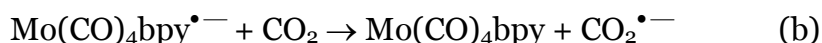


Figure 4.25; Current ratio of the 1st reduction of $\text{Mo}(\text{CO})_4\text{bpy}$ with and without CO_2 as a function of scan rate measured in cell 1.

The above plot, figure 4.25, takes the peak currents of the first reduction of $\text{Mo}(\text{CO})_4\text{bpy}$ in the presence and absence of CO_2 as a ratio to give a measure of catalytic enhancement as a function of scan rate. The characteristic shape of the

data give an insight into the mechanism by which the catalysis proceeds and was found to be in keeping with an E_rC_i' mechanism, whereby a reversible electron transfer (a) is followed by an irreversible chemical reaction (b) following;



k' is the pseudo first order homogeneous electron transfer rate constant allowing quantification of the rate at which the electron is transferred between the active catalyst, $[\text{Mo(CO)}_4\text{bpy}]^{\bullet-}$ and CO_2 molecules where $k' = k[\text{CO}_2]$.

The mechanism by which the CO_2 reduction is catalysed by $\text{Mo(CO)}_4\text{bpy}$ was found to be (through investigation of the peak separation vs scan rate plot seen in the previous section) E_rC_i'. Once the reaction scheme is known it is possible to apply an existing treatment to the data in order to deduce k' .

This existing E_rC_i' treatment has been investigated using the voltammetric and amperometric data collected. The estimation of this value was ascertained using the working curves (reproduced in figures 2.4 and 2.8) provided in Bard and Faulkner's *Electrochemical Methods*.^[141]

4.4.3.1. Cyclic voltammetry derived k' ;

For the cyclic voltammetric data the ratio of the peak currents for the first reduction of $\text{Mo(CO)}_4\text{bpy}$ in the presence (i) and absence (i_d) of CO_2 for a variety of scan rates were used, along with the plot given in figure 2.4 to gather $\lambda^{1/2}$ values.

An array of different current ratios for the various scan rates were found experimentally which led to a selection of $\lambda^{1/2}$ values. It was found that there was variation through the values with, particularly some of the faster scan rates (where the current ratio tended to be lower), being near to the DP zone of the plot and the very slow scan rates (having much higher current ratios) falling in the KP zone.

The values of $\lambda^{1/2}$ obtained can then be used in equation 2.12 to calculate k' , where C_z^* is the concentration of CO_2 .

The bulk concentration of CO_2 in saturated THF at room temperature and pressure is given as being 0.205 M^[166] and saturated NMP under the same conditions is quoted as having a CO_2 concentration of 0.145 M.^[167] This is much higher than the concentration of catalyst employed of 0.5 to 1 mM, so assuming that the solutions were saturated (or at least approaching saturation) the concentration of CO_2 would be well over 100 times that of the catalyst, which would satisfy the assumption made that the CO_2 concentration remains unchanged with respect to catalyst allowing the mechanism to be considered pseudo first order.

Although the rate constant should be a single value the values of $\lambda^{1/2}$ led to k' ranging from $<1 \text{ s}^{-1}$ for the slow scan rates and $>50 \text{ s}^{-1}$ for the fastest scan rates sampled and tended to follow this trend of very high apparent k' values for the highest scan rates and low k' for the low ones for all of the various trials of different data gathered.

The average k' for each data set was found to be $\sim 10 \text{ s}^{-1}$.

The relationship above is predominantly made up of constants and the scan rate which is controlled by the potentiostat therefore unlikely to be a source of significant error suggesting that either the mechanism is more complex than thought or that there are assumptions made which do not hold true in this case.

There is an underlying assumption that the concentrations in the bulk solution are representative of those at the electrode surface which may not be the case. If there were, for example, specific adsorption interactions with the electrode the concentrations could be very different to those measurable in the bulk solution and the assumption of diffusion control of the process would not hold. The effect of specific surface interactions is discussed in section 5.3.

4.4.3.2. Chronoamperometric k' determination;

A very similar approach was taken with the chronoamperometric data (the plot of which is given in figure 4.16). The current ratio was determined for various times during the potential step and used to establish λ values via the plot presented in figure 2.8.

The potential step data showed a consistent trend toward larger λ values at higher values of t as is expected from the higher λ values in the voltammetry seen for the CVs measured at lower scan rates. Also this extra CO_2 catalysis current with time could be a result of the accumulation of active species as suggested in the earlier analysis.

The results from the chronoamperometric experiments showed much less of a spread of values however only 5 points were taken for each potential step length

value, at times avoiding the charging current contribution, so steady state for $\text{Mo}(\text{CO})_4\text{bpy}$ without CO_2 was reached with the CO_2 catalysis not settling into a maximum current until later.

The k' values were established using equation 2.16 and were found to range from 2.0 s^{-1} to 10.8 s^{-1} over all of the repeats of the experiment and the different t values, with the average found to be $\sim 5.0 \text{ s}^{-1}$.

The errors associated with these k' values, although lower than those linked to the values determined using the CV data, are still significant making it hard to draw any meaningful conclusions regarding the kinetics of this electron transfer.

4.5. Product detection;

The detection, identification and quantification of CO₂ reduction products in the systems of interest, particularly in the presence of Mo(CO)₄bpy, has been an important aspect of the research undertaken with various methods trialled.

This has proved to be one of the most challenging aspects of the project for two main reasons;

- 1) The separation of the constituents of the electrochemical system, even without CO₂ or reduction products to consider is difficult. The presence of electrolyte, catalyst and relatively viscous organic solvents means that traditional liquid separation techniques employing standard columns such as chromatography are not well suited as the high concentration of ions would be expected to deactivate their surface rapidly. Searching for the small organic CO₂ reduction products in solution amongst the high concentrations of solvent (containing C=O, C-C and C-H bonds), electrolyte (C-C and C-H bonds), the electrocatalyst (C=O, C-C and C-H bonds) and any unreacted CO₂ means that many spectroscopic techniques such as IR, Raman and UV-vis are less than ideal as the background solution is likely to possess large responses in the regions of interest, which may mask the smaller product related signals and make them harder to discern.
- 2) The low relative concentration of CO₂ reduction products generated in a standard electrochemical experiment, such as CV or chronoamperometry, over the usual experimental second to minute

timescales is not significant enough for detection by most techniques, particularly in such a challenging system. This necessitates the need for bulk electrolysis of the system with a large electrode applying potential over larger (>10 minutes) lengths of time. This process can lead to side reactions, not typically observed under the short time experiments, becoming much more significant, even dominant, as well as breakdown of the solvent and electrolyte which are stable over the usual electrochemical timescale at a standard working electrode.

Bulk electrolysis can also present experimental design challenges as the presence of small quantities of impurities can have over-emphasised effects on the system. As well as the need for a large working electrode, there are also additional requirements for the reference and counter electrodes. The reference electrode, in order to prevent drift in potential over the lengthy experiment, must be particularly well made and separated from the bulk solution. This is typically the case however in usual electrochemical experiments the bulk solution composition is not expected to alter significantly whereas bulk electrolysis is specifically aimed at altering the bulk of the analyte. This change in electrolyte and subsequently the reference electrode environment will mean that the reference electrode potential can also be subject to change. Typically the reference is encased within glass and filled with electrolyte separated from the bulk solution by a partially permeable frit. The degree to which the frit allows movement of solution must be very low in order for the reference electrode to remain reliable over the entirety of bulk electrolysis, without which the potential applied may vary through the duration.

The choice of potential to apply to the $\text{Mo(CO)}_4\text{bpy}$ system is also a major consideration as the complex has multiple reductions which, although clearly separated in the cyclic voltammetry undertaken, are still relatively close so the applied bulk electrolysis potential must be carefully selected to ensure only the reduction of interest is reached.

Another major difference between this and the usual electrochemical set up is the positioning of the counter electrode. The potential of the counter electrode is set so as to ensure the desired potential is observed at the working electrode but this can mean that extreme potentials are applied within the system, particularly when there is resistivity between the electrodes. Generally this is not considered a significant effect given the small quantities of oxidation or reduction occurring, however the counter electrode size must be scaled to match that of the working electrode for the bulk electrolysis, resulting in a very large electrode of unknown potential over a long period being included in the system. The products formed from reactions here must be segregated from those of the working electrode for meaningful interpretation of product analysis. The importance of positioning the working and counter electrodes correctly with respect to each other is also important to avoid ‘hotspots’ where the current flows through the path of lowest resistance and can result in only a small portion of the solution investigated actually being subject to the electrolysis. This can result in excess heating of the solvent system and even boiling which can again be a source of confusion and misrepresentation of the data gathered.

Given the array of challenges faced with solution phase product analysis and the observation of bubble formation during CO_2 electrocatalysis at the working electrode when held for prolonged periods at fixed potential, the investigation

into product formation was split into two; analysis of the headspace gas post bulk electrolysis and investigation of the solution and electrode surface.

4.5.1. Gaseous Product Detection;

The investigation of the gas phase bulk reduction products from the headspace of the sealed electrochemical cell employed two analytical techniques, gas chromatography (GC) and Fourier transform infrared spectroscopy (FTIR).

4.5.1.1. Gas Chromatography;

The GC measurements required the use of two specific columns, despite the absence of electrolyte in the sample, due to the detrimental effects of CO₂ on the standard molecular sieve column surface. Bulk electrolysis was carried out in CO₂ saturated Mo(CO)₄bpy (0.5 mM) THF/TBABF₄ (0.1 M) solution at a large gold mesh electrode (with a surface area of approximately 12.5 cm²). A CV was recorded prior to bulk electrolysis which, despite the increase in electrode size, remained characteristic of the CO₂ saturated system as shown in figure 4.26.

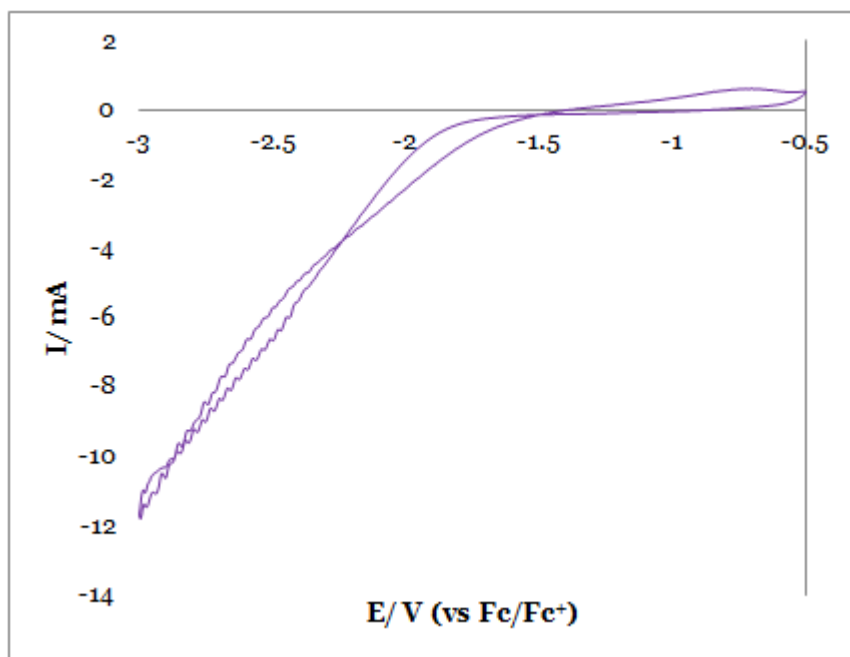


Figure 4.26; CV of $\text{Mo}(\text{CO})_4\text{bpy}$ (0.5 mM) in CO_2 saturated as cell 2 except measured at bulk gold mesh electrode (approximately 12.5 cm^2) in bulk electrolysis cell.

The potential for bulk electrolysis selected was just past the first reduction of the $\text{Mo}(\text{CO})_4\text{bpy}$ at -2.2 V vs the employed Fc/Fc^+ reference electrode with the chronoamperogram given below in figure 4.27.

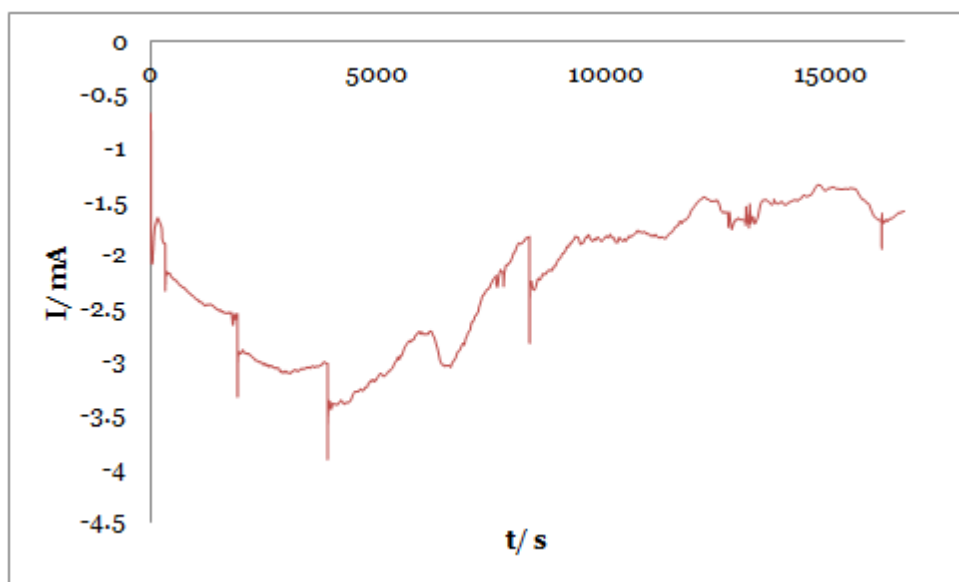


Figure 4.27; Bulk electrolysis current response when -2.2 V applied to the $\text{Mo}(\text{CO})_4\text{bpy}$ (0.5 mM) in CO_2 saturated cell 2 except measured at bulk gold mesh electrode (approximately 12.5 cm^2) in bulk electrolysis cell.

The potential was held for the bulk electrolysis for 4.6 hours (16572 s) passing a total charge, Q , of 36.75 C. The response seen was not smooth due to the changing working area as bubbles built up on and were released from the electrode surface. The large bubbles resulted in the big step-like like features observable at 320, 1920, 6210 and 8330 s with the associated spikes in current analogous to the initial double layer charging spike seen upon application of potential, as regions of the surface under the bubbles are re-exposed. The average current observed was between -1.5 and -3.5 mA and appeared to show a decrease in current with time. The drop in current with time is expected in bulk electrolysis of a fixed quantity of reactant. The use of a sealed cell rather than constantly bubbling CO_2 means that upon application of potential the conversion of CO_2 from solution to reduced species results in the available concentration diminishing with time however the large bulk electrolysis cell was specifically designed to have a small headspace ($\sim 20 \text{ cm}^3$) but a large volume of solution (350 cm^3).

If this solution was assumed to be saturated with CO_2 , approximately 0.07 mol is initially available for reduction.^[166] If a one electron transfer is assumed to proceed with 100% Faradaic efficiency at the observed current of -2 mA, the time required to reduce half of the CO_2 present would be well over $1.5 \times 10^6 \text{ s}$ (approximately two and a half weeks). The apparent drop in current with time, although in part attributable to the loss of the most accessible CO_2 , is much more likely to result from the deactivation of the electrode due to the build up of small, relatively stable gas bubbles on the electrode surface.

The bulk electrolysis cell employed for the generation of gas samples, unlike the standard electrochemical cells used, was not transparent so the observation of

bubble formation at the working electrode was assumed from the chronoamperogram and electrode conditions post electrolysis. This meant the evolution of gas from reactions at the counter electrode was not monitored however the cell was designed so that although housed in the same solution, the headspace associated with the working and counter electrodes was segregated as illustrated in figure 3.4 in the experimental section (chapter 3).

The headspace prior to CO₂ reduction was primarily CO₂ from the saturation process, however as air was not specifically removed from the cell trace quantities of CO from air may be expected. The quantity would be in the region 0.1 to 0.5 ppm of the already small proportion of air.^[53]

The gas samples from the headspace were taken using a gas tight syringe, inserting a needle through the sealed balloon filling (illustrated in figure 3.4) and injected directly, using sample valve method, into the GC (Agilent 7890A series). This was equipped with a 5Å molecular sieve column (valve 1, 0.01 to 10 min) for detection of CO and CH₄, however this column is poisoned by CO₂ so a PlotQ column (valve 2) was switched on at the CO₂ elution time, which was found to be 3.2-4.8 min.

The results showed, in all samples made, the presence of CO in the headspace. The elution times associated with the various gases detected were as follows; CO₂ at 3.95 min, CO at 8.3 min and also O₂ and N₂ at 6.6 and 7.4 min. The presence of relatively high levels of atmospheric gases (O₂ and N₂) detected in the samples were due to contamination of the sample with air and mean no quantitative analysis of the products formed from the bulk reduction could be

carried out, however the quantity of CO consistently observed was above that of O₂ therefore evidence of its generation as a CO₂ reduction product.

4.5.1.2. Fourier Transform Infrared Spectroscopy;

The other technique employed for headspace gas analysis was FTIR spectroscopy where the distinct C≡O and O=C=O bond stretching and vibrational modes allow for the identification of two these gases.

From electrolysis carried out in the standard electrochemical cell where the electrodes are all clearly visible, no evidence of gas generation at the counter electrode was observed with bubbles seen exclusively at the working electrode. As such, for the preparation of the samples for FTIR the headspace of the cell employed was no longer segregated.

This allowed the use a smaller volume of electrolyte and thus lessened the quantity of Mo(CO)₄bpy required. These experiments were designed to confirm that the CO observed in the GC measurements with the NMP solvent and also, measure a 'blank' to assess the behaviour of the Mo(CO)₄bpy system in the absence of CO₂.

The bulk electrolysis undertaken was similar to that for the GC sample preparation with the CVs and chronoamperometry presented in figures 4.28 and 4.29.

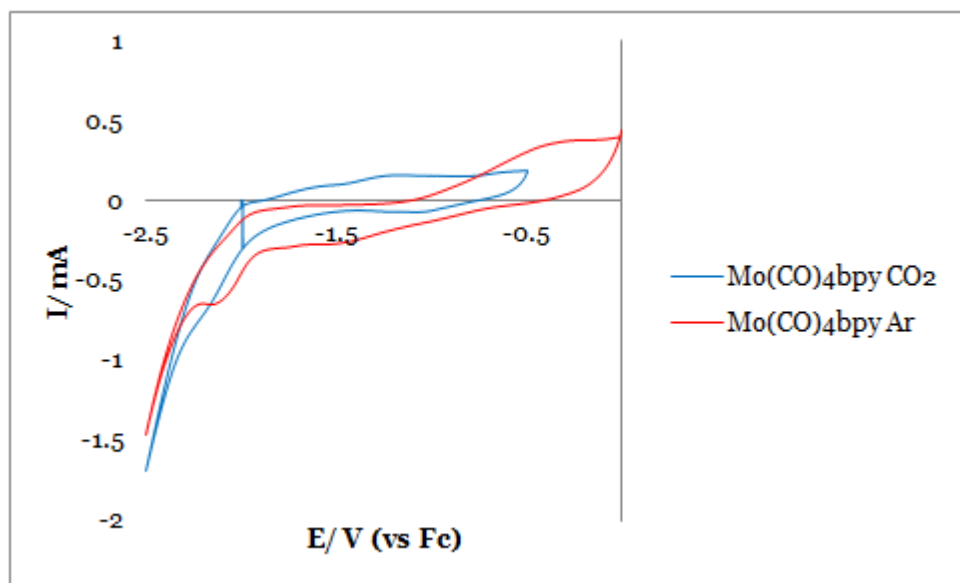


Figure 4.28; CV of Mo(CO)₄bpy (0.5 mM) as cell 1 except measured at bulk gold mesh electrode (approximately 12.5 cm²) in the presence (blue) and absence (red) of CO₂.

Again the CVs showed clear evidence of the Mo(CO)₄bpy redox processes with potentials for the bulk electrolysis chosen 50 mV past the first reduction at -2.1V, prior to the increase in current observed at -2.3 V. The reversibility of the Mo(CO)₄bpy in the absence of CO₂ does not appear as close to one as at a standard working electrode however the features can still be discerned.

The CO₂ and Ar saturated solutions employed were of the same volume, concentration and the same freshly cleaned electrodes and cell employed for the electrolysis, the chronoamperograms for which are given in figure 4.29.

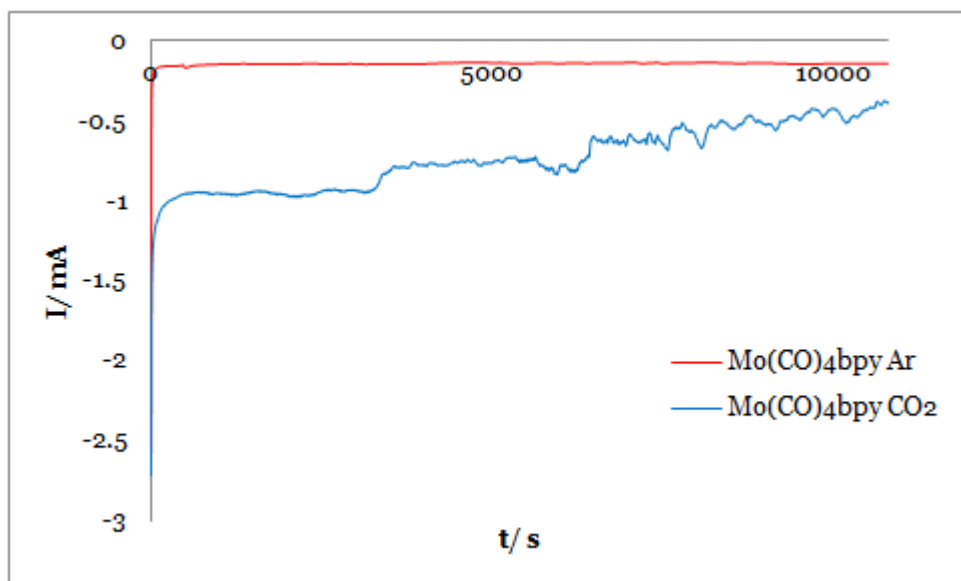


Figure 4.29; Bulk electrolysis current response when -2.2 V applied to the Mo(CO)₄bpy (0.5 mM) as cell 1 except measured at bulk gold mesh electrode (approximately 12.5 cm²) in the presence (blue) and absence (red) of CO₂.

As can be seen from figure 4.29 the CO₂ saturated solution clearly resulted in higher currents and total charge passed over the same experimental times implemented than the system in the absence of CO₂. This is in keeping with the previous electrochemical measurements made, indicative of CO₂ electrocatalysis. The surprising results seen from the FTIR analysis of the samples are given in figures 4.30 and 4.31.

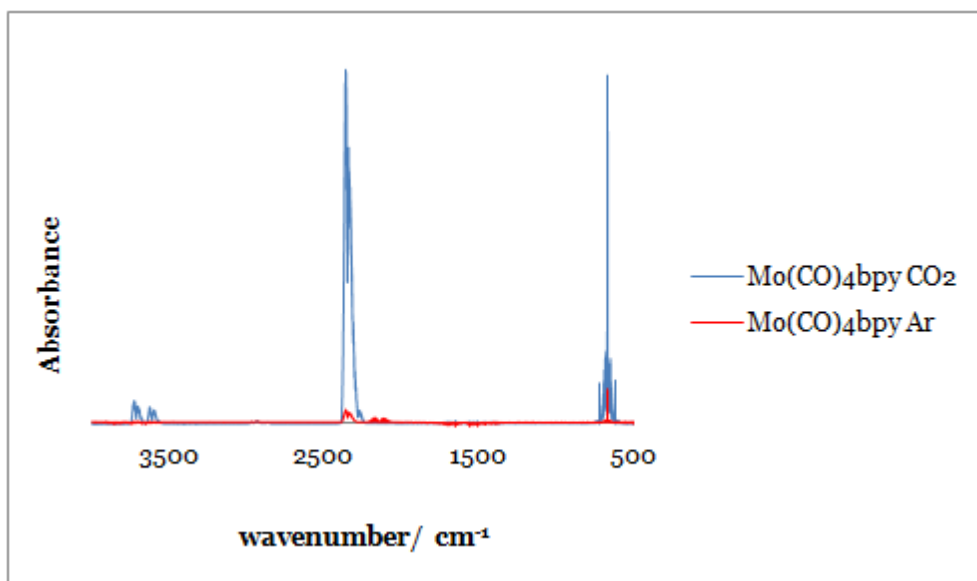


Figure 4.30; FTIR spectra of the headspace gas post bulk electrolysis in the presence (blue) and absence (red) of CO₂ corresponding to the data in Figure 4.29.

The IR spectra obtained from the two headspace samples show distinct differences over the full wavelength range analysed as seen in figure 5p. This is primarily due to the high un-reduced CO₂ concentration from the headspace of the CO₂ saturated system which was absent in the Ar degassed ‘blank’ Mo(CO)₄bpy system with bands due to CO₂ seen at approximately 670, 2200 and 3640 cm⁻¹.

When the area of interest pertaining to CO detection is enlarged, given in figure 4.31, an unexpectedly higher CO concentration can be observed to be present in the gas sample taken from the ‘blank’ CO₂ free system.

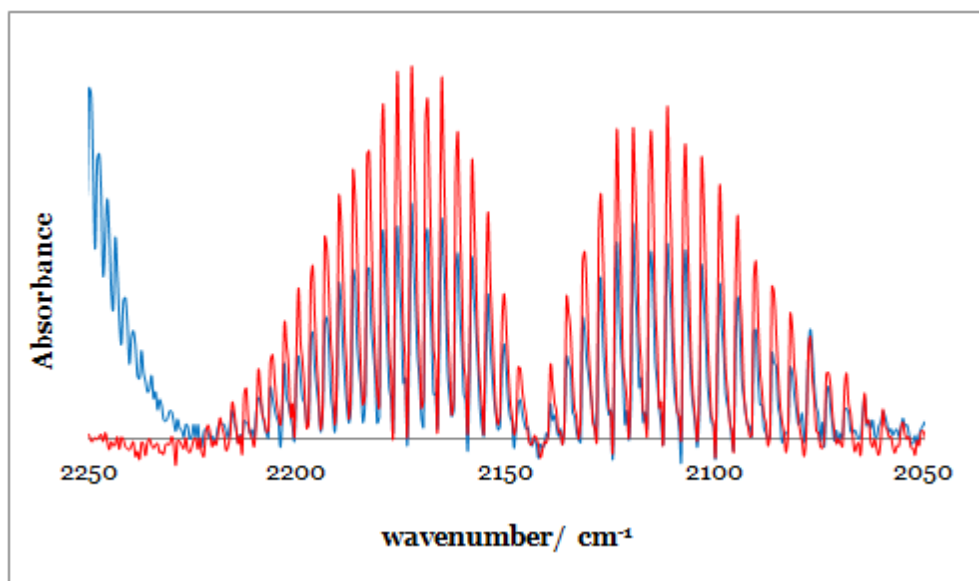


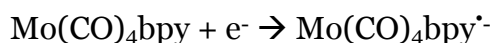
Figure 4.31; Enlargement of the CO region of the FTIR spectra given in Figure 4.30.

The significantly higher current associated with the CO₂ saturated Mo(CO)₄bpy system, (Figure 4.29), yet lower CO concentration detected is perhaps indicative of CO not being the main reduction product in this system. The higher current observed and clear gas evolution observed exclusively in this system does tend to conflict with this conclusion. The experiment was repeated however the same results were obtained with the CO₂ saturated solution consistently generating less CO than the ‘blank’.

The presence of CO in the headspace of the Mo(CO)₄bpy electrolysis in the absence of CO₂ is clear evidence that in the absence of CO₂, to accept the additional electron density from Mo(CO)₄bpy^{•-}, under bulk electrolysis conditions significant quantities of the tetracarbonyl radical anionic species undergo labilisation and loss of carbonyl ligands which, due to their low solubility and high quantity are lost from solution as carbon monoxide.

The loss of CO from the tetracarbonyl complex under standard electrochemical conditions with a standard electrode, even with lengthy timescales, was not evident in the voltammetry until much more negative applied potentials. The observed CO loss prior to this can be rationalised in a number of possible ways;

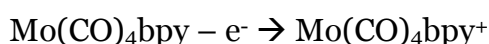
- 1) Shift in the reference electrode potential during electrolysis. This is however unlikely from the consistent current observed and CVs measured before and after the electrolysis showed no evidence of potential shift.
- 2) The build up of the radical anions near the electrode over the long time period, not attainable when the relatively small standard electrode employed over similar time scales, results in side reaction with the possibility of electron transfer between the radicals perhaps in a scheme similar to that suggested below;



The generation of the tricarbonyl species through voltammetry was not possible until after the second reduction however the generation of so many excited radicals near the electrode may mean that intermediates formed from the reaction of these may be easily reduced or otherwise enhance lability.

- 3) The carbonyl loss was not associated with the reduction of the complex and was instead a result of oxidative processes occurring at the counter

electrode. Bubbles were not observed at either however gas was detected therefore evidently generated, suggestive of its smooth gradual loss from solution rather than vigorous bubbling at the electrode. This means that for the experiments conducted without compartmentalising the electrodes such as those conducted for the FTIR, either electrode could be responsible. The loss of CO upon oxidation of Mo(CO)₄bpy has been reported to proceed via the following steps;^[108]



The study of CO loss from Mo(CO)₄(N-N) species (where N-N= bpy or other alpha diimine ligand) was investigated by other groups in a variety of solvents, not including NMP, with the polarity and degree of coordinating behaviour exhibited by the solvents found to greatly affect the cation stability.^{[107][108]} When coordinating solvents such as acetonitrile were employed as a solvent the tetracarbonyl was observed to lose two carbonyl groups to form a dicarbonyl solvent coordinating molybdenum complex upon dication formation. The oxidations were found at 0.629 V and 1.490 V vs Ag/AgCl, both of which are well within the range of potentials which could be reached at the counter electrode in order to maintain the negative potential at the working electrode and could help explain why a relatively low concentration of catalyst species yielded such high quantities of CO.

The lesser extent of CO formation seen for the CO₂ system suggests that the oxidation of Mo(CO)₄bpy may not be resultant in the CO concentration

enhancement as the two systems would be expected to have equivalent degrees of this process.

4.5.2. Non-gas Phase Product Analysis;

The search for non-gas phase products was split in to two approaches; the spectroscopic investigation of the solution both in and ex-situ, predominantly carried out by collaborators, and the electrochemical attempts to detect and identify any species adsorbed on the electrode surface.

4.5.2.1. Electrode;

Given the well defined surface of the gold working electrode after cleaning but prior to voltammetry, and the probable electrochemical CO₂ reduction products including CO which may adsorb and also insoluble carbonates and oxalates which could be expected to alter the working area of the electrode if formed, the comparison of working electrode pre and post CO₂ reduction was investigated. An example showing the gold acid voltammetry pre and post CO₂ reduction is given in Figure 4.32.

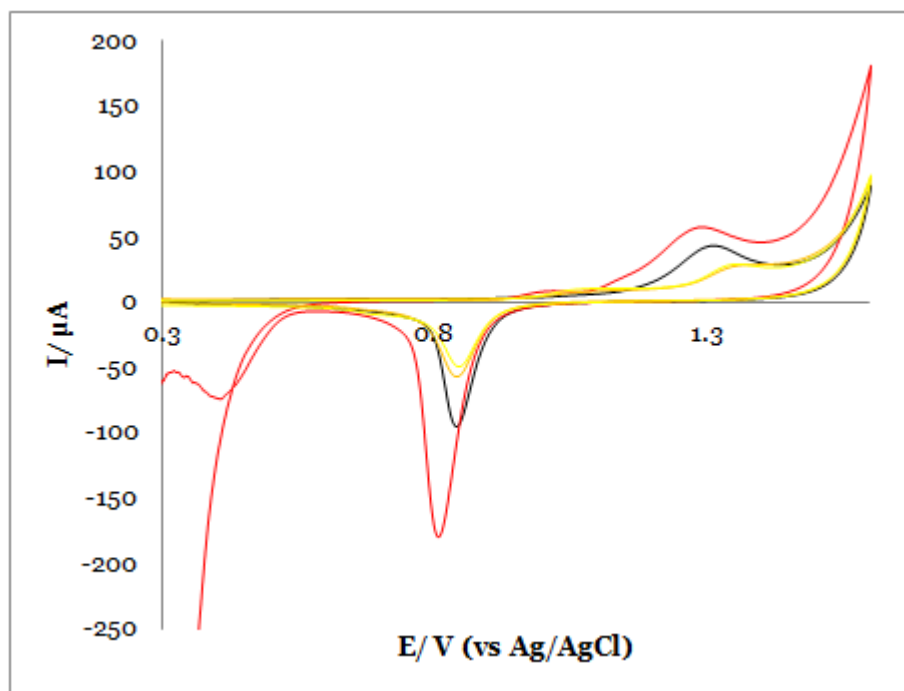


Figure 4.32; Cyclic voltammogram of Au working electrode (2 mm d) in 0.1 M H₂SO₄ prior to (black) and post use (red and yellow, two different experimental runs) in Mo(CO)₄bpy CO₂ reduction system cell 1. Scan rate 100 mV s⁻¹.

As seen by the difference in response between not only the pre- and post-electrolysis acid voltammetry, but also the disparity between two similarly prepared post-electrolysis responses (red and yellow of figure 4.32) indicates that the electrode surface may be altered slightly by employment however the alteration in the CV response in acid does not appear distinct or reproducible with one trial (red) resulting in an increase in oxide reduction and formation and an additional peak with the other (yellow) showing less current response for all processes.

The voltammetric response associated with CO adsorbed on gold in aqueous solution is distinctive and documented by previous groups with the anticipated oxidation taking place in the gold oxide formation region of the CV ($E = 0.6$ to

1.6 V vs RHE^[192]) therefore apparent as a significant current enhancement in this region.

As seen from Figure 4.32 this response was not found in any of the trials of the post CO₂ reduction electrode but was also not observed upon saturation of the aqueous system with CO or employment in NMP where CO had been bubbled.

A possible explanation for this may be related to the adsorption process showing a potential dependence i.e. CO is only adsorbed while the electrode is held at a negative potential. The trials described involved the disconnection of the electrode upon moving between the non-aqueous and aqueous system and due to the acidity of the aqueous medium, the application of fairly positive potentials compared to those required in an alkali system where oxidation starts over 200 mV prior to that in acid.^{[21][192]} This procedure may have resulted in the desorption of any adsorbed CO species in transit.

The electrode showed fairly consistent lowering of working area after electrolysis and voltammetry were conducted in the NMP-CO₂-Mo(CO)₄bpy system which were manifest in a lessening in the charge associated with the oxide stripping peak in the acid voltammetry however this effect did not result in dramatic differences and as such the deactivation may be attributable to trace contaminants in solution, not necessarily CO₂ reduction products.

The lack of detectable species on the electrode surface may in itself be useful information. The presence of the molecular catalyst in solution through which the electron transfer to CO₂ is believed to occur could mean that, rather than reduction products forming at the electrode, as would be expected in the absence of a catalyst (or an electrode-bound catalytic species) products may be

expected to occur in the bulk solution and as such are considerably less likely to be bound to the electrode.

4.5.2.2. Spectroscopic Measurements of Solution;

In-situ IR and UV vis measurements were made by collaborators in Reading employing an optically transparent thin layer electrochemical (OTTLE) cell. In NMP, as predicted, the solvent response masked much of the region of interest with respect to product detection although gas evolution at the working electrode was seen to occur. The monitoring of the $^{13}\text{CO}_2$ peak during the electrochemical experiments conducted provided clear evidence of CO_2 electrocatalysis beginning at the first redox potential of $\text{Mo}(\text{CO})_4\text{bpy}$. In the THF system small quantities of carbonate were detected suggestive of the disproportionation of CO_2 however when compared with the rate of loss of the $^{13}\text{CO}_2$ this was established to be a very minor reaction route.

4.6. Conclusion;

From the electrochemical studies of Mo(CO)₄bpy, although not wholly conclusive in some areas, a number of interesting discoveries were made and points requiring further research identified.

From the electrochemical analysis in the absence of CO₂ in both THF and NMP on the gold electrode the first reduction (1), was found to be reversible with the radical anion generated stable over all of the time scales investigated through CV at a range of scan rates and chronoamperometry.



The DFT calculations undertaken indicate that the additional electron was localised on the bipyridyl group of the parent complex.

The second reduction (2), found at ~620 mV more negative, exhibited reversible behaviour only at the highest scan rates employed (1500 mV s⁻¹).



This is in good qualitative agreement with the existing literature, although the potentials vary somewhat to those previously reported (given in Table 1.3).

Features previously unreported which were found consistently in both THF and NMP systems are a third reduction at -3.2 V and the emergence of an oxidative peak upon the application of overpotentials more negative than -2.9 V. The peak emerges between those associated with the reoxidations of (1) and (2), with the new oxidation, although not spectroscopically verified, thought to be due to

a tricarbonyl species formed from the dissociation of CO from Mo(CO)₄bpy²⁻ at sufficiently negative potentials, (3) and (4);

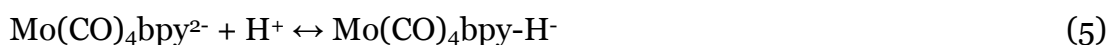


From the reversibility of the first redox couple in the voltammetry, even upon application of large negative overpotentials, the formation of the tricarbonyl species is proposed to be reversible but will be discussed in more detail later.

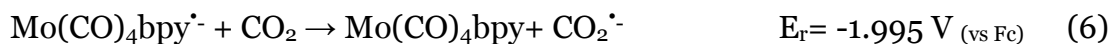
One aspect which was clearly illustrated was that the emergence of the oxidative peak, thought to be due to the tricarbonyl species, was not evident until later than the second reduction in contrast to the literature reports for similar systems.^[89]

The observation of the unreported third reduction may well be due to the large negative potential window provided by the electrolyte-solvent-electrode system used, allowing more negative potentials to be explored than previous researchers. The nature of this third reduction is unclear however it may be linked to the reoxidation process.

The protonation and deprotonation of the reduced complex at the bipyridyl ligand is another possibility (5), if the dianionic complex reactivity were analogous to that of di-reduced bipyridine, however with purely electrochemical measurements discerning between the two prospective reactions is impossible.



Mo(CO)₄bpy was shown to exhibit catalytic activity toward CO₂ reduction, lowering the overpotential (6) and offering current enhancement when compared to the direct CO₂ reduction in the same system (7).



The catalytic activity was observable from the reduction associated with Mo(CO)₄bpy^{•−} formation, although was seen to offer more significant current enhancement at higher overpotentials.

There was an element of time dependence evident in particularly the chronoamperometry gathered, and cross-overs found in the CVs, suggesting the accumulation of the catalytic species. The cross-overs seen in the voltammetry are indicative that at potentials lower than −2.0 V a catalytic radical species is formed on the forward scan, which once present results in enhancement of the CO₂ reduction.

The addition of water and contamination with oxygen were not found to have a significant effect upon the stability of Mo(CO)₄bpy or its CO₂ reduction catalysing properties.

The evaluation of the diffusion coefficients and rate constants was also undertaken with the experimental data yielding *D* values consistent with those predicted by the Wilke-Chang and Stokes-Einstein relationships. The electron transfer rate constants for the first and second reduction of the complex and the proposed transfer of the electron between the reduced complex and CO₂

reflective were all evaluated showing reasonable correlation with E_{rC_i} and E_{rC_i}' mechanistic modelling respectively.

Further work to assist the understanding of the function of the complex and the electrochemical system is addressed in the following chapter.

Product analysis from the bulk electrolysis undertaken was less than successful preventing qualitative analysis of Faradaic efficiencies and other parameters associated with the evaluation of catalysis. The detection of significant CO formation in the CO₂ reduction system during the gas phase analysis through GC and FTIR, although may be representative of CO as a reduction product, was somewhat undermined by the detection of what appears to be slightly higher quantities of CO formed during the 'blank' run where no CO₂ was present.

The attempts to investigate product formation at the electrode surface were unsuccessful although this may be due to a potential dependence not taken into consideration during the experimental design.

The collaborative *in situ* IR and UV measurements of the solution phase have been hindered, particularly in NMP (the solvent in which the majority of the work was undertaken), by the large solvent absorbance in the region in which products may be anticipated.

The detection and quantification of the products of CO₂ reduction within this system is vital for the further analysis of the efficiency and turn-over rates yet have thus far proved impossible to glean. This is the main area within the presented research which needs both some careful consideration and further experiments.

5. System Optimisation and Spectroelectrochemical Investigation

5.1. Catalyst Structure Investigation and Optimisation;

As discussed in an earlier dedicated chapter, $\text{Mo(CO)}_4\text{bpy}$ (the structure of which is shown in figures 1.17 and 4.1) was found to interact with, and in some systems aid, the electroreduction of carbon dioxide.

This chapter seeks to address and rationalise how the various structural components of $\text{Mo(CO)}_4\text{bpy}$ affect its behaviour and importantly the catalysis, and documents the exploration and associated optimisation of the electrocatalyst structure.

The intermediates, including the active catalytic species, formed upon reduction of $\text{Mo(CO)}_4\text{bpy}$ and analogous systems, were also investigated.

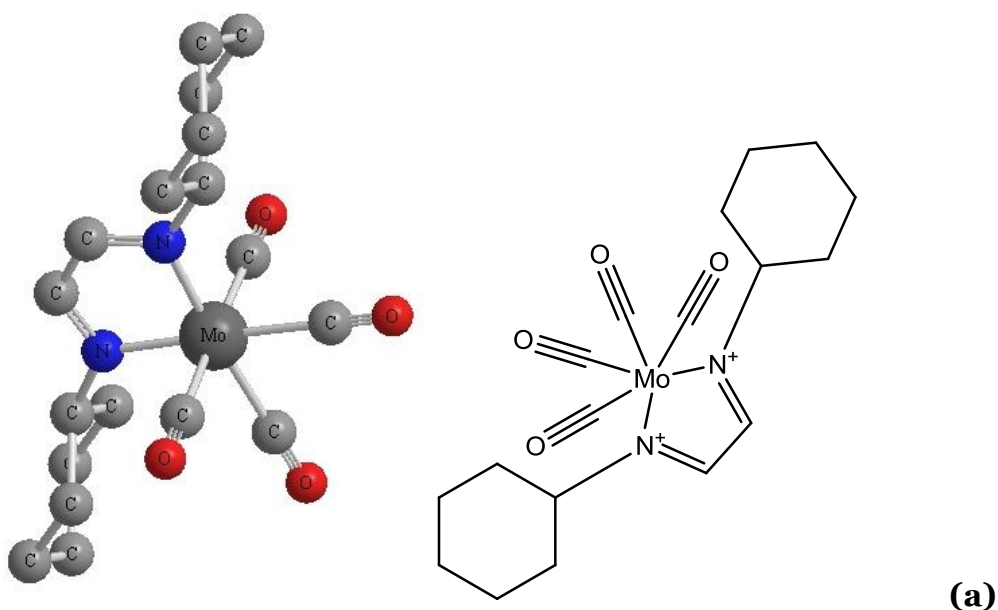
5.1.1. Diimine ligands;

The properties of the $\text{Mo(CO)}_4\text{bpy}$ complex in the systems investigated were governed, or at least very heavily influenced, by the presence of the bipyridyl

ligand. The redox chemistry observed was all primarily associated with the bipyridyl as it contained the predominantly localised LUMO and SLUMO.

Bipyridine is an example of a particularly well studied diimine, employed widely for a variety of purposes including incorporation into complexes and polymers implemented in the ongoing investigation of CO₂ reduction catalysis, especially for photochemical systems but also electrochemical and photoelectrochemical catalysis.

An array of different molybdenum tetracarbonyl α -diimine complexes, Mo(CO)₄($\alpha\alpha$ -LL'), were investigated electrochemically to explore the effects of the diimine structure on the redox chemistry and subsequently CO₂ reduction. The structures of the range of compounds employed are given in figure 5.1.



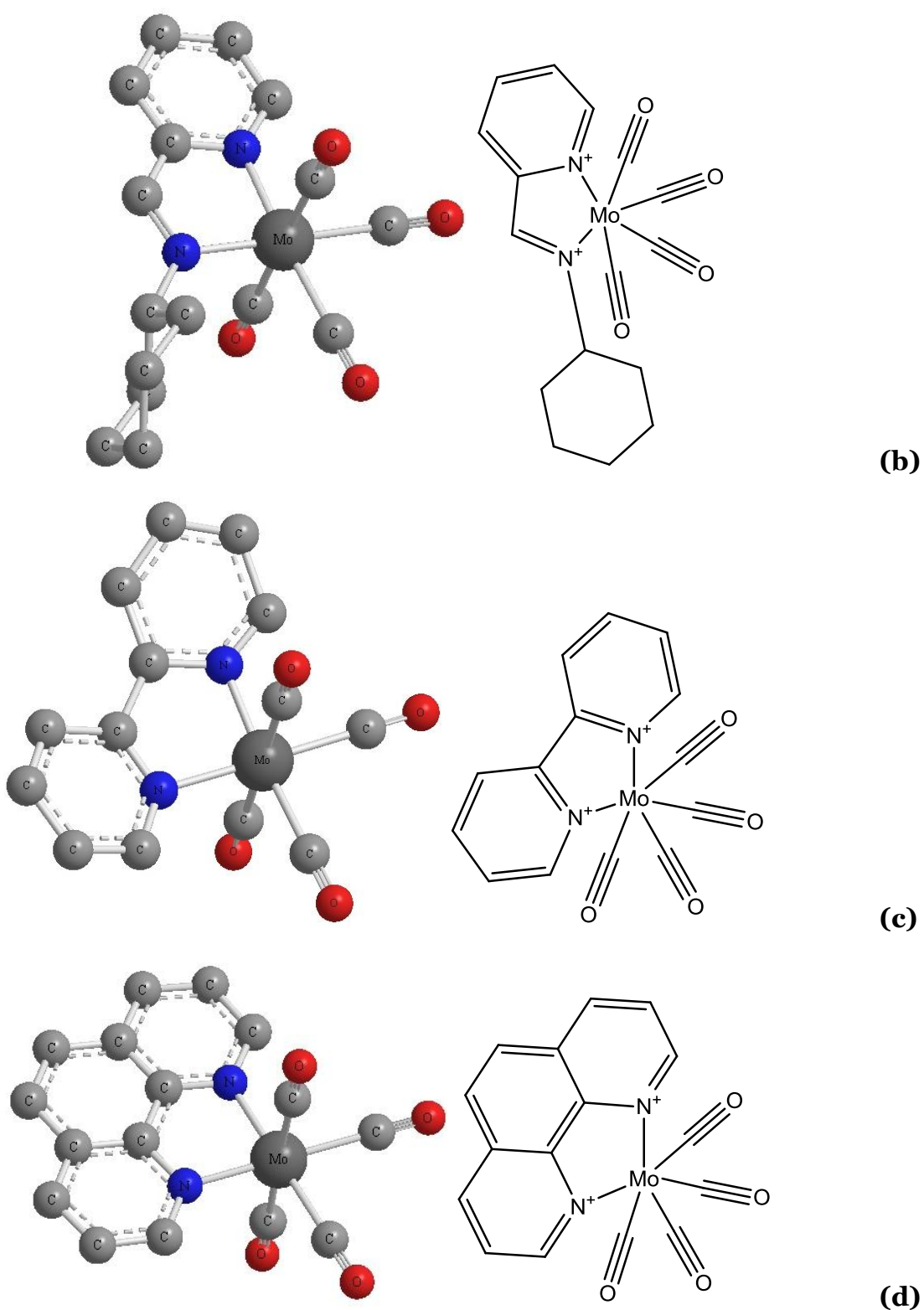


Figure 5.1; Structure of Molybdenum tetracarbonyl complexes. **(a)** = Molybdenum tetracarbonyl dicyclohexylethylthlenediimine (DAB), **(b)** = Molybdenum tetracarbonyl N-(2-pyridinylmethylene) cyclohexamine (PyCa), **(c)** = Molybdenum tetracarbonyl 2,2'-bipyridine (bpy), **(d)** = Molybdenum tetracarbonyl 1,10-phenanthroline (PHEN).

The structures vary in their expected electron delocalisation ability from $\text{Mo(CO)}_4\text{DAB}$ **(a)** with the least conjugation expected to be least able to stabilise negative charge, $\text{Mo(CO)}_4\text{PyCa}$ **(b)** which consists of a pyridyl group, $\text{Mo(CO)}_4\text{bpy}$ **(c)** with a bipyridyl and then the complex containing the ligand with the highest degree of conjugation, $\text{Mo(CO)}_4\text{PHEN}$ **(d)**.

The cyclic voltammetric responses for each of the complexes **(a)** to **(d)**, showing the first reversible redox process seen upon application of a negative potential, are given in figure 5.2.

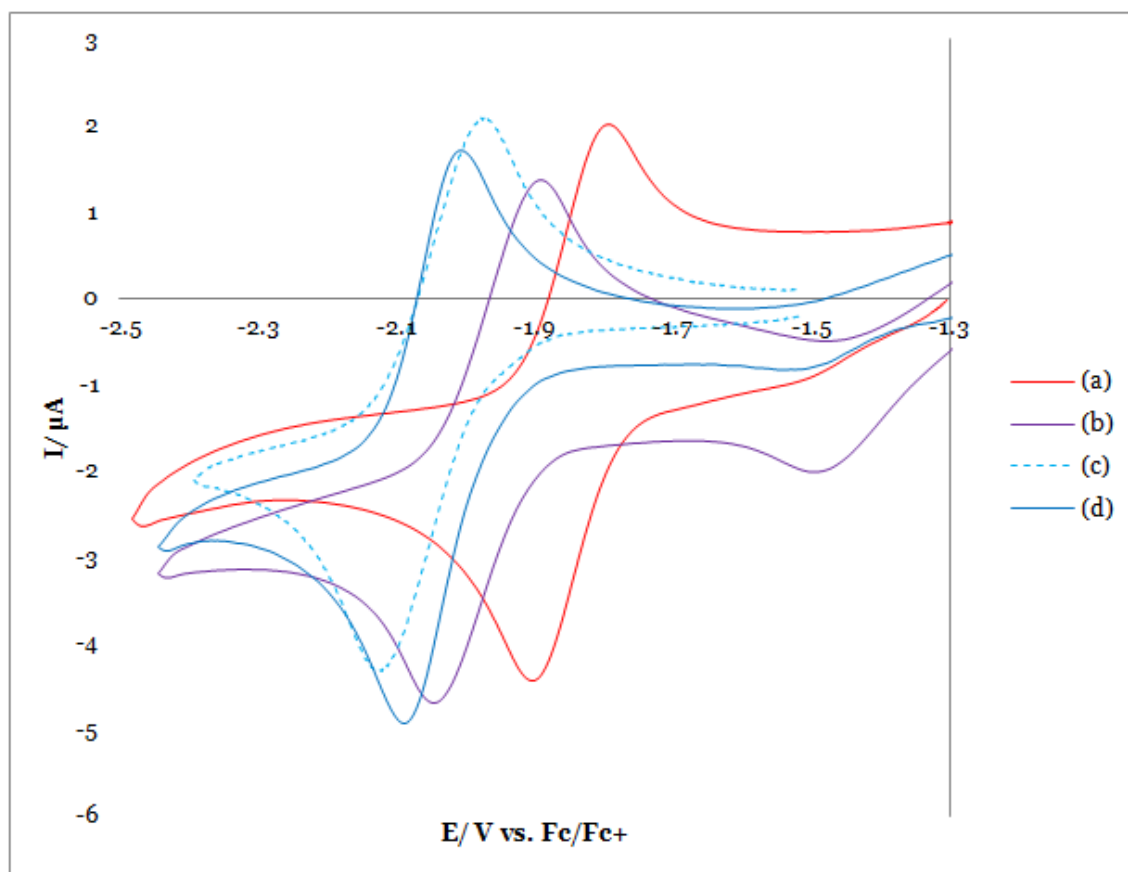


Figure 5.2; Cyclic Voltammogram for **(a)** to **(d)**. $\text{Mo(CO)}_4(\alpha\text{-LL}')$ at ~ 0.5 mM, in cell 2 under argon. Scan rate 200 mV s^{-1}

As can be seen above the complexes each underwent a reversible first reduction at similar potentials, of in THF ca. -2 V vs ferrocene. From initial inspection the trend in reduction potentials does not seem to follow the degree of conjugation

of the ligand as one may expect given that the LUMO for each complex is strongly associated with the α -diimine.

Upon investigation of the half-wave potential, $E_{1/2}$ defined by equation 5.1, or standard potentials of each process, E^0 , rather than the E_{red} , differences in the trend can be observed;

$$E_{1/2} = \frac{E_{red} + E_{ox}}{2} \quad (5.1)$$

where the E_{red} and E_{ox} are the potentials corresponding to the peak reductive and peak oxidative currents seen respectively.

The half-wave and standard potentials are related by equation 5.2 and 5.3^[141];

$$E_{1/2} = E^{0'} - \frac{RT}{nF} \ln \sqrt{\frac{D_{red}}{D_{ox}}} \quad (5.2)$$

$$E^0 = E^{0'} - \frac{RT}{nF} \ln \frac{a_{red}}{a_{ox}} \quad (5.3)$$

where the D_{red} and D_{ox} are the diffusion coefficients of the reduced and oxidised species and a_{red} and a_{ox} are activity coefficients for the reduced and oxidised species. With the one-electron reversible redox systems investigated, where no chemical reaction or significant structural change is anticipated upon the one electron reduction, the diffusion coefficients and activity constants can be assumed to be identical therefore, $E_{1/2} \cong E^0$.

The standard potentials of the reduction become increasingly negative upon incorporation of ligands with increasing delocalising ability, (moving from **(a)** to **(d)**) the values for which are given in Table 5.1;

Complex	E^o /V vs Fc/Fc ⁺	E^o /V vs Fc/Fc ⁺	ΔE / V
	1 st reduction	2 nd reduction	$E_{red(1^{st})}-E_{red(2^{nd})}$
(a) Mo(CO) ₄ DAB	-1.85	-2.79	0.944
(b) Mo(CO) ₄ PyCa	-1.96	-2.86	0.902
(c) Mo(CO) ₄ bpy	-2.03	-2.69	0.659
(d) Mo(CO) ₄ PHEN	-2.05	-2.70	0.648

Table 5.1; The standard redox potential of the 1st and 2nd reductions of complexes **(a)** to **(d)** (corresponding to CV Figure 5.1) and the difference in potential between the first and second redox processes.

The difference between the trend in E_{red} and E^o is attributed to the difference in resistive effects between measurements.

The resistivity in the cyclic voltammetry seen for the four complexes differs.

Although the measurements were made in the same electrolyte-solvent system which tends to be considered the largest source of resistive effects, resistivity of the system also is influenced by other factors including differences in oxygen content, temperature and electrode positioning within the cell. In the somewhat challenging and resistive THF system it is quite possible that a small increase in solvent path length could result in a more resistive voltammetric response. This would be reflected in an increase in the peak separation with heightening resistivity shifting the reductive process to more negative, and oxidative to more positive potentials, than would be observed in an ideal system.

The employment of microdisk electrodes, in an attempt to adapt the experimental design to avoid resistive effects, resulted in no clear voltammetry,

with a steady state current failing to be reached and electron transfers not discernible. This is perhaps further evidence of the importance of the electrode surface.

The use of the half-wave or standard potential avoids this factor as the midpoint around which the peaks are seen would be expected to remain constant within the same system despite slight alteration in ohmic drop and resistivity.

Of the four different molybdenum tetracarbonyl diimine complexes **(a)** to **(d)**, the one possessing the DAB ligand had the least negative E^o for reduction. Of the different diimine ligands incorporated into the complexes this one possesses the least conjugation and, unlike the other three complexes, has no pyridyl character.

The DAB, once incorporated into the complex, is expected to interact to a greater extent than the other complexes with the metal centre. This occurs through metal to ligand charge transfer, due to the overlap between the unoccupied π^* DAB orbital and the d-orbitals of the metal centre resulting in π -back bonding^[108]. This may well result in the DAB complex's properties being influenced by the metal centre more profoundly, and also the LUMO no longer being as localised upon the ligand. The molybdenum metal centre is stable in an array of oxidation states and could exert influence through the overlap, assisting the reduction.

The ability of the complexes to stabilise and accept multiple electrons is reflected in the potential difference (ΔE) between the first and second reduction. This data is presented in Table 5.1. The complexes incorporating DAB and PyCa ligands (**(a)** and **(b)**) have a much larger ΔE and very negative second

reduction, not only compared with the first reduction but also the other 2 complexes, $\text{Mo(CO)}_4\text{bpy}$ and $\text{Mo(CO)}_4\text{PHEN}$.

Evidence of reoxidation associated with the dianionic species formed was evident for $\text{Mo(CO)}_4\text{PHEN}$ and $\text{Mo(CO)}_4\text{bpy}$ (although clearly not reversible), with a suggestion of a peak in the $\text{Mo(CO)}_4\text{PyCa}$ system, however the reoxidative peak was completely absent in the $\text{Mo(CO)}_4\text{DAB}$ voltammetry at 200 mV s^{-1} , as illustrated below in figure 5.3, indicative of a very unstable dianion over the timescale trialled.

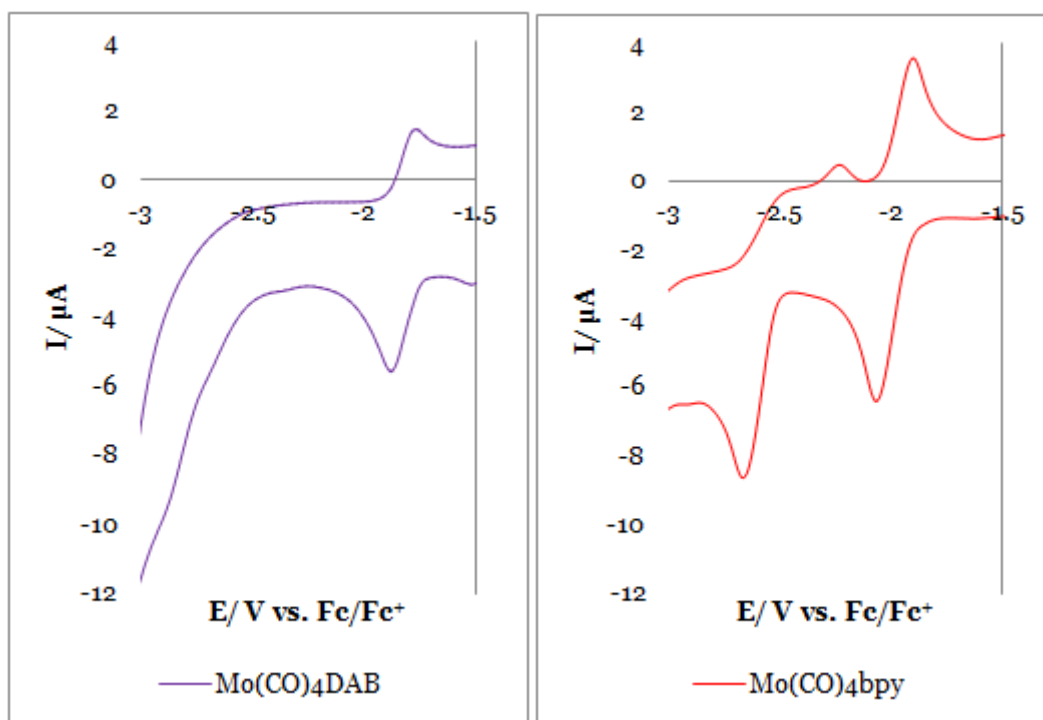


Figure 5.3: Cyclic Voltammogram for (a) $\text{Mo(CO)}_4\text{DAB}$ and (c) $\text{Mo(CO)}_4\text{bpy}$ respectively, $\sim 0.5 \text{ mM}$, cell 2 under argon. Scan rate 200 mV s^{-1} .

As can be observed in figure 5.3, the second reduction of $\text{Mo(CO)}_4\text{DAB}$ is observed close to the edge of the reductive window available in the system employed. This is due to the more negative potential needed to form the $[\text{Mo(CO)}_4\text{DAB}]^{2-}$, resulting in the peak being harder to discern than for the

other complexes. A CV showing the response for $\text{Mo}(\text{CO})_4\text{bpy}$ over approximately the same potential range is given for comparison with the clear second reduction and distinguishable back-peak upon reoxidation.

The complexes **(a)** to **(d)** were then reduced in the presence of CO_2 with an example of the voltammetry presented in figure 5.4.

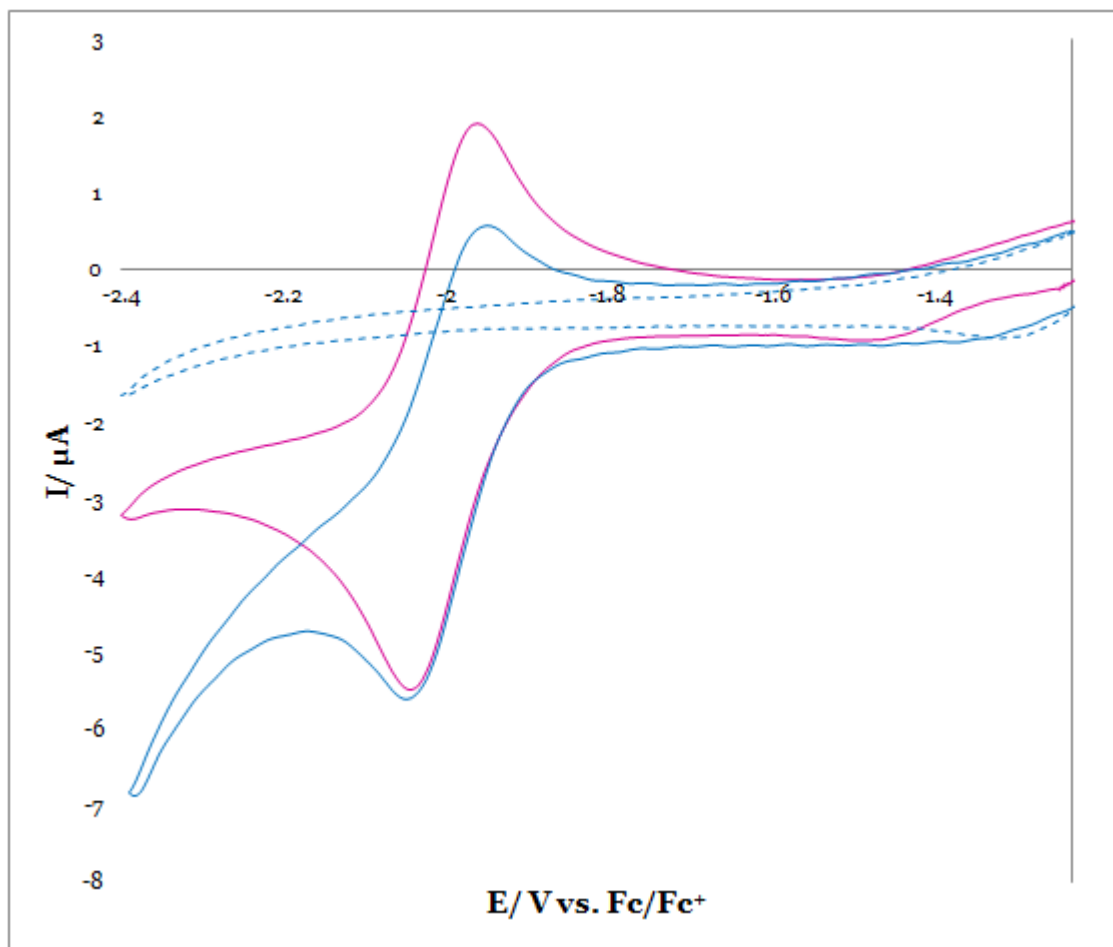


Figure 5.4; Cyclic Voltammogram for **(d)**. $\text{Mo}(\text{CO})_4(\text{PHEN})$ at $\sim 0.5 \text{ mM}$, cell 2 under argon (pink) and upon saturation with CO_2 (blue) and CO_2 saturated electrolyte solution in the absence of $\text{Mo}(\text{CO})_4(\text{PHEN})$ (dashed blue). Scan rate of 200 mV s^{-1} .

For each of the trialled complexes **(a)** to **(d)** an enhancement in CO_2 reduction current was observed. This effect appeared to be most pronounced in the case of **(c)** and **(d)**, where PHEN and bpy were included, although prospective

differences between experimental measurements, both analogous to those experienced during the complex investigation in the absence of CO₂ and also the exact CO₂ concentrations attained in each of the systems, presents a high degree of ambiguity in the qualitative analysis of this. As described in the Mo(CO)₄bpy section, the mono and dianionic species formed upon reduction were both observed to exhibit catalytic ability with respect to the electroreduction of CO₂ (although this was found to be dependant to an extent upon the exact experimental conditions employed).

Upon consideration of this activity there are three different possible mechanisms through which the CO₂ catalysis seems likely to proceed;

The first of which is an inner-sphere electron transfer involving a specific interaction between the reduced diimine ligand of the complexes and the CO₂ molecule. This would seem reasonable as the diimine ligand is where the majority of the extra electron density is found in the active catalyst molecules, as seen in the DFT studies (Figure 4.5 of chapter 4). The CO₂ reduction process could proceed through formation of an adduct or a more subtle rearrangement of electron density in the approaching CO₂ molecule, where electron transfer could be expected to be easier than through an outer-sphere mechanism.

Although as stated, this is a specific interaction which is dependent upon the chemical nature of the ligand all complexes **(a)** to **(d)** showed activity. The chemical reactivity could be expected to differ somewhat between complexes as the diimine ligand is exchanged however the complexes do all show similar reduction potentials and due to the differences in metal-ligand interaction and

conjugation between the ligands, the electron density found at the reduced ligand may be comparable.

It is possible that the interaction between CO₂ and the reduced ligand is not so specific that the CO₂ molecule approaching the complex distinguishes between the somewhat similar bidentate electron-rich α -diimine groups, therefore all of the complexes show enhancement, but those better able to bond or interact with CO₂, **(c)** and **(d)**, which do not possess the sterically hindering cyclohexane groups (which are not expected to interact in the electron transfer), showing higher catalytic activity.

A second possibility is that the CO₂ molecule may interact, again through an inner-sphere mechanism, at the molybdenum metal centre of the complexes replacing a labile carbonyl group in a manner analogous to the well documented [Re(CO)₃bpy]²⁻.^[85-88] This could help explain the apparent lack of (or low) influence of the identity of the LUMO possessing group on the reductive catalysis. There is evidence of lability of a carbonyl group discovered during the investigation of Mo(CO)₄bpy as discussed in its dedicated chapter 4 which may support this hypothesis.

The other possible mechanism worth consideration is an outer-sphere electron transfer process. The fact that, despite the differences in structure and electron density distribution at the ligand, all of the complexes gave some degree of catalytic enhancement to the reduction of carbon dioxide may suggest that, rather than undergoing a specific chemical interaction with the CO₂, the complex's ligands may act more as a redox catalyst. In this case the catalysis observed is due to the greater accessibility of the electrons to be transferred to

the CO₂ as they are found in a 3D dispersion in the form of the reduced species in solution rather than just at the electrode surface, basically a kinetic effect.

The difference in observed activity between the **(a)**, **(b)**, **(c)** and **(d)** could be attributed to not only the degree of hindrance upon approaching the ligand but also the degree of exposed high electron density ligand available for electron transfer; bpy and PHEN groups would be easier to approach from all directions and offer a larger area of delocalised negative charge where the electron transfer could proceed than DAB or PyCa.

Of these three options all are plausible and the data could be interpreted in a manner to support each, however the apparent lack of required structural specificity in the ligand does tend to suggest that the outer-sphere mechanism plays a role, although perhaps not exclusively. The combination of redox and chemical catalysis may be the best explanation for the observed behaviour. The potential at which CO₂ reduction begins in the Mo(CO)₄ αα-diimine catalysed system is up to 500 mV less negative than direct CO₂ reduction on the already fairly active gold working electrode under the same conditions, with enhanced CO₂ related current seen over the whole potential range explored.

The fact that the CO₂ reduction begins at a less negative potential in the presence of the diimine complexes is indicative of an inner-sphere mechanism, with the catalysis seen at the first reduction for each of the complexes occurring before the CO₂ reduction in the uncatalysed system. This is attributed to the relative ease of passage of the electron between the active catalyst and the CO₂ compared to that between the electrode and CO₂. This could be due to a distortion in the CO₂ electron distribution upon approaching the catalyst as the

CO₂ molecule is polarised by the molybdenum complex. The Mo(CO)₄ α-diimine would be expected to attract the δ⁺-carbon of the CO₂ therefore bending the molecule, assisting with the energy demanding shift in geometry of the CO₂ molecule from linear CO₂ to the bent CO₂⁻ and accelerating the electron transfer. The enhancement in current seen in the presence of the catalyst from the second reduction onward is however at potentials already associated with the beginnings of direct uncatalysed CO₂ reduction therefore may be attributable to outersphere electron transfer, enhancing the electron availability, rather than, or as well as, specific interaction with the CO₂ itself.

5.1.2. Effect of the Metal Centre;

The role of the molybdenum metal centre and the extent of its influence over the behaviour of the Mo(CO)₄bpy complex was investigated through exploration of analogous complexes in which the molybdenum was replaced with the neighbouring members of the group 6 triad of the periodic table, i.e. chromium and tungsten.

Both Cr(CO)₄bpy and W(CO)₄bpy, in common with Mo(CO)₄bpy, already have had their electrochemical (and many other) properties documented as discussed in the introduction (section 1.4).^[108]

As mentioned in the Mo(CO)₄bpy chapter, the electrochemical properties of these complexes show a significant dependence upon the system employed for the measurements. Alteration between different solvents in particular is

expected to have a very pronounced effect upon electrochemical potentials as the properties of the complexes are strongly influenced by the polarity of the solvent. The dependence upon the solvent nature is immediately evident as upon moving between different solvents there is a visible alteration in the strong colour of the solution, solvatochromism.

This effect has been studied and reported by previous researchers, particularly for the $\text{Cr}(\text{CO})_4\text{bpy}$ system^{[108][112]}. They found excitation of the metal to ligand charge transfer (MLCT), the transition responsible for the strong colour of the complexes, resulted in the same increase in electron density on the bipyridyl ligand as the one electron reduction. It can be safely assumed that the solvent effect is not trivial, particularly for the chromium tetracarbonyl complex but also for the chemically and structurally similar molybdenum and tungsten analogues.

$\text{M}(\text{CO})_4\alpha\alpha$ -diimines in general are reported to be more polar when in their ground state than in their corresponding excited or reduced state therefore the electroreduction of the complexes tends to require more negative potentials in more polar solvents where the ground state of the complex is better stabilised than the anionic product of reduction.^[108]

THF and NMP, the two solvents employed throughout the investigation of these complexes, are both classified as dipolar aprotic solvents however NMP does have a higher rating on the polarity index of solvents, a greater dipole moment and relative permittivity than THF as seen in table 5.2.^{[168]-[170]}

	Relative permittivity, ϵ (25°C)	Dipole moment, μ / D
THF [a]	7.6	1.75
Py [b]	12.4	2.37
NMP [c]	31.5	4.09

Table 5.2; Relative permittivity and dipole moments of the solvents investigated; tetrahydrofuran (THF), pyridine (Py) and N-methylpyrrolidone (NMP)^[a] from ref [168] ^[b] from ref [169] ^[c] from ref [170]

The addition and nature of electrolyte, as discussed in the DOSY section (chapter 7), can influence the behaviour of the solvent compared to that of the pure substance.

In the measurements made in both the THF and NMP electrolyte systems the voltammetry showed no difference between the two solvents, with the reduction of $\text{M}(\text{CO})_4\text{bpy}$ occurring at the same potential in both. From this it seems that, despite the alteration in polarity, they offer comparable stabilisation to the neutral complexes.

The $\text{Cr}(\text{CO})_4\text{bpy}$ and $\text{W}(\text{CO})_4\text{bpy}$ in the absence of CO_2 gave very similar voltammetric response to $\text{Mo}(\text{CO})_4\text{bpy}$, as expected, with the only differences observed being a shift in potential as can be seen in table 5.3. Included in the table is also uncomplexed bipyridine for comparison.

	E^o /V vs Fc/Fc ⁺	E_{red} / V vs Fc/Fc ⁺
	1 st reduction	2 nd reduction
Cr(CO)₄bpy	-2.16	-2.78
Mo(CO)₄bpy	-2.03	-2.69
W(CO)₄bpy	-1.89	-2.55
bpy	-2.87	-3.57

Table 5.3; Redox potentials of M(CO)₄bpy where M=Cr, Mo, W and of uncomplexed bipyridine. All measurements made in cell 2 at 200 mV s⁻¹ with an analyte concentration of ~0.5 mM.

The experimental values are in keeping with those previously reported [108][119][121][164] with only slight variations in absolute values in potential seen between the uncomplexed and complexed bipyridine. The shift from the literature values can be attributed to the differences in the systems in which the data was gathered as, although THF was employed as a solvent, there were alterations in the following; working electrode employed (platinum rather than gold), the electrolyte anion (hexafluorophosphate rather than the tetrafluoroborate), implementation of IR compensation in measurements (not implemented in gathering the above data) and the referencing system used (voltammetry was measured against a silver pseudo-reference electrode then translated to quote vs. SCE rather than measured directly against a stable Fc/Fc⁺ reference electrode).

From the comparison of the redox potentials of ligated and unligated bipyridine seen in table 5.3 it is clear that complexation has a pronounced effect. The potential is shifted positive upon incorporation into the tetracarbonyl complexes by 0.71 to 0.98 V. This is in agreement with the literature which suggests a ΔE of 0.7 V.^[108]

The observed shift to more positive reductive potentials upon complexation is a commonly seen effect with the magnitude of ΔE dependent upon the nature of both the metal centre and the presence and behaviour of any accompanying ligands.

In this investigation tetracarbonyls were employed for all three comparisons which are known to offer a degree of σ stabilisation to the negative group through their electron withdrawing properties, although only a very small proportion of electron density is expected to transfer to these groups upon reduction of the complex. This would be expected to remain relatively constant for the different $M(CO)_4bpy$ complexes.

The positive potential shift is primarily due to central field effects as a result of the positive nature of the metal centres and their stabilising effect on the anionic species formed. From the DFT calculations undertaken (discussed in chapter 4) and existing literature, the LUMO of $M(CO)_4bpy$ is known to be localised on the bipyridyl group with the metal participation in the redox orbital very small, essentially zero^{[108][112]}. The identity of the metal centre may therefore be expected to have little effect on the redox potentials however a shift of 0.27 V in the 1st reduction potential is observed upon moving from W to Cr. This is presumably reflective of the M positive charge's increasing ability to offer stabilisation to the reduced bipyridyl upon moving down the group from chromium to the larger, more diffuse tungsten.

The second reduction of each complex does not appear to be as heavily influenced by the metal centre as the ΔE between the first and second reduction remains similar for unligated bipyridine and the ligated bipyridyl groups of the

$\text{M}(\text{CO})_4\text{bpy}$ complexes, varying by 0.08 V. This is attributed to shielding effect from the electrons already accepted.^[108]

Upon saturation of the solutions with CO_2 each of the tetracarbonyl complexes were seen to interact with the CO_2 , showing current enhancement from the 1st reduction potential and more negative as seen in the $\text{Mo}(\text{CO})_4\text{bpy}$ chapter. The voltammetric response seen when the tungsten analogue was employed in both the presence and absence of CO_2 is given in figure 5.5.

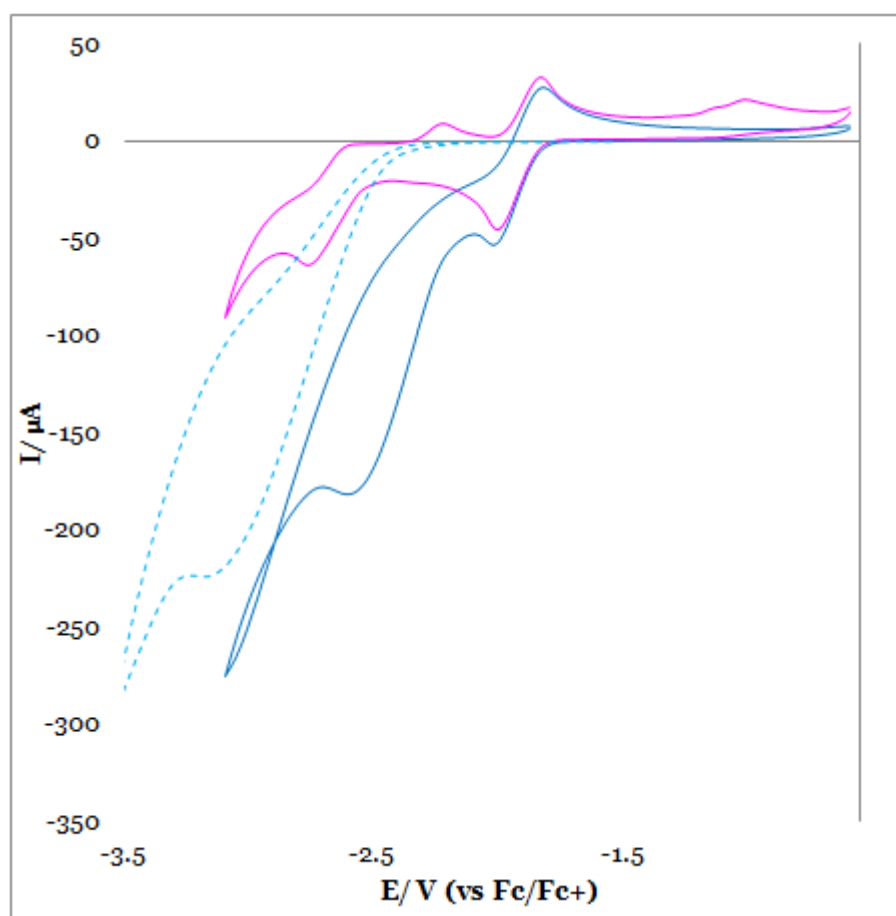


Figure 5.5; Voltammetry of $\text{W}(\text{CO})_4\text{bpy}$ (10 mM) both with (blue) and without (pink) CO_2 and direct CO_2 reduction in the same system (turquoise dashed). Measurements made in cell 1 at 200 mV s^{-1}

The features seen in the above voltammetry are analysed at length in the Mo(CO)₄bpy chapter with the same conclusions drawn for the Cr and W analogues.

As shown in table 5.3, W(CO)₄bpy is reduced at a slightly less negative potential when compared to the Mo(CO)₄bpy and Cr(CO)₄bpy, giving a larger potential window in which the radical anion formed upon the one electron reduction can participate in electrocatalysis of CO₂ before direct CO₂ reduction is expected to begin. A related feature, seen particularly clearly in the above W(CO)₄bpy voltammetry (figure 5.5), when compared to some of the corresponding Mo(CO)₄bpy and Cr(CO)₄bpy CVs, is the alteration in the reduction current-oxidative current ratio for the first reduction upon the introduction of CO₂. In the absence of CO₂ the first reduction, at -1.89 V, is seen to be reversible, however in the presence of CO₂ there is an increase in the reductive current seen for this process and on the reverse scan a lower oxidative current. This voltammetric feature is reasonable if the radical formed upon reduction were to pass its extra electron to the CO₂ molecules fairly rapidly reforming the neutral species as the same W(CO)₄bpy molecule would be available for reduction more than once in each cycle, a so called EC' process. Similarly if the [W(CO)₄bpy]^{•-} formed passes an electron to CO₂ reforming W(CO)₄bpy prior to the point of reoxidation, there would be a less oxidative current observable as there would be less radical present able to transfer the electron back to the electrode.

The fact that this process is somewhat clearer when employing the tungsten based tetracarbonyl is perhaps indicative of enhanced electrocatalytic ability.

In contrast to the $\text{M}(\text{CO})_4\text{bpy}$ voltammetry, the unligated bipyridine did not show any current enhancement when compared to direct CO_2 reduction, on the contrary, its presence appeared to lower the current associated with CO_2 as illustrated in figure 5.6.

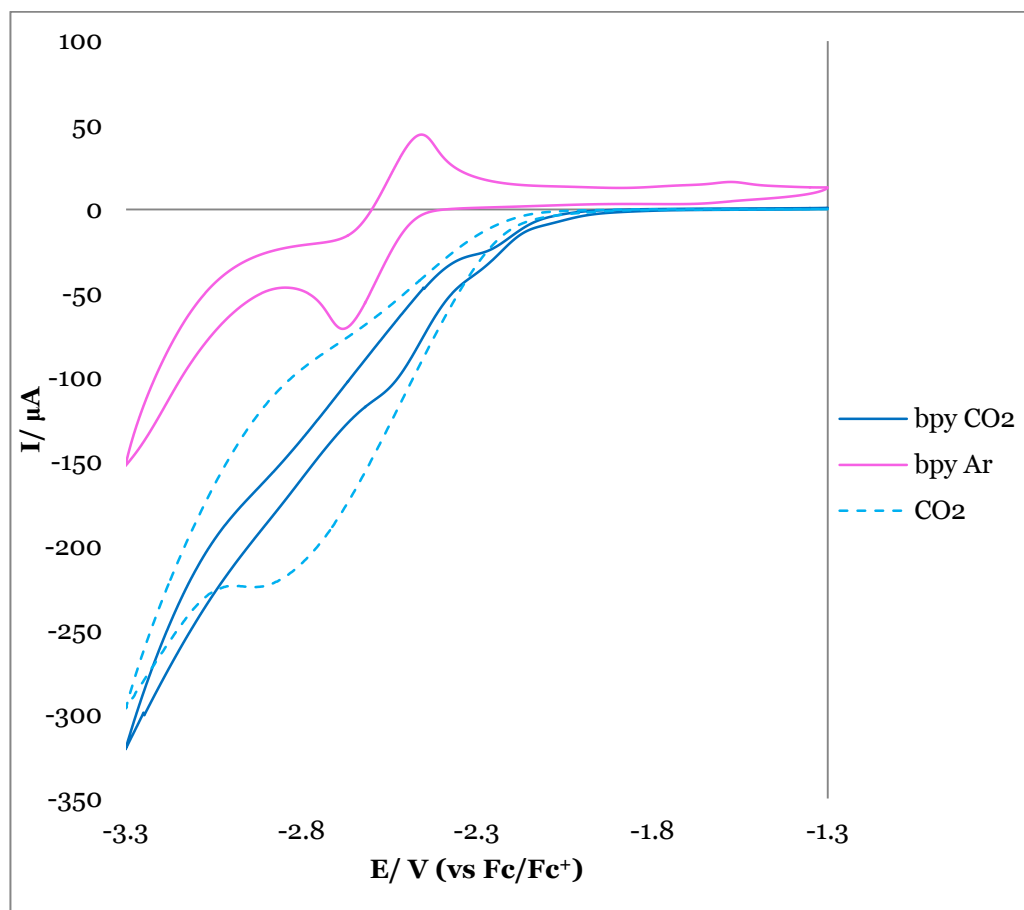


Figure 5.6; Voltammetry of bipyridine (10 mM) both with (blue) and without (pink) CO_2 and direct CO_2 reduction in the same system (turquoise dashed). Measurements made cell 1 at 200 mV s^{-1}

In systems incorporating photoexcitation and an inactive working electrode material and differing solvents, not only does the reduction of bipyridine require a less negative applied voltage to form its reduced potentially active state, the comparative direct CO_2 reduction may well occur at a completely different potential and can be expected to follow different reduction pathways yielding different products dependent upon proton availability, solvent, electrolyte,

working electrode as well as many other more subtle effects offering CO₂ reduction enhancement.^{[8] [16][60] [102]}

In the system employed for the voltammetry seen in figure 5.6 the working electrode was freshly polished gold which offers a catalytic surface for many reactions, therefore allowing CO₂ reduction at a lower overpotential than may be observed at a less active material such as carbon.^{[8][16]} Also all of the energy required to reduce the bipyridine was supplied by the electrode rather than a mixture of photo and electrochemical excitation as trialled by other groups.^[98]

Another point to consider is adsorption effects. Bipyridine is known to adsorb strongly on gold surfaces^{[171]-[174]} and with its reduction occurring at more negative potentials than the direct CO₂ reduction, the presence of adsorbed groups on the surface may deactivate the electrode with respect to CO₂ reduction. The reduction rather than a direct transfer between the electrode and CO₂ could be forced instead to occur via the reduced bipyridine (therefore at a more negative potential) and also associated kinetics of the electron transfer would now be dependent upon two steps rather than one; the transfer of the electron to the bipyridine then from the bipyridine to the CO₂.

5.1.3. Effect of Additional Substituents on the Bipyridyl Ligand;

In experiments analogous to the previous exploration of the nature of the diimine in the complex upon its activity, the effect of modification of the bipyridyl ligand upon the behaviour of the molybdenum tetracarbonyl was investigated.

The substituted bipyridine ligands included the incorporation of nitro and alkyl groups into the complex at the 4,4' and 5,5' positions as shown below in figure 5.7.

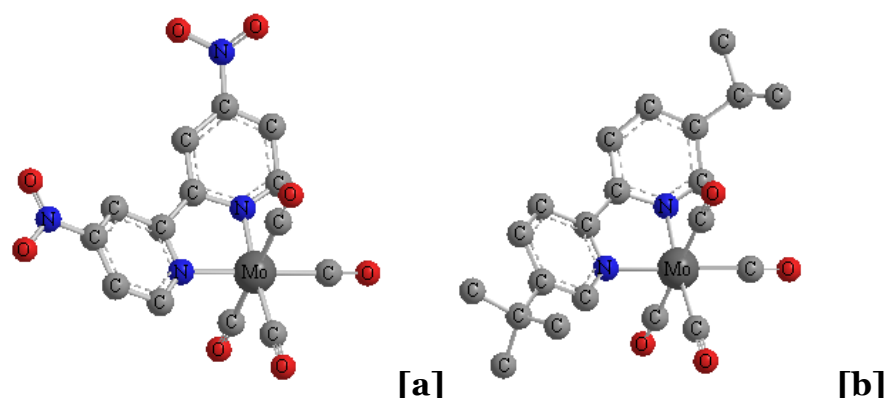


Figure 5.7; Molybdenum tetracarbonyl with **[a]** 5,5'-di-nitro substituted 2,2'-bipyridyl ligand, **[b]** 4,4'-di-tertiary butyl substituted 2,2'-bipyridyl ligand.

From initial inspection of the altered molecular structure, figure 5.7 **[a]**, the inclusion of electron withdrawing nitro-groups on the bipyridine was expected to lower the magnitude of the reduction potential of the molecule, as the extra charge stabilisation and more extensive delocalisation of the negative charge upon reduction of the complex would make it easier for the bipyridyl group to accept an electron.

The voltammetry undertaken, however suggests that the above argument is oversimplified. The first reduction of the molecule was no longer reversible and despite increases in concentration and extra time spent de-gassing the solution,

a clear CV was not obtained. Upon saturation of the solution with CO₂ the reduction of the carbon dioxide was seen at a potential corresponding to that of direct CO₂ reduction and there was no sign of interaction with the ‘catalyst’ molecule in the CV.

The significant change in reversibility of the first reduction could be due to the nitro-group being more easily reduced than the bipyridine species and rather than the expected charge delocalisation over the molecule, the reduction may instead have been localised on the more reactive nitro-group. The one electron reduction of aromatic nitro-compounds in the absence of a proton source is reported as reversible,^[175] as is the one electron reduction of the bipyridyl group of the tetracarbonyl complex in the absence of the nitro-groups.

The lack of reversibility observed is therefore indicative of either a multiple electron transfer or the presence of a suitable proton donor source in the system resulting in the irreversible reduction of the nitro group.

The fact that the reduced molecule did not interact with CO₂ could be explained by the absence of a stable radical formation as the electrons transferred are consumed in the NO₂ reduction therefore not available for catalysis.

Given that no reversible electron transfer processes were observed for **[a]** over the whole potential range in the absence of CO₂ this seems likely.

The tertiary butyl substituted bipyridyl complex **[b]** was expected to act in the opposite manner to the nitro substituted analogue as the groups added are electron donating, therefore would be expected to increase electron density on the bipyridyl ligand containing the LUMO of the complex, making it less able to accept an extra electron and therefore harder to reduce.

As seen in figure 5.8, the CV recorded in the presence of this complex is very similar to that seen for the $\text{Mo(CO)}_4\text{bpy}$ without the tertiary butyl groups but, as expected, the first reduction was observed at a slightly more negative potential.

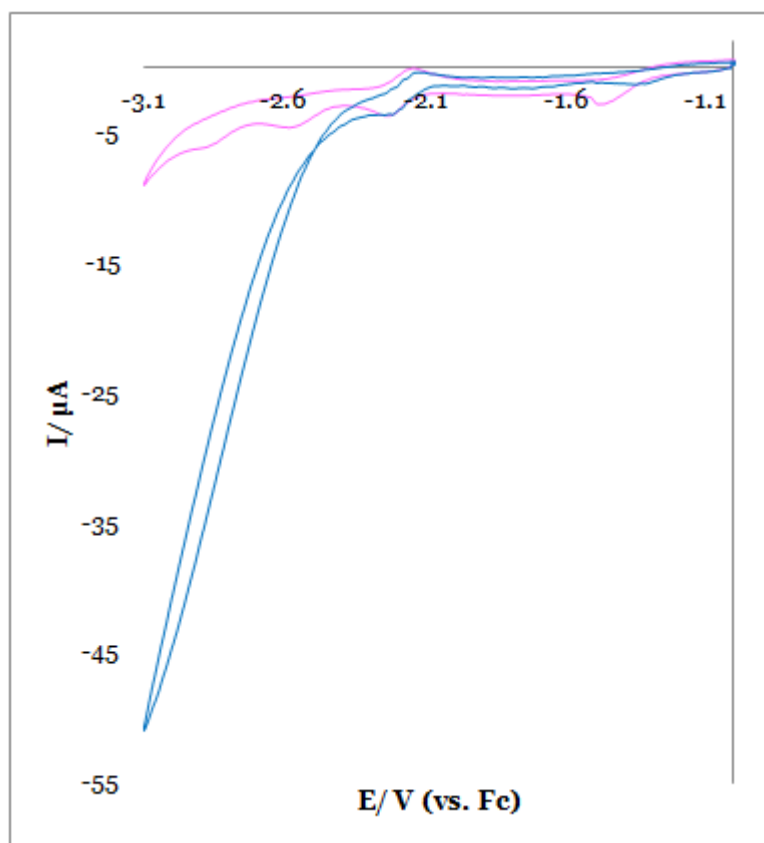


Figure 5.8; Cyclic Voltammogram for [a]. $\text{Mo(CO)}_4(4,4'\text{-di-}t\text{-butyl-2,2'-bpy})$ at ~ 0.5 mM, in cell 2 under argon (pink) and upon saturation with CO_2 (blue). Scan rate 200 mV s^{-1} .

The differences in voltammetry obtained between [b], figure 5.8, and the complex containing the un-substituted bipyridyl ligand explored in the $\text{Mo(CO)}_4\text{bpy}$ chapter, include a shift to more negative potentials by $\sim 300 \text{ mV}$. This is presumably due to the first reduction potential being strongly affected by the identity of the bipyridyl ligand as it contains the LUMO of the molecule and the tertiary butyl groups are known to be strongly electron donating. The potential difference between the first and second reduction is lower than that observed for the unsubstituted bipyridyl with the second reduction still

occurring at approximately the same potential of -2.6 V. The alkyl substituted molecule **[b]** still showed an interaction with CO₂ when it was introduced to the system. Its effects were not as significant as that of the un-substituted complex in that the potential at which the reduction began was not altered as considerably, however there was still an observable CO₂ current enhancement when compared to CO₂ reduction in the absence of a catalyst.

5.1.4. Pyridine and pyridinium;

5.1.4.1. Addition of Catalytic Quantities;

One of the most prominent of recent CO₂ electrocatalytic systems reported recently is based on the simple organic molecule pyridine. Protonation of pyridine (Py) to give pyridinium cations (PyH⁺), upon reduction is reported to form the active species, the neutral pyridinium radical (PyH[•]).^{[98]-[102]}

Much work has been done within the original group responsible for this discovery investigating a variety of solvents and electrode materials as well as photoelectrochemical excitation and optimisation of the catalyst structure.

The work has not been universally acclaimed however with important aspects of the workings and proposed mechanisms still disputed.^[16]

As a fairly novel electrochemical solvent, the effects of the combination of NMP and pyridine species upon CO₂ reduction has yet to be reported. We note, however, that NMP is widely used to disperse graphene and carbon nanotubes

and as such has attracted interest for electrochemical studies with these materials.^[176]

As the name suggests bipyridine is a dimer of pyridine and is an integral component, thought to be the active group, of the tetracarbonyl complexes upon which this research is based. Consequently the activity of this simple molecule may yield pertinent information with respect to these systems.

Pyridine was added to the NMP electrolyte system (10 mM) and its voltammetry measured in the presence of both argon and CO₂ with the response shown by the dotted lines in figure 5.9.

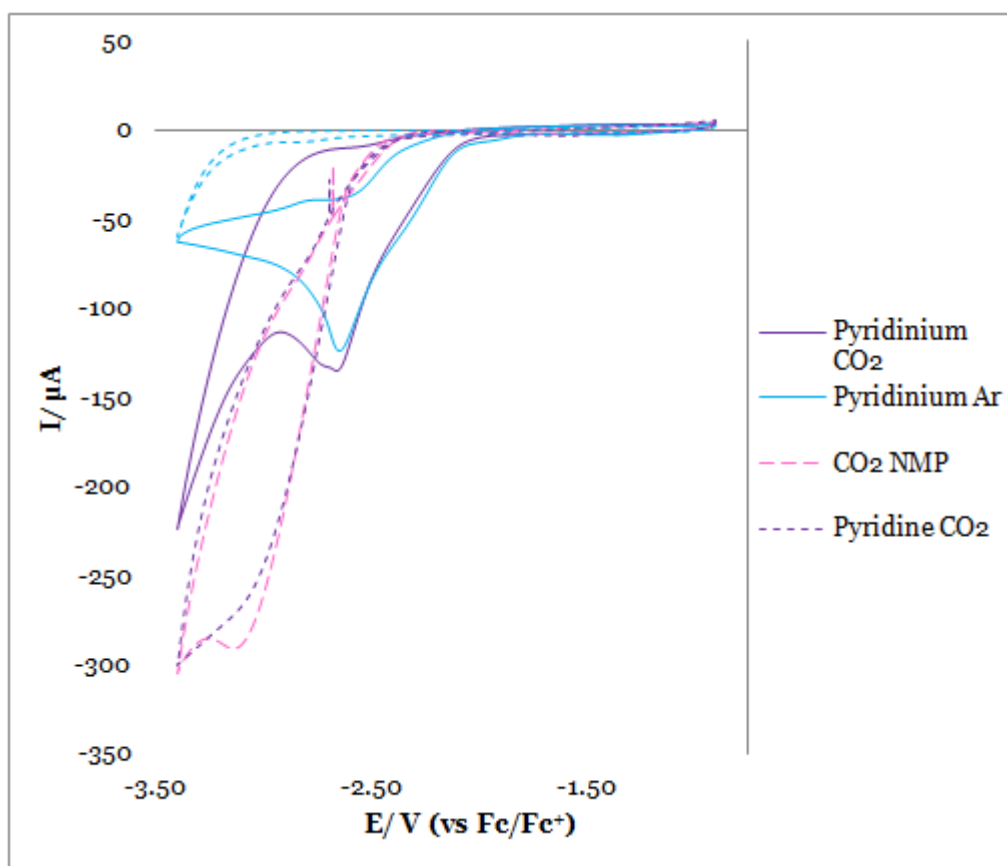


Figure 5.9; Cyclic Voltammogram for pyridine (10 mM), dashed lines and pyridinium (10 mM pyridine + 10 mM trifluoroacetic acid), solid lines, in cell 1 under argon (blue) and CO₂ (purple). CO₂ reduction in NMP + 0.1 M TBABF₄ plotted for comparison (pink long dashed). Scan rate 200 mV s⁻¹.

As anticipated there were no significant features or CO₂ enhancement observed over the potential range investigated, with the CO₂ reduction in the presence of pyridine overlaying the current response seen in the absence of any other additives to the NMP electrolyte.

The addition of equimolar quantities of trifluoroacetic acid to the system resulted in the protonation of pyridine to form pyridinium ^{[98][102][177]} and the voltammetric measurements were repeated. The responses observed are shown in figure 5.9 by the solid lines.

The reduction of PyH⁺ to PyH• can be seen clearly just after -2.5 V. Unlike bipyridine reduction this process is not reversible.

Upon addition of CO₂ to the system a current enhancement is observed upon reaching the pyridinium radical formation potential with CO₂ reduction overpotential lowered when compared with CO₂ reduction in the absence of pyridinium (pink long dashes of figure 5.9) by approximately 100 mV.

From -2.6 V to the edge of the CV window however there appears to be considerably more CO₂ reduction taking place in the uncatalysed system than in the presence of pyridinium with currents three times as high at -3 V without PyH⁺.

When the pyridinium response is subtracted from the CV leaving only the CO₂ derived current, the comparison with the direct CO₂ reduction is shown in figure 5.10, and reveals that there is less CO₂ related current is seen in the presence of pyridinium than in its absence.

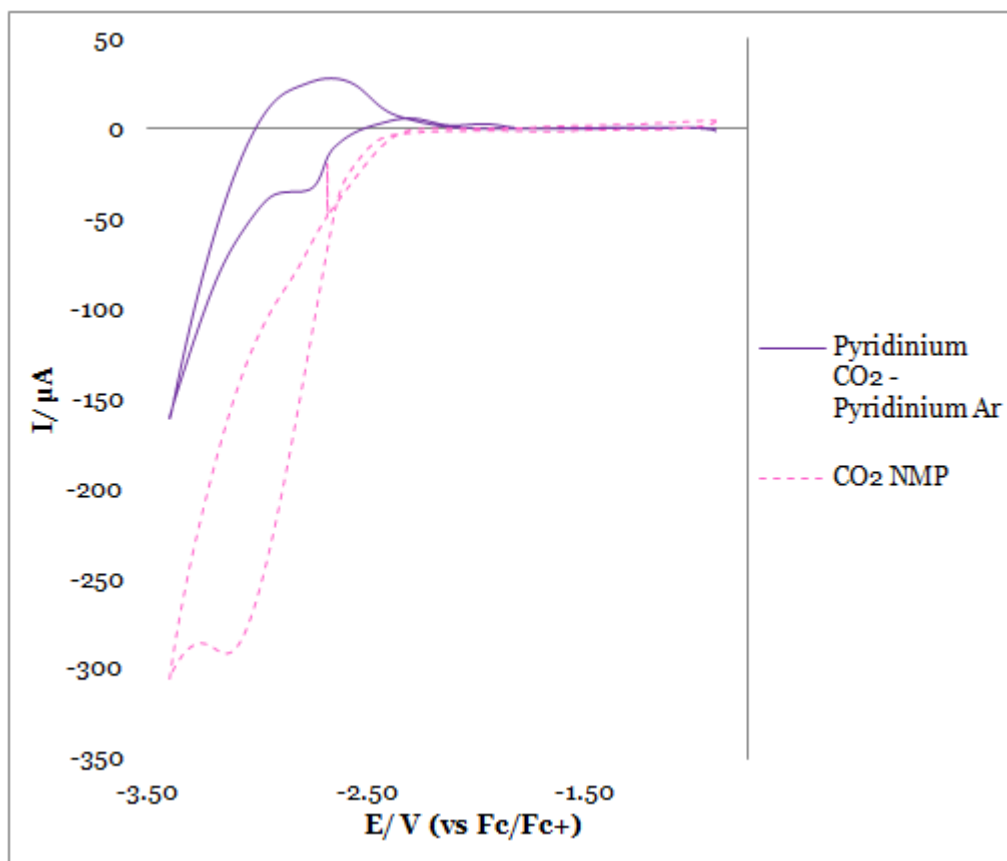


Figure 5.10; Direct CO₂ response (pink) compared against CO₂ pyridinium ‘catalysed’ response (purple): Pyridinium corrected for response in presence of Ar signal. Original data given in figure 5.9.

From this analysis it seems that the documented CO₂ reduction catalysing effects reported by other groups associated with pyridinium^{[98]-[102]} are not observable within this system. The systems are however considerably different in both working electrode material and solvent which could account for this apparent inconsistency.

5.1.4.2. Pyridine as a Solvent;

The health concerns over the impact of exposure to pyridine as well as its unpleasant aroma and flammability have, despite its wide use in various other areas of chemistry, led to it being far from a favoured electrochemical solvent.

Pyridine does have a large negative electrochemical potential window and, given the prominence of electrocatalysts derived from or incorporating pyridine groups for CO₂ reduction, exploration of CO₂ reduction in pyridine itself seemed worthwhile.

The working electrode and electrolyte were kept as gold and TBA(BF)₄ to remain consistent with the NMP and THF systems.

Figure 5.11 presents the cyclic voltammetry gathered in pyridine in the presence and absence of CO₂ both prior to and after the addition of water to the system.

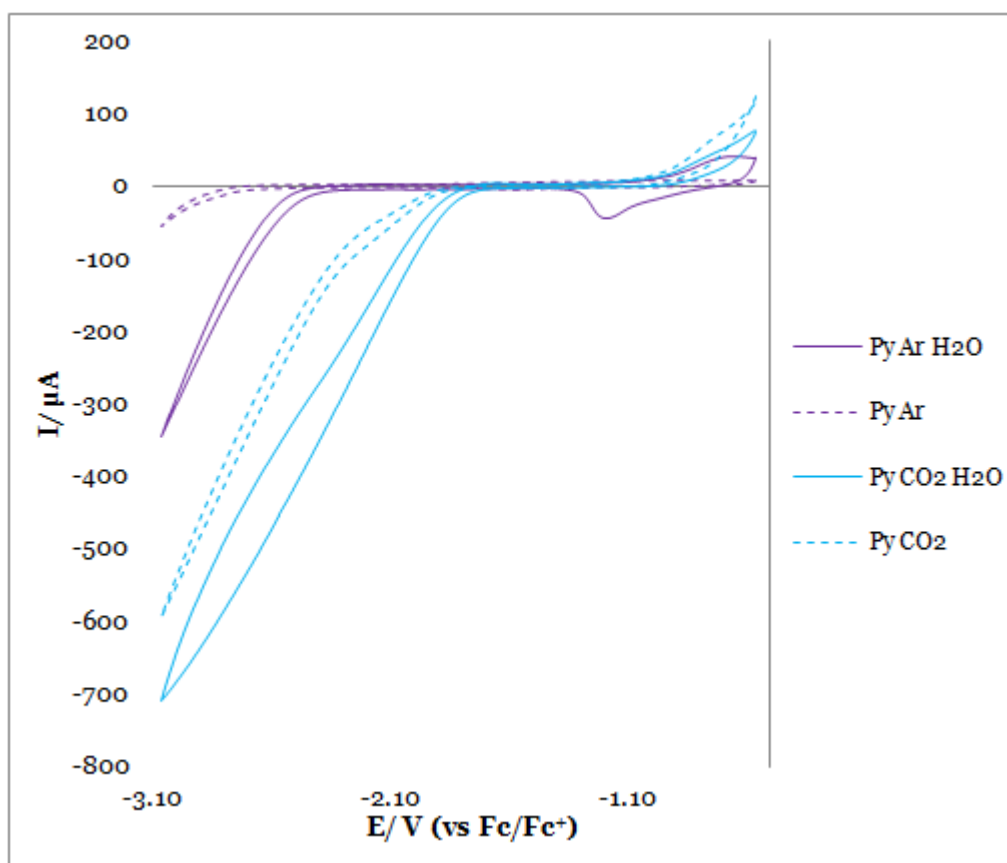


Figure 5.11; Cyclic voltammetry employing pyridine as solvent with TBABF₄ (0.1 M) in the presence (blue) and absence of CO₂ (purple), with (solid) and without (dashed) 10% H₂O. Au WE (2 mm d) employed at a scan rate of 200 mV s⁻¹. Pt wire pseudo reference and Fc calibration (as used for cell 1).

As anticipated the pyridine electrolyte in the absence of CO₂ and water showed no distinct features and a low current. Upon introduction of water (5% by volume) in the absence of CO₂ a set of peaks around -1 V emerged, due to the water introduced to the system with the water influencing the gold electrode oxidation processes (Au-OH oxidation and reduction),^{[54][77][78]} and the negative edge of the window, where bulk reduction of solution began, was shifted more positive by approximately 300 mV. This shift was presumably due to the H₂O reduction processes beginning.

Upon saturation of the pyridine solution with CO₂, reduction was observed to start just before -2 V.

This CO₂ reduction current began at the same potential with and without the addition of water however the current was seen to increase sharply in the presence of H₂O whereas in the 'dry' solution, the CO₂ reduction current remained steadily lower for 750 mV before reaching a comparable rate of increase. Clearly the presence of the water had an effect. As no H₂O reduction was seen at potentials more positive than -2.5 V in the absence of CO₂, it seems reasonable that the water, rather than undergoing direct reduction is instead altering the mechanism by which the CO₂ reduction proceeds by interacting with the reduced CO₂ species and offering a different reaction pathway by providing protons. An accessible proton source can lead to the production of more highly reduced products and appears to have a positive impact upon the associated CO₂ reduction currents if not altering the overpotential at which the process begins.

Cyclic voltammetry of the same systems were also measured with a more negative vertex potential with the scans going as negative as -4 V as illustrated by figure 5.12.

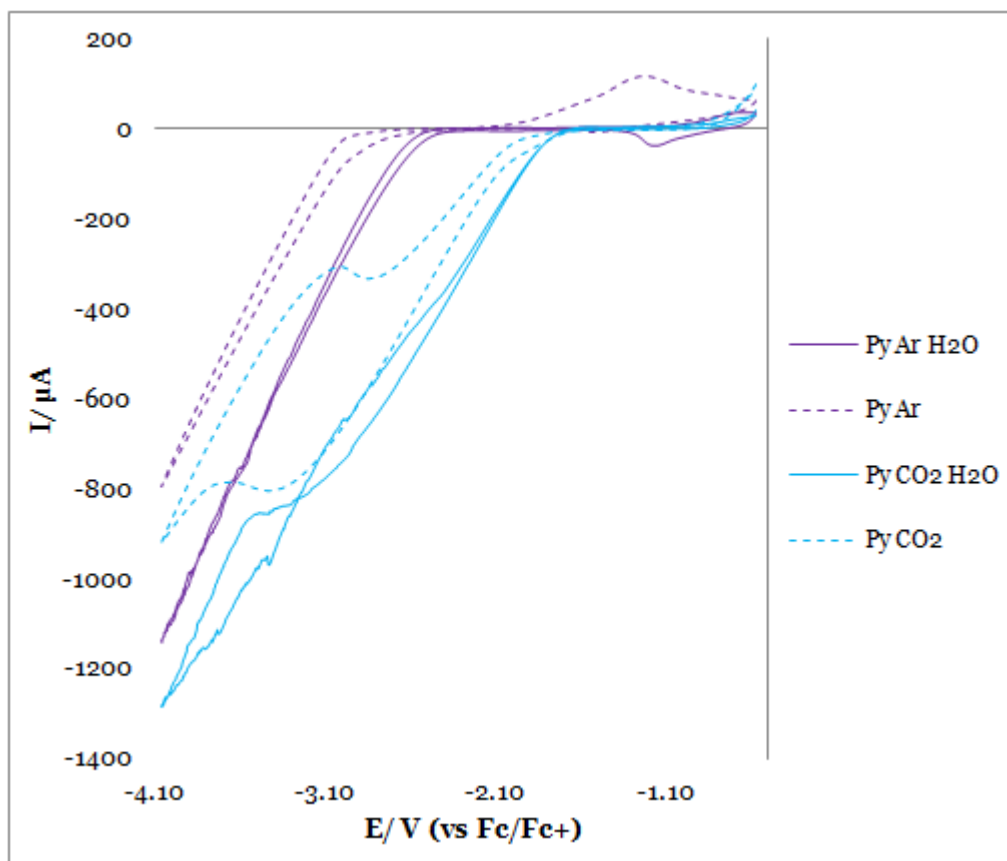


Figure 5.12; Cyclic voltammetry employing pyridine as solvent with TBABF₄ (0.1 M) in the presence (blue) and absence of CO₂ (purple), with (solid) and without (dashed) 10% H₂O. Au WE (2 mm d) employed at a scan rate of 200 mV s⁻¹. Pt wire pseudo reference and Fc calibration (as used for cell 1).

In figure 5.12 the breakdown of H₂O in the systems to which it was added can be seen clearly by the jagged voltammetry at potentials more negative than -3 V. The jagged appearance is a result of gas bubble formation and movement on the working electrode altering the available working area. Upon the application of more negative potentials the form of the CO₂ reduction region now appears more wave-like with a peak observable at -3.1 V on the forward scans for CO₂ both with and without additional water present.

The CO₂ response in the presence of water shows a crossover and higher current on the back scan than in the 'dry' voltammetry. The proportion of this current

which can be ascribed to CO₂ reduction is unclear however as water reduction is also prevalent in this potential range.

The voltammetry for the 'dry' non-CO₂ saturated system shows the emergence of an oxidative peak on the back scan not observed for the other systems or in the voltammetry investigating the less negative potential range. This suggests that whatever the reduction product is, presumably a pyridine anionic species, is either not formed in the presence of CO₂ and H₂O or interacts with CO₂ or H₂O transferring the electron density to one of these reducible species therefore re-oxidation at the electrode does not take place.

The analysis of the overall effect of the substitution of pyridine for NMP seems to show the lowering the overpotential associated with CO₂ electroreduction by something in the order of 300 to 500 mV dependent upon the system with current densities associated with CO₂ reduction comparable when $\Delta E \approx 0.5$ V.

The stabilisation of the CO₂ and its reduction products experienced in the two different solvents are likely to vary to an extent as NMP has a higher polarity than pyridine, however pyridine's properties tend to fall between those of THF and NMP and upon investigation these two solvents were found to have no significantly different behaviour with respect to CO₂ reduction. The possibility of specific pyridine-CO₂ interactions, not related simply to the electrostatic bulk properties, is quite real however and may result in the observed lowered overpotential and higher current response.

However, as discussed at various points throughout this work, altering the solvent may have effects that could lead to the misrepresentation of data.

Pyridine and NMP possess similar properties with comparable CO₂ solubilities,

with just over 5% difference between the two.^{[167][178]} This would suggest that associated currents should be directly comparable which is not necessarily true as, for example, there is a difference in viscosity to consider. The viscosity of NMP is twice as high as the value for pyridine,^{[136][179]} therefore the diffusion of analyte within the system would be slower, lowering the expected current.

The lowering of the overpotential observed is quite significant however the exact degree is difficult to say with confidence from this data. The measurements were made versus a platinum pseudo reference electrode with ferrocene added as a internal calibrant, which although standard practise for the translation of potentials between different solvent systems^[155] is less reliable than employment of a stable reference electrode for the system. The standard potential of the ferrocene redox couple had been shown to vary somewhat in different solvents and the addition of the internal calibrant assumes that the pseudo reference has remained at a constant potential throughout measurements which may not be true.

These preliminary results are however interesting and may merit further investigation and validation. The addition of acid to the pyridine system may also yield favourable effects upon CO₂ reduction.

5.2. *In situ* EPR Spectroelectrochemistry;

An aspect of the catalysed CO₂ electroreduction of interest is the identification of the intermediates formed during the process. This would allow for a better understanding and prospective confirmation of the proposed mechanism through which the electron transfer occurs.

Given that the suggested CO₂ reduction mechanism involves radical anionic species, a technique which lends itself well to the study of such species is *in situ* EPR spectroscopy where unpaired electrons can be detected and the environment of the electron elucidated. The basic physical concepts of EPR are analogous to those of NMR, but instead of transitions between nuclear spin states, electron spins are excited with only paramagnetic species detectable. This specificity in signal origin allows for, within this system, only the electro-generated radicals to be observable with no background solvent contribution to the spectra gathered in need of isolation.

A catalogue of EPR spectra was developed investigating not only the primary catalytic active species of interest, Mo(CO)₄bpy^{•-} but also uncomplexed bipyridyl radical bpy^{•-}, the tungsten tetracarbonyl analogue W(CO)₄bpy^{•-} and a molybdenum tetracarbonyl with di-methyl substituted bipyridyl group, Mo(CO)₄-5,5'-dimethylbpy^{•-} to see the effect of the complexation, nature of the metal centre and nature of the bipyridyl ligand on the EPR response of the unpaired electron.

For all of the species investigated the cyclic voltammetry associated with the electroreduction took a similar form with two discrete one electron transfers

easily observable, albeit at differing potentials dependent upon the identity of the analyte as can be seen in the preceding sections (chapter 4 and section 5.1).

5.2.1. $\text{Mo(CO)}_4\text{bpy}$ Measurement and Modelling;

The EPR spectrum for the electrogenerated $\text{Mo(CO)}_4\text{bpy}^{\bullet-}$ in NMP with TBABF_4 (0.1 M) electrolyte is given below in Figure 5.13.

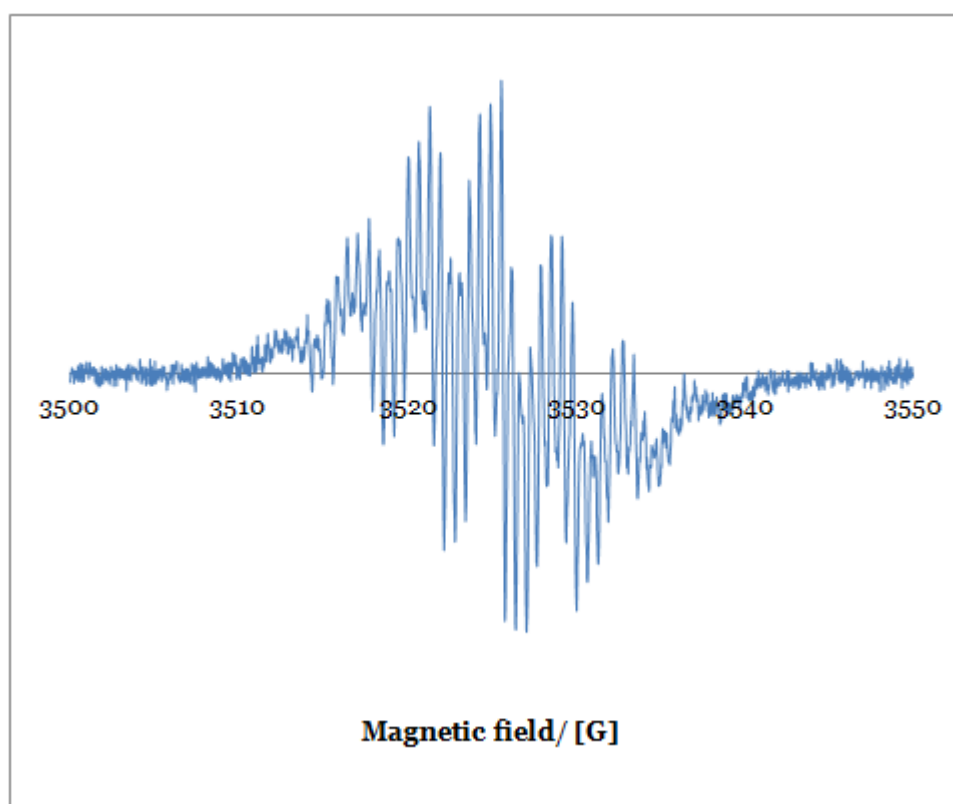


Figure 5.13; EPR spectrum of electrogenerated $\text{Mo(CO)}_4\text{bpy}^{\bullet-}$ in 0.1 M TBAF in Ar degassed NMP, $\text{Mo(CO)}_4\text{bpy}$ (10 mM) -1.7V (vs Ag wire) applied Pt wire WE at RT. Mod. Freq: 100 kHz, Mod Amp:1.0 G, X-band frequency: 9.878 GHz.

From Figure 5.13 the complexity of the signal reveals much about the environment of the paramagnetic radical. From the DFT studies undertaken as well as voltammetry and prior literature, the singly occupied molecular orbital

(SOMO) of the anionic radical formed upon reduction of the complex, where the additional electron density resides, is localised on the bipyridyl ligand. The spin density of the radical anion which is detectable experimentally in EPR is the total electron density of electrons of one spin minus the total electron density of the opposite spin. DFT calculations were performed by Dr J. McDouall using the specifications detailed in section 4.2.1.1. The resultant DFT SOMO simulation results in the distribution shown in Figure 5.14.

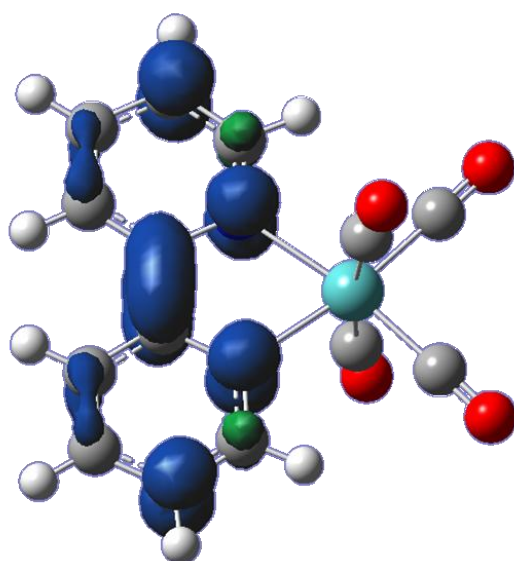


Figure 5.14; DFT calculated spin density of $\text{Mo(CO)}_4\text{bpy}^{\bullet-}$

The spin density shows striking similarity to the DFT predicted LUMO electron distribution seen in Figure 4.5 of chapter 4, as expected with the electron spin density localised on the bipyridyl ligand.

Thus, the EPR spectrum of $\text{Mo(CO)}_4\text{bpy}^{\bullet-}$ is expected to be very similar to that of $\text{bpy}^{\bullet-}$ measured in the same system. The *in situ* EPR spectroelectrochemical response for the bipyridine solution is given in Figure 5.15.

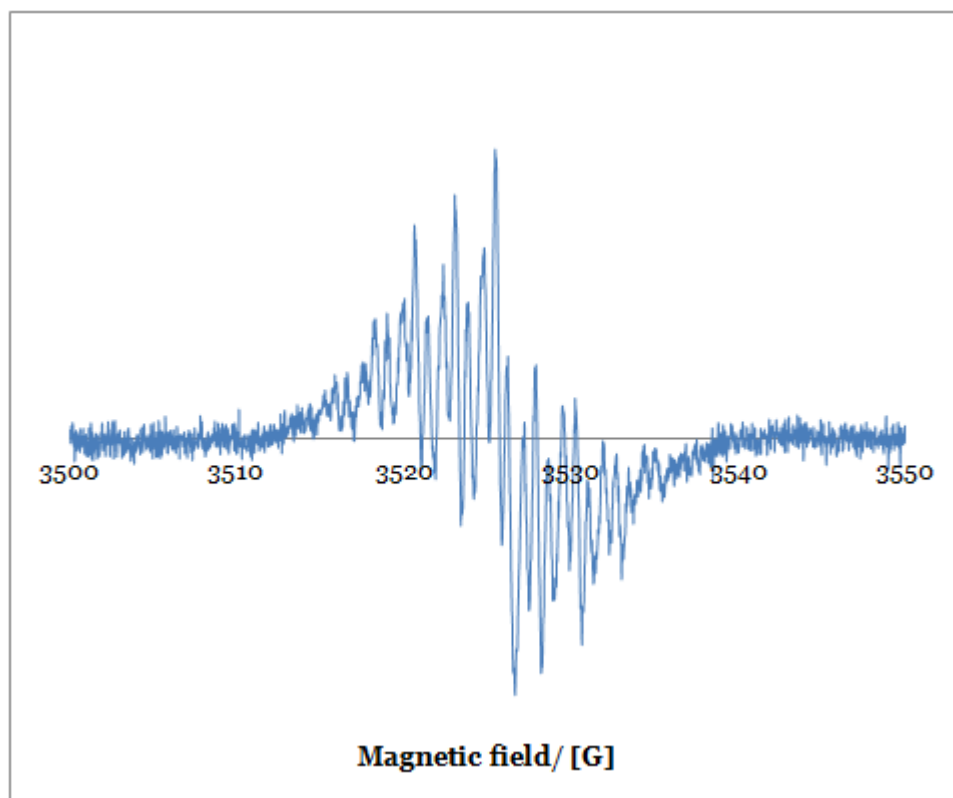


Figure 5.15; EPR spectrum of electrogenerated $\text{bpy}^{\bullet-}$ in 0.1 M TBAF in Ar degassed NMP, bpy (10 mM) -1.9 V (vs Ag wire) applied Pt wire WE at RT. Mod. Freq: 10 kHz, Mod Amp: 0.1 G, X-band frequency: 9.878 GHz

When compared there are striking similarities between the spectra of complexed and unligated bipyridine species. Complexation of the bipyridine has had an effect on the ratios of the hyperfine coupling constants however the apparent splittings are the same for both systems. The $\text{Mo}(\text{CO})_4\text{bpy}^{\bullet-}$ is expected to possess additional splitting when compared with $\text{bpy}^{\bullet-}$ as a result of coupling to the molybdenum metal centre (spin 5/2), the two spectra are presented overlaid in Figure 5.16.

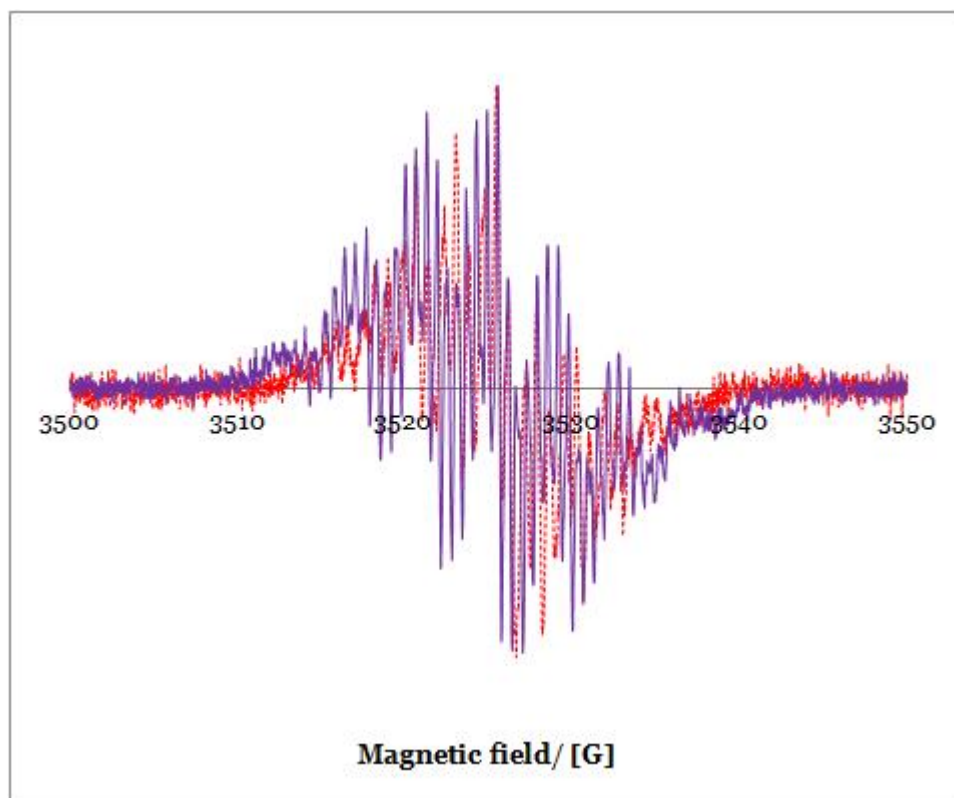


Figure 5.16; EPR spectra of electrogenerated $\text{bpy}^{\bullet-}$ (red) and $\text{Mo(CO)}_4\text{bpy}^{\bullet-}$ (purple) given in Figures 5.13 and 5.15

From the overlay, the $\text{Mo(CO)}_4\text{bpy}^{\bullet-}$ EPR signal shows additional small peaks either side of the bulk signal not seen in the $\text{bpy}^{\bullet-}$ spectrum, these are attributed to the hyperfine-coupling interactions with the transition metal centre of the complex resulting in molybdenum satellites. The impact of the molybdenum is comparatively small, not only due to the small spin density expected in this region of the radical, but also as a result of the low natural abundance of EPR spin active molybdenum isotopes, ^{95}Mo =15.92% and ^{97}Mo =9.55% compared with >99% active nitrogen and hydrogen species.^[180]

The EPR spectra of the $\text{Mo(CO)}_4\text{bpy}^{\bullet-}$ and $\text{bpy}^{\bullet-}$ have both been reported previously in the literature although not all of the hyperfine constants and experimental parameters for the molybdenum complex were available.^{[118][119]}

The two examples of $\text{Mo(CO)}_4\text{bpy}^{\bullet-}$ spectra previously reported were both measured in THF. The earlier of the papers generated the radical, amongst other related species, through chemical reduction with sodium and potassium metal.^[118] Ion pairing of the radical anions was reported to affect the spectra as splitting from Na^+ was observed in the EPR spectra of the unligated bipyridyl species investigated where sodium was employed as the reductant. The influence of Na^+ was however no longer observed once the bipyridyls were incorporated into metal tetracarbonyl complexes.

The later paper including an EPR study of $\text{Mo(CO)}_4\text{bpy}^{\bullet-}$ generated through application of a “short electrolytic pulse” employing a mercury pool working electrode and TBAPF_6 electrolyte and potential of -1.55 V (vs SCE attached via a salt bridge).^[119] This was assumed to be an *ex situ* measurement but few experimental details were given. Hyperfine coupling constants and the g_{iso} value for their spectra were provided, however due to the differences in the solvent and electrolyte the resultant hyperfine coupling is not directly comparable to the results presented in Figure 5.13, measured in NMP with TBABF_4 , as coupling is strongly dependent upon the solvent polarity and proticity which differ between THF and NMP (see table 5.2). The g_{iso} value, as discussed later, is related to the exact field applied to the sample which was not provided.^[145]

Modelling and simulation of the $\text{Mo(CO)}_4\text{bpy}^{\bullet-}$ spectra was undertaken. The DFT calculated spin densities provided data for a simulation. For the evaluation of EPR parameters an all electron basis on Mo was used^[181] and an additional two tight s functions were added to all atoms, with exponents obtained in geometric sequence from the two inner-most s functions of the parent basis set. Relativistic effects were included using the zero-order regular approximation

(ZORA) and the appropriate picture change transformation of the hyperfine operators. The EPR calculations were performed with the ORCA program.^[182] The simulation was undertaken using Simfonia^[183], the result of which is plotted together with the measured EPR response in Figure 5.17.

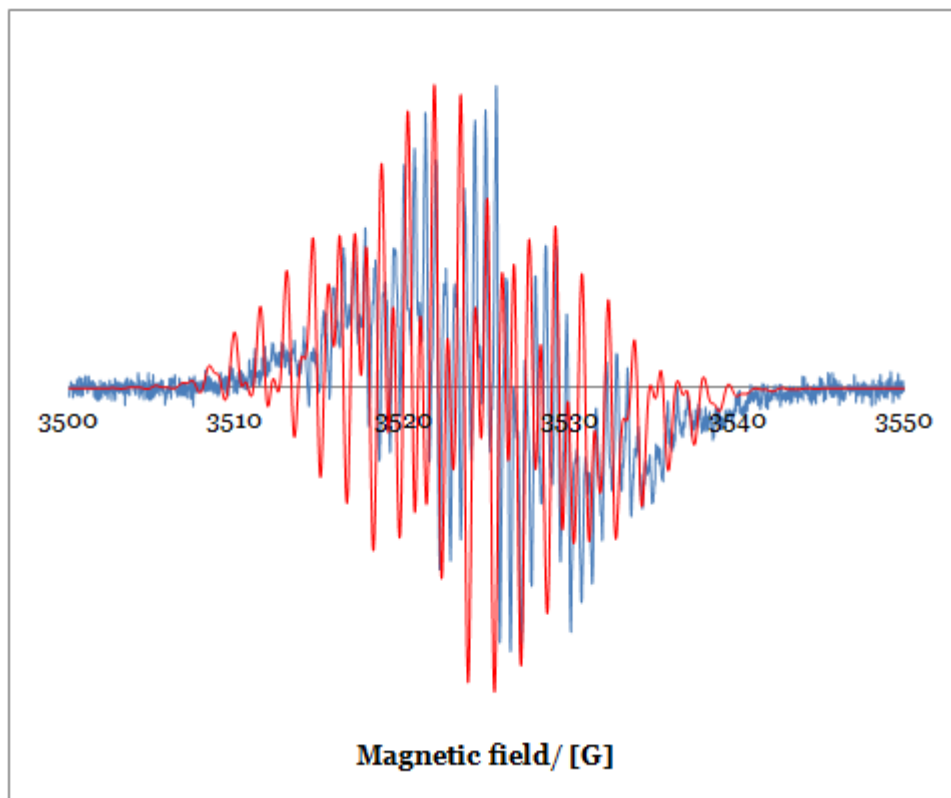


Figure 5.17; EPR spectrum of electrogenerated $\text{Mo(CO)}_4\text{bpy}^{\bullet-}$ (as seen in figure 5.13) in blue and simfonia simulation using the DFT calculated EPR parameters in red. The instrumental parameters were kept consistent with those used experimentally with the following isotropic hyperfine coupling constants; $a_N=3.18$, $a_{H1}=5.7$, $a_{H2}=1.5$, $a_{H3}=1.0$, $a_{Mo}=1.89$ G and g-value= 2.0001.

The experimental and simulated spectra share some common characteristics however clearly do not overlay exactly with the numbers of peaks present as well as their relative intensities not particularly well reflected.

A second, separate model was produced using the program Easyspin^[184], based heavily on the hyperfine coupling constants reported in literature for the

bipyridine radical anion and is given, along with the experimentally gathered $\text{Mo(CO)}_4\text{bpy}^{\bullet-}$ in Figure 5.18.

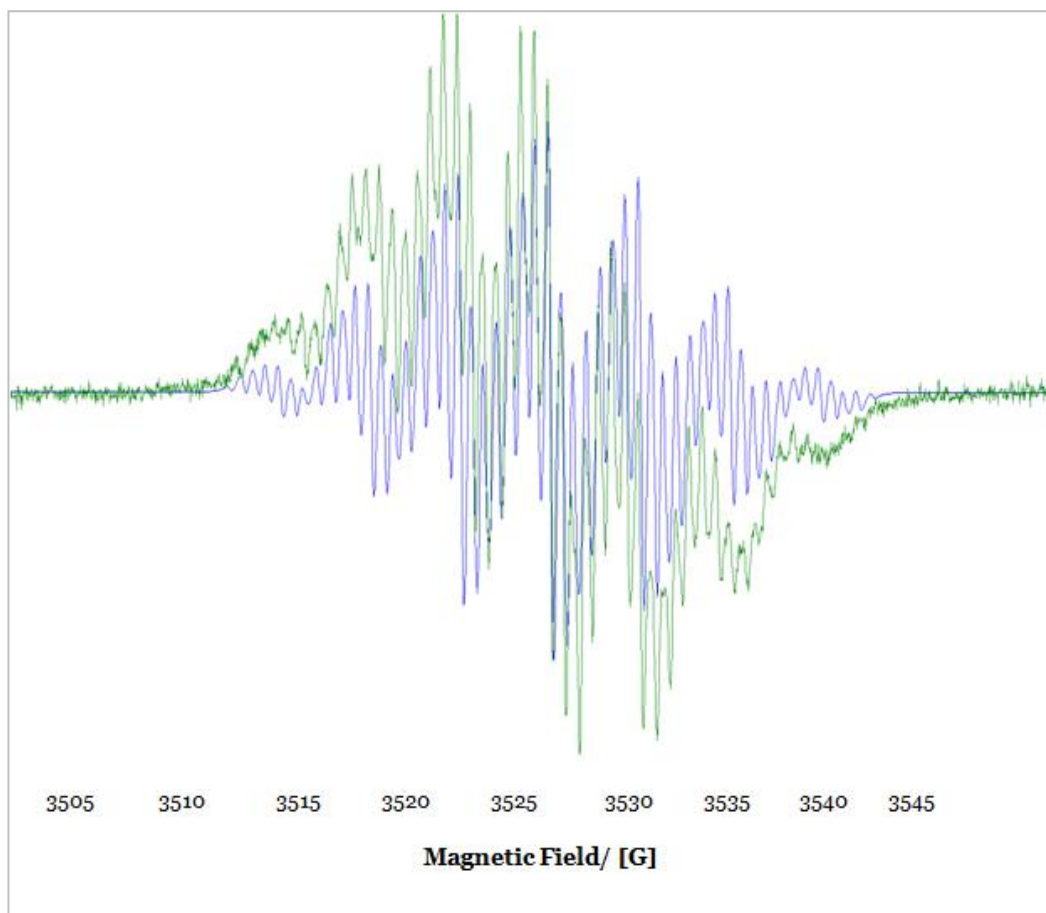


Figure 5.18; EPR spectrum of electrogenerated $\text{Mo(CO)}_4\text{bpy}^{\bullet-}$ (as seen in Figure 5.13) in green and easyspin simulation in blue. The instrumental parameters were kept consistent with those used experimentally with the following isotropic hyperfine coupling constants; $a_N=4.2$, $a_{H1}=4.2$, $a_{H2}=1.1$, $a_{H3}=0.6$, $a_{H4}=0.7$ G and g_{iso} -value= 2.0001.

The correlation between the experimental and simulated data in this case is very clearly very high. The simulated lines do not overlay exactly with the experimental spectrum due to tumbling effects however the number and position of the signals matches almost exactly. This model's parameters have two important differences to the DFT based spectrum;

1. The molybdenum species does not feature.

2. The largest hyperfine coupling constant given by the DFT data was for a proton ($I = 1/2$), here the nitrogen ($I = 1$) and the proton have equal highest influence on the splitting.

The presence or absence of the coupling to the metal centre, as discussed earlier, would not be expected to significantly impact on the form taken by the EPR response. The apparent higher influence of the nitrogen atoms of the bipyridyl than that predicted by DFT may be explained through compensation changes in the LUMO upon reduction by orbitals which are not directly involved in the reduction process. These changes may include additional delocalisation and differing complex metal to ligand charge transfer, MLCT and back-bonding interactions between the Mo and bpy.^{[107][108]} The metal and ligand are bound through the nitrogen atoms of the bipyridyl group therefore this change could be expected to alter the electron spin density at these atoms.

5.2.2. Analogous Complexes;

The EPR spectrum of $\text{W}(\text{CO})_4\text{bpy}^{\bullet-}$ was also measured *in situ* upon electrogeneration. Given the localisation of the radical upon the bipyridyl group, as seen from the comparison and modelling of $\text{Mo}(\text{CO})_4\text{bpy}^{\bullet-}$, the spectra were expected to be very similar however, as seen in Figure 5.19 there are observable differences.

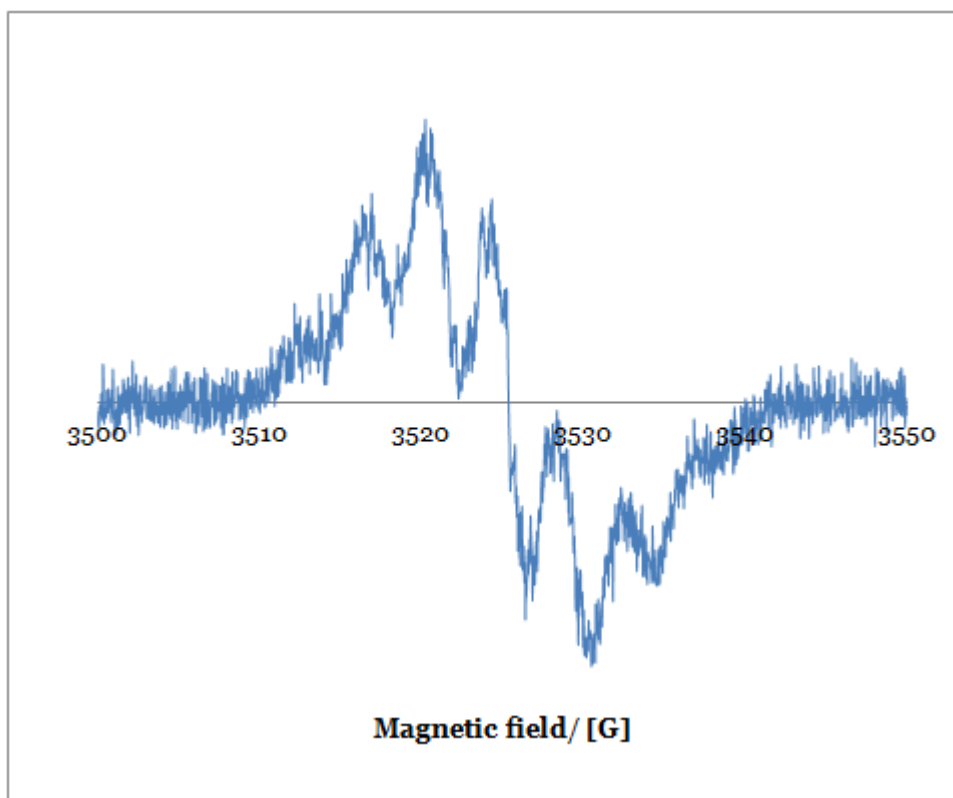


Figure 5.19; EPR spectrum of electrogenerated $\text{W(CO)}_4\text{bpy}^{\bullet-}$ in 0.1 M TBAF in Ar degassed NMP, $\text{W(CO)}_4\text{bpy}$ (10 mM) -1.7 V (vs Ag wire) applied Pt wire WE at RT. Mod. Freq: 10 kHz, Mod Amp: 0.1 G, X-band frequency: 9.878 GHz.

The form of the EPR response for $\text{W(CO)}_4\text{bpy}^{\bullet-}$ is the same as $\text{Mo(CO)}_4\text{bpy}^{\bullet-}$, showing the expected similarity in the main electron-nuclear coupling to the two equivalent nitrogen atoms of the bipyridyl group, however less hyperfine coupling is seen for the tungsten species. The Mo and W tetracarbonyl EPR spectra are overlaid in figure 5.20 where this can be clearly observed.

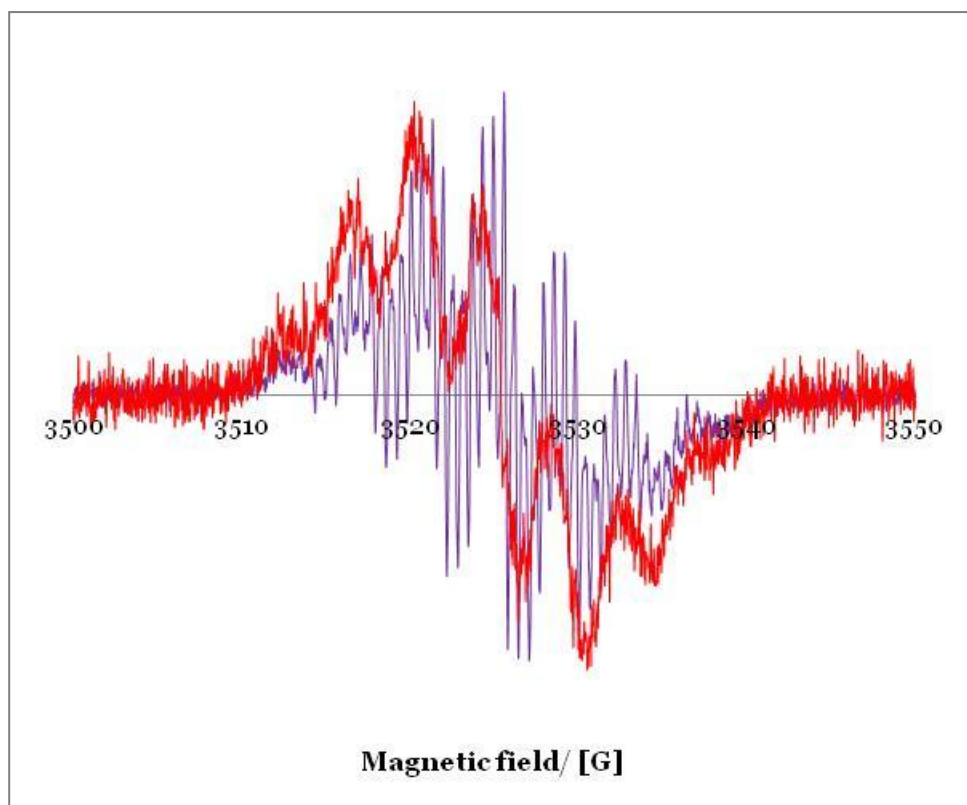


Figure 5.20; EPR spectra of electrogenerated $\text{W(CO)}_4\text{bpy}^{\bullet-}$ (red) and $\text{Mo(CO)}_4\text{bpy}^{\bullet-}$ (purple) given in figures 5.19 and 5.13

The loss of the hyperfine resolution upon the exchange of metal centre is suggestive of the splitting being associated with coupling to the Mo and W nuclei. However due to the low abundance and influence the metal centre is expected to exert over the EPR spectra of the anionic radicals, and over the complexes in general, this seems unlikely. Influence of the tungsten upon the system in particular is not anticipated to be detectable due to its spin;^{95,97} $^{95,97}\text{Mo}$ $I=5/2$ which offers distinctive splitting however ^{183}W $I=1/2$ (abundance 14.3%), therefore is liable to be considerably harder to distinguish from other $I=1/2$ nuclei present. From the modelling, aside from the nitrogen atoms, the other atoms predicted to show large hyperfine interactions are the equivalent protons found at the 5,5' position on the bipyridyl.

EPR investigation of the molybdenum tetracarbonyl complex possessing a substitution on the bipyridyl group at this position yielded the spectrum presented in Figure 5.21.

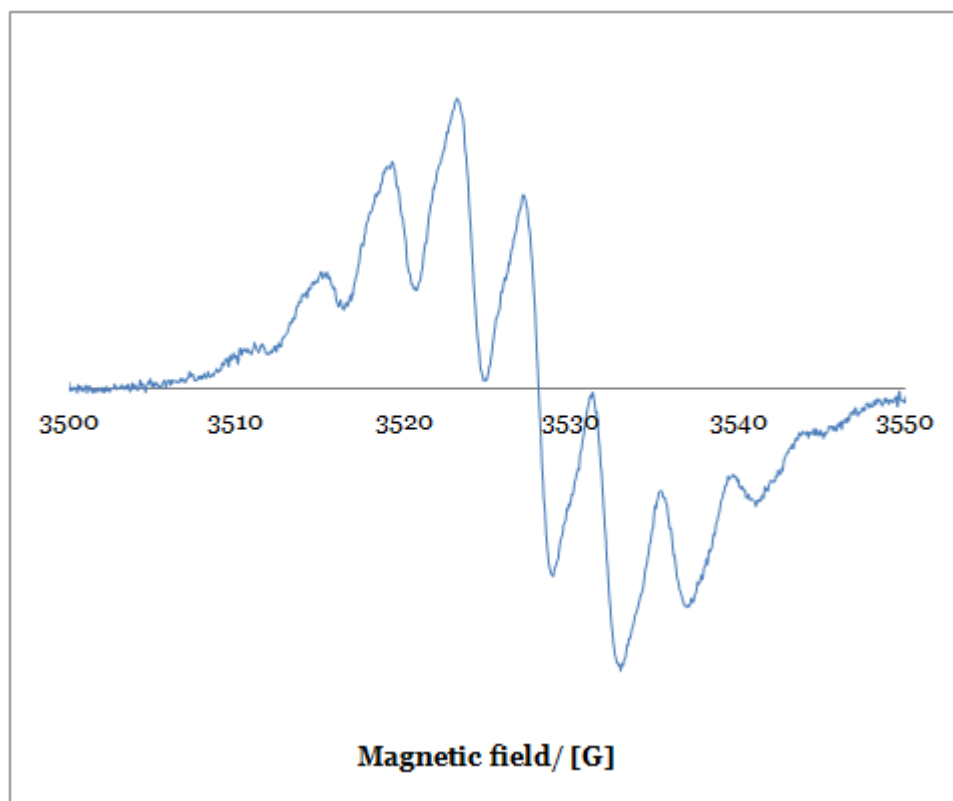


Figure 5.21; EPR spectrum of electrogenerated $\text{Mo}(\text{CO})_4[5,5'\text{-dimethylbpy}]^{\bullet-}$ in 0.1 M TBAF in Ar degassed NMP, bpy (10 mM) -2 V (vs Ag wire) applied Pt wire WE at RT. Mod. Freq: 10 kHz, Mod Amp:0.1 G, X-band frequency: 9.878 GHz

The spectrum seen for $\text{Mo}(\text{CO})_4[5,5'\text{-dimethylbpy}]^{\bullet-}$ is very well resolved. It clearly shows the loss of the proton splitting resulting in a spectral appearance not dissimilar to that observed for $\text{W}(\text{CO})_4\text{bpy}^{\bullet-}$, therefore it can be concluded that the absence of hyperfine splitting seen upon the exchange of Mo for W in the complex leads to a loss in the detection of this coupling.

An analogous report of the free and chromium tetracarbonyl complexed bipyridine and 5,5'-dimethylbipyridine EPR spectra found, in contrast to the

spectra seen in figure 5.21, apparent additional hyperfine structure lines upon substitution at the 5,5' position. This was again carried out in a different solvent system employing metal reductant with few experimental parameters given, although calibrated g_{iso} values for the complexes and unligated species investigated were provided. The g_{iso} values were found to remain similar for the free bpy and 5,5'-dimethyl substituted bpy radicals (2.0026 and 2.0025 respectively) however a distinct shift in g_{iso} was seen between $Cr(CO)_4bpy$ and $Cr(CO)_4[5,5\text{'-dimethylbpy}]$ of 2.0023 to 2.0004.^[118]

A similar shift in g_{iso} value is apparent in Figure 5.22 from the overlay of the $W(CO)_4bpy^{\bullet-}$ and $Mo(CO)_4[5,5\text{'-dimethylbpy}]^{\bullet-}$ EPR spectra measured.

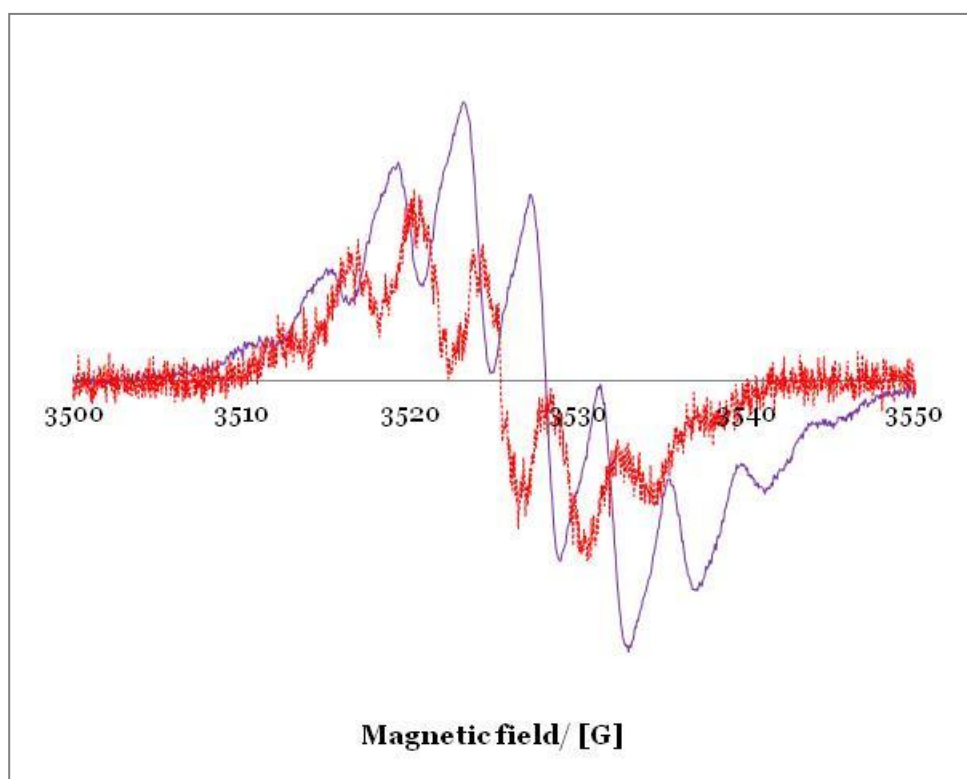


Figure 5.22; EPR spectra of electrogenerated $W(CO)_4bpy^{\bullet-}$ (red) and $Mo(CO)_4[5,5\text{'-dimethylbpy}]^{\bullet-}$ (purple) given in Figures 5.19 and 5.21

The g_{iso} -value, or g-factor is given by Equation 5.4;

$$g_{\text{iso}} = \frac{h\nu}{\mu_B B_0} \quad (5.4)$$

where h is Planck's constant, ν is the frequency of the microwaves, μ_B is the Bohr magneton and B_0 is the magnetic field strength.

Table 5.4 gives the experimental g-values of the spectra shown above.

Observed g_{iso} -value	
Mo(CO)₄bpy^{•-}	2.0018
bpy^{•-}	2.0013
W(CO)₄bpy^{•-}	2.0026
Mo(CO)₄[5,5'-dimethylbpy]^{•-}	2.0001

Table 5.4; Experimental g_{iso} -values for the EPR spectra of the radicals investigated.

As can be seen from Table 5.4, the g_{iso} -values seen for the unligated bipyridyl radical and the ligand incorporated into the Mo and W tetracarbonyl complexes are fairly similar, however upon substitution the value drops considerably.

The field corrections for the spectra measured were not all fully documented which may result in slight variation within the g_{iso} -values however the observed trend is consistent with that seen in the literature for similar systems.

The fact that the g_{iso} -value for the Mo(CO)₄[5,5'-dimethylbpy]^{•-} is lower may be construed as indicative of a significant change in spin-orbit coupling upon removal of the protons in the 5,5' positions of bipyridyl, however as can be seen from Equation 5.5 this is not necessarily the case;^[146]

$$g_{iso} = g_e \left(\frac{a^2 n \lambda}{\Delta E} \right) \quad (5.5)$$

where g_e is the free electron g-value, a is a covalency parameter, λ is a spin orbit coupling constant and ΔE is the energy gap to the excited state.

The $\text{Mo(CO)}_4\text{bpy}$ in NMP (10 mM) gave a strongly coloured deep red solution however the $\text{Mo(CO)}_4[5,5'\text{-dimethylbpy}]$ was yellow in the same solvent and concentration, indicating differing energy gaps between ground and excited state between the two complexes. The potentials required in order to generate the radicals were different with the $\text{Mo(CO)}_4[5,5'\text{-dimethylbpy}]^{\bullet-}$ requiring -2 V compared with -1.7 V for the $\text{Mo(CO)}_4\text{bpy}^{\bullet-}$ vs. the employed silver wire pseudo-reference electrode. The difference in energy is affected by the stabilisation offered by the solvent, as seen through solvatochromism and the variation in redox potentials upon moving solvents. It is reasonable that the incorporation of methyl groups into the complexed bpy ligand could lead to significant alteration in the solvent interactions with this group.

This difference in energy gap is therefore likely to have affected the g_{iso} values observed rather than spin-orbit coupling effects.

It is interesting that the coupling effect of this proton shows a much larger effect on the spectra than ligation of the bipyridyl group or exchange of the metal centre.

5.2.3. Addition of CO₂ to the System;

Having successfully gathered the spectral responses expected for the various anionic radical species in the absence of CO₂, the EPR response of Mo(CO)₄bpy^{•-} in the presence of CO₂ was investigated.

When the applied potential corresponded to the first reduction of the Mo(CO)₄bpy in the absence of CO₂ a strong signal was detected from 10 mM molybdenum complex electrolyte system very quickly (spectrum shown in Figure 5.13), however when the system was saturated with CO₂ this radical was no longer detectable.

The applied potential was varied over a wide negative range and reduced temperature measurements trialled however, even at temperatures as low as 240 K no radicals, complex based or otherwise, were detected.

This supports the idea that the unpaired electron is transferred from the [Mo(CO)₄bpy]^{•-} to the CO₂ molecule and also suggests that this transfer is rapid as no adduct or radical is detectable via EPR.

Once the electron is transferred to CO₂ in solution to generate CO₂^{•-} this radical is rapidly lost forming CO₂ reduction products. The carbon dioxide anionic radical is very reactive with low stability and not detectable in solution without the employment of a spin trap or stabilised by adsorption^[146] so the absence of this spectrum in the spectroelectrochemical system was expected.

When the CO₂ saturated Mo(CO)₄bpy system was left running over 72 hours a signal was eventually generated however it is likely that this may be related to the loss of CO₂ from the solution both through its consumption in the

electrocatalytic reduction, but also due to escape from the cell over the lengthy time period. The response can be seen below in Figure 5.23 alongside the $\text{Mo(CO)}_4\text{bpy}^{\bullet-}$ generated in approximately 3 minutes in the absence of CO_2 .

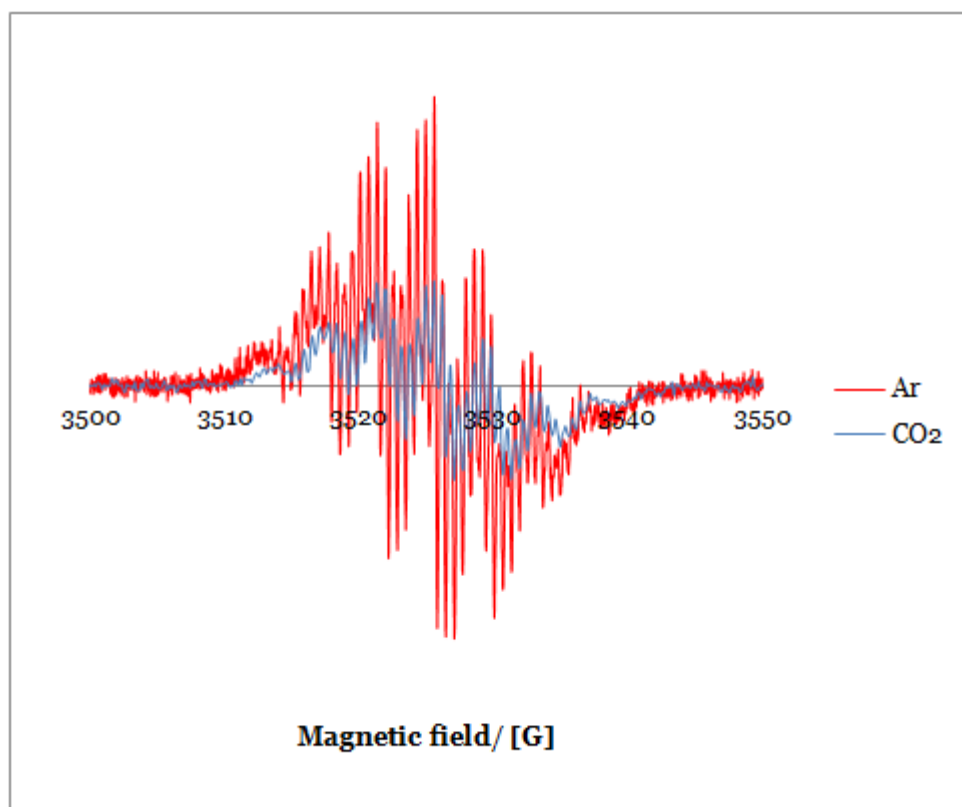


Figure 5.23; EPR spectrum of electrogenerated $\text{Mo(CO)}_4\text{bpy}^{\bullet-}$ in 0.1 M TBABF₄ in Ar/ CO_2 saturated NMP, $\text{Mo(CO)}_4\text{bpy}$ (10 mM) -1.7 V (vs Ag wire) applied Pt wire WE at RT. Mod. Freq: 100 kHz, Mod Amp:1.0 G, X-band frequency: 9.878 GHz

The signal generated after the prolonged reduction is clearly that of $\text{Mo(CO)}_4\text{bpy}^{\bullet-}$, indicating that despite having been employed as a catalyst for a long period the complex shows no evidence of any significant alteration in structure.

The analogous introduction of CO_2 to the $\text{W(CO)}_4\text{bpy}$ and bipyridine system had the same result, no radicals were detected. The currents seen for the chronoamperometric reduction process in the presence of CO_2 tended to be higher than in its absence as would be expected for the electrocatalytic CO_2

reduction process. However, as the electrode was changed regularly and the exact working area exposed may have altered each time, this effect was not investigated quantitatively.

5.2.4. Solvent Effects;

Another interesting observation made whilst implementing the *in situ* EPR spectroelectrochemical set up was the difference seen in the different solvents.

Both THF and NMP were initially investigated, however in THF the expected analyte radicals were not detected despite numerous attempts even at reduced temperature.

The EPR spectrum of $\text{Mo}(\text{CO})_4\text{bpy}^{\bullet-}$ has been previously reported in THF at room temperature^[119] suggesting that the mono-reduced molybdenum species is stable over the time scale needed for measurement however the spectrum consistently attained was that of a much simpler radical shown in Figure 5.24.

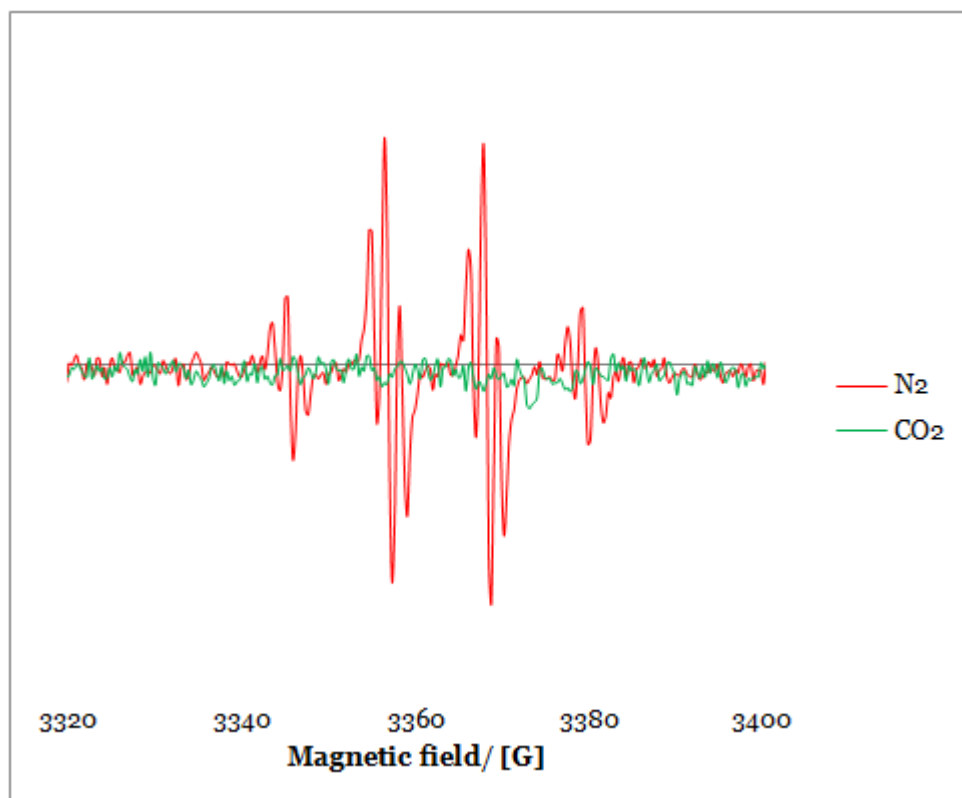


Figure 5.24; EPR spectrum generated upon application of -2.0 V (vs Ag wire) in 0.1 M TBABF₄ in N₂/CO₂ saturated THF, Mo(CO)₄bpy (10 mM) applied Pt wire WE at RT. Mod. Freq: 100 kHz, Mod Amp:0.30 G, X-band frequency: 9.438 GHz

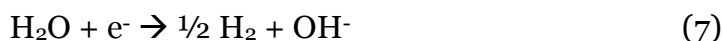
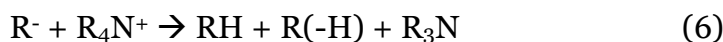
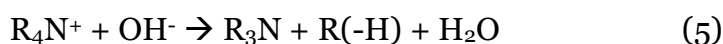
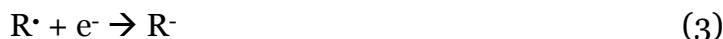
The spectrum attained was only seen in the absence of CO₂ leading to the conclusion that the radical formed either interacts with CO₂ or the saturation of the electrolyte solution removes the impurity responsible for the generation of the signal. In the absence of an applied potential no signal was generated.

The EPR spectrum given in Figure 5.24, from modelling undertaken, is a 1:3:3:1 quartet corresponding to an electron environment where coupling to five spin $\frac{1}{2}$ nuclei has occurred. The identity of these nuclei is however not clear.

Oxygen, a likely contaminant, has spin $\frac{3}{2}$ and any superoxide formed would be expected, like CO₂•⁻, to react rapidly therefore, under the experimental conditions employed, be undetectable.

If however the superoxide radical reacted to form a more stable radical this could be detectable, possibly reacting with the electrolyte, TBABF₄.

Tetrabutylammoniumsuperoxide has been reported as a stable species in several aprotic solvents ^[53] however THF was not been listed among them. The reduction of TBA⁺ is not expected until significantly more negative potentials than those applied, however it has been reported to act as a proton donor at potentials prior to this through a Hofmann elimination type mechanism where a beta-hydrogen is attacked by a base to yield tributylamine and butene and, in the presence of trace water, butane.^[185] The reduction mechanism may be similar to that suggested for TBA⁺ reduction in scheme 5.1 below (adapted from [185]);



Where R= C₄H₈

Scheme 5.1; A possible electrolyte reduction pathways highlighting radical formation.

Through this mechanism there are two organic radicals formed; the tetrabutylammonium radical R₄N[•] in (1) and the subsequent butenyl radical R[•], from its decomposition in (2). The reduction given above, rather than being initiated by an electron transfer from the electrode, may be through the electron transfer of the superoxide radical. As well as the electrolyte there is also solvent

and analyte present from which the generation of different radicals is also possible.

The best fit structure for the source of the anomalous signal would appear to be an ethyl radical however this signal is unlikely to be observed, even at reduced temperature in the absence of spin-trapping. The spectra observed does not show any evidence of coupling to anything possessing $I > 1/2$ therefore the radical appears not to contain nitrogen ($I = 1$) leaving only R^\bullet from scheme 1 as a possibility. The limited literature reports of butenyl radicals show that this is in keeping with the spectrum observed.^{[186]-[188]}

The absence of a signal in the presence of CO_2 is consistent with superoxide playing a role in the unknown radical generation as, not only would the enhanced CO_2 solubility be able to more effectively remove trace oxygen, but O_2 had been previously reported to activate CO_2 ^{[165][199]} therefore, if formed would be expected to be lost rapidly in the presence of CO_2 as it reacted to form CO_2 reduction products.

The same maybe true of the butenyl radical species.

The fact that the $Mo(CO)_4bpy$ radical was not detectable in the THF system although very easily observed in NMP suggests that NMP may have stabilising effects upon the radical. This is plausible given its higher polarity compared with THF and the radical formed upon reduction of $Mo(CO)_4bpy$ is expected to be highly polar. There is another possibility however, more related to the ease of contamination of the solvent. THF being very volatile and prone to solvation of oxygen, is easily contaminated through use, particularly as it has a tendency to

dissolve plastics in its vicinity, and may have just not been suitable for use in a poorly sealable cell containing electrodes with a Teflon insulating layer.

Another possibility to consider, due to the cell set up is that the radical generated was not formed at the working electrode, but was formed through oxidation at the counter or auxiliary electrode. The cell set up was such that the three electrode wires were arranged to have the working electrode situated in the microwave cavity, however it is possible that oxidised species could have been formed at the counter and diffused up through the tube. This does not explain the lack of the expected signal, however no more time was spent investigating this anomaly.

5.3. The Effect of Working Electrode Material;

The vast majority of the voltammetric investigation of the $\text{Mo}(\text{CO})_4\text{bpy}$ complex has been measured using a gold working electrode.

Gold was selected from the array of possible working electrode materials for a variety of reasons, primarily its well definable surface.^{[77][78]} (see also 3.1.1.)

A clean gold surface gives a distinctive and clear voltammetric response when cycled in acid which, when incorporated into the electrode preparation regime allows the reproducibility of the electrode surface conditions and active working area of the electrode to be evaluated and quantified.^[191] CVs taken prior to and

post experimentation may be compared to assess electrode deactivation, alterations in surface roughness and monitor the presence of adsorbed species.

Direct CO₂ reduction has been shown, through extensive research conducted over many decades, to be strongly dependent upon the electrode material. Even slight differences in surface preparation of the electrode can have pronounced effects upon the potentials, mechanism and product distribution associated with CO₂ reduction. Differences in pre-experimental treatment of the working electrode can alter the atomic surface of polycrystalline material, such as the gold macro-electrode employed, potentially altering the adsorbed species and proportions of oxides present, surface roughness and the atomic surface make up. Differing single crystal faces possess different electronic characteristics and surface chemical reactivity. Therefore, significant deviations within the bulk electrode composition can be anticipated to impact upon any catalytic activity and the adsorption properties of the surface.^[8]

The addition of the molecular electrocatalyst to the system may be expected to negate surface dependence effects, however dependence on electrode surface identity tends not to be verified in publications. The assumption of independence was explored by measuring the same voltammetry on two additional commonly employed solid electrodes; platinum and glassy carbon. These electrode materials were not employed initially as both had potentially detrimental attributes for CO₂ reduction experiments.

Platinum, like gold, has an easily identifiable, well defined CV response in acid where oxide formation and stripping as well as hydrogen adsorption and desorption can be employed to quantify the surface area and absence of

adsorbed species and contaminants on the surface.^[79] Platinum is a catalytic material for many reactions lowering their activation energies through specific adsorption, however it is well known to strongly adsorb carbon monoxide, so much so that is employed in CO detection devices.^[189] CO desorption is energetically demanding, which can result in a deactivation of the surface. The presence of CO, or at least CO-like species, is considered highly likely during CO₂ reduction in a non-aqueous system therefore implementation of a platinum working electrode in this system introduces a significant risk of electrode deactivation and subsequent experimental challenges, as well as additional source of inaccuracy and inconsistency in measurements made.

Glassy carbon is a popular choice for electrode material. It is generally considered less active than platinum or gold, and is well suited to many applications, however the surface is much less easily definable compared with the metal electrodes discussed, with the mechanical polishing employed in electrode preparation unlikely to give identical surfaces due to the complex and changeable structure of glass-like carbon with the presence of more active “edge” carbons and functional groups (commonly phenyl, carboxyl and carbonyl) at the surface unavoidable. As well as the variable functionalisation of the electrode there is also evidence of changing morphology of the glassy carbon electrode surface upon application of a potential.

The biggest worry in employing a glassy carbon electrode in the CO₂ reduction system is the prospective product analysis. Differentiating the carbon based species possibly derived from the electrode and those formed from CO₂ would be challenging and may result in the misrepresentation of product distributions and efficiencies. Another consideration to be made is the possibility of

sequestration of the CO₂ into, and reaction with, the glassy carbon itself, with a dense polycarboxylated species formed in a non-aqueous CO₂ saturated solution having been recently reported upon application of reductive current.^[190]

In order to minimise the influence of variables other than electrode material (such as analyte concentration, solvent purity etc), the freshly prepared electrodes were employed in rotation in the same solution, positioned in the same manner within the cell.

5.3.1. Mo(CO)₄bpy Stability at Varied Electrode Materials;

The same CV response was therefore anticipated for each of the electrodes employed, particularly for the argon degassed Mo(CO)₄bpy solution, however as seen in figure 5.25 this was not observed to be the case.

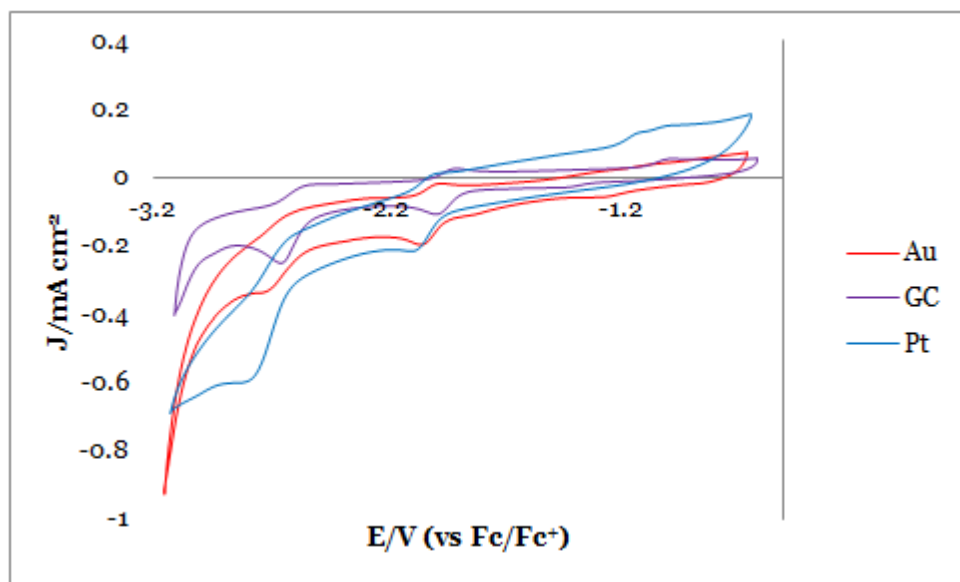


Figure 5.25; CV response plotting current density vs. applied potential of 0.5 mM Mo(CO)₄bpy in cell 1, measured at Au, Pt (d= 2 mm) and GC WE (d= 3 mm). Scan rate employed was 200 mV s⁻¹.

The voltammetry measured at the platinum electrode, the blue trace of figure 5.25, appears more resistive and shows increased background current or capacitance compared to the response observed on the gold and most significantly in contrast to the very flat glassy carbon CV. This contributes to the overall effect of the $\text{Mo(CO)}_4\text{bpy}$ redox features being considerably less well defined than when the other electrodes are employed, however in addition to the extrication challenges the background current introduces, the redox processes of the $\text{Mo(CO)}_4\text{bpy}$, particularly the re-oxidative peaks, do not seem to occur to the same degree as on Au and GC.

Platinum is a noble metal, therefore unreactive however as previously mentioned is catalytic for an array of processes due to its adsorption abilities. The lessened degree to which the expected $\text{Mo(CO)}_4\text{bpy}$ redox processes are observed may be due to the destabilisation of the complex through adsorption on the electrode surface in an arrangement which results in the complex, or reduced complex formed, being less stable than during the equivalent process on Au or GC.

A possible explanation for this may be related to the known affinity of Pt and CO, a constituent of the tetracarbonyl complex. This affinity may result in the $\text{Mo(CO)}_4\text{bpy}$ being orientated as depicted in the schematic figure 5.26 (a);

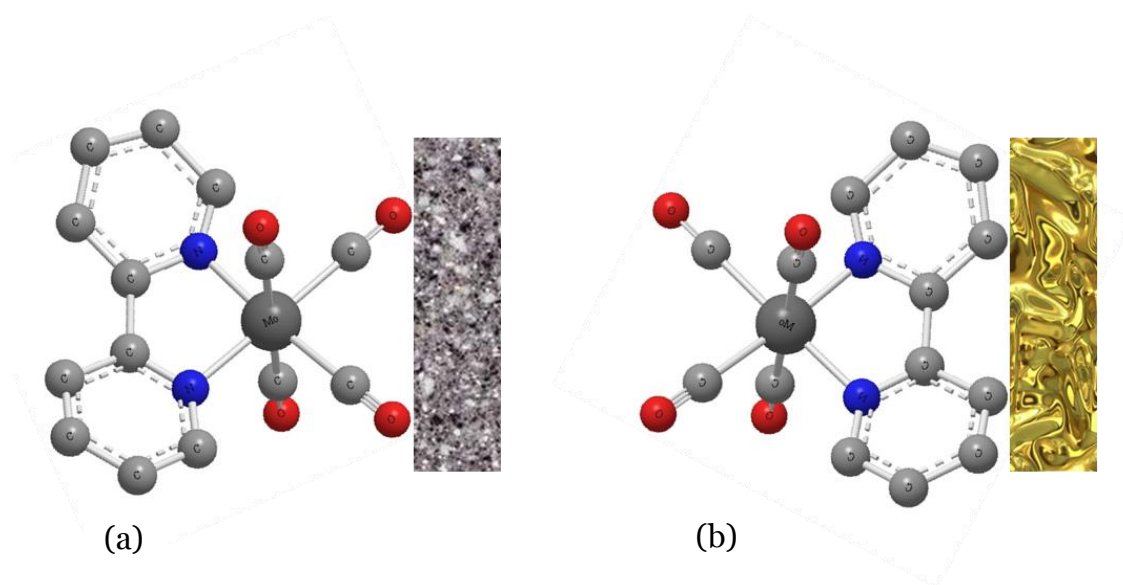


Figure 5.26; Schematic depicting possible $\text{Mo(CO)}_4\text{bpy}$ -electrode orientations.

In figure 5.26 (a) the CO groups of the $\text{Mo(CO)}_4\text{bpy}$ are closest to the electrode, possibly adsorbed, with the orbital in which the extra electron density is localised upon the one electron reduction furthest from the surface. If this arrangement were adopted, necessitating the transmittance of electron density through the whole complex, it could result in the destabilisation and relatively hindered electron transfer process.

Gold has a reported affinity for bipyridine,^{[171]-[174]} possibly preferring an adsorption mode similar to that depicted by figure 5.26 (b) where the orbital in which the electron density is localised upon reduction is closest to, possibly adsorbed on, the electrode surface negating the possible destabilising electron transmittance in order to form the expected anionic radical species.

The glassy carbon CV, shown in purple in figure 5.25, showed a considerably larger and flatter negative potential window. This is attributed to the less active nature of the GC compared with the Au and Pt, resulting in enhanced stability of the electrolyte and solvent at the electrode surface.

All of the $\text{Mo(CO)}_4\text{bpy}$ reduction features are seen clearly in the voltammetry employing the glassy carbon electrode over all of the potential ranges trialled, there is however an oxidative feature expected which is consistently absent; the reoxidative peak thought to be associated with the tricarbonyl species.

As previously discussed, upon application of potentials in excess of the second reduction, when investigating $\text{Mo(CO)}_4\text{bpy}$ behaviour at a gold electrode, an oxidative peak emerges between those associated with the oxidation of the dianion and that of the monoanionic radical.

From figure 5.27 however, where potential excursions to values significantly more negative than the $[\text{Mo(CO)}_4\text{bpy}]^{2-}$ formation potential were performed, no new peak was observable on the back scan.

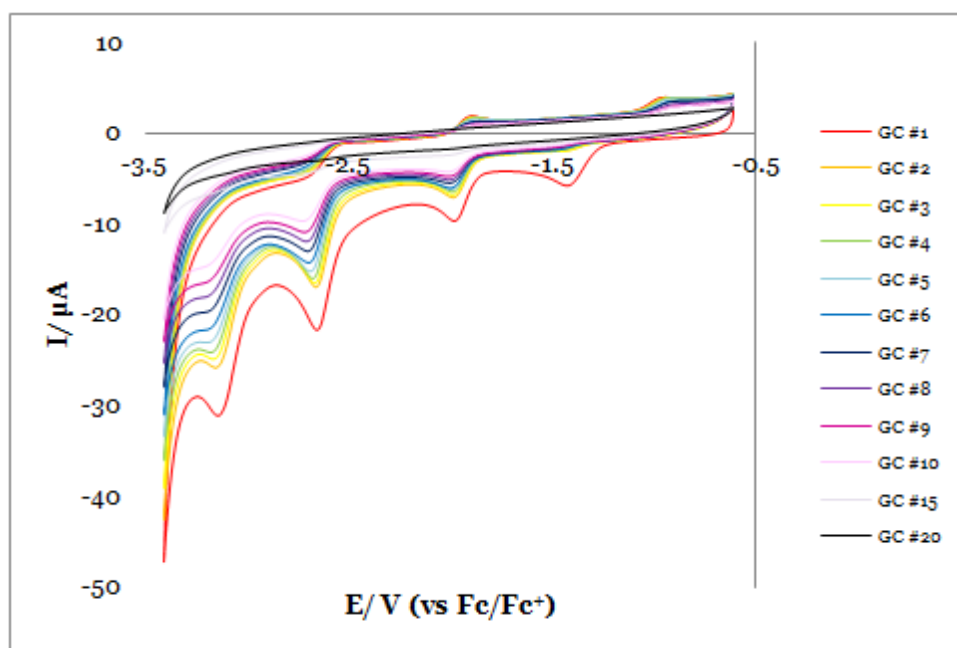


Figure 5.27; CV of 0.5 mM $\text{Mo(CO)}_4\text{bpy}$ in cell 1 except measured at GC WE ($d = 3$ mm). Scan rate employed was 200 mV s^{-1} . #1-#20 successive scans plotted.

As can be seen upon inspection of the oxidative response in the region of interest (between approximately -2 and -2.5V) no oxidation is seen suggesting

the formation of the tricarbonyl species (or other intermediate structure responsible for this peak) does not occur on GC, or that the tricarbonyl species is not electroactive in this system. This apparent electro-deactivation could be due to limited stability or the lack of specific adsorptive properties offered by the glassy carbon when compared with the gold surface, resulting in the tricarbonyl not being available at the electrode for reoxidation.

What is very significant over this potential range is the loss of features with repeat cycles. The first scan shown in figure 5.27 in red, shows four reductions, the first of which being oxygen reduction, only seen on the very first scan, followed by three reductions. These three reductions appear to correlate well to those observed on Au; formation of the anionic radical, the formation of the tetracarbonyl dianion and the third reduction, associated with the generation of the tricarbonyl species, which is linked on gold to the introduction of the new oxidation.

On glassy carbon this oxidation is not seen and the current drops with each cycle to the point where after just twenty cycles at 200 mV s^{-1} , no complex response is observable (shown in black on figure 5.27). If the potential is not taken as negative as the third complex associated reduction the voltammetry (stopping at ca. -3 V), is much less significantly influenced by consecutive cycling on GC as seen in figure 5.28.

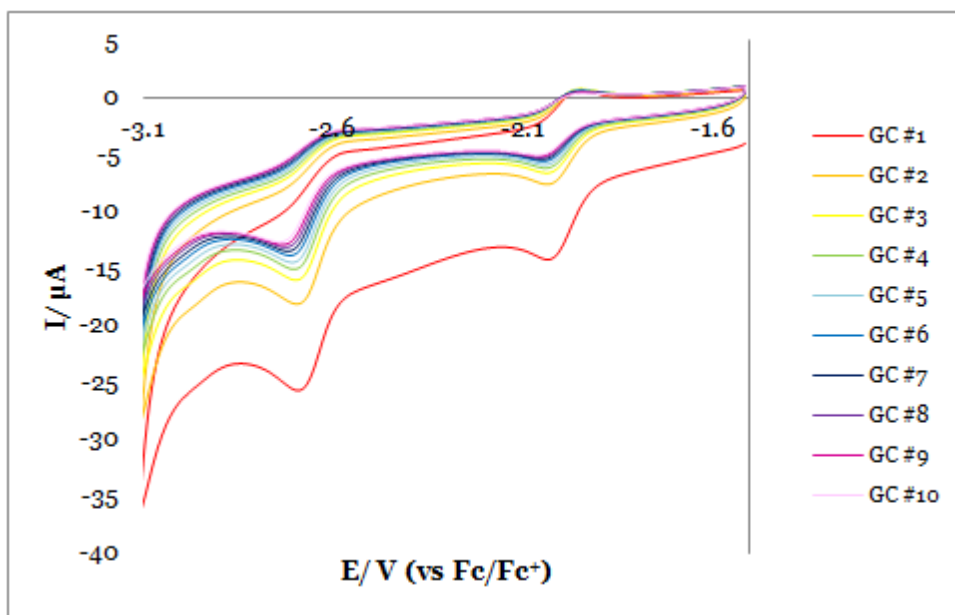


Figure 5.28; CV of 0.5 mM $\text{Mo(CO)}_4\text{bpy}$ in cell 1 except measured at GC WE ($d = 3$ mm). Scan rate employed was 200 mV s^{-1} . 1st scan indicated by the dashed line. #1-#10 successive scans.

The deviation in current response between the first and subsequent scans, although significant shows, a very small change in the reductive current associated with the complex reduction, instead showing a large drop in the background current. This is presumably due to reduction of impurities in solution and on the electrode surface. The drop in complex peak current at the second reduction between scan #1 to #10 is approximately 15% for figure 5.28 where the most negative vertex potential is -3.1 V. For the same reductive peak current drop, between scan #1 to #10, when the negative potential range is extended to include the third reduction over 50% of the current was lost (figure 5.27).

Figure 5.29 shows voltammetry gathered over a similar negative potential range but at a slower scan rate and for three times as many scans, at a gold electrode.

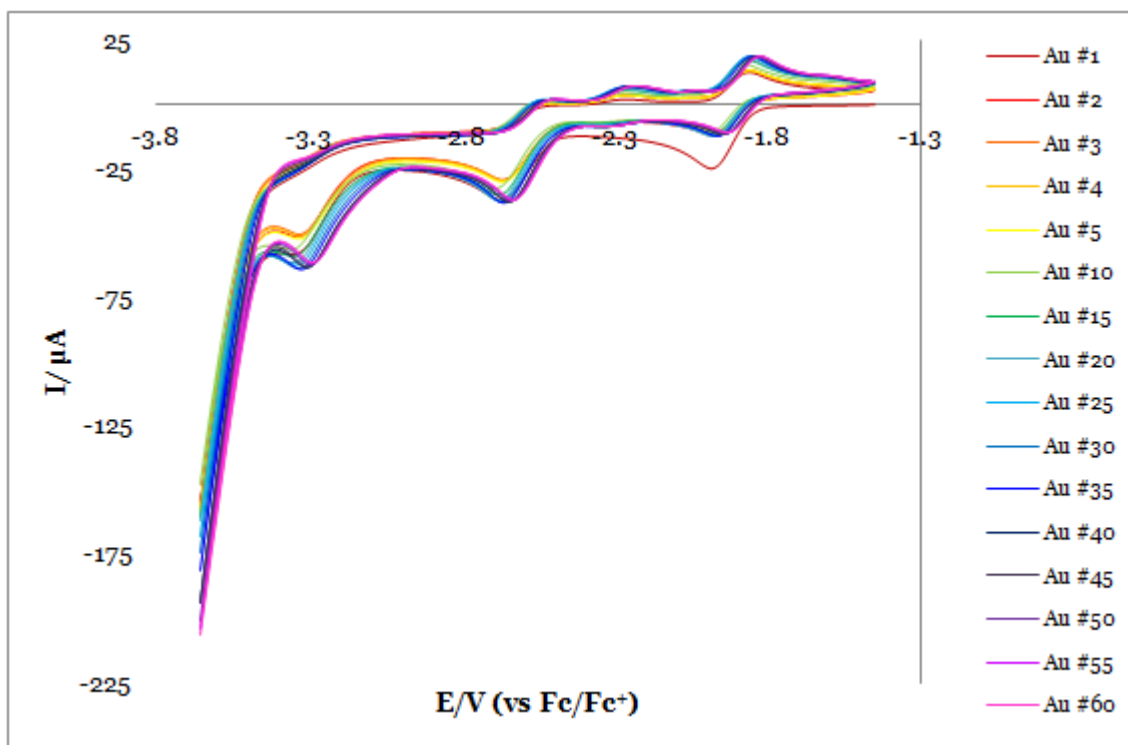


Figure 5.29; CV of 0.5 mM $\text{Mo(CO)}_4\text{bpy}$ in cell 1 (measured at Au WE ($d= 2$ mm)). Scan rate employed was 100 mV s^{-1} .

The higher number of scans and slower scan rate would be expected to make any side reactions and deactivation more pronounced in this voltammetry but as shown there is no loss in the $\text{Mo(CO)}_4\text{bpy}$ related features with a slight enhancement with scan observable in some of the processes.

One of the aspects not fully understood from analysis of the $\text{Mo(CO)}_4\text{bpy}$ system on Au was how the tricarbonyl species and the lost CO could recombine, regenerating the tetracarbonyl starting material, as logic would suggest that CO would be lost into the bulk solution, possibly even from the solution altogether, upon generation due to the concentration gradient and its low solubility in the solvents employed. This idea of loss of $\text{Mo(CO)}_4\text{bpy}$ as the tricarbonyl is formed appears to fit with what is observed with the voltammetry measured at glassy carbon. This offers support to the proposed idea that the $\text{Mo(CO)}_3\text{bpy}$ species

and CO generated upon reaching the third reduction potential are specifically adsorbed at the Au electrode allowing for re-complexation of the labile CO which, upon the GC surface is not the case.

Scanning of the potential over a similar range on the platinum electrode for comparison proved challenging as peak definition was rapidly lost upon application of potentials below -2.5 V, as seen in figure 5.30.

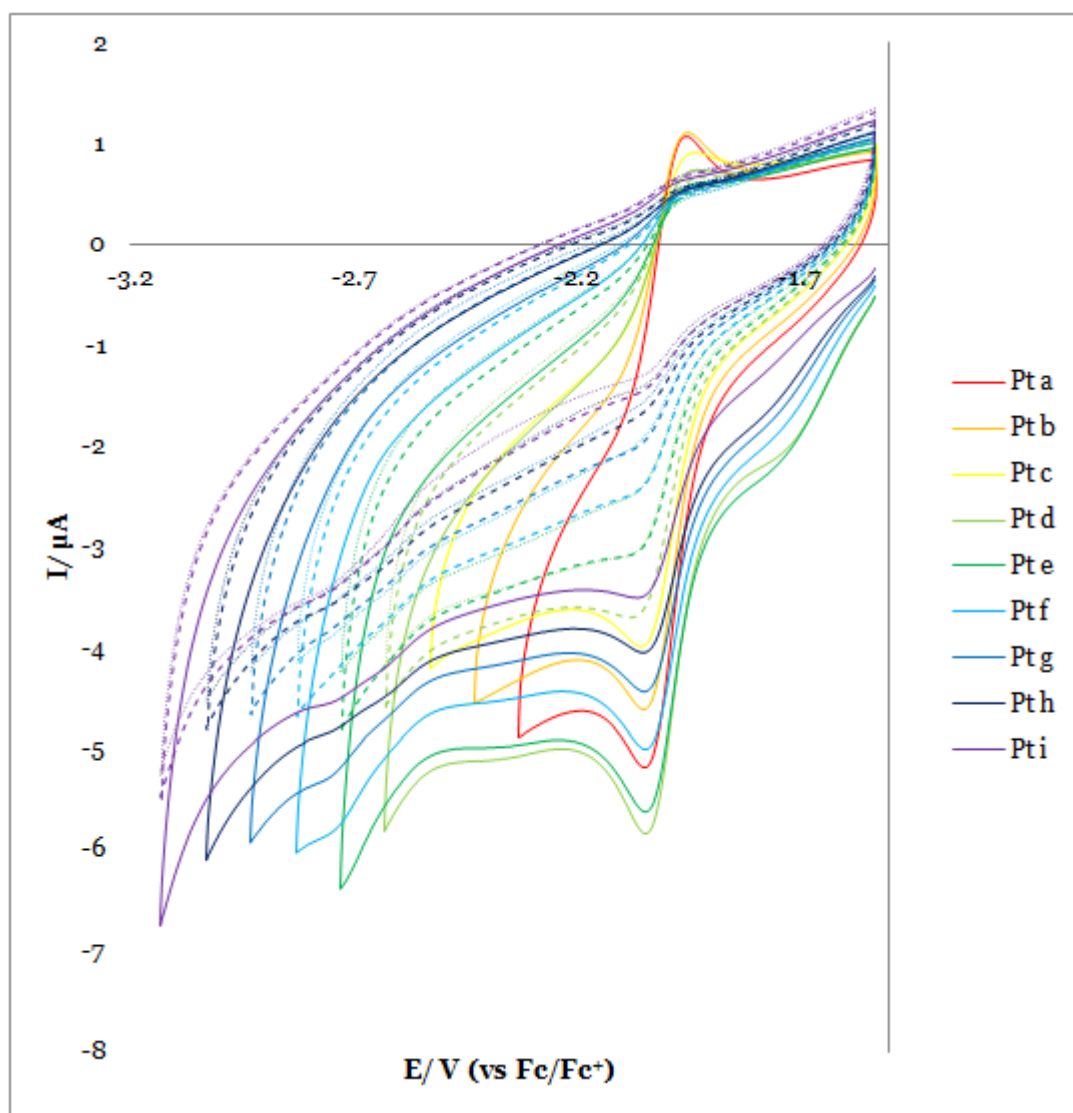


Figure 5.30; CV of 0.5 mM Mo(CO)₄bpy in cell 1 except measured at Pt WE (d= 2 mm). Scan rate employed was 200 mV s⁻¹ with varied negative vertex potentials. 1st scan shown by solid lines with subsequent scans shown in dashed and dotted lines.

Figure 5.30 shows a series of CV measurements made utilising the same initial potential, just prior to the first $\text{Mo(CO)}_4\text{bpy}$ redox process, and scanning to increasingly negative vertex potentials measuring three scans at each range.

For the potential ranges a, b and c of figure 5.30, where the scan is reversed before the second reduction of $\text{Mo(CO)}_4\text{bpy}$ is observed, the three scans overlaid well with the first redox peaks, related to $\text{Mo(CO)}_4\text{bpy}^\bullet$ formation and reoxidation, clearly discernable. For the potential range d, after the initial first reduction is observed as anticipated, the beginnings of the second reduction is reached. Once this process begins to occur, upon reversal of the potential sweep direction the $\text{Mo(CO)}_4\text{bpy}^\bullet$ reoxidation peak previously present at ca -2 V, is no longer seen as a distinctive feature in the voltammetry, instead of the peak there is more of a “hump”. The second and third scans measured over this same potential range, shown by the dashed and dotted lines respectively, measured directly afterwards show a pronounced drop in current associated with the first reduction, with peak current approximately a third lower than that seen on the initial scan.

Upon scanning more negative this current drop at the first reduction between the first and subsequent scans reaches a point where almost two thirds of the current seen on the initial scan is lost by the second, as illustrated in figure 5.31.

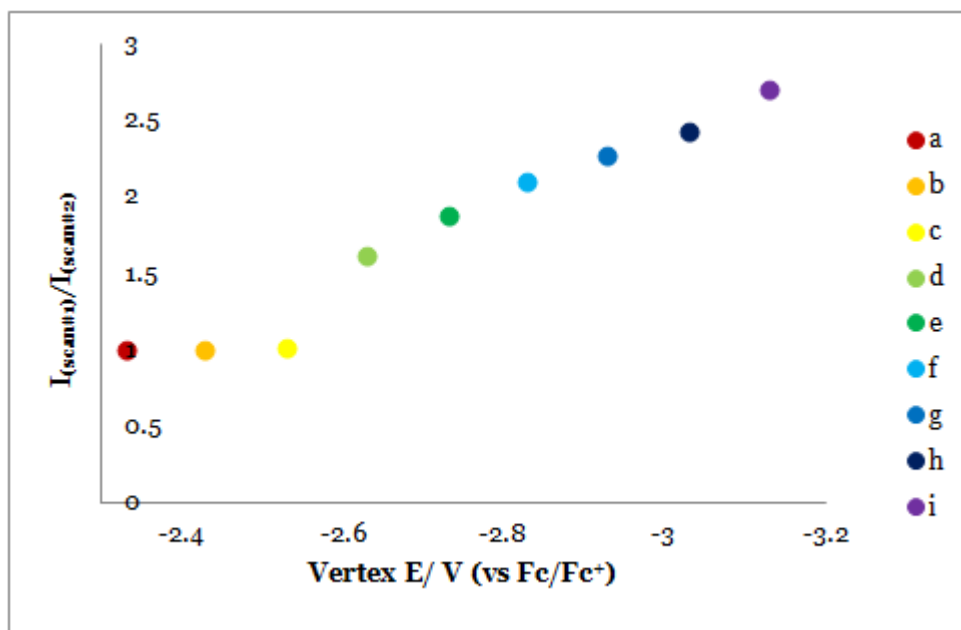


Figure 5.31; Plot showing the ratio of peak currents associated with the first reduction of Mo(CO)₄bpy for the first and second scans ($I_{p(\text{scan}\#1)}/I_{p(\text{scan}\#2)}$) as a function of negative vertex potential on Pt. Corresponding voltammetry is given in figure 5.30.

By the time the measurements involving application of -3 V are reached, scans two and three show features so indistinct they are barely discernible against the capacitive background current. Possible reasons for this behaviour are two fold with destruction of the analyte and the deactivation of the working electrode surface both likely and interdependent, with the destruction of Mo(CO)₄bpy yielding CO, responsible for the deactivation. The electrode deactivation appears to show a potential dependence as once the system is allowed to return to the positive open circuit potential for a few seconds the redox features are once again observable. This is in keeping with CO adsorption as this would only be anticipated to occur at potentials negative of the potential of zero charge.^{[192][193]}

Time spent at the open circuit potential would also allow the diffusion of fresh analyte to the electrode surface.

Despite the apparent stability of the first redox process of $\text{Mo(CO)}_4\text{bpy}$ on platinum from figure 5.30, when this small range was subject to more repeated scans ($\times 100$), the features were lost as can be seen in figure 5.32.

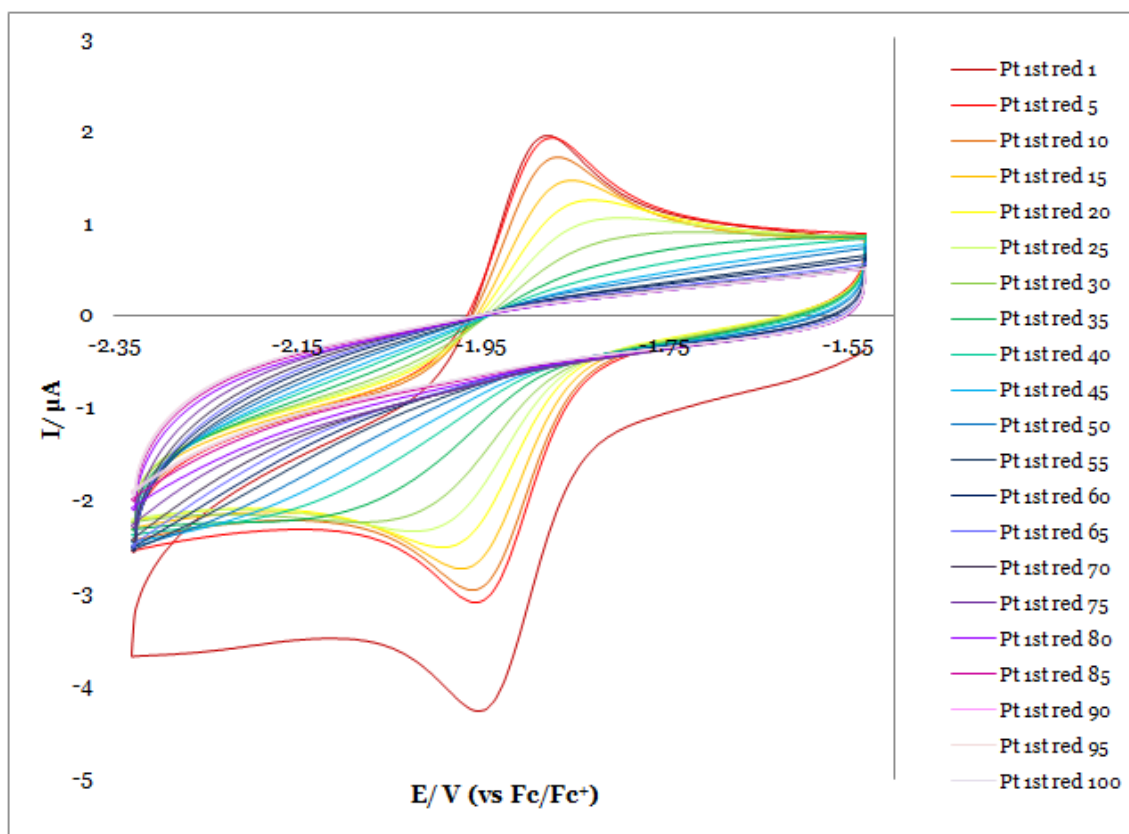


Figure 5.32; CV of 0.5 mM $\text{Mo(CO)}_4\text{bpy}$ in cell 1 except measured at Pt WE ($d= 2$ mm). Scan rate employed was 200 mV s^{-1} for 100 consecutive scans with every 5th plotted.

This loss of peaks, despite the more modest potential range employed tends to suggest that there is an element of time dependence to the deactivation. Each of the scans took a measurement time of approximately 8 s therefore each of the CV's plotted above were measured at an interval of approximately 40 s. In figure 5.30 however, the largest potential range took just 16 s to collect data for and between the first and second CV measurement, but despite this there is a much more significant current drop than observed in figure 5.32. This implies that the

application of extreme potential impacts much more upon the electrode deactivation than simply time. The absolute current for the reduction and re-oxidation seen in figure 5.32 are plotted as a function of scan number in figure 5.33.

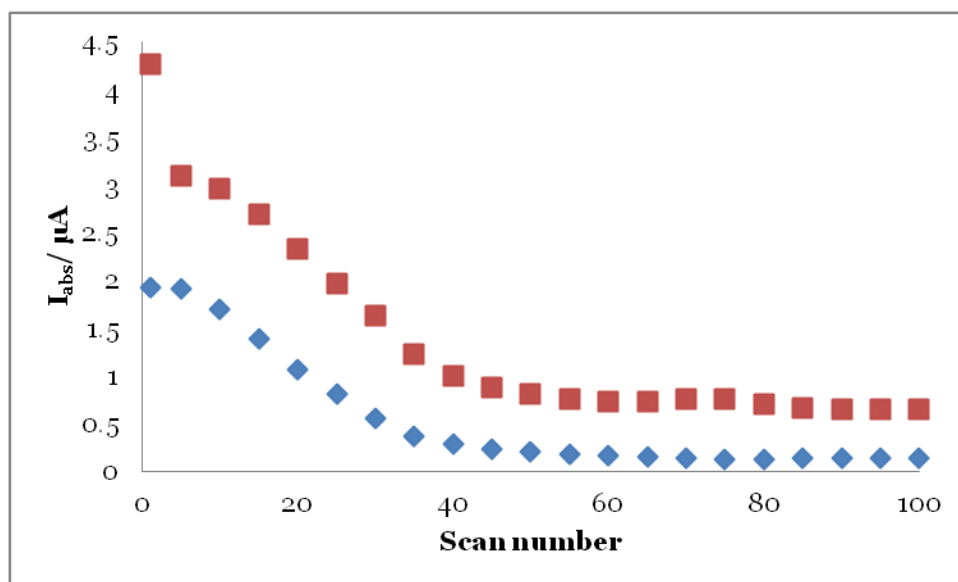


Figure 5.33; Absolute current for the $\text{Mo}(\text{CO})_4\text{bpy}$ reduction (red) and subsequent reoxidation (blue) as a function of scan number. Corresponding CV Figure 5.32.

From figure 5.33, the reductive current appears significantly higher than the corresponding reoxidation despite the reversible appearance of the CV in figure 5.32. This additional reductive current seen is due, to a significant degree, to background current, accurate subtraction of this feature proved challenging due to the movement of the baseline with successive scans. The absolute currents presented in figure 5.33 are instead the peak currents taken directly from the voltammetry with no corrections made. The reductive (red) and oxidative (blue) responses appear to show a similar curve, just offset by between 5 to 13 μA . The trend seen in the plot shows clearly the deactivation of the electrode with scan number with the drop in reductive current mirrored by the drop in reoxidation

which, initially decreases considerably with scan (#1 to #45), but later settles to a relatively constant response (#45 to #100). From the CV (Figure 5.32), scan #40 is the last point in the measurements where the peaks associated with the $\text{Mo}(\text{CO})_4\text{bpy}$ have definition and in subsequent scans are no longer discernible from the background. The difference in current between the reductive and oxidative responses does change with scan. Scan #1 shows an anomalously high reduction, which is a fairly common feature on the first scan of a set and is attributed to the reduction of any contaminants on the electrode or in the solution. Scans #5 to #25 show a high ΔI of $\sim 12 \mu\text{A}$, which drops in later scans. This particularly high region could be, in part, related to a lack of reversibility of $\text{Mo}(\text{CO})_4\text{bpy}$ with the disparity between I_{red} and I_{ox} more apparent in this region where the complex response is clearest and electrode relatively fresh. Scans #30 to #45 show a higher degree of change in ΔI with scan with it dropping from $11 \mu\text{A}$ to $6 \mu\text{A}$. This could be attributed to the build up of the deactivating species, now present in a high enough concentration to have the most pronounced effect on the electrode surface. Scan #50 onward show no significant change, possibly as by this point the deactivation is significant, with only slight further losses in the CV current possible. The CO adsorption related deactivation seems a likely culprit with the initial few cycles perhaps generating CO through loss of carbonyl from the complex, which once accumulated result in the deactivation of the platinum surface.

On a gold working electrode, aside from the drop between the anomalously high first scan (probably due to the impurities introduced to the solution upon the exchange of the electrodes being reduced) it can be seen in figure 5.34, that

repetitive cycling over the first redox process shows much less variation and ultimately, no significant deactivation.

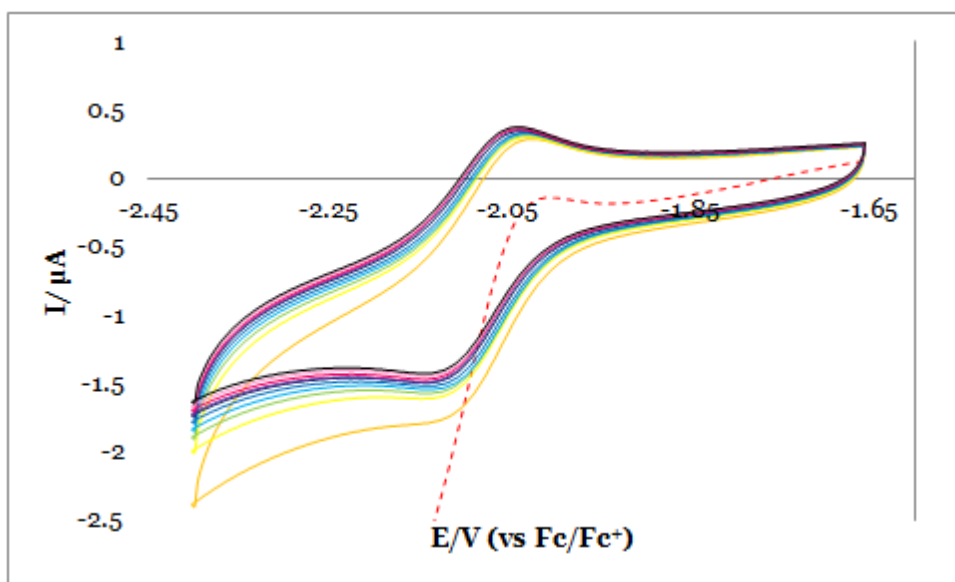


Figure 5.34; CV of 0.5 mM $\text{Mo(CO)}_4\text{bpy}$ in cell 1 (measured at Au WE ($d=2$ mm)). Scan rate employed was 200 mV s^{-1} for 100 consecutive scans with every 10th plotted.

Using the data collected for the first scans of the voltammetry gathered employing each of the different electrodes the effect of the electrode material on the peak separation, apparent diffusion coefficient and reversibility of electron transfer were investigated.

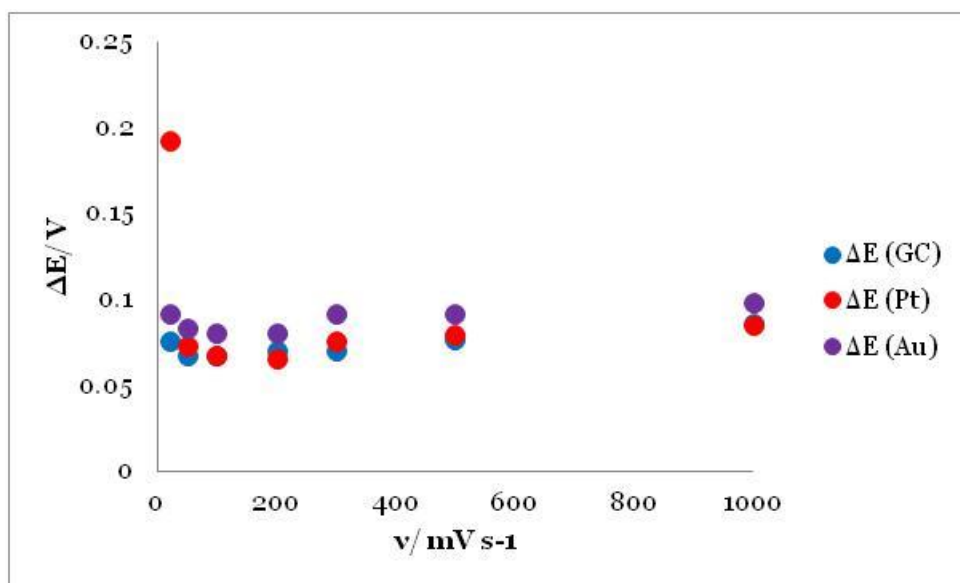


Figure 5.35; A plot showing the peak separation as a function of scan rate for the first redox peaks of $\text{Mo}(\text{CO})_4\text{bpy}$ measured at GC, Pt and Au electrodes

The peak separations of the $\text{Mo}(\text{CO})_4\text{bpy}$ redox couple studied were fairly constant for all of the differing electrodes at all of the scan rates trialled varying between 65 and 80 mV for the bulk of measurements made (see figure 5.35), which is of the order of magnitude anticipated for a one electron transfer in the NMP system. The measurements made at 20 mV s⁻¹ and 1000 mV s⁻¹ showed a degree of deviation, however, the voltammetry associated with these points was atypical; in the case of the slowest scan rate the CV measured was seen to be somewhat less than reversible, particularly on the platinum surface with the peak separation over double that expected. The doubling of the peak separation is perhaps indicative of an electron transfer greater than one which is in keeping with the destabilisation and complex destruction on platinum determined earlier, where multiple electron transfer may occur. The measurements made at the highest scan rate are subject to more resistive effects than those seen at slower scan rates which tends to result in an increase in peak separation,

particularly in non aqueous systems which tend to be prone to heightened resistivity as a result of the increased viscosity and lower polarity.

The peak separations showed no evidence of significant adsorption of the analyte species as none of the values dropped significantly with the measurements made at the platinum electrode, considered to be the most likely to exhibit significant adsorption characteristics, as platinum showed slightly larger ΔE values; the opposite of the expected lowering of ΔE anticipated for an adsorbed redox species.^{[60][141]}

The data plotted in figure 5.36 shows the peak current for the first reduction of Mo(CO)₄bpy at the various electrode materials as a function of the square root of scan rate.

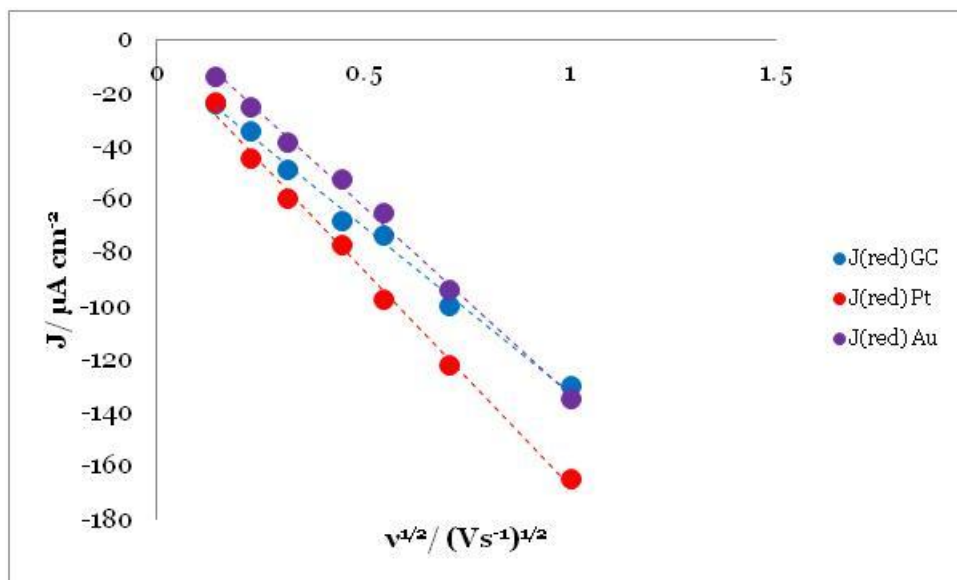


Figure 5.36; A Randles-Sevcik plot showing the current density as a function of the square root of the scan rate for the first redox peaks of Mo(CO)₄bpy measured at GC, Pt and Au electrodes.

The data points for each electrode show excellent linear correlation with the r^2 values consistently above 0.99. The Randles-Sevcik equation (2.6) allowed the

determination of the diffusion coefficients resulting in D values within $0.5 \times 10^{-6} \text{ cm}^2 \text{ s}^{-1}$ of each other, as would be expected for measurements made in the same solution, values for which can be found in table 5.5.

Electrode material	$D_{[\text{Mo}(\text{CO})_4\text{bpy}]} / \times 10^{-5} \text{ cm}^2 \text{ s}^{-1}$
Glassy Carbon	0.9 ± 0.005
Gold	1.1 ± 0.004
Platinum	1.4 ± 0.006

Table 5.5; Diffusion coefficient of $\text{Mo}(\text{CO})_4\text{bpy}$ in NMP calculated from the Randles-Sevcik plot for GC, Pt and Au electrodes.

The D value determined for the $\text{Mo}(\text{CO})_4\text{bpy}$ when the glassy carbon electrode was employed was found to be slightly lower than that seen for the corresponding value on gold, with the value measured at platinum slightly higher still.

The final comparison of the $\text{Mo}(\text{CO})_4\text{bpy}$ voltammetry in the absence of CO_2 is the degree of reversibility observed at the different surfaces, shown in figure 5.37 where the current ratio (of oxidative and reductive current) is plotted against scan rate employed for the three different electrodes.

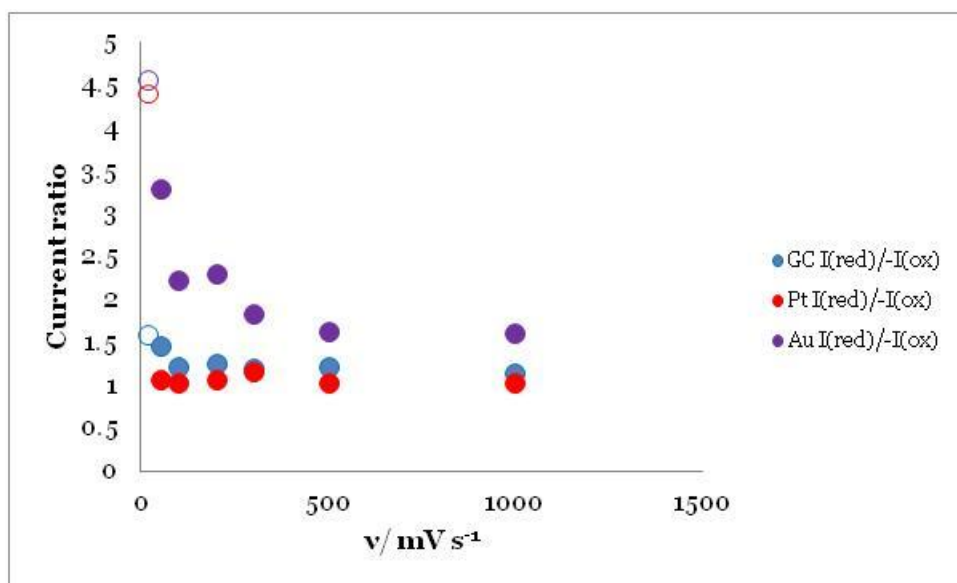


Figure 5.37; The ratio of peak currents (reductive/-oxidative) for the first redox process of $\text{Mo}(\text{CO})_4\text{bpy}$ vs. scan rate at GC, Au and Pt WE. The open circles highlight the current ratio seen at the lowest scan rate sampled, 20 mV s^{-1} . First scan.

From the voltammetry collected in the same solution at the different electrodes the reversibility of the first redox process in $\text{Mo}(\text{CO})_4\text{bpy}$ reduction can be seen to vary, not just with scan rate, but also with the differing electrode material.

In a surprising alteration in behaviour, figure 5.37 shows the gold surface yields the least reversible voltammetry. This is in complete disagreement with figure 4.3 of the $\text{Mo}(\text{CO})_4\text{bpy}$ chapter(4), where the peak current ratio for this process remained constant at unity over all of the scan rates employed (of which the range was greater). In contrast, platinum, expected to show a degree of deviation from reversibility appears to be, in the most part, the closest to reversible.

The reasons for this are two-fold; the behaviour of $\text{Mo}(\text{CO})_4\text{bpy}$ at the various electrodes has already been shown to differ. On gold, a common feature is an enhancement in current on the first scan which settles to give a more reversible

and reproducible CV upon subsequent scans in contrast to platinum and glassy carbon where the first scan gives a reasonably reversible response which is lost to varying extents (dependent upon potential range and time spent scanning) upon later scans. Given that figure 5.37 is offering a comparison of the first scans this would offer the best chance of observing reversibility at platinum and glassy carbon, however it includes the addition reductive current for gold.

The other factor to consider is the experimental design. The same solution was used for all of the measurements made meaning the cell was not kept sealed throughout as the working electrodes were regularly exchanged. This may lead to the introduction of significantly more oxygen and other contaminants than would be expected in a typical experiment which, although presumed to be present to similar degree for all measurements and was kept to a minimum by flushing the headspace with argon, may well affect the voltammetry differently when different electrode materials are employed.

What is evident from this plot is that at very low scan rates under the conditions employed only the voltammetry measured at the glassy carbon electrode showed a reasonable degree of reversibility. This is highlighted on figure 5.37 by the open circles with those representing the Pt and Au points showing over four times as much reductive current than re-oxidative when the CV scan rate is 20 mV s⁻¹. The fact that the huge reductive enhancement compared to the oxidative is only seen on the metal electrodes could be due to either the metals being more sensitive to the presence of trace oxygen contamination of the solution or the [Mo(CO)₄bpy]⁻ being less stable at the electrode surface.

From inspection of the voltammetry from which the data was gathered to construct figure 5.37 the former seems true of the gold surface but the latter seems more plausible for the platinum. The stability of the radical at Pt has already been established to be low over longer time periods and this is observable in the voltammetry with the Au system showing a clear $[\text{Mo}(\text{CO})_4\text{bpy}]^{\cdot-} \rightarrow [\text{Mo}(\text{CO})_4\text{bpy}]$ peak which is completely absent in the platinum voltammetry at this low scan rate. For the rest of the GC and Pt points of figure 5.37 a reasonable degree of reversibility is observed, particularly upon application of the more moderate scan rates (100-500 mV s⁻¹).

5.3.2. The Addition of CO₂ to the Mo(CO)₄bpy System at Varied Electrode Materials;

The addition of CO₂ to the system resulted in a surprising difference in behaviour of the Mo(CO)₄bpy toward CO₂ electrocatalysis upon the different electrode surfaces.

The activity on gold was consistent with the previously discussed voltammetric response, showing significant CO₂ current enhancement from the first reduction of Mo(CO)₄bpy onward with no evidence of complex or electrode deactivation. Upon substituting the gold working electrode for platinum and glassy carbon however the behaviour of the complex toward CO₂ was altered.

The voltammetry of the CO₂ saturated Mo(CO)₄bpy system measured on glassy carbon, two examples of which are given in figures 5.38 and 5.39, showed a current enhancement from the first redox potential onward on the initial scan.

The degree to which the current enhancement was seen at this potential tended to vary somewhat between experiments. From -2.2 V to -2.5 V onward this additional current increases significantly showing almost double the current seen in the absence of CO₂ by the time the second reduction of Mo(CO)₄bpy was reached.

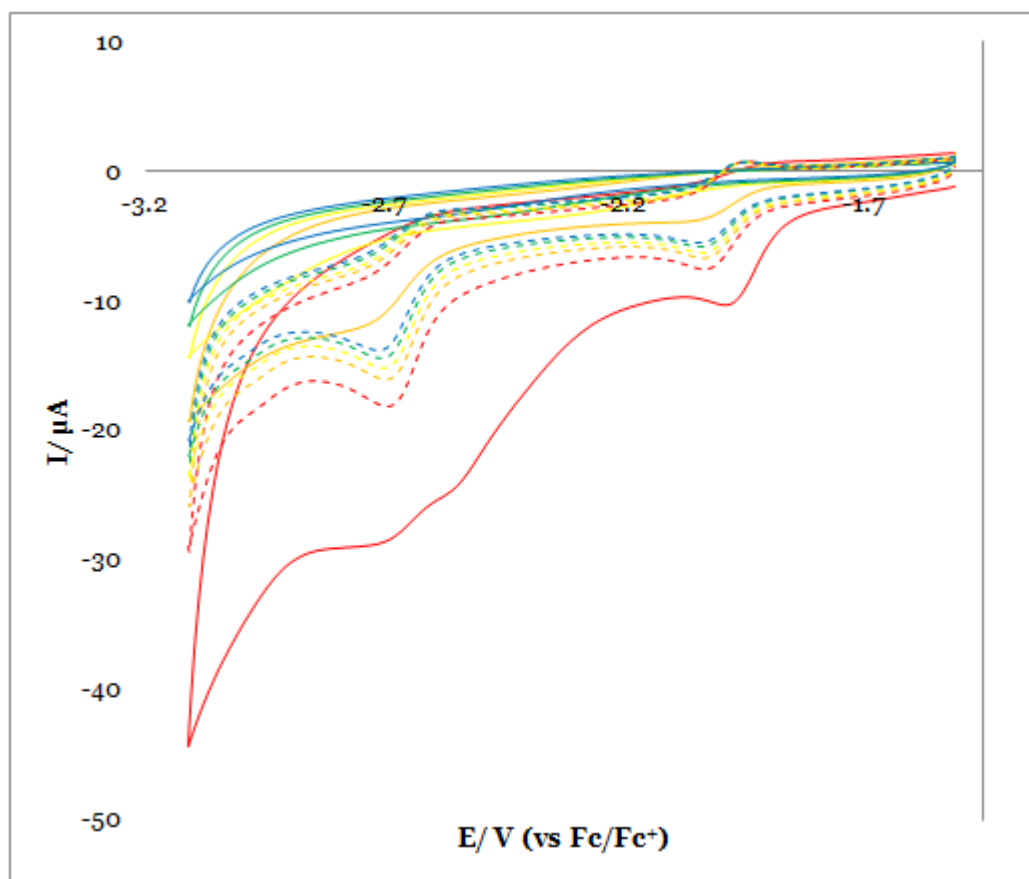


Figure 5.38; CV of 0.5 mM Mo(CO)₄bpy in cell 1 except measured at GC WE (d= 3 mm) in the presence (solid lines) and absence (broken lines) of CO₂. Scan rate employed was 200 mV s⁻¹. 5 subsequent scans shown for each system.

The direct CO₂ reduction, in the absence of the complex, was not observable until application of approximately -3.0 V in this system and the analogous THF set up (shown in figure 5.39), so this additional current is evidence of a significant lowering of the overpotential of CO₂ reduction.

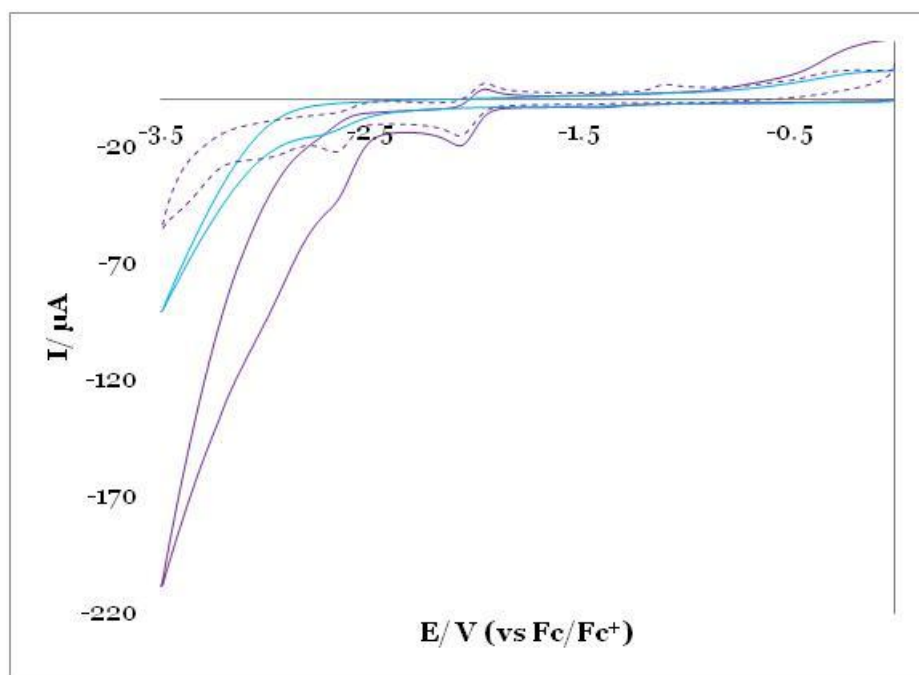


Figure 5.39; CV of 1 mM $\text{Mo(CO)}_4\text{bpy}$ in cell 2 except measured at GC WE ($d = 3$ mm) in the presence (solid lines) and absence (broken lines) of CO_2 with direct CO_2 reduction also shown (pale blue) Scan rate employed was 200 mV s^{-1} . 1st scans shown for each system.

One of the features commonly seen in the analogous experiments with a gold working electrode is a crossover region. This was not observed in any of the GC voltammetry despite the wide range of vertex potentials and scan rates employed in THF or NMP.

The reoxidation associated with the neutral complex reformation is observable on the first back scan as a slight shoulder in the CV. The extent of reoxidation observed was also less than consistent with different experiments although it was always seen to a lesser extent than for the corresponding voltammetry in the absence of CO_2 .

In the voltammetry seen in figure 5.38 there is a significant deactivation of complex or electrode activity with scan which, as can be seen by comparison of the dashed and solid lines, occurred much more rapidly than any current drop

seen in the absence of CO₂ over the same potential range. CO₂ is highly soluble in both NMP and THF, significantly more so than oxygen, therefore the solution is less likely to contain contaminants from dissolved air than in the absence of CO₂ however there seems to be evidence of a destabilisation of the complex.

This could be explained by the complex carbonyl ligands being more labile in the presence of CO₂, possibly forming a tricarbonyl species at a less negative potential than that observed when CO₂ is absent from the system due to the Mo(CO)₄bpy-CO₂ interaction. On the gold surface this CO group is believed to be reversibly lost as discussed earlier, however on glassy carbon there is some evidence that the original species is not regenerated therefore current related to the Mo(CO)₄bpy is lost. By scan 5 of figure 5.38, in the presence of CO₂ (solid blue line), the voltammetry seen strongly resembles that seen for the direct CO₂ reduction on GC with no features discernible and very little current seen over this potential range.

The deactivation of the system was not observed to be consistent between experiments however in the trials showing more significant CO₂ reduction enhancement the deactivation was seen more quickly which supports the above idea.

The current enhancement associated with the 2nd reduction of Mo(CO)₄bpy remains larger for a greater number of scans suggesting that the application of the higher overpotential allows the system to overcome the deactivation.

The inconsistencies found with the GC experiments may well be due to differences in the preliminary electrode surface structure and groups and therefore its activity and ability to stabilise the reduced molybdenum species

formed. Glassy carbon activity is very much dependent upon the surface chemistry of carbon-oxygen functionalities with the presence of quinines, phenols and other oxygen containing groups^[194] and, as discussed earlier, the surface is not as reproducible as those of the metal electrodes.

The fact that some experiments with glassy carbon showed activity from the first redox peak region (figure 5.38) and some needed application of potentials nearer to the second, (as seen in figure 5.39), before significant enhancement in CO₂ reduction was observed could also be related to electrode surface inconsistencies.

When implemented as an electrode, glassy carbon is reported to have a higher double layer capacitance than traditional metal counterparts.^[195]

The surface structure and different double layer properties may slow the electron transfer between the electrode and the molybdenum complex, with the response differing between runs as the surface differs. This stands in contrast to the electron transfer seen at metal electrodes, particularly if, as discussed above, the reduction on gold does not proceed via an uncomplicated outersphere mechanism. In the absence of specific adsorption interactions on the electrode surface the electron transfer may be expected to proceed relatively slowly through the electrical double layer.

In all of the experiments trialled despite the varied degree of both lowering of overpotential and stability of the complex an enhancement in CO₂ reductive current was consistently seen at potentials where direct reduction of CO₂ in the system is not possible. The fact there is evidence to suggest the Mo(CO)₄bpy

species is not always regenerated and CO₂ electrocatalysis related current is subsequently lost is indicative of specific surface requirements for the effective catalytic function of the complex employed, which glassy carbon cannot consistently provide.

The voltammetry of Mo(CO)₄bpy on the platinum surface did not yield reproducible clear peaks in the absence of CO₂, and upon addition of CO₂ to the system this was again seen to be the case with peaks partially masked by the slanted CV response. Figure 5.40 compares the first and fifth scans of the Mo(CO)₄bpy over the first reduction potential range in the presence and absence of CO₂.

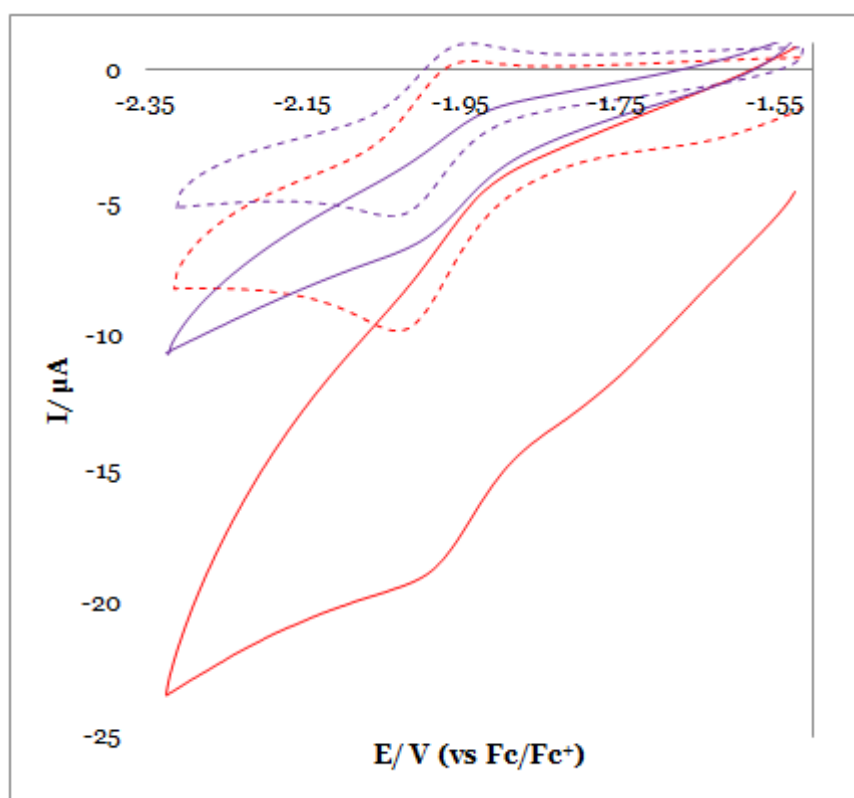


Figure 5.40; CV of 0.5 mM Mo(CO)₄bpy in cell 1 except measured at Pt WE (d= 2 mm) in the presence (solid lines) and absence (broken lines) of CO₂. Scan rate employed was 200 mV s⁻¹. 1st scan= red, 5th scan= purple.

Over this potential range in the presence of CO₂ there is substantially more current observed than in its absence and a suggestion of peaks which correspond to the Mo(CO)₄bpy complex are observable even after consecutive scans are executed. In this voltammetry however the CO₂ reductive current seems to show an enhancement before the first reduction of the complex occurs. This is in contrast with the well studied gold voltammetry where no CO₂ reduction current is seen until the first reduction is reached. The analysis of the data is made more challenging by the tendency of the Mo(CO)₄bpy related peaks on platinum to lose current with scan and upon application of very negative potentials, however for the corresponding scan number the CO₂ data still seems to show additional current seen by comparison of the purple dashed and solid lines of figure 5.40 and also over a wider potential window in figure 5.41.

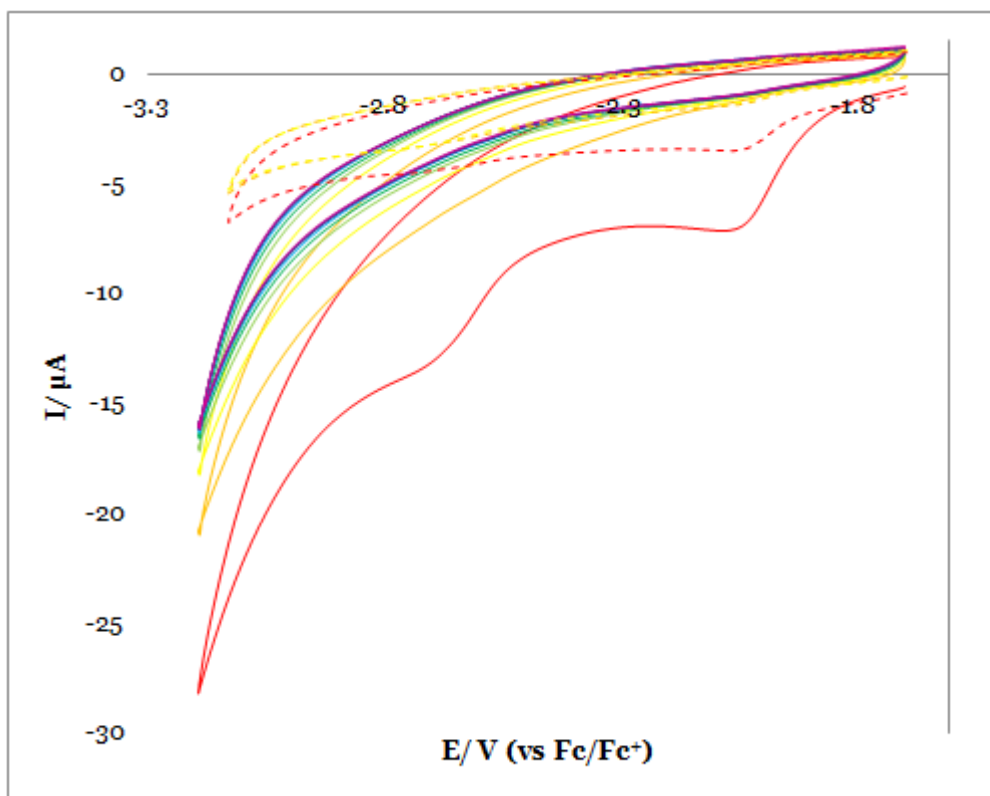


Figure 5.41; CV of 0.5 mM Mo(CO)₄bpy in cell 1 except measured at Pt WE (d= 2 mm) in the presence (solid lines) and absence (broken lines) of CO₂. Scan rate employed was 200 mV s⁻¹. Scans 1 to 10 shown for CO₂ saturated solution and 1 to 3 for the corresponding system in the absence of CO₂.

From figure 5.41 the voltammetric behaviour over the larger potential range, incorporating the application of more negative potentials, is comparable to that seen on glassy carbon in figure 5.38. On the first forward scan at the potentials associated with the reduction of the Mo(CO)₄bpy complex and subsequently there is additional current clearly observable, due to the CO₂ electroreduction aided by the reduced complex species. Upon the back scan however the reoxidation associated with these processes is not evident and upon subsequent cycling none of the redox peaks are observed. The reductive current seen by the third and fourth scans is much lessened and seen to occur in the potential region associated with direct CO₂ in this system.

In the case of platinum there was some evidence of alteration in the electrode surface after CO₂ reduction with the open circuit potential becoming very positive for a number of minutes after the prolonged application of negative potentials and, in some voltammetry the formation of a large oxidative peak not observed upon employment of the other electrode materials, an example of which is given in figure 5.42.

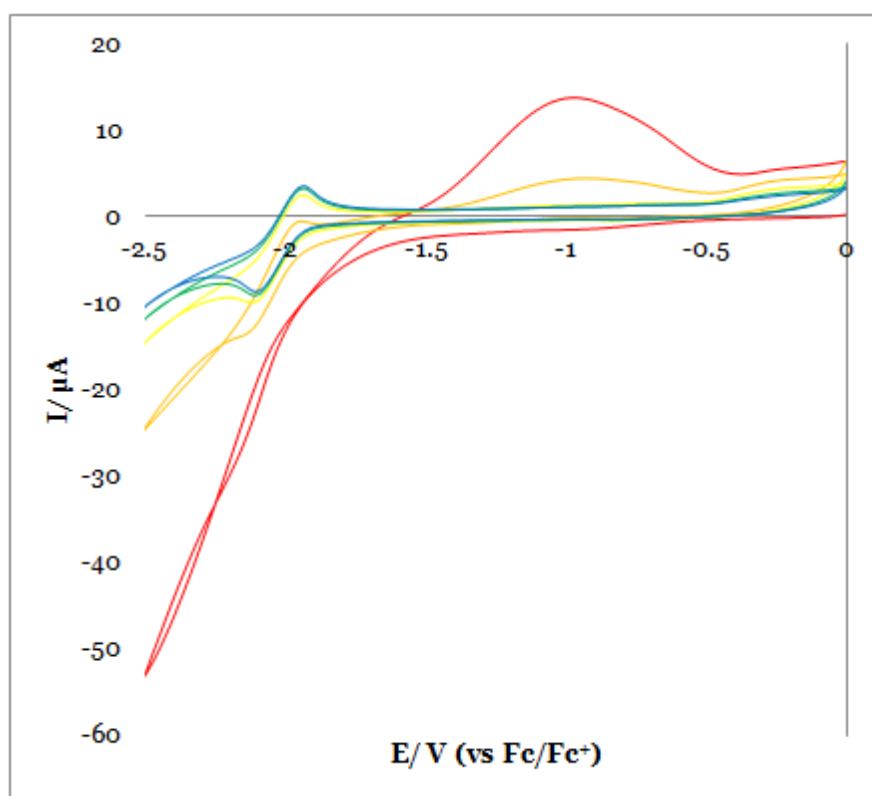


Figure 5.42; CV of 5 mM Mo(CO)₄bpy in cell 2 except measured at Pt WE (d= 2 mm) in CO₂ saturated solution. Scan rate employed was 200 mV s⁻¹. Scans 1 to 5 shown.

The oxidative region seen in figure 5.42 was not observed consistently however the peak was seen to recur in more than one set of experiments employing different solutions on different days. The spikes in open circuit potential seen in many of the other experiments support this idea of an oxidation after CO₂ reduction even when the peaks were not observed.

From the initial CV a clear enhancement in current is seen just prior to the first reduction, in keeping with figures 5.40 and 5.41, but unlike these the current response for the CO₂ reductive region shows a crossover (previously only observed on gold) and instead of no oxidative current, here a large oxidation is seen between -1.5 V and 0.5 V. The second scan, measured directly afterward, shows less current enhancement but still the crossovers and the first redox peaks of the complex become clear. There is an oxidative current region seen on the back scan over the same potential range as that of the first scan but with a significantly lower peak current. For the remainder of the 5 scans measured the oxidative peak was not significant and the Mo(CO)₄bpy peaks are seen clearly and not lost as rapidly with scan as may be expected for this potential range. The Mo(CO)₄bpy is however present at a significantly higher concentration (an order of magnitude higher at approximately 5 mM rather than the 0.5 mM employed for the majority of experiments) which could explain the increased clarity of the associated features.

This information suggests that perhaps, as well as the less well stabilised complex, an intermediate is formed in the initial negative sweep of the cyclic voltammetry which acts as an inhibitor to further catalytic behaviour of the system. A possible candidate is CO adsorption which could deactivate the platinum surface. This deactivation process is potential dependant and is reversed once the potential is allowed to become more positive.

The analysis and comparison of the effect of the working electrode material upon the Mo(CO)₄bpy system, particularly with respect to its influence on CO₂

reduction, strongly suggests that effective electrocatalytic behaviour is dependent upon the employment of specific electrode material.

Whether or not the $\text{Mo(CO)}_4\text{bpy}$ can be considered to act as a catalyst when combined with the less ideal electrode surface is difficult to determine as there is a distinct possibility that it is not reformed therefore may be more accurately termed an activator in the system. It may be that the GC and Pt surfaces are altered by the application of negative potentials, therefore are deactivated preventing the effective electron transfer between the electrode and the $\text{Mo(CO)}_4\text{bpy}$ in solution. With the initial enhanced CO_2 current seen in all systems, there is significant evidence of the $\text{Mo(CO)}_4\text{bpy}$'s catalytic ability.

It can be concluded that for the longevity and effective electrocatalysis of CO_2 the combination of the gold working electrode and $\text{Mo(CO)}_4\text{bpy}$ seems to be optimal, offering reproducible data and least evidence of deactivation.

5.4. Conclusion;

From the various aspects of the electrochemical catalysts and system investigated a number of further conclusion can be drawn.

The study of the array of analogous $\text{M(CO)}_4\alpha\alpha$ -diimines allowed the investigation of the impact of the constituents of the organometallic complex $\text{Mo(CO)}_4\text{bpy}$ explored in chapter 4. The identity of the diimine, anticipated as the most likely to show significant effect from literature reports and as this ligand possesses the localised LUMO, was found to have less of an effect upon

the redox potentials of the first reduction and activity toward CO₂ reduction of the complex than the identity of the metal centre.



The inclusion of additional groups upon the bipyridyl ligand is shown to have the most pronounced effect, altering the behaviour of the complex most significantly.

All of the complexes investigated with a reduction potential less negative than that of direct CO₂ reduction showed a degree of catalytic activity toward CO₂ reduction. Bipyridine and phenanthroline were found to be the optimal ligands despite possessing the most negative reduction potentials to form the active state, proposed due to the larger delocalised electron density allowing for easier electron transfer, with tungsten proving to be the optimal metal centre exhibiting significant CO₂ current enhancement from the first reduction potential, as with Mo(CO)₄bpy, however at a less negative potential.

Bipyridine, pyridine and pyridinium were found to exhibit no catalytic activity toward CO₂ reduction when added in catalytic quantities to the NMP system, however, when pyridine was employed as the electrochemical solvent, CO₂ reduction appeared to proceed at a less negative overpotential, and with high current efficiencies, compared to NMP and THF.

The EPR studies confirmed the conclusion from DFT calculations that the LUMO of Mo(CO)₄bpy is localised upon the bipyridyl ligand through the striking similarity of the spectra recorded for the complexed and free radical anionic species and subsequent modelling of the spectra. The lack of detectable

EPR spectra upon the addition of CO₂ to the system strongly supports the proposed electron transfer from the radical anionic species and CO₂ and suggests that the rate of this is high, confirming the k' evaluated in chapter 4.

The THF system yielded no EPR signal for Mo(CO)₄bpy^{•-} under the same experimental conditions as employed for those in NMP, however a radical proposed to originate from Hoffmann elimination of the tetrabutylammonium cation was seen. The reason for this was unclear and could be further investigated.

Another important conclusion established from the data presented within this chapter was the strong surface dependence of Mo(CO)₄bpy stability and its effectiveness toward CO₂ electrocatalysis.

The significant effect of the working electrode material upon the system is indicative of adsorption being an important process within the reduction mechanism. Platinum was found to promote the breakdown of Mo(CO)₄bpy at only modest potentials with some evidence of additional electrode deactivation, hypothesised due to CO blocking the electrode surface. When glassy carbon was employed as the working electrode, although the complex appeared stable over the first two reductions, upon application of more negative potentials the new oxidative peak found to emerge in the studies on gold was absent and the voltammetric response associated with the complex was rapidly lost.

The electrocatalysis of CO₂ reduction by Mo(CO)₄bpy was observed in all of the systems however upon Pt the current enhancement was short lived with the CO₂ current dropping rapidly upon successive cycling and the glassy carbon electrode eliciting inconsistent behaviour, but again showing signs of

deactivation. The gold working electrode was found to offer the greatest enhancement in CO₂ current, stability of the complex and was the only surface where successive cycling did not lead to evidence of significant deactivation of the system.

6. The Influence of Electrolyte Identity upon CO₂ Reduction in NMP;

Throughout the non-aqueous electrochemistry conducted in this research, in both THF and NMP, the electrolyte employed as the standard system was tetrabutylammonium tetrafluoroborate, TBABF₄.

The reason for this choice was the good solubility of the electrolyte in the solvents employed and the fact that it offers a particularly large cathodic potential window with no electrolyte reduction evident until substantially more negative potentials than required to explore CO₂ reduction.^[53]

There have been reports in the literature which suggest that when employed during CO₂ reduction TBA⁺ may have a more active role in the system than as a simple charge carrying entity. A variety of behaviour has been attributed to the cation in the CO₂ reduction systems investigated including; as an aid in product selectivity by providing a specific hydrophobic environment at the electrode surface, lowering the CO₂ reduction overpotential through reaction between the TBA[•] radical formed on reduction and CO₂, and functioning as a proton source allowing formation of hydrogen containing CO₂ reduction products.^{[49][50]}

Generally speaking the TBA⁺ is present in excess when compared to the CO₂ in solution because of the limited solubility of CO₂ and the nature of the supporting electrolyte however in the systems investigated in this work the CO₂ concentration was actually higher.^{[166][167]}

Increase of the TBA⁺ concentration however showed no significant impact on the current or potential associated with CO₂ reduction. If the TBA⁺ were reacting with the CO₂ this increase in availability at higher concentration may be expected to increase the corresponding current, however upon more thorough contemplation this is perhaps not the case. The proposed mechanism of the catalysis-like promotion of CO₂ reduction^[49] follows the scheme given below where NR₄⁺ is the tetraalkylammonium species;



The NR₄⁺ is clearly reformed so would only be required in catalytic amounts with its role in electron transfer to form the CO₂^{•-} radical.

If the TBA⁺ were to be reacting through proton donation to the reduced CO₂ species, the TBA⁺ would not be reformed however each TBA⁺ is in possession of multiple protons (36) so if each of these were potentially available there would be a significantly higher concentration of abstractable hydrogens than of CO₂ in solution at the initial concentration after all.

In order to investigate the role of the TBA⁺ in the system employed, the electrolyte was exchanged for ones possessing alkali metal cations, namely lithium, sodium and rubidium tetrafluoroborates. The metal cations, M⁺, ensure no additional protons are available and are reported to possess suitably large negative potential windows^[53] so CO₂ reduction should still be evident in all systems.

6.1. Electrochemical Investigation of M^+ ;

Direct CO_2 reduction in CO_2 saturated solution of M^+ was trialled and compared with the equivalent CO_2 reduction response in TBA^+ voltammetry, the result of which is given in figure 6.1.

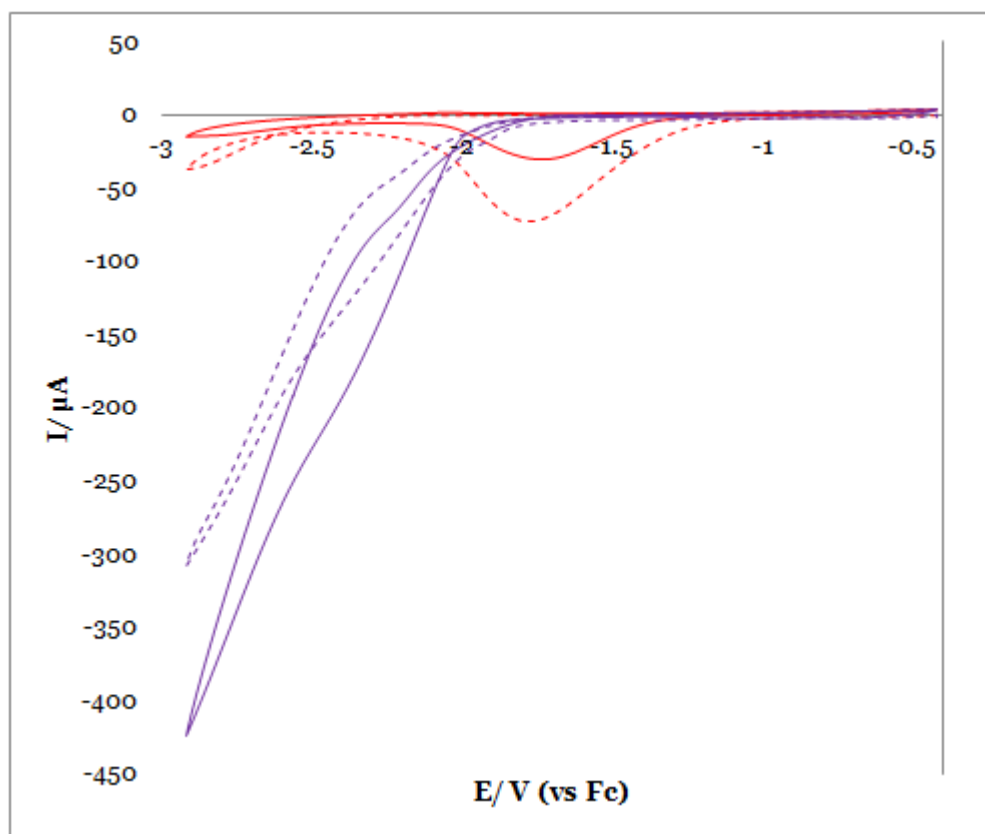


Figure 6.1; CV of CO_2 saturated NMP at Au WE (2 mm d) with NaBF_4 (0.1 M) in red and TBABF_4 (0.1M) in purple supporting electrolyte. Scans 1 (dashed) and 5 (solid) shown. Scan rate 200 mV s^{-1} .

Initial inspection of the CV response shows, despite the same freshly prepared gold working electrode employed and comparable CO_2 saturation, (with both systems subject to an excess of three hours with CO_2 gas bubbling through the solution, and CO_2 flowing through the headspace of the cell during the measurements), significantly more reductive current was seen when TBA^+ was present compared to Na^+ over the more negative potential range -2.2 V onward.

This could be considered supportive of the reported assessment where TBA⁺ is responsible for enhanced CO₂ reduction. The trend of lower CO₂ current without TBA⁺ was found with all of the different metal cation containing electrolytes trialled. Upon inspection of the CO₂ reduction response in the presence of Na⁺, again found consistently throughout all of the different M⁺ systems, there is a region of reduction prior to the expected onset of CO₂ reduction in the TBA⁺ system which is not observable in the absence of the metal cations.

This region was explored more carefully in the presence and absence of CO₂ for the M⁺ systems as can be seen in figure 6.2.

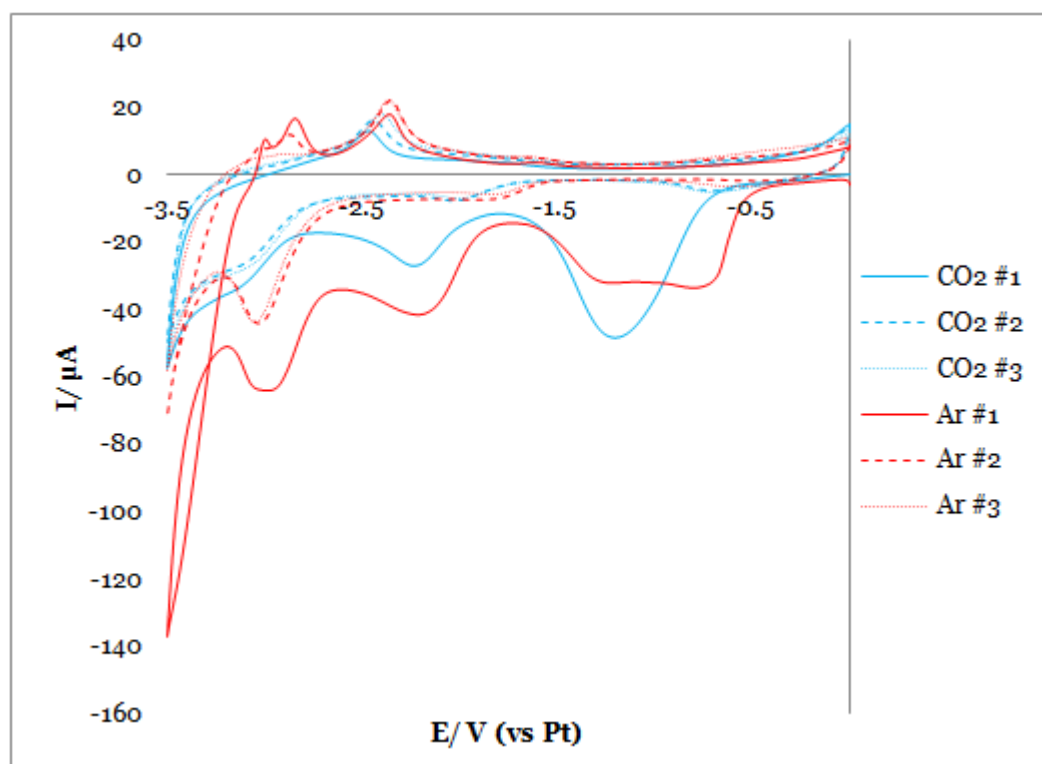


Figure 6.2; CV of Ar degassed and CO₂ saturated NMP at Au WE (2 mm d) with LiBF₄ (0.1 M) supporting electrolyte. Scans 1 to 3 shown for each. Scan rate 200 mV s⁻¹.

As can be seen in figure 6.2 a number of interesting observations can be made;

- 1) The Li⁺ 'blank' measured in argon degassed solution shows clear peaks and current so is clearly undergoing reaction in the absence of CO₂.

- 2) More current is seen in the absence of CO₂ over most of the potential range.

Very similar voltammetry was found for all of the alkali metal cations on both platinum and gold working electrodes, with the peaks shifted or less clear on occasion, but the same processes evident.

The current processes at approximately -1 V, -2 V and -3 V are attributed to alkali metal cation reduction.

The potentials at which the bulk metal ion reduction was undergone were predicted by the Born model^[141] (6.1), where the known standard redox potential of the metal ions in aqueous solution can be converted to give the expected Gibbs energy change, therefore reduction potential in a different solvent environment.

$$\Delta G = \frac{N_a z^2 e^2}{8\pi\epsilon_0 r_i} \left(\frac{1}{\epsilon_{NMP}} - \frac{1}{\epsilon_{H_2O}} \right) \quad (6.1)$$

where ΔG is the free energy change upon moving an ion of radius r_i and charge z from water, with relative permittivity ϵ_{H_2O} to NMP, with a relative permittivity ϵ_{NMP} . e and ϵ_0 are constants, the charge of an electron and vacuum permittivity respectively.

The change in free energy can then be related to the shift in potential using equation (6.2);

$$\Delta G = -nFE \quad (6.2)$$

where n , the number of electrons transferred is one and F is the Faraday constant.

The values of the standard redox potential in aqueous solution, the predicted values upon solvation in NMP and the observed experimental reduction potential in the absence of CO₂ for the bulk metal deposition for each of the metal cations employed are given in table 6.1.

Cation	Literature standard potential $E^{\circ}_{(aq)} / V \text{ (vs Fc)}$	Predicted potential via Born model $E^{\circ}_{(NMP)} / V \text{ (vs Fc)}$	Observed potential (experimental) $E_{(NMP)} / V \text{ (vs Fc)}$
Li⁺	-3.59 (-3.04)	-3.45	-3.60
Rb⁺	-3.53 (-2.98)	-3.46	-2.91
Na⁺	-3.29 (-2.74)	-3.18	-2.72

Table 6.1; Literature, predicted and observed M⁺ reduction potentials. Literature values in aqueous phase translated to vs. Fc via ref [141] Original values vs. SHE given in parentheses taken from ref [196]. Predicted values calculated via (6.1) and (6.2). Observed values measured in 0.1 M solution at Au WE (2 mm d) by CV (200 mV s⁻¹) with Fc added after initial measurement as internal calibrant.

From the data given in table 6.1 it can be shown that the Born model predicts that each of the M⁺ cations are more easily reduced in NMP than H₂O, with the magnitude of the positive potential shift expected Li⁺ > Na⁺ > Rb⁺. This was not observed to be the case experimentally with Rb⁺ and Na⁺ experiencing the

largest positive shift in potential, $\Delta E_{\text{obs}} \approx 0.6$ V rather than the predicted $\Delta E_{\text{pre}} = 0.077$ V and $\Delta E_{\text{pre}} = 0.109$ V, respectively.

Li^+ reduction was observed at a much more negative potential than predicted with the experimental value approximately the same as the reduction in aqueous solution. The position of the ferrocene redox potential may alter slightly upon alteration of the electrolyte but this would not explain the magnitude of the deviation seen. It is much more likely that chemical interactions between the cations and NMP occur. These interactions are not taken into consideration by the Born model where the solvation effects are assumed to be a result of long range electrostatic effects. There is also trace water present in the NMP. Lithium ions being the smallest ($r = 90$ pm) and more electronegative species would be expected to be much more adept at attracting any trace water from bulk solution into its solvation shell than the larger rubidium and sodium ions, which could also be expected to minimise the expected shift. The fact that the Li^+ ions remained hard to reduce is evidence of some extra stabilisation of the ion not accounted for by the relative permittivity of the solvent.

Na^+ (116 pm) and Rb^+ (166 pm) are both reduced at more positive potentials than predicted, indicating that the opposite is true and that these ionic species are subject to additional destabilisation therefore favour reduction to form the metal.

The Gibbs energy of transfer of monovalent cations from water to various non-aqueous solvents have been measured experimentally and reported. This data does not take into consideration the effect of the electrolyte anion so values may

not be expected to correspond exactly however the values found for the transfer from water to NMP were given as follows; $\Delta G(\text{Li}^+) = -35 \text{ kJ mol}^{-1}$, $\Delta G(\text{Rb}^+) = -8 \text{ kJ mol}^{-1}$ and $\Delta G(\text{Na}^+) = -15 \text{ kJ mol}^{-1}$.^[197] This would correlate to expected M^+ reduction potentials in NMP of $E(\text{Li}^+) = -3.95 \text{ V}$, $E(\text{Rb}^+) = -3.61 \text{ V}$ and $E(\text{Na}^+) = -3.35 \text{ V}$, which although not the exact experimental potentials observed, is however now showing the same trend in reducibility with Li^+ the hardest and Na^+ the easiest to reduce. The lack of applicability of the Born model to the systems investigated may be indicative of intricate solvent-electrolyte interactions.

The relationship between oxidative and reductive peaks seen prior to bulk reduction was explored by variation of the vertex potentials and dependence upon contaminants checked through the addition of water and varying degrees of de-aeration of the solution with the peaks observed in the absence of CO_2 in the non-aqueous system assigned as follows;

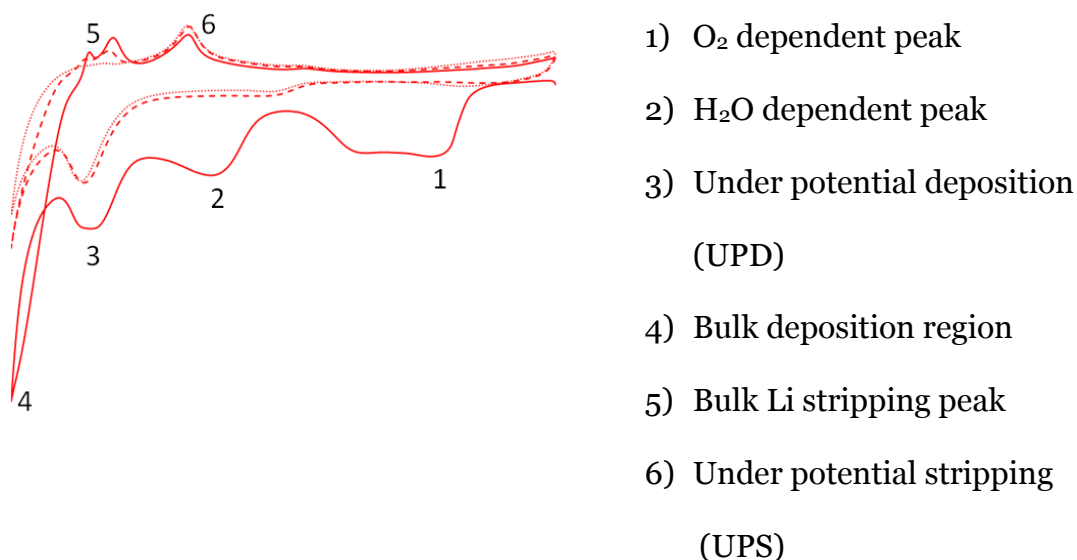


Figure 6.3; CV of Ar degassed NMP at Au WE (2 mm d) with LiBF₄ (0.1 M) supporting electrolyte. Scans 1 to 3 shown (solid line #1, dashed line #2 and dotted line #3). Scan rate 200 mV s⁻¹.

The voltammetry of lithium salts in non-aqueous aprotic solvents at noble metal electrodes has been investigated by other groups, and although LiBF₄ and NMP have not been specifically employed, the voltammetric characterisation is in keeping with earlier findings.^{[54]-[59]}

The first process seen, 1 in figure 6.3, has been reported as being linked to oxygen reduction. With Li⁺ present in non-aqueous solution the reduced oxygen species react to form superoxide and lithium peroxide (LiO₂ and Li₂O₂ respectively). The broad shoulder is consistent with two different processes giving two different products. This peak is only seen on the first scan which fits the expected behaviour as the formation of this layer at the electrode surface is reported to deactivate the electrode surface toward further oxygen reduction.^[54]

When the solution was better sealed and thoroughly degassed with argon the magnitude of the current associated with this peak could be lessened although not eliminated completely strongly supporting the correspondence of the data gathered in NMP with that available in the literature.

Process 2, associated with H_2O reduction, was seen to grow much larger upon addition of extra water to the system. The water reduction in the presence of Li^+ results in formation of a lithium hydroxide layer at the electrode surface (LiOH).^[54] This layer is not completely deactivating towards further water reduction as reduction in this region can be seen on subsequent scans. The potential is shifted however this could well be due to the pH change as well as the change in nature of the working electrode.

Process 3 is consistent with the reported under potential deposition (UPD) of lithium.^[54] This is lithium metal deposition that occurs prior to the potential required for bulk deposition of lithium, process 4. The oxidative peak 6 is the corresponding underpotential stripping (UPS) peak which shows an equivalent charge to the UPD.

The bulk deposition of lithium, process 4, shows a “nucleation loop” on the first scan which is characteristic of metal deposition,^{[54][59]} with the corresponding stripping peaks marked as process 5. Less deposition and associated stripping is seen in subsequent scans over this potential range where only the very initial bulk deposition is observed, however when this process was investigated over a more negative range, and with potentials held for varied lengths of time in this area, the deposition and stripping regions responded as expected and were reproducible with scan. The oxidative charge for the stripping process was generally observed to be less than the charge seen on the reduction (process 4 of Figure 6.3). A suggested reason for this is the formation of Li-Au alloys in the same potential region which has been reported by other researchers.^{[54]-[58]}

The system in the presence of CO_2 is presented in figure 6.4.

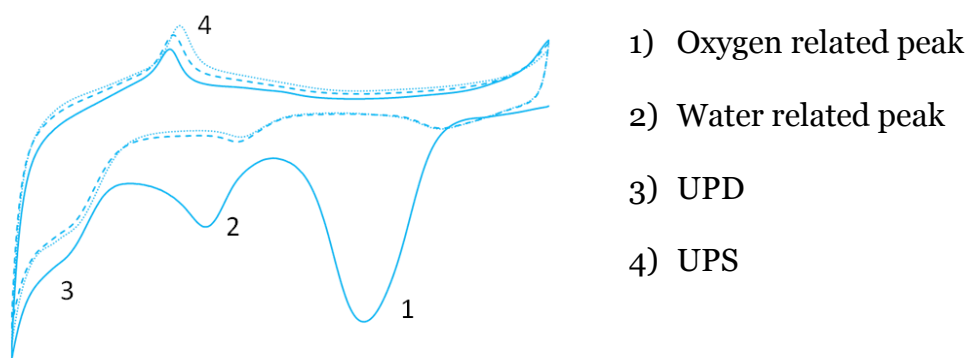


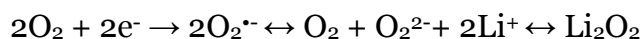
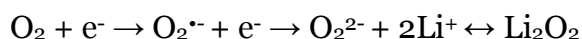
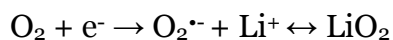
Figure 6.4; CV of CO₂ saturated NMP at Au WE (2 mm d) with LiBF₄ (0.1 M) supporting electrolyte. Scans 1 to 3 shown (solid line #1, dashed line #2 and dotted line #3). Scan rate 200 mV s⁻¹.

The processes seen upon saturation of the electrolyte solution with CO₂ are in the same potential regions as previously reported in the literature, however there are definite differences seen, some of which are quite unexpected.

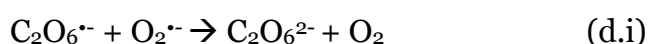
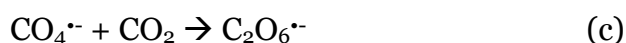
Processes 2, 3 and 5 are as described above in relation to the CO₂ free system although not observable to the same degree with the hydroxide layer formation, UPD and bulk deposition all reduced significantly in the presence of CO₂.

This is seemingly due to the difference in process 1, labelled above as oxygen related. This peak no longer shows a shoulder and is consistently the most pronounced feature in the voltammetry (until very extreme potentials where bulk deposition begins) in CO₂ saturated M⁺ solution. This finding is at odds with the expected lower concentration of oxygen present in CO₂ saturated solution. CO₂ is very soluble in NMP and, from the voltammetry gathered with TBA⁺ supporting electrolyte, O₂ is not present in quantities approaching the concentration required for this peak to be attributable solely to oxygen. In the

absence of CO₂ the reduction of trace oxygen forms the previously discussed LiO₂/Li₂O₂ layer.^[54] The proposed mechanistic steps for this are as follows;



In the presence of CO₂ however, the O₂^{•-} formed, rather than interacting with the Li⁺ directly may instead react with CO₂, present at a much higher concentration than O₂, or even Li⁺, which would then react with itself and Li⁺ to form, presumably lithium carbonate or oxalate type species, a possible mechanism for which is given below;



The stabilisation offered by the presence of the lithium counterions and possible electrode surface adsorption means that the intermediates considered above, found to lack stability in other systems, could form lithium salts and yield stable products not just the peroxydicarbonate, C₂O₆²⁻, reported from the reaction of CO₂ and O₂ with TBA⁺ supporting electrolyte in DMSO.^[198] Also the availability of O₂ and superoxide may affect the distribution of products.

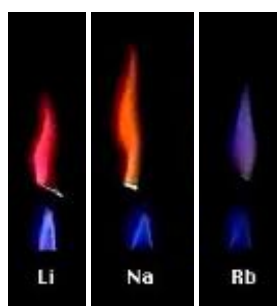
Superoxide has been reported by several groups to result in the activation of carbon dioxide in non protic systems.^{[165][199]}

It is known from previously reported data that the nature of the electrolyte employed may affect the product distribution of CO₂ reduction. Specifically differences in the cationic charge, hydrophobicity and charge density have all been shown to result in changes to the reaction pathway undertaken by CO₂ upon reduction.^[8] The small Li⁺ and the other M⁺ trialled, possesses a much higher charge density than the large TBA⁺ and as such are more likely to form insoluble ionic species.

Li₂CO₃ and Li₂C₂O₄ are both very insoluble species in most solvents^{[8][97][141]} and likely to cause the observed electrode deactivation if formed at the electrode surface.

Application of the potential associated with process 1 for both the systems with and without CO₂ and then removal of the working electrode from the solution, sonication in pure solvent to remove any electrolyte and flame testing led to confirmation that the processes seen in this potential region are, in fact, different.

The electrodes with the potential held at the potential of this first peak in the absence of CO₂ showed no evidence of metallic species remaining on the electrode surface after sonication, however each of the CO₂ systems, when subject to the same potential and sonication process, gave distinctive coloured flames corresponding to the nature of the metal cation employed.



Another difference seen between the CO₂ free and saturated systems was the appearance of the electrode after employment.

In the absence of CO₂, the electrode surface appeared discoloured and dull after use, particularly apparent on the gold surface but also noted on platinum. This darkening of the surface was not observed in the presence of CO₂ during almost all experiments run with all of the different metal cations. Initially, the darkened electrode was thought to be due to the formation of impurities at the surface of the electrode however upon cycling in acid the voltammetry suggested instead a significant roughening of the surface. An example of a gold CV measured in H₂SO₄ prior to, and after use, in the CO₂ free M⁺ system is given below in figure 6.5.

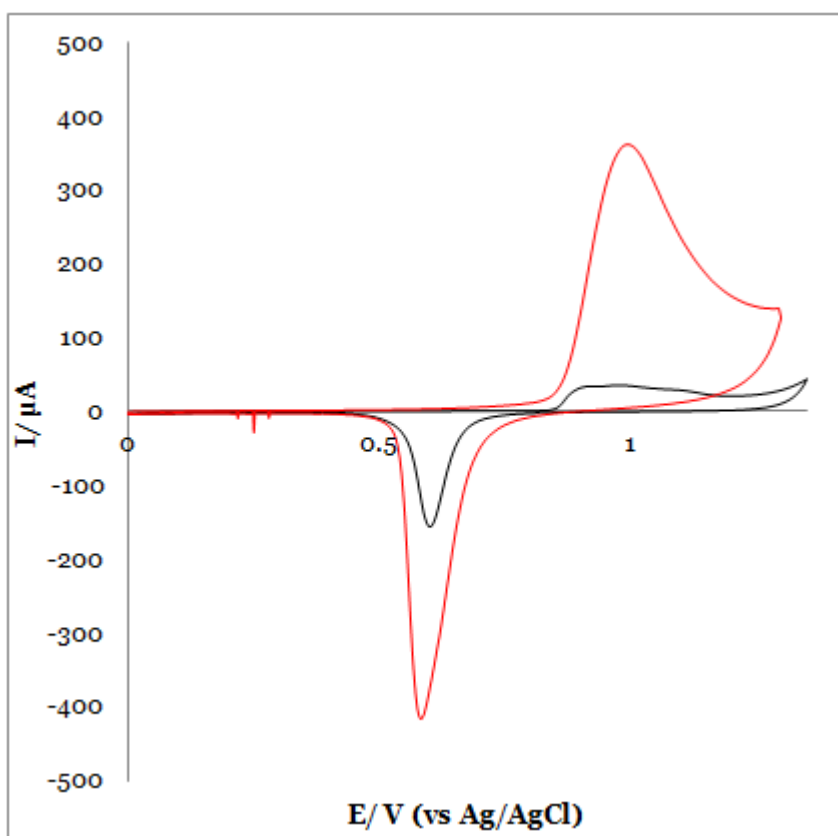


Figure 6.5; CV measured at Au WE (2 mm), in 0.1 M H₂SO₄ prior to (black) and after (red) use in LiBF₄ NMP solution in the absence of CO₂. Scan rate 100 mV s⁻¹.

The features seen in figure 6.5 are consistent with the response expected at a clean gold electrode in acid however the charge associated with the oxide formation and stripping, seen at 1.0 V and 0.6 V, is considerably higher after use. Both this and the apparent darkening of the electrode surface are attributed to a significant increase in surface roughness and subsequently actual working area of the electrode. After repetitive cycling in acid (up to $\times 100$) the voltammetric response was shown to settle back to, or close to, the CV seen prior to use.

In the M^+ systems without CO_2 , gold oxidation and reduction processes were present which were not seen in the presence of CO_2 which can be seen particularly clearly in figure 6.6.

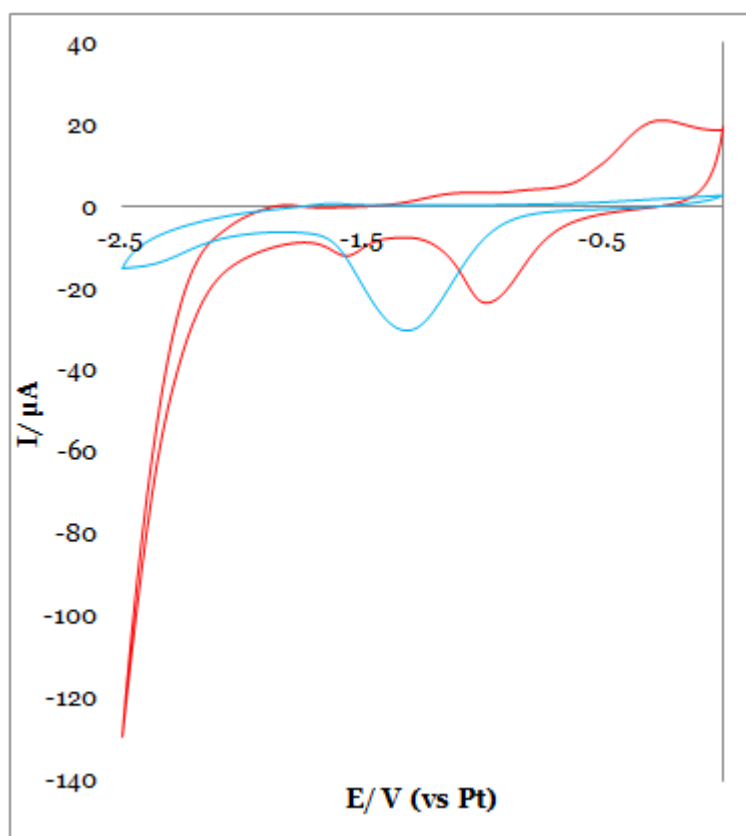


Figure 6.6; CV of Ar degassed (red) and CO_2 saturated (blue) NMP at Au WE (2 mm d) with $NaBF_4$ (0.1 M) supporting electrolyte. Scan #3 shown. Scan rate 200 mV s^{-1}

The oxidative peak found between -0.5 V and 0 V in the degassed response of figure 6.6 and its corresponding reduction, seen just before -1 V are thought to be due to gold oxidation and reduction. The presence of the LiOH layer (seen to a significant extent only in the absence of CO₂) has been reported to enhance this process which may explain why the voltammetry over the same potential range measured in CO₂ saturated NaBF₄, seen above in blue, shows the emergence of no such peaks.^[54] This gold oxidation and reduction combined with the much higher degree of lithium metal deposition, stripping and alloy formation and destruction could well result in the roughening of the gold as in this system, unlike the CO₂ saturated M⁺ systems, there is clear evidence of the gold taking an active role in the reactions. In the presence of CO₂, a protective, insoluble deactivating layer over the gold surface seems to be formed early on with the gold showing no signs of oxidation and reduction and no deposition until much more negative potentials than seen in the absence of CO₂. The acid cycling of the gold electrode after use in the CO₂ saturated system over the potential range prior to bulk reduction, in contrast to the response seen in figure 6.6 in the absence of CO₂, shows no significant enhancement with a slight reduction in the oxide stripping and formation charges seen in some cases.

6.2. Surface Enhanced Raman Spectroscopy;

6.2.1. *In situ* Surface Enhanced Raman Spectroscopy;

The nature of the surface processes and deposits formed on the electrode surface upon application of potential were investigated using surface enhanced Raman spectroscopy, SERS.^[146] As a gold working electrode was employed

throughout the electrochemistry this technique is well suited as a probe for this system as roughened gold is reported to be one of the most active surfaces for SERS.^[200] Gold surfaces have been reported to offer significant augmentation of signals of species found at the surface over similar wavenumber regions, 300-2000 cm^{-1} , using the same HeNe laser source. The enhancement in signal intensity from the surface enhancement effect can be up to 10^{10} allowing much greater sensitivity than seen in traditional Raman spectroscopy which relies upon a relatively weak inelastic scattering effect. The mechanism by which the SERS effect occurs is not particularly well understood although is dependent upon not just the surface as the name may suggest, but also the metal-molecule charge transfer and an allowed molecular resonance.^[200]

The interpretation of SERS spectra can be challenging as the traditional selection rules for Raman activity no longer necessarily hold as the adsorption of species at the electrode surface can result in an alteration in symmetry of the molecule and different adsorption sites or applied potential on the same surface can result in different chemi- or physisorption which in turn can result in signal loss, gain and alterations in wavenumber, strength or form of the signal response.^[147]

With this caveat in mind, the *in situ* Raman spectra were measured over the full potential range for the lithium electrolyte NMP system, with and without CO_2 , with the aim of assessing any differences seen. These spectra are given, along with a plot showing the applied potentials and corresponding current responses for each spectrum in figures 6.7, 6.8 and 6.9.

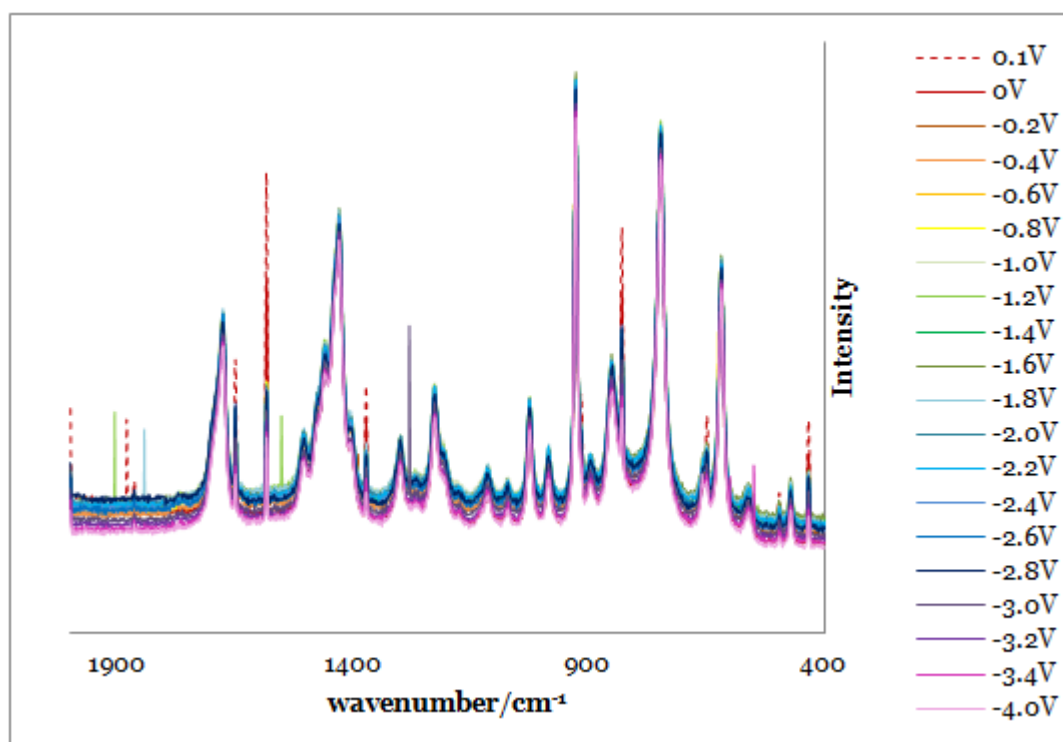


Figure 6.7; In situ SERS: LiBF_4 (0.1 M) in Ar degassed NMP at an electrochemically prepared gold foil working electrode (1 cm^2) at potentials 0.1 V to -4.0 V vs Pt (corresponding E-I response given in figure 6.10)

From figure 6.7 all of the most significant features observable are attributed to the NMP in the system and found consistently for all of the SERS measurements made in solution. The dominating high intensity NMP signals are found throughout the explored window with peaks seen at 1676, 1504-1404, 1380, 1300, 1225, 1174, 1115, 1071, 1025, 986, 924, 891, 849, 745, 650, 619, 562 and 473 cm^{-1} . The identity of these signals was verified through comparison of the spectra with a literature report of SERS conducted in NMP and also the consistency with which these features were seen.^[201]

There are however subtle peaks, which are not NMP related, at 1649, 1581, 1371, 891, 829, 648, 496, and 432 cm^{-1} . These features show a potential dependence and decrease in intensity with increasingly negative applied potentials. Peaks found at 986 and 473 cm^{-1} are thought to be NMP related but do also show a degree of potential dependence. The identity of the molecules responsible for

the other potential dependent features are all seemingly H₂O and O₂ related species such as H₂O 1650,^[147] Li-OH 1550 and Li-O species found at 450-650^{[54][59]}. An enlargement is given in figure 6.8;

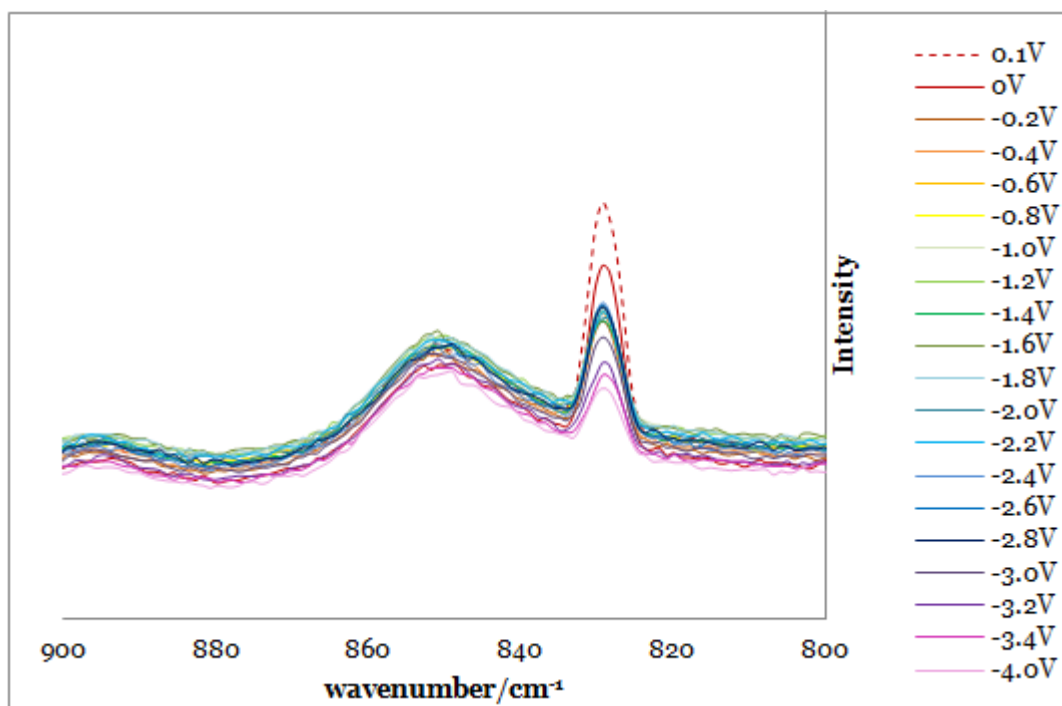


Figure 6.8; An enlargement of the region 800-900 cm⁻¹ of figure 6.7. In situ SERS LiBF₄ (0.1 M) in NMP at an electrochemically prepared gold foil working electrode (1 cm²) at potentials 0.1 V to -4.0 V vs Pt (corresponding E-I response given in figure 6.10).

Upon closer inspection of the potential dependent peaks, as shown in figure 6.8, they are clearly distinguishable from the non-potential dependent solvent background. An unexpected feature of these peaks is that each of the signals drops in intensity rather than shifting with potential resulting in different peaks. This suggests that the water and oxygen species, known to interact with the surface at specific potentials, are present on the Au surface prior to their reduction. Rather than seeing the reaction products as a new peak, there tends to be a change in shape and intensity of the existing peak with a lowering in intensity as lithium and lithium oxides and hydroxides deposit and the

proportion of SERS inducing gold at the surface lowers. From the degree of drop in intensity with potential, a typical example of which is seen in figure 6.8, upon application of -0.1 V onward the signal intensity drops by approximately a quarter compared with 0 V, but then remains stable through the UPD processes until the bulk deposition is seen to occur at -2.8 V when it starts to drop significantly with potential. This is presumably due to the deactivation due to the relative large quantities of lithium formed, compared to the permeable monolayer thickness of the Li-O, Li-OH and Li-H at less negative potentials.

As mentioned earlier and clearly seen from figure 6.8, the oxygen and water related peaks seen in figure 6.7 are reduced in amplitude with increasingly negative applied potential. This is in keeping with the build up of the lithium deposits lowering the amount of gold surface available for Au-O interactions. Li-Au and Li-Li interactions are expected to give a SERS response at the highest frequencies, therefore the highest wavenumber region of the spectra, at approximately 300-500 cm^{-1} and below.^[59] This signal would be expected to increase with applied potential however this was not observed. The wavenumber range investigated was 400 cm^{-1} and higher so it is possible that the frequencies were insufficiently high to detect these bonds as the only peaks seen below 500 cm^{-1} either decrease with applied potential or remain constant however there is evidence from the electrochemistry undergone whilst making the SERS measurements that the lithium deposition region was reached, (see figure 6.10).

The same experimental procedure was then carried out with the only difference being, prior to sealing of the cell and measurement of the SERS, the solution was saturated with CO_2 . The resultant spectrum can be seen in figure 6.9.

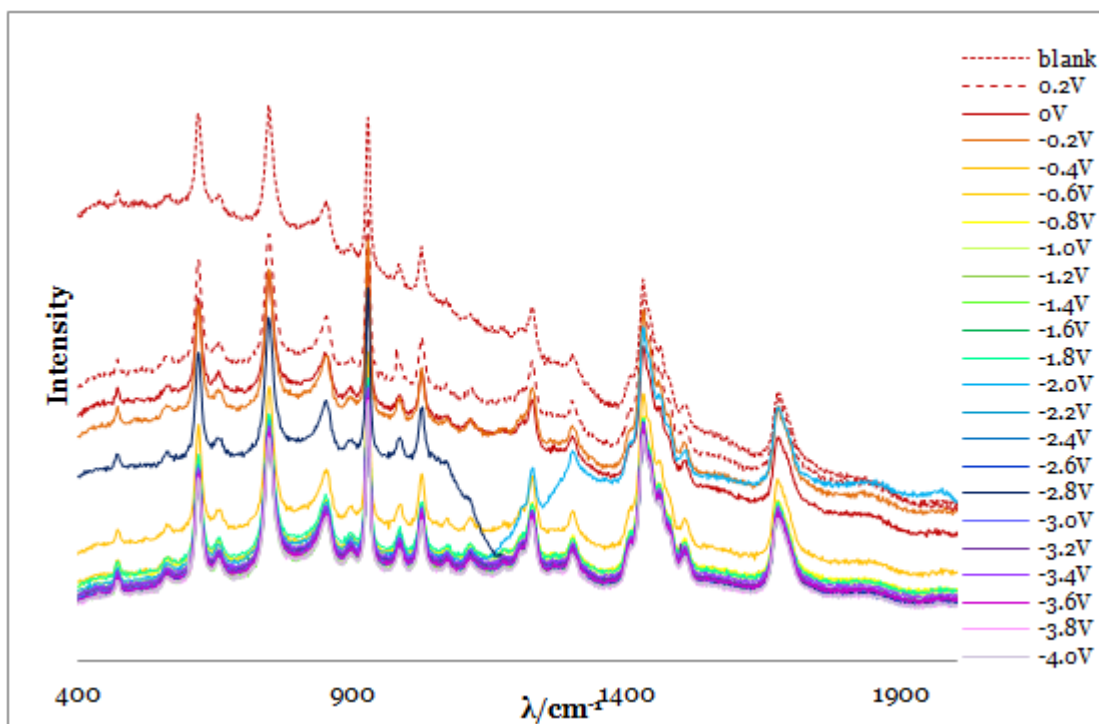


Figure 6.9; In situ SERS of CO₂ saturated LiBF₄ (0.1 M) in NMP at a electrochemically prepared gold foil working electrode (1 cm²) at potentials 0.2V to -4.0 V vs Pt (corresponding E-I response given in figure 6.10)

The SERS measurements made in CO₂ saturated LiBF₄ solution did not possess the flat and consistent background intensity seen in the previous spectrum (figure 6.7). This was attributed to inconsistencies in the positioning of the cell and laser whilst measurements were made with any perturbation of the cell or laser resulting in ‘sloshing’ of solution and as consequently changes in the electrode position, solvent pathlength and distance from the laser. Despite the movement in the background peaks are still evident, however upon saturation with CO₂ the H₂O and O₂ features seen clearly in figure 6.7 are absent or significantly decreased. The reasons for the loss of these features was addressed earlier; lower oxygen content and deactivation of the gold surface due to the accumulation of the passivating layer during the early stages of the experiment. CO₂ is reported as giving Raman peaks at 1275 and 1382 cm⁻¹ in aqueous solution.^[147] A slight suggestion of these features can be observed however they

are not particularly clear, perhaps as the CO_2 observed at these Raman shifts is not adsorbed at the electrode surface therefore not subject to SERS enhancement. There is the possibility that the adsorbed CO_2 features may be more effectively masked by the NMP signal, or if adsorbed the CO_2 molecule may no longer be in possession of Raman active modes. Li-CO_2 related features are expected to emerge in the regions $800\text{-}900\text{ cm}^{-1}$ and $1300\text{-}1700\text{ cm}^{-1}$ upon application of potentials more negative than -1 V (vs. Pt) as, from inspection of figure 6.10, this is the potential at which the initial deactivating layer formation begins.^[54] These features are however not apparent with no peaks found to alter significantly with applied potential above the solvent and background.

The current responses for the various applied potentials corresponding to the in situ measurements shown in figures 6.7 and 6.9 are given in figure 6.10.

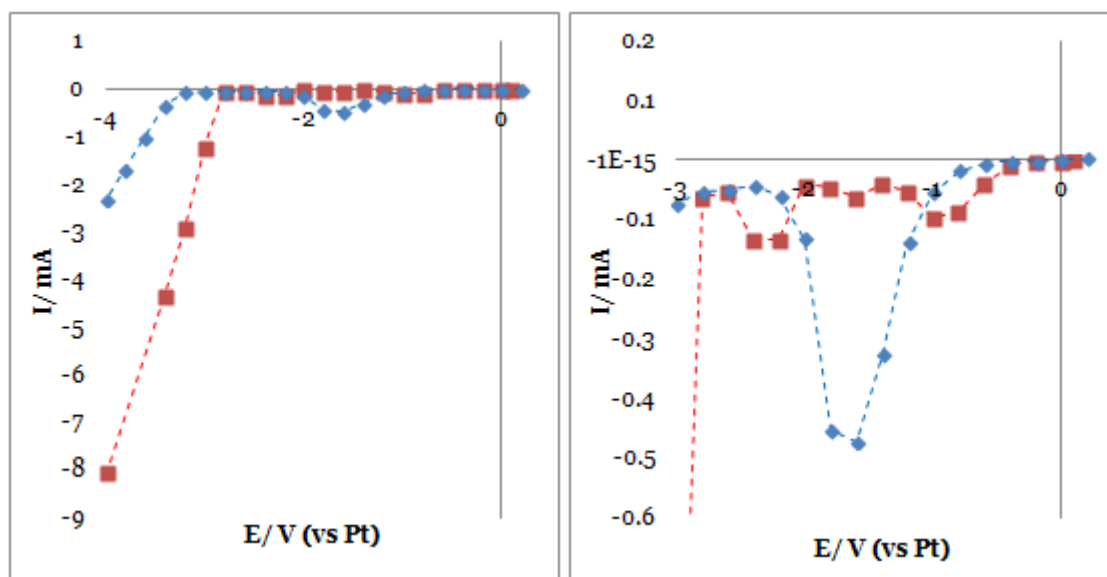


Figure 6.10; Current response for the initial 30 s of each of the applied potentials corresponding to the in situ SERS gathered. Red points show measurements made in the absence of CO_2 in the $\text{LiBF}_4\text{-NMP}$ system described above, blue correspond to the CO_2 saturated system. Left shows the full current- potential range observed with the plot on the right an enlargement to show the processes occurring at less negative potentials more clearly.

From the comparison of the current responses seen for the in situ measurements with the various applied potentials in both the presence and absence of CO₂ and the cyclic voltammetry given in figure 6.2, it is clear that the same processes were undergone and that the saturation of the system with CO₂ gives different surface products and activity. Both the CO₂ saturated and Ar degassed systems show evidence of the underpotential deposition features and bulk reduction of Li⁺. The bulk process was seen to occur 500 mV more negative in the presence of CO₂ but with the first surface altering reactions seen well before -1 V for both systems.

As the Li-CO₂ species were not clear, a SERS investigation of the TBA⁺-CO₂-NMP system was undertaken in the hope that there may be observable differences to assist in the assignment. The spectrum is given in figure 6.11.

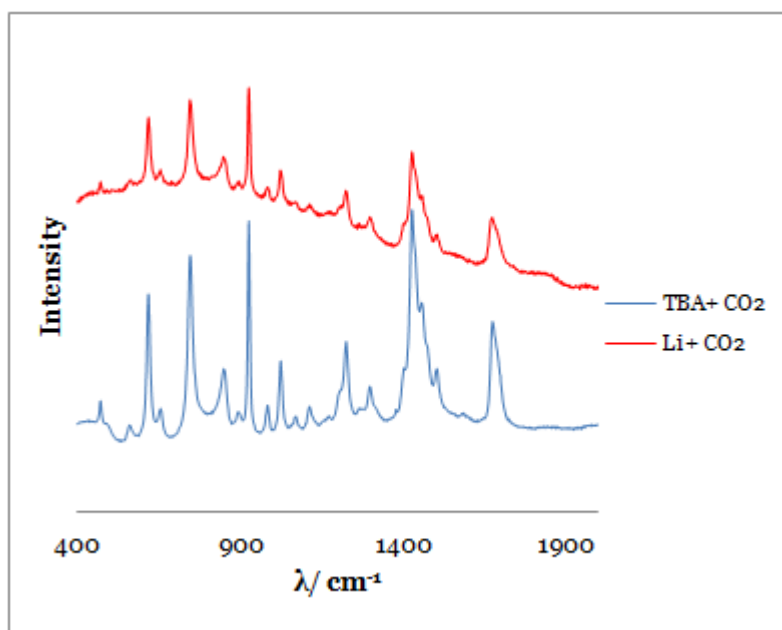


Figure 6.11; SERS for CO₂ saturated NMP with TBA⁺ (blue) and Li⁺ (red) supporting electrolyte in the absence of applied potential.

From direct comparison of the CO₂ saturated Li⁺ and TBA⁺ SERS results there is evidence of a slight lessening in the features at 1340 cm⁻¹ in the TBA⁺ system

however against large background features the assessment may be slightly subjective.

The dominance of NMP in all of the in situ SERS trials led to the suspicion that the solvent may be adsorbed on the gold itself, therefore as well as the high concentrations present its Raman response may also be amplified by the gold surface. The BF_4^- species with an anticipated active mode giving a peak at 510-560 cm^{-1} was never observed which is in keeping with the SERS effect being responsible for NMP enhancement as at the negative electrode the adsorption of the anion would be unlikely. However it is possible that the BF_4^- signal may have been masked by a NMP signal in this region. In order to determine whether the strong NMP signal was associated with its high concentration or surface resonance enhancement, the pathlength of the laser through NMP to the gold surface was altered with a Raman spectrum gathered at each. The resultant spectra and plot showing the intensity of the peak at 745 cm^{-1} against volume of NMP added to the cell are given in figures 6.12 and 6.13 respectively.

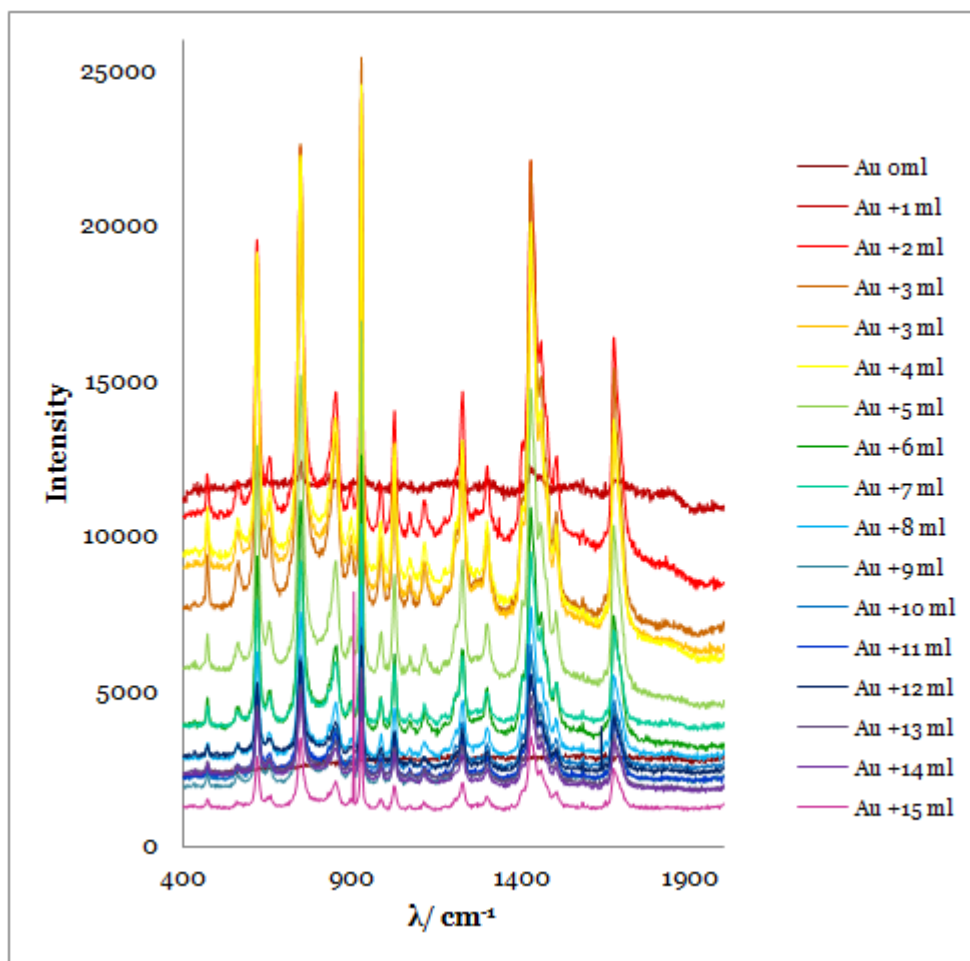


Figure 6.12; SERS of NMP on electrochemically prepared Au foil in the absence of applied E with varied solvent pathlengths.

As the solvent pathlength was altered the background intensity can be seen to shift with it increasingly dramatically upon addition of small volumes of NMP then decreasing with subsequent solvent added. The solvent pathlength itself was not measured however varied from 0 cm (pure Au in the absence of NMP and not completely covered until the addition of 2 cm³) to approximately 4 cm (upon addition of 15 cm³).

The peak heights (from their individual baselines) as a function of solvent volume can be seen in figure 6.13.

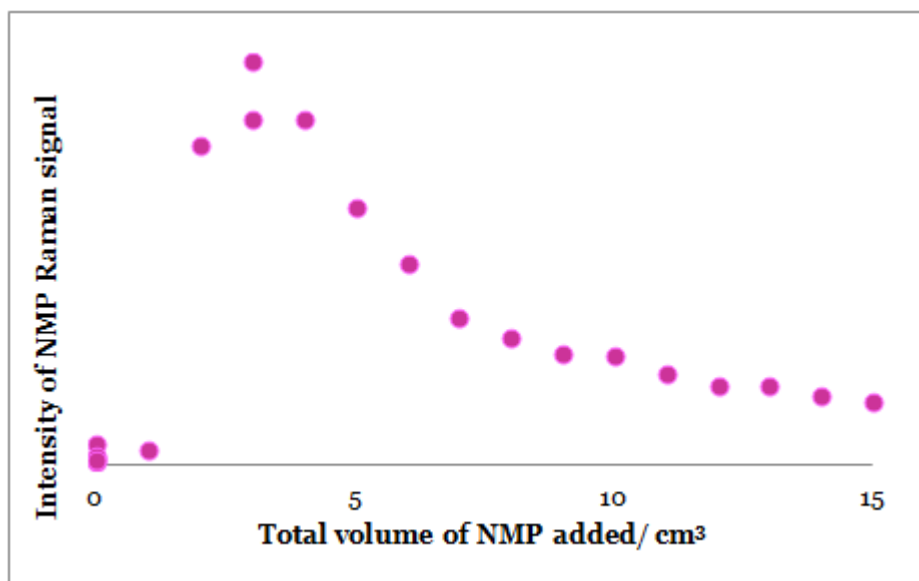


Figure 6.13; Plot of NMP Raman peak intensity response as a function of volume of NMP, corresponding to Raman spectra in Figure 6.12.

The huge increase in intensity of the Raman peak at 2 cm³ corresponds to the volume at which the electrode surface was entirely covered in NMP. The highest Raman signal response is seen with the lowest volumes of solvent rather than increasing with increasing quantities of NMP. This is suggestive of the SERS effect causing amplification of the NMP spectra through interaction with gold seen most clearly when the Au surface is more accessible at the shorter solvent pathlength. Increasing the volume of NMP in the pathlength results in lost signal from the laser or less detectable scattered response from the gold.

In order to negate the large solvent background the investigation of the gold surface was trialled *ex situ* where there was no requirement for the presence of solvent during the SERS.

6.2.2. *Ex situ* Surface Enhanced Raman Spectroscopy;

After collection of some CVs over the full range of the reductive window chronoamperometry was employed applying -3.2 V, a potential just prior to the bulk Li^+ reductive region, for an hour in CO_2 saturated Li^+ -NMP system with CO_2 kept flowing through the headspace of the cell during measurement. The gold foil electrode was then removed from the cell and thoroughly washed in NMP and water, sonicated in acetone, rinsed and allowed to dry.

The electrode surface appearance post-reduction was atypical for gold employed in the CO_2 saturated system; one side of the foil remained shiny as expected, however the underside of the electrode experienced a degree of darkening usually seen only in the absence of CO_2 . The reason for this is not clear however the applied potential was fairly negative and the time period for which it was held was longer than usual. Both sides of the Au were investigated with SERS, the results of which are given in figures 6.14 and 6.15.

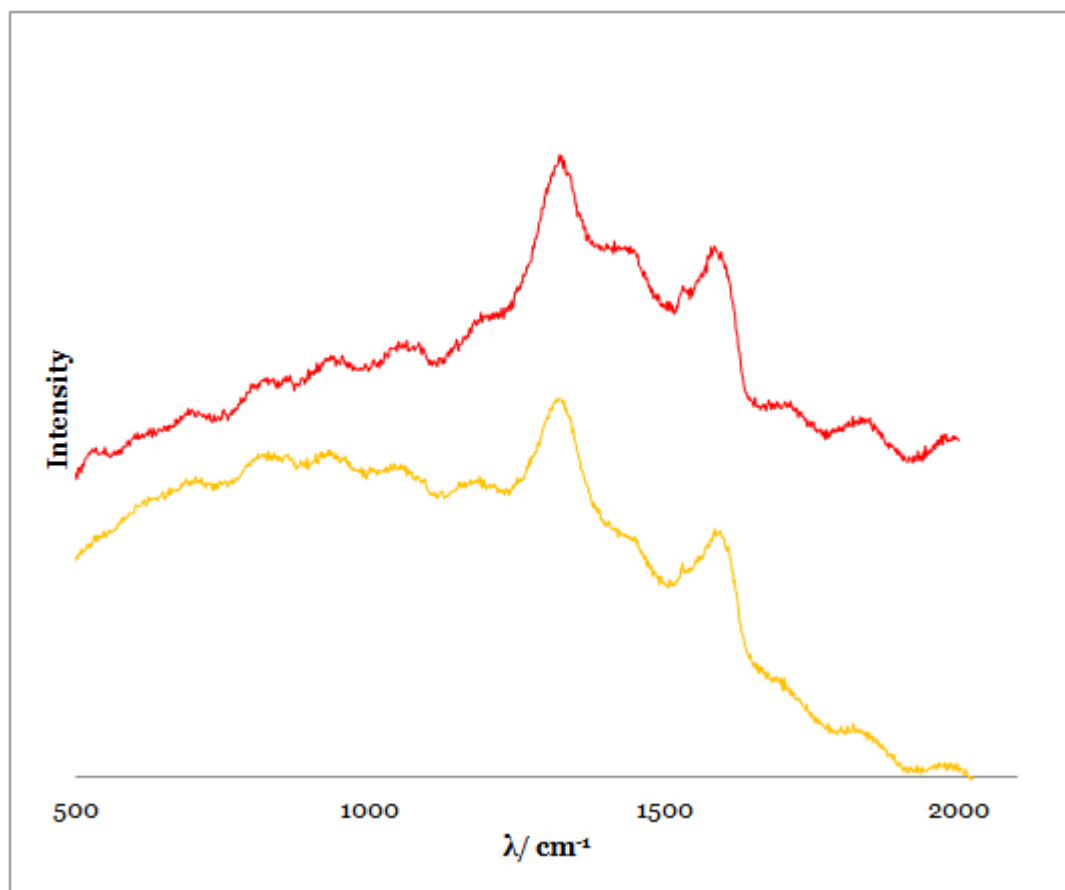


Figure 6.14; SERS of Au WE after application of negative potential in CO₂ saturated NMP with LiBF₄ (0.1 M). Red and gold lines represent separate results from different areas of the shiny side of the electrode

The spectra on both the rough and shiny sides of the electrode were subject to the same power and number of accumulations as the *in situ* measurements with several spots on each side of the sample investigated. In the absence of NMP the peaks seen were not sharp and well defined, particularly on the shiny side as seen in figure 6.14. However these smaller signals were no longer masked by large NMP peaks. Unsurprisingly, given the obvious disparity in appearance, the two sides of the gold foil electrode after the electrochemical preparation of the sample gave quite different spectra showing distinct and different features.

Figure 6.14, showing the SERS for the shiny side, has more features than the darkened side. The most prominent peak, seen at approximately 1320 cm⁻¹

corresponds well to a known Raman shift due to OCO_2Li species (reported previously at 1327 cm^{-1}).^[146] The other large peak seen at $1500\text{--}1600\text{ cm}^{-1}$ corresponds to the Raman shift for Li_2CO_3 (1525 cm^{-1}).^[54]

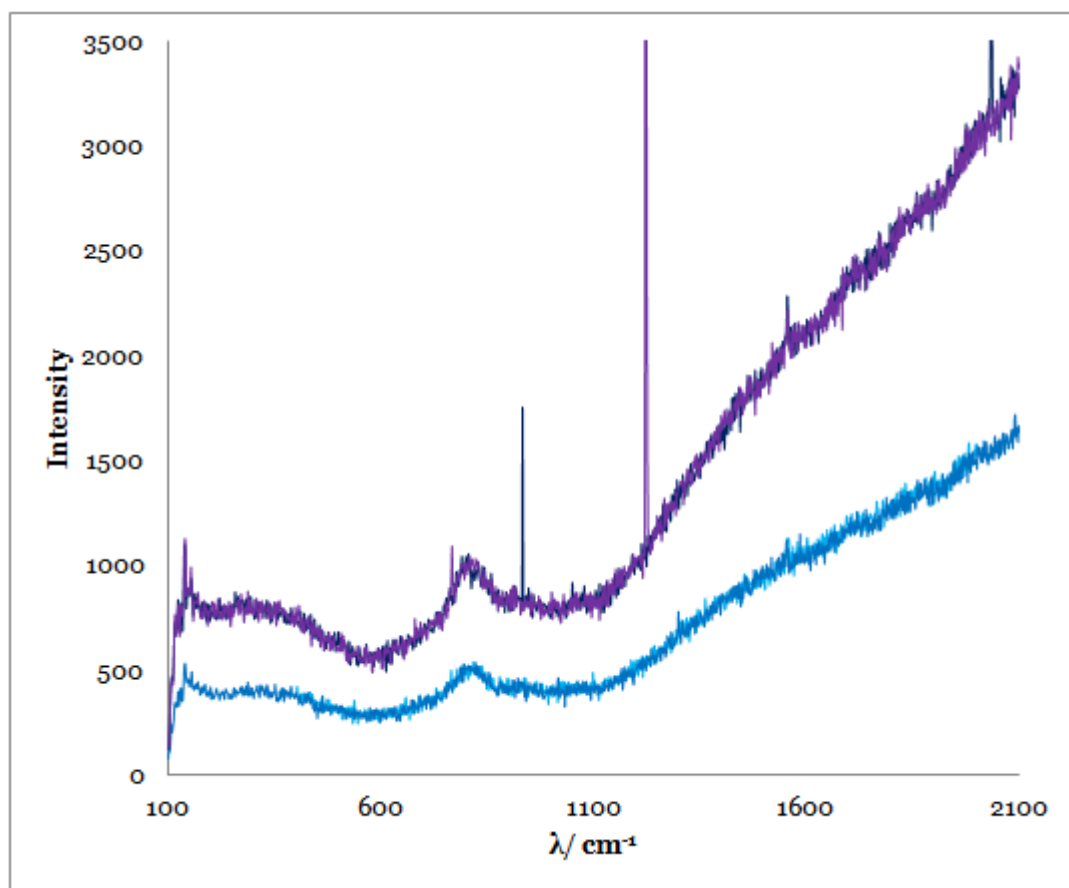


Figure 6.15; SERS of Au WE after application of negative potential in CO_2 saturated NMP with LiBF_4 (0.1 M). Blue and purple lines represent separate results from different areas of the darkened side of the electrode

The darkened, dull side's spectrum, figure 6.15 showed two features, one at 790 cm^{-1} and one, in a previously unexplored very low wavenumber region. The 790 cm^{-1} peak is not observed in the spectrum of the shiny side of the electrode. This could be due to the differences in bonding or adsorption on the shiny and darkened surface of the same species, however a peak associated with Li_2O_2 has been reported at 808 cm^{-1} which is well within the fairly broad peak.

The peak at 130 cm^{-1} is in a region not previously investigated and is due to the very low frequency signals from M-M bonds.

The *ex situ* spectra, despite offering the clearest SERS of Li^+ related species cannot be considered as reliable as *in situ* measurements as the surface species under investigation, dependent upon their nature, could be expected to alter to an extent upon removal from the solvent environment and exposure to air, during the cleaning and drying process and upon loss of applied potential to the electrode. The evidence of carbonate species is however consistent with the voltammetry and expected products from the reaction of CO_2 and lithium or lithium oxide species.

The initial point of the investigation was to establish whether tetraalkylammonium cations in CO_2 reduction offered any specific enhancement to the process. From the experimental results thus far, it is clear that any comparison with M^+ in the system employed within this work would reflect very favourably on the organic cations however it is possible that any ‘enhancement’ may in fact be due to the lack of the detrimental effect of M^+ on the electrode activity.

In an attempt to determine whether TBA^+ possesses ‘catalytic’ properties toward CO_2 reduction both TBA^+ and M^+ electrolytes were mixed in various proportions with the total supporting electrolyte concentration kept constant and CO_2 reduction performed to see if any TBA^+ related enhancement was still evident in the presence of M^+ . This was trialled employing both $\text{LiBF}_4/\text{TBABF}_4$ and $\text{NaBF}_4/\text{TBABF}_4$ systems with the same activity seen for both; as soon as M^+ was present CO_2 reduction currents observed were lower than those seen in the pure

TBA⁺ system. Once the ratio of M⁺ to TBA⁺ surpassed approximately 1:4, the voltammetry was dominated by M⁺ features. This can be seen in figure 6.16.

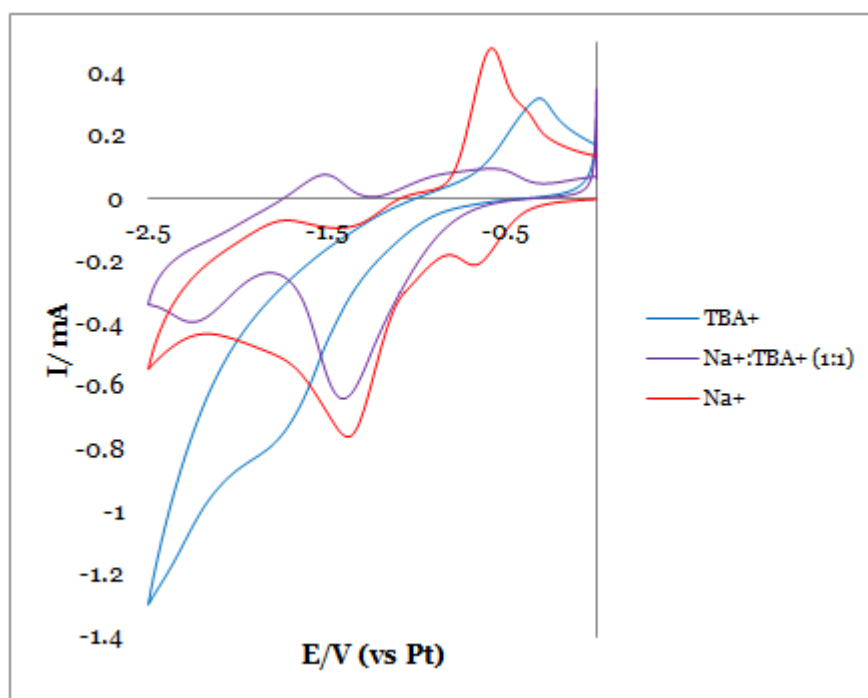


Figure 6.16; CV of CO₂ saturated NMP at Pt foil WE (approx 1 cm²) with TBABF₄ (0.1 M), TBABF₄:NaBF₄ 1:1 (0.1 M total supporting electrolyte concentration) and NaBF₄ (0.1 M) supporting electrolytes. Scan #1 shown. Scan rate 200 mV s⁻¹.

Although the Na⁺ and Na⁺:TBA⁺ mixture CVs do not overlay exactly they do clearly share important features such as the CO₂ related UPD peak at -1.3 V in figure 6.16 and where the CO₂ reduction in the pure TBA⁺ system is well underway, -1.7 V onward, it has yet to start in the mixture or Na⁺ system. Current densities of a similar magnitude are not observed until over a volt later as shown in figure 6.17.

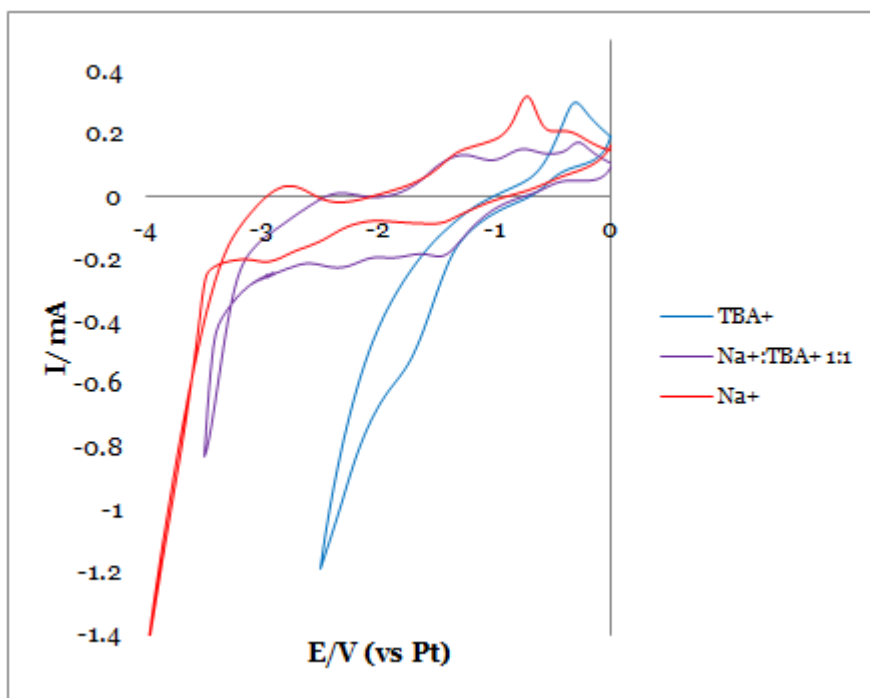


Figure 6.17; CV of CO₂ saturated NMP at Pt foil WE (approx 1 cm²) with TBABF₄ (0.1 M), TBABF₄:NaBF₄ 1:1 (0.1 M total supporting electrolyte concentration) and NaBF₄ (0.1 M) supporting electrolytes over different potential ranges. Scan #3 shown. Scan rate 200 mV s⁻¹.

The negative current densities after -3 V observed for the systems containing Na⁺ may well be due to metal ion reduction rather than CO₂ reduction.

This experiment strongly suggests that, rather than TBA⁺ having a positive effect on CO₂ reduction, it is the lack of M⁺ which is more significant in this system as insoluble films associated with M⁺ block CO₂ reduction at less negative potentials.

6.3. Conclusion;

From the investigation of the electrolyte identity upon CO₂ reduction in NMP it was established that the electrolyte behaviour was not necessarily purely that of a charge carrying entity with alteration of the cation employed within the system shown to result in considerable variation of CO₂ reduction potential and associated current response.

It was found in the NMP system at both gold and platinum electrodes that the TBA⁺ system showed considerably higher currents and lower overpotential for CO₂ reduction than when M⁺ was present (where M⁺ = Na⁺, Li⁺, Rb⁺). The rationale behind this was investigated with no evidence found for catalytic interaction of TBA⁺ with CO₂ however, suppression of reduction in the presence of M⁺ was decisively proven taking place well before the potential of M⁺ reduction to deposit M.

The mechanism by which this repression occurs was ascertained through CV and chronoamperometry with the array of M⁺BF₄⁻ and TBA⁺BF₄⁻ supporting electrolytes in the presence and absence of CO₂ combined with flame testing and Raman spectroscopy.

The study showed decisively that in presence of M⁺ and CO₂ persistent CO₂-incorporating M based films were rapidly formed on the electrode surface, resulting in no observable difference through examination of the surface by the naked eye, unlike those formed in the absence of CO₂ in non-protic solvent.

The deactivating films were formed at potentials substantially lower than CO₂ reduction in the presence of TBA⁺ therefore altering the electrode surface prior to 'direct' CO₂ reduction. CO₂ was found as part of the layers when just -1.0 V

was applied therefore a reactive species is presumably formed at this potential which reacts with CO_2 to give a reduced, yet electrode deactivating, inorganic ionic species (LiOCO_2 and Li_2CO_3 were detected via Raman but $\text{Li}_2\text{C}_2\text{O}_4$ and $\text{Li}_2\text{C}_2\text{O}_6$ expected depending upon CO_2 concentration and potential) which was found to be strongly adsorbed on the electrode surface and insoluble in NMP, acetone and water and not removable through sonication.

Where TBA^+ and M^+ were employed simultaneously in the system, the resultant voltammetry shared the majority of features with the pure M^+ system with CO_2 reduction repressed therefore supporting the conclusion that the ‘catalytic effect’ associated with TBA^+ may well be due to the comparison with the deactivated M^+ system, rather than any enhancement offered by the former.

7. Electrochemistry vs. NMR;

Electrochemical measurements are widely used to access diffusivity data of electroactive species providing an easily accessible and supposedly reliable way of quantifying diffusion as well as simultaneously imparting insight into kinetic and thermodynamic parameters of molecules in solution.

There are an array of possible electrochemical experiments from which the diffusion coefficient can be obtained with various degrees of accuracy afforded, however one of the most commonly implemented is cyclic voltammetry measured at a variety of scan rates with the peak current being related to the diffusion coefficient by the Randles-Sevcik equation (2.6).^[141]

Another extensively implemented electrochemical experiment for the investigation of diffusion is chronoamperometry where the current observed at a fixed potential as a function of time can be used with the Cottrell equation (2.15) to elucidate D .^[141]

A completely different, yet popular, technique for determining the diffusion coefficient of a species is diffusion ordered NMR spectroscopy (DOSY) which, as the name suggests, is a NMR technique where the signals of different species are separated according to their diffusion coefficient.^[132]

DOSY techniques measure the attenuation of NMR signals in a heterogeneous magnetic field using a pulsed field gradient spin echo (PFGSE) experiment. The degree of signal attenuation is a function of the magnetic gradient pulse

amplitude and occurs at a rate proportional to the diffusion coefficient of the analyte described by the Stejskal-Tanner relationship (7.1);^[202]

$$S = S_0 e^{-D\gamma^2 \delta^2 G^2 \Delta'} \quad (7.1)$$

where S is the spin signal amplitude, S_0 is the spin signal amplitude in absence of diffusion (constant), γ is the gyromagnetic ratio for the ^1H nucleus (constant), δ is the duration of the gradient pulse, G is the experimentally varied gradient amplitude and Δ' is the effective diffusion encoding delay. This effective delay is set as one of the experimental parameters and is defined as (7.2);

$$\Delta' = \left(\frac{\Delta - \delta}{3} \right) \quad (7.2)$$

In the above (7.2), Δ simply denotes the time between two pulses in the sequence.

7.1. Practical considerations in measurement method selection;

There are various practical advantages and disadvantages to both methods to consider such as;

- Cost and availability of the equipment
 - Not only does NMR require substantially more costly equipment and maintenance other considerations need to be made such as the acquisition of appropriate deuterated solvent, preferably with a dissimilar molecular weight to the analyte. It is important also to

consider the effect deuteration may have upon the solution behaviour including diffusion.

- Temperature range required
 - Convection induced by non-homogeneous solution temperature is more of a pronounced issue when moving away from ambient conditions and can lead to the collection of misleading data. There may be the need to implement additional experimental and data handling steps for both techniques, although particularly for DOSY, where in the absence of a concentration gradient to drive diffusion and the relative length of the data gathering, the random convective currents can have a high impact upon mass transport. It is possible to compensate for this by running convection compensated DOSY pulse sequences however this leads to the loss of signal amplitude with only half of the uncompensated signal detectable. The introduction of a convection component into the DOSY system may not be easily identifiable and lead to over-estimation of the diffusion coefficient. In electrochemistry, particularly cyclic voltammetry, the presence of significant convection would be observable in the form taken by the voltammogram, by the deviation from the typical diffusion limited peak shape, particularly at lower scan rates. The utilisation of a hydrodynamic technique such as rotating disk or flow cell, where a large controlled convective flow is generated, can render the contribution from naturally occurring random convection negligible.^{[141][142]} This has the additional benefit of yielding a

limiting steady state current rather than the less accurate peak current measurement.

- Time scale
 - DOSY provides a rapid and direct measurement of a diffusion coefficient from a single experiment once the pulse sequence desired is known whereas electrochemical determination, particularly through cyclic voltammetry, tends to rely upon a set of data being gathered through several experiments and the subsequent analysis of the data obtained.
- Prior knowledge of the system
 - For interpretation of electrochemical data to yield an accurate diffusion coefficient the area of the working electrode, concentration of analyte and the number of electrons transferred must be known. For NMR the availability of a known diffusion coefficient within the system is important for calibration, usually the solvent however is known. Any tendency of the analyte to undergo self association or interaction with the solvent or electrolyte is also valuable knowledge for both methods of determination, as any complex formation will result in the dimension, the shape and consequently the diffusion coefficient changing.

There is another significant factor for consideration when attempting to quantify diffusion within a system; the differing measurement techniques provide access to different diffusion coefficients.

7.1.1. Mutual Diffusion Coefficient

Diffusion in the presence of a concentration (or chemical potential) gradient, as described above by Fick's diffusion equations (2.1 & 2.2), results in net transport. Standard cyclic voltammetry (at a macro electrode with usual electrochemical concentrations and unstirred solution) is a prime example of this. At the electrode's surface during the redox process the concentration of the analyte is always very low. The electron transfer to or from the electrode means the analyte is constantly interacting to form different species, therefore being effectively removed or consumed creating a concentration gradient. Diffusion to the electrode from the bulk solution is driven by this deficiency in the analyte in the vicinity of the electrode and in most cases (except where there are slow electron transfer kinetics relative to mass transport) is the rate determining step and limits the peak current obtained.

This concentration gradient means the system is not in equilibrium with the diffusion resulting in an increase in the entropy of the system as it brings the system closer to equilibrium. It is designated mutual, inter or chemical diffusion, with its quantification termed the mutual (inter or chemical) diffusion coefficient.

7.1.2. Self Diffusion Coefficient

Diffusion is still present in the absence of a concentration (or chemical potential) gradient and is the random spontaneous mixing of molecules termed self, intra or tracer diffusion. For mutual diffusion to occur the system cannot be

in equilibrium, conversely here self diffusion can occur under equilibrium conditions. DOSY is a non-invasive analytical technique through which the innate chemical environment of the sample is preserved throughout the experimental analysis and allows for the relatively straightforward measurement of the self diffusion coefficient, D^* . The magnetisation, excitation and relaxation undergone by the analyte molecules through the course of the measurement does not strongly affect the random motion within solution for most species, with the incorporation of specific pulse sequences into the experiment allowing offset of magnetisation induced deviation in behaviour in those cases where it is necessary.

7.1.3. Relationship between mutual and self diffusion coefficients;

At infinite dilution values the self and mutual diffusion coefficients are identical;^[203]

$$D = D^* \quad (7.6)$$

However the practical application of such a relationship is challenging due to the defining and subsequently, working in infinite dilution.

The inter-relation of the mutual and self diffusion coefficients in a non ideal binary mixture is described by the following (7.7);^{[203][204]}

$$D = D^* \left\{ 1 + \frac{d \ln \gamma_i}{d \ln x} \right\} \quad (7.7)$$

In equation (7.7), $\left\{1 + \frac{d \ln \gamma}{d \ln x}\right\}$ is a thermodynamic factor within which γ is the activity coefficient and x is the corresponding mole fraction (which is directionally proportional to the concentration as shown in equation (7.9)). This is the factor defining the difference between diffusion coefficients. It can also be written in terms of the change in concentration, c_i and activity, a_i as seen in equation (7.8) derived as follows.

$$D = D^* + D^* \frac{c_i}{\gamma_i} \frac{d\gamma_i}{dc_i} \quad (7.7a)$$

$$da_i = \gamma_i dc_i + c_i d\gamma_i \quad (7.7b)$$

$$D = D^* \left(1 + \frac{da_i - \gamma_i dc_i}{\gamma_i dc_i}\right) \quad (7.7c)$$

$$D = D^* \left(\frac{da_i}{\gamma_i dc_i}\right) \quad (7.7d)$$

$$D = D^* \frac{c_i}{a_i} \left(\frac{da_i}{dc_i}\right) \quad (7.7e)$$

$$D = D^* \frac{d \ln a_i}{d(\ln c_i)} \quad (7.8)$$

The interconversion of these relies upon Raoult's and Henry's laws, a form of which is given in equation (7.9) which define activity in terms of concentration.^{[205][206]}

$$a_i = \gamma_i \frac{c_i}{c_i^\theta} \quad (7.9)$$

In equation (7.9) c_i^θ is the unit of concentration (1 mol dm⁻³ or 10³ mol m⁻³) included to preserve the lack of dimensionality of the activity. γ is the activity coefficient, a correction factor quantifying deviation from ideal behaviour.

At very low concentrations, the activity and concentration are interchangeable as seen in equation (7.10).

$$a_i \approx \frac{c_i}{c_i^\theta} \quad (7.10)$$

The definition of 'low concentration' is however again, non-quantitative.

D is not constant and can deviate from D^* if the activity coefficient, γ_i , varies significantly over the concentration gradient which produces diffusion. If the variation is not pronounced over the concentration range in question the following inequality (7.11) holds true, under which conditions D is assumed constant and equivalent to D^* .

$$\left(\frac{c_i}{\gamma_i}\right) \left(\frac{\partial \gamma_i}{\partial c_i}\right) \ll 1 \quad (7.11)$$

These diffusion laws rely on assumptions of ideal behaviour of solutions and are applicable only when analyte concentration is in the appropriate range and activity or intermolecular interaction is not altered through the experimental process through which the diffusion coefficient is measured.

7.2. Diffusion Ordered Spectroscopy (DOSY); Diffusion of $\text{Mo(CO)}_4\text{bpy}$

Comparisons of diffusion coefficients experimentally gathered by both electrochemical and NMR techniques are under-represented in the literature with systems investigated often being significantly altered between the two techniques as discussed in section 1.5.^{[133]-[135]}

No published diffusion coefficients have been reported for $\text{Mo(CO)}_4\text{bpy}$, the catalytic species of interest. Various equations which can be used to estimate this parameter exist, for example the Stokes-Einstein equation (2.3), however DOSY-NMR has the potential to provide an almost instantaneous and accurate measurement.

7.2.1. Diffusion Ordered Spectroscopy; Diffusion of $\text{Mo(CO)}_4\text{bpy}$ in the absence of electrolyte

The system investigated electrochemically was measured using DOSY-NMR by simply swapping the solvent (THF) for its deuterated analogue ($\text{d}_8\text{-THF}$ or TDF) with the concentration of analyte and temperature kept consistent. In contrast to the electrochemical measurements however, electrolyte was not added to the solution. This was decided for several reasons;

- The presence of tetrabutylammonium ions, particularly at the relatively high concentration used for electrochemical measurements would mean the introduction of a lot of protons into the system making the spectrum much more complicated.

- Tetrabutylammonium tetrafluoroborate and $\text{Mo(CO)}_4\text{bpy}$ have similar radii ($\sim 5 \times 10^{-10} \text{ m}$)^[53] and molecular masses (329 g mol^{-1} compared to 364 g mol^{-1}), which is not desirable for DOSY as it can make the identification of discrete signals more challenging.
- The most recent literature exploring the comparison of NMR and electrochemically-derived diffusion coefficients used a very similar electrolyte (tetrabutylammonium perchlorate, TBAP rather than TBABF_4) and non-aqueous solvent system. This report stated that the presence or absence of electrolyte had no effect upon the diffusion coefficient values obtained.^[135]

The DOSY experiment was carried out in a heterogeneous magnetic field by applying a series of gradient spin echoes. The spins experienced a different magnetic field as a result of their position in the sample tube. Due to self diffusion, the 180° pulse of the spin echo did not refocus all of the magnetisation, which led to an attenuated signal as the gradient amplitude was varied as seen in figure 7.1.

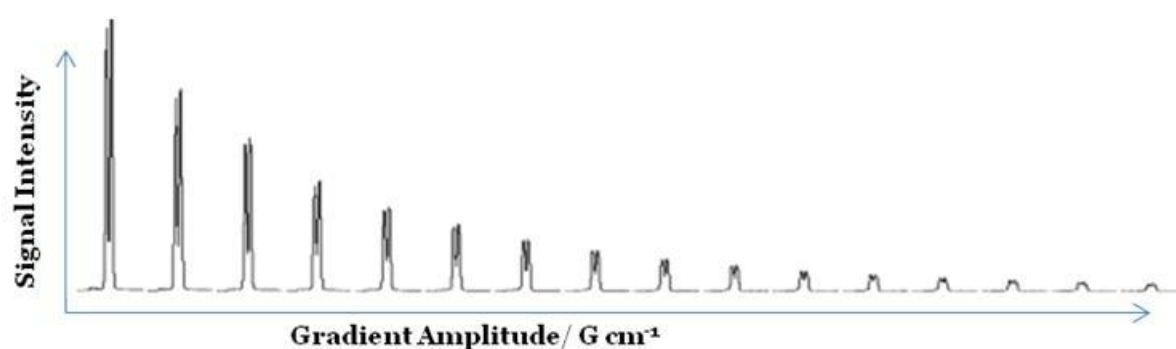


Figure 7.1; Experimental data from the $\text{Mo(CO)}_4\text{bpy}$ experiments showing the attenuation of NMR signal for the varied gradient amplitudes trialled.

The amplitude of the attenuated signals measured as a function of gradient amplitude are fitted using the Stejskal-Tanner relationship, equation (7.1), to yield the DOSY-NMR spectrum seen in figure 7.2 where the diffusion coefficient is plotted against the chemical shift of the signal.

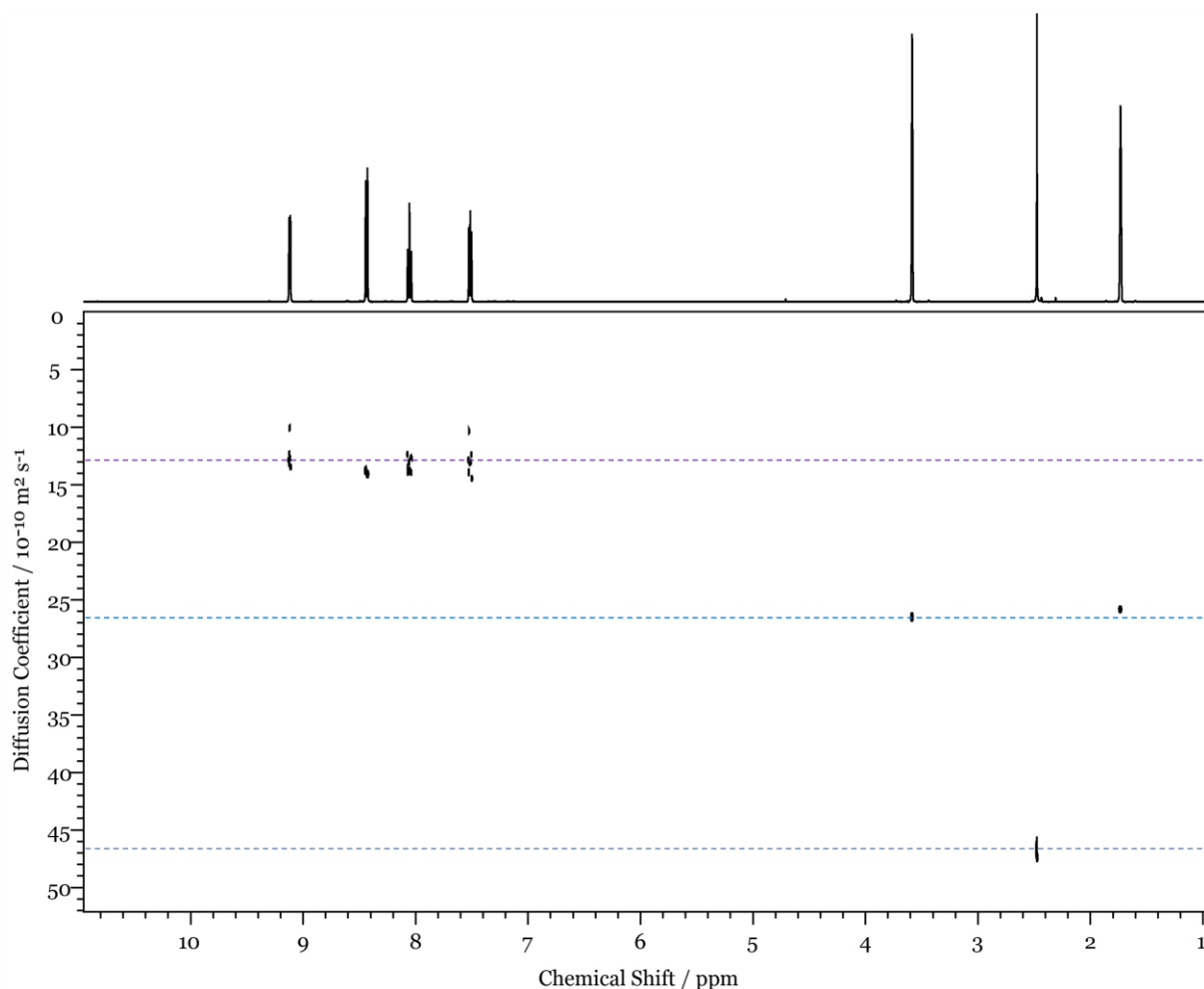


Figure 7.2; DOSY-NMR spectrum of $\text{Mo(CO)}_4\text{bpy}$ (0.5 mM) in $\text{d}_8\text{-THF}$

The species observable with diffusion coefficients of approximately 2.65 and $4.69 \times 10^{-5} \text{ cm}^2 \text{ s}^{-1}$ (plotted as 26.5 and $46.9 \times 10^{-10} \text{ m}^2 \text{ s}^{-1}$) are attributed to the solvent, a result of the non-fully deuterated content of the THF and trace water contamination, respectively. The self diffusion coefficients of THF and $\text{d}_8\text{-THF}$ in $\text{d}_8\text{-THF}$ are available in the literature and are quoted as $2.84 \times 10^{-5} \text{ cm}^2 \text{ s}^{-1}$ for the normal (protonated) THF and $2.61 \times 10^{-5} \text{ cm}^2 \text{ s}^{-1}$ for the corresponding

deuterated material at 25°C, so the observed experimental values are in good agreement with this.^[207]

These solvent molecules are much smaller and more mobile than both the bulky Mo(CO)₄bpy species in solution resulting in their significantly higher diffusion coefficients as expressed in the Stokes-Einstein equation (2.3), diffusivity (*D*) is inversely proportional to the molecular radius of the diffusing species (*r*).

From this the importance of dynamic viscosity of the solvent becomes apparent. The substitution of the solvent protons by deuterons does lead to a change in viscosity with d₈-THF having a dynamic viscosity 0.411-0.557 cP between 15 and 45°C^[207] and the viscosity of un-deuterated THF lying in the range 0.402-0.5250 cP over the same temperature interval,^{[207][208]} however as these viscosities are known this can be corrected for accurately as seen later.

The region of interest containing the signals due to the molybdenum complex is found in the left hand section of figure 7.2 with chemical shift values of between 7.4 to 9.2 ppm.

There are four signals seen which correspond to the four different proton environments within the Mo(CO)₄bpy complex which are highlighted in figure 7.3.

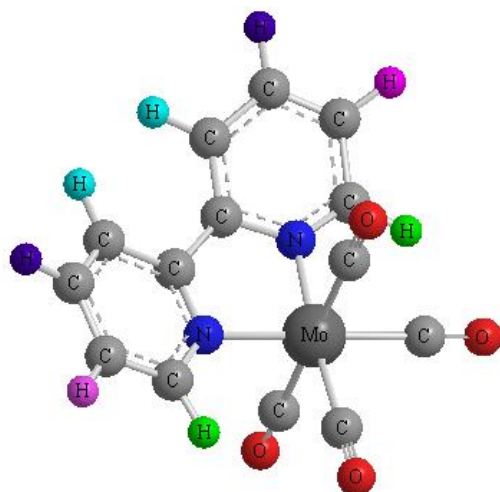


Figure 7.3; Molecular structure of $\text{Mo}(\text{CO})_4\text{bpy}$ illustrating the different proton environments.

The green, pink, blue and turquoise protons of the bipyridyl group emphasise the four different environments which account for the presence of four peaks. From the one dimensional NMR spectrum across the top of figure 7.2 it can be seen these signals are split into two sets of doublets and two triplets. Two of the proton environments (green and turquoise) have only one neighbouring spin $\frac{1}{2}$ nuclei therefore are split once to give doublets of 1:1 intensity, and two of the proton environments (pink and purple) have protons each side therefore experience coupling to both and the signal is split to give the observed 1:2:1 triplets. The peaks widths in the diffusion dimension are determined by the standard errors, σ_D , and were fairly small therefore showed a good statistical fit.

From the measurement in $\text{d}_8\text{-THF}$ the diffusion coefficient was found to be $1.29 \times 10^{-5} \text{ cm}^2 \text{ s}^{-1}$. The viscosity change between the deuterated and protonated solvents can be accounted for, as stated above, via the Stokes-Einstein equation and quite simply a correction factor for the dynamic isotope effect upon viscosity η_r given in equation 7.12;^[207]

$$\eta_r = \frac{\eta_D}{\eta_H} \quad (7.12)$$

η_D is the dynamic viscosity of the deuterated solvent and η_H is the viscosity of the normal solvent, which in this instance were for d₈-THF (0.501 cP) and THF (0.464 cP) at 25°C giving a diffusion coefficient for Mo(CO)₄bpy in THF as 1.39 × 10⁻⁵ cm² s⁻¹.

This value is somewhat higher than the electrochemically determined D value of 9.9 × 10⁻⁶ cm² s⁻¹.

A potential source of this disagreement in the values obtained was the difference between the systems investigated. The addition of electrolyte to the solution was investigated to see if its effects were indeed negligible, the results of which can be seen in figure 7.4.

7.2.2. Diffusion Ordered Spectroscopy; Diffusion of $\text{Mo(CO)}_4\text{bpy}$ in the presence of electrolyte

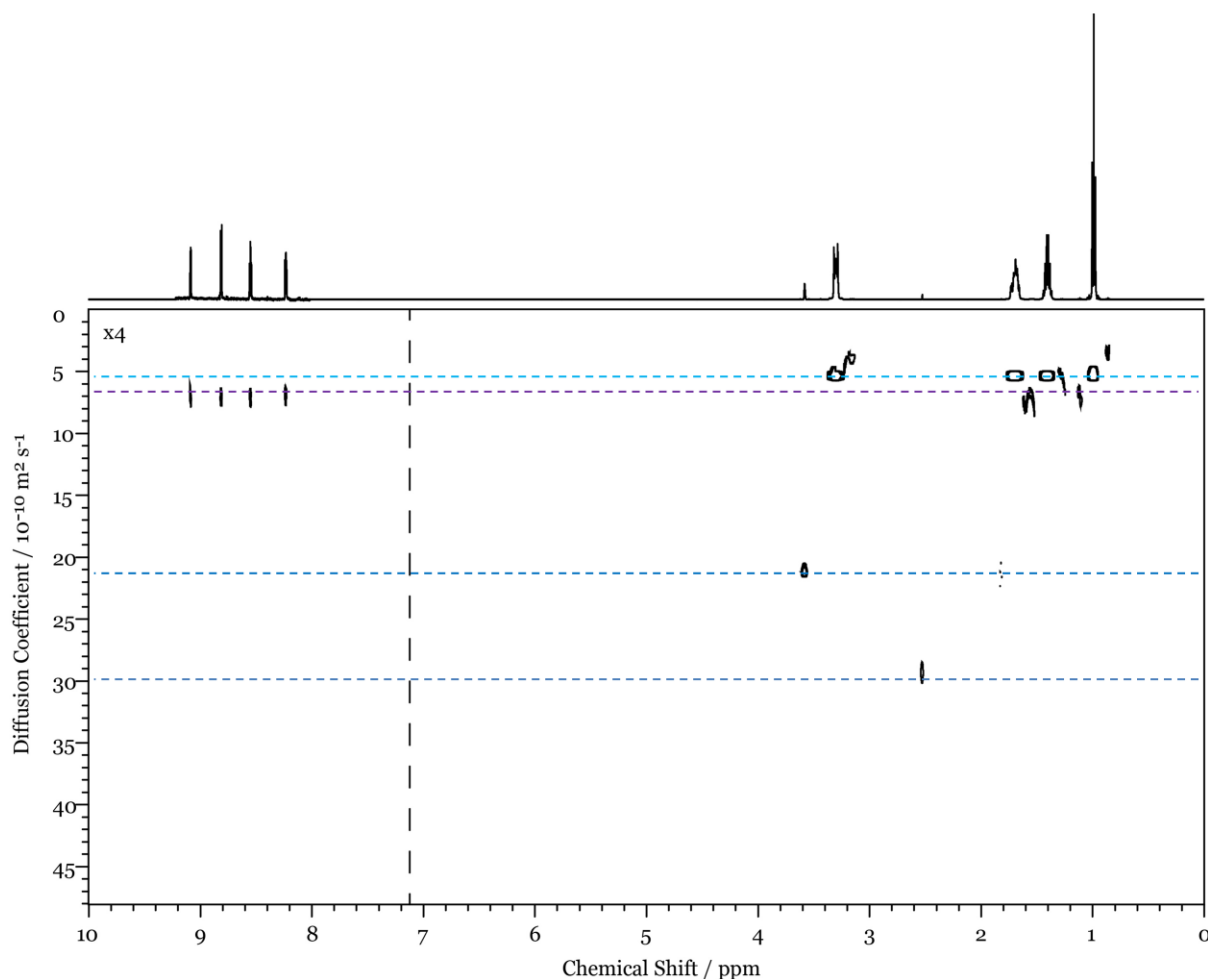


Figure 7.4; DOSY-NMR spectrum of $\text{Mo(CO)}_4\text{bpy}$ (0.5 mM) in $\text{d}_8\text{-THF}$ with TBABF_4 (0.1 M).

The cluster of signals found in the top right of the spectrum with a chemical shift of $\delta > 4$ ppm and D^* values of between 3 and $8 \times 10^{-6} \text{ cm}^2 \text{ s}^{-1}$ (or $\times 10^{-10} \text{ m}^2 \text{ s}^{-1}$ as plotted above) not seen in figure 7.2, are associated with the tetrabutylammonium cations. There are 36 protons per cation and 200 times the concentration of supporting electrolyte present as analyte, which explains the high intensity of these signals and their corresponding 2D peaks, seen along the top of figure 7.4, compared to those found with chemical shifts of > 8 ppm

associated with the $\text{Mo(CO)}_4\text{bpy}$ which, due to this huge intensity difference is plotted in a separate scale (magnification $\times 4$).

The signals previously observed due to the protons of $\text{Mo(CO)}_4\text{bpy}$ and the trace solvents are still found with the same chemical shifts however their diffusion coefficients have been altered with the addition of electrolyte resulting in seemingly pronounced differences for the smallest molecule, water (or more likely HDO) and the largest, $\text{Mo(CO)}_4\text{bpy}$. The diffusion coefficients obtained in the presence and absence of electrolyte are collected in table 7.1.

	$10^5 \times D^* / \text{cm}^2 \text{s}^{-1}$ DOSY $\text{d}_8\text{-THF}$	$10^5 \times D^* / \text{cm}^2 \text{s}^{-1}$ DOSY $\text{d}_8\text{-THF} +$ 0.1 M TBABF₄
$\text{Mo(CO)}_4\text{bpy}$	1.29	0.71
H_2O (or HDO)	4.69	2.90
THF (or $\text{d}_{(8-n)}\text{-THF}$)	2.65	2.12
TBA⁺	-	0.74

Table 7.1; Diffusion coefficients obtained using DOSY at 298.5 K

From table 7.1 it is clear all of the diffusion coefficient values obtained have dropped upon the incorporation of TBABF₄ to the system. This change in diffusion coefficient (ΔD) does not correlate with the drop expected if the viscosity of solution had been uniformly altered by the addition of electrolyte, as it is not apparently proportional to the molecular radii or mass of molecules.

The addition of electrolyte to the solution, particularly in the relatively high quantities to correspond with the voltammetric measurement concentration,

could be expected to lower diffusivity as the presence of the ions would cause hindrance and obstruction effects.

Another possible contributing factor is that the similarity of the chemical shift experienced by the water protons and those of the TBA⁺ means the signals may have experienced a degree of overlap, potentially resulting in perturbation in the diffusion coefficient values.

The diffusion coefficient calculated for TBA⁺ from the Stokes-Einstein equation (2.3) and a literature value for the ionic radius of the cation in solution^[53] gives a predicted $D^* = 9.1 \times 10^{-6} \text{ cm}^2 \text{ s}^{-1}$. Extrapolation of a value measured in DCE^[209] by correcting for the viscosity differences between the solvents gave $D^* = 1.18 \times 10^{-5} \text{ cm}^2 \text{ s}^{-1}$, both of which are above that acquired experimentally, which suggests that perturbation due to overlap may not be the case. If the amalgamation of discrete signals were to transpire the expectation would be for one D^* signal to increase and one to decrease resulting in a medial value for each, rather than the observed drop in both TBA⁺ and water diffusion, and would also fail to explain the effect on the Mo(CO)₄bpy value.

The addition of the electrolyte had a very pronounced effect upon the diffusion of trace water in the system. With an electrolyte containing small hard ions there would be an expectation of solvation, which would explain the shift in the diffusion behaviour of the water molecules, but the degree of solvation for the larger TBA⁺ (and smaller BF₄⁻) would be low, however this does not rule out the possibility of hydrogen bonding and other electrostatic interactions. The organometallic complex, Mo(CO)₄bpy, contains the electron-withdrawing bipyridyl group on one side of the molecule with electron donating carbonyl

groups occupying the other positions around the metal centre (as can be seen in figure 7.3) so would be expected to be a fairly polar species. THF although classified as a polar aprotic solvent, has a much lower relative permittivity^[53] than water so it is possible that the trend in ΔD may be reflective of the polarity and therefore degree of interaction with the charged electrolyte that the species exhibit with the trend seemingly $\text{Mo(CO)}_4\text{bpy} > \text{H}_2\text{O} > \text{THF}$.

The D^* value for $\text{Mo(CO)}_4\text{bpy}$ in the presence of electrolyte, once corrected for the viscosity change upon moving to the deuterated solvent, is $7.6 \times 10^{-6} \text{ cm}^2 \text{ s}^{-1}$.

Whatever the origin of the lowering of the observed diffusivity, when the values for $\text{Mo(CO)}_4\text{bpy}$ measured in the presence of electrolyte by NMR and electrochemistry are compared, even with the isotopic effects considered the DOSY value found was lower than the anticipated electrochemically evaluated $9.9 \times 10^{-6} \text{ cm}^2 \text{ s}^{-1}$.

It is, however, closer to this previously determined D value than the D^* found in the absence of electrolyte suggesting that either the electrolyte's associated viscosity effects or the hindrance expected from the presence of extra molecules in the self diffusion measurements are important in both techniques and consistency in the measurement media seems advantageous.

As the actual D value for the $\text{Mo(CO)}_4\text{bpy}$ complex is unknown in an attempt to verify the results a compound of known diffusion coefficient was trialled, namely ferrocene.

7.2. Ferrocene;

7.2.1. Introduction to Ferrocene;

Ferrocene, $\text{Fe}(\text{C}_5\text{H}_5)_2$ or Fc, consists of two cyclopentadienyl rings bound to an iron metal centre to give a sandwich compound as depicted in figure 7.5.

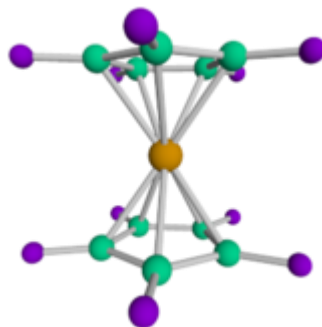


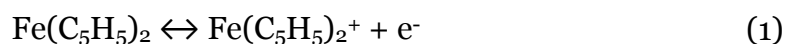
Figure 7.5; Structure of ferrocene

It is widely used in electrochemistry due to its stability and well defined accessible redox chemistry and is often implemented as an internal standard for calibrating potentials in non-aqueous systems (as discussed in the chapter 3). Accordingly, there are numerous literature values for the diffusion coefficient in an array of solvents and conditions available from electrochemical literature where it is considered an ideal system.

Ferrocene has a novel ^1H -NMR spectrum as all protons are equivalent resulting in a characteristic strong single resonance peak, consequently the NMR features have also been well documented with literature including DOSY spectra with several groups adopting it as a calibrant for D^* measurement, making it yet again an ideal system.^{[133][135][210]}

7.3.2. Electrochemical measurement;

The one electron oxidation of ferrocene to form the ferricinium cation (reaction 1) was studied in the THF-TBABF₄ system (cell 2) previously utilised for the study of Mo(CO)₄bpy.



The cyclic voltammetry for this process exhibits typical reversible characteristics with the voltammetric peak current ratio of reverse and forward scans equal to unity ($i_{\text{ox}}/i_{\text{red}} = 1$) over the time scales trialled as shown in figure 7.6.

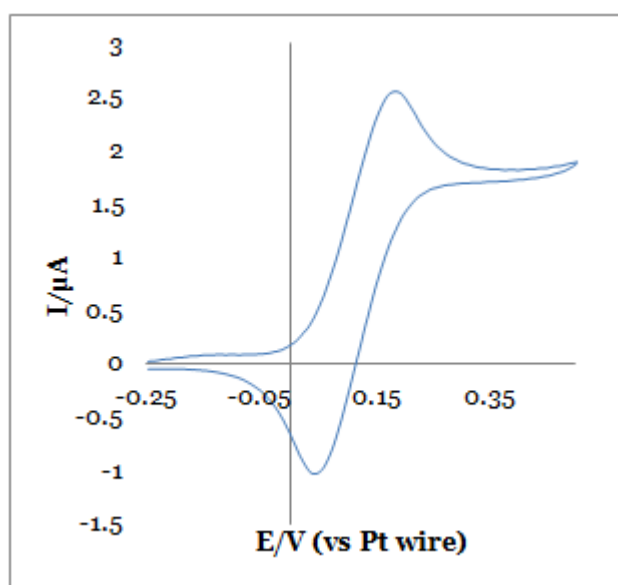


Figure 7.6; CV of ferrocene (0.5 mM) in cell 2 at 20 mV s⁻¹

In the cyclic voltammogram where the anodic and cathodic potentials of the ferrocene redox process are observable (figure 7.6) it is possible to see that despite appearing ideal, upon close inspection the peak separation ΔE , even at a scan rate of just 20 mV s⁻¹ is approximately twice the expected 59 mV^[141] for a

reversible one electron transfer ($\Delta E \approx 130$ mV). The number of electrons transferred is well known for this oxidation therefore this deviation from ideality is attributable to uncompensated resistivity of the solvent. A similar ΔE increase has been observed by other groups working in non-aqueous solvents with an ohmic drop often reported in non-aqueous voltammetry when compared to the more traditionally studied aqueous systems.^{[155][211]}

As well as being resistive, THF is prone to oxygen contamination upon exposure to air which, outside of an inert atmosphere, limits the use of a rotating disk electrode (RDE), which needs space for the electrode to rotate freely and therefore cannot be sealed. The RDE-THF system is unsuitable for investigation of negative potentials where oxygen reduction results in large current obscuring other responses, or oxygen sensitive electrochemical processes, however the oxidation of ferrocene is neither of these things.

As suggested in the experimental section, there are advantages to the use of hydrodynamic techniques such as RDE voltammetry, one of which is the steady state response obtained, with the limiting current offering a substantially more reliable measurement than the diffusion limited peak current response of cyclic voltammetry at a stationary electrode, as can be observed from the ferrocene response in figure 7.7.

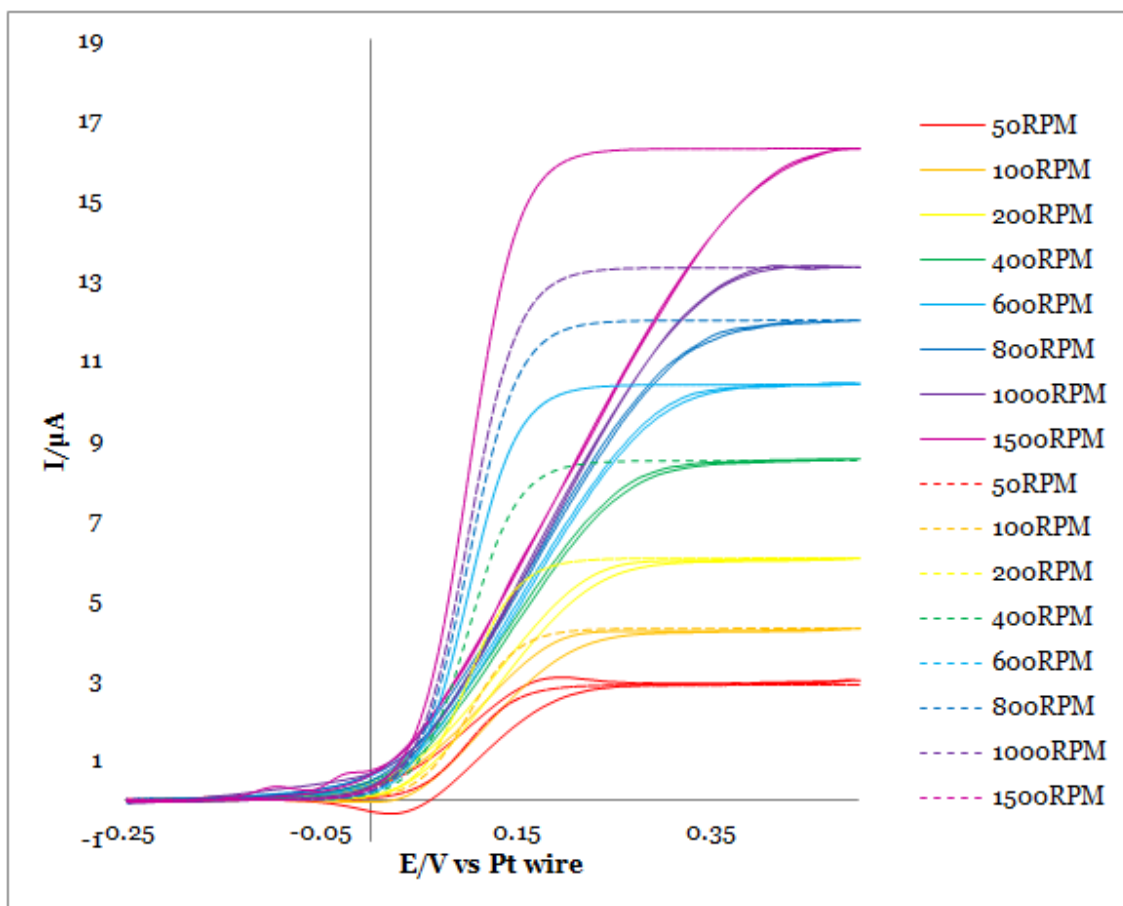


Figure 7.7; Cyclic Voltammogram of Ferrocene (0.5 mM) measured at a Rotating Disk Electrode (Au 2 mm diameter) in Ar saturated THF with 0.1 M TBA(BF₄) at room temperature and pressure. 1st scan shown. Scan rate= 10mVs⁻¹. At various rotation speeds. Experimental shown by unbroken lines and calculated ideal data shown by dotted lines.

The ideal data was calculated using equations (7.13) and (7.14):

$$I = I_l \frac{e^{\theta}}{(1 + e^{\theta})} \quad (7.13)$$

$$\theta = \frac{nF(E - E^0)}{RT} \quad (7.14)$$

where E is the applied potential, E^0 is the standard potential and R is the gas constant.

When the experimental and the ideal response in figure 7.7 are compared, the ideal (broken line) suggests that the steady state limiting current (I_l) for all

rotation speeds except 50 RPM, should be reached sooner, in time or potential, than is observed. As previously discussed with respect to increased ΔE (figure 7.6) this is attributed to resistive effects from the solvent. The electrode positioning for RDE voltammetry requires the working and counter electrodes to be sited further apart than in a traditional non-hydrodynamic setup in order to avoid disruption of the well defined velocity profile of the solvent to the RDE. This inevitably leads to a perturbation in the previously optimised experimental design minimising the solvent path-length between these electrodes.

The cyclic voltammogram (CV) measured at the slowest rotation speed, 50 RPM, seen in red in figure 7.7, shows peaks at the slowest rotation speed, 50 RPM, at 0.02 V and 0.18 V, which indicate that diffusion is still playing a role in transport. The peaks are lost as rotational frequency is increased and convection dominates. These features were also observed when the experiment was run with a higher concentration of ferrocene (5.0 mM compared to 0.5 mM).

As discussed in greater detail in the experimental techniques section, despite convection control a thin layer of solution remains relatively immobile at the electrode surface so the diffusion coefficient still features in the Levich equation (2.18).

The Levich plot of the data from the rotating disk (see figure 7.8), yields a diffusion coefficient for ferrocene of $1.4 \pm 0.01 \times 10^{-5} \text{ cm}^2 \text{ s}^{-1}$ which is in close agreement with the values available in literature measured in similar systems, where THF was employed as a solvent, by electrochemical techniques of $1.5 \times 10^{-5} \text{ cm}^2 \text{ s}^{-1}$ [141] and $1.8 (\pm 1) \times 10^{-5} \text{ cm}^2 \text{ s}^{-1}$. [212][213]

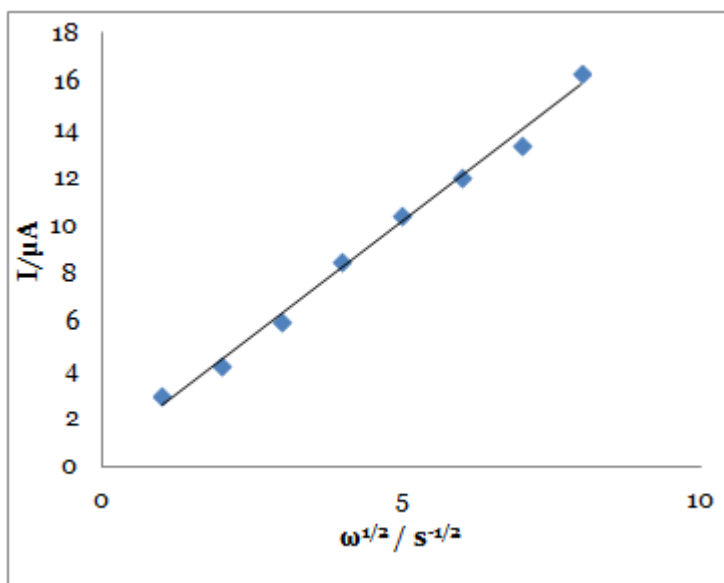


Figure 7.8; Levich plot corresponding to the data shown in figure 7.7. The line represents the linear regression obtained.

With the confirmation of the electrochemical diffusion coefficient value the corresponding DOSY systems were investigated both with and without the addition of electrolyte to the d_8 -THF.

7.3.3. DOSY measurement;

The experimental data was gathered in the same manner as that for the $\text{Mo}(\text{CO})\text{bpy}$ the resulting spectra are given in figure 7.9.

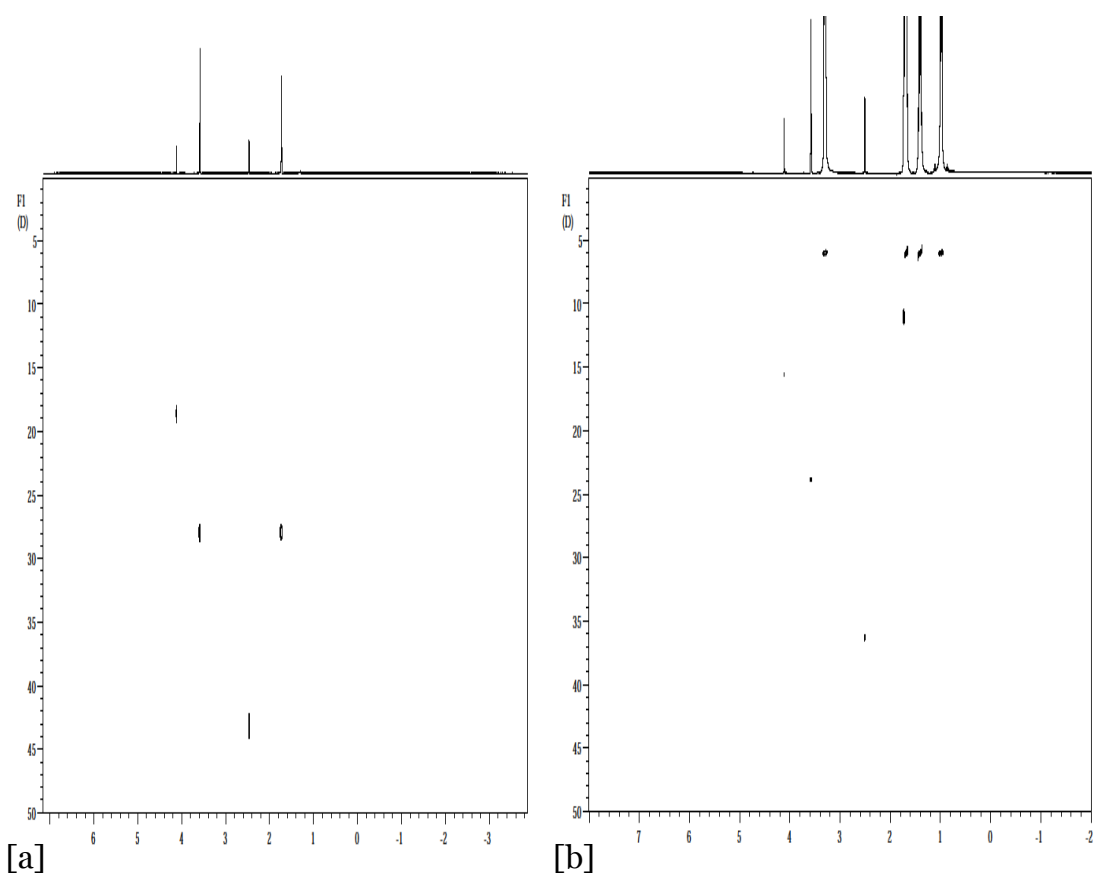


Figure 7.9; [a] Ferrocene DOSY without electrolyte. [b] Ferrocene DOSY with TBABF₄ (0.1 M) present.

From the above figure 7.9 depicting the DOSY spectra of ferrocene with and without the addition of electrolyte to the system, a shift in the diffusion coefficients obtained can be observed, as previously seen for the Mo(CO)₄bpy system.

The collected diffusion coefficient data for all of the system components is presented in table 7.2.

	$10^5 \times D^* / \text{cm}^2 \text{s}^{-1}$	$10^5 \times D^* / \text{cm}^2 \text{s}^{-1}$
	DOSY $\text{d}_8\text{-THF}$	DOSY $\text{d}_8\text{-THF} +$ 0.1 M TBABF_4
Ferrocene	1.86 ± 0.20	1.55 ± 0.027
H₂O (or HDO)	4.32 ± 0.34	3.63 ± 0.12
THF (or $\text{d}_{(8-n)}\text{-THF}$)	2.79 ± 0.18	2.39 ± 0.012
TBA⁺	-	0.59 ± 0.0048

Table 7.2; Diffusion coefficients obtained using DOSY at 298.5 K

This data relates to values for D^* for ferrocene in $\text{d}_8\text{-THF}$. When these values were transformed to correspond to standard non-deuterated THF, taking into account the slightly differing viscosities using equation 7.12, the electrochemical and DOSY values are directly comparable. The DOSY determined D^* value for Fc converted for THF without electrolyte was found to be $2.01 \times 10^{-5} \text{ cm}^2 \text{s}^{-1}$, whilst in the presence of electrolyte this dropped to $1.68 \times 10^{-5} \text{ cm}^2 \text{s}^{-1}$. The electrochemically measured, and literature supported, value of $1.4 \times 10^{-5} \text{ cm}^2 \text{s}^{-1}$ is reasonably close to the DOSY measurement with electrolyte, showing a deviation of 20%.

In deciding to support the values with added electrolyte there are some considerations which need to be made.

Ferrocene is a symmetrical molecule, unlike $\text{Mo(CO)}_4\text{bpy}$, therefore not in possession of a strong permanent dipole moment, potentially limiting the interaction of the ferrocene molecule with the electrolyte added when compared to the molybdenum complex in the analogous system. This could explain the lesser extent to which the addition of electrolyte affected the diffusion of

ferrocene compared with $\text{Mo}(\text{CO})_4\text{bpy}$ DOSY experiments, with ferrocene experiencing a mere $1/6^{\text{th}}$ decrease and $\text{Mo}(\text{CO})_4\text{bpy}$ D^* dropping by almost a half upon addition of the same concentration of the same electrolyte to the same solvent.

There is a possibility that the addition of electrolyte has a notable impact upon the viscosity of the solvents used for measurements. Initial measurements made on THF with and without 0.1M TBABF_4 electrolyte showed an drop in viscosity by approximately 10% upon addition of electrolyte.^[214]

Addition of salt to water has very pronounced effects upon its physical properties so does not seem unreasonable that the tetrabutylammonium salt may impact upon the intermolecular forces, particularly those which are electrostatic in character such as hydrogen bonds, within THF.^[136]

10% is smaller than the alteration in D experienced by the Fc indicative of other contributing factors as well as the effect of viscosity (assuming the initial data is correct).

7.4. Ferrocene derivatives, the effect of charge;

The tentative conclusion reached through the measurement of ferrocene, with and without electrolyte, left questions regarding the applicability of DOSY as a complementary technique to electrochemistry for diffusivity measurement. The effects of analyte charge within a simpler aqueous system were duly investigated in case the deviations from the expected behaviour within the $\text{Mo}(\text{CO})_4\text{bpy}$ system were associated with polarity, the presence of charge would be expected

to alter significantly the diffusion coefficients evaluated with the different methods.

A set of three similar complexes were investigated using both methods. The compounds examined were all ferrocene derivatives with one cationic, one neutral and one anionic species the structures of which can be seen below in figure 7.10.

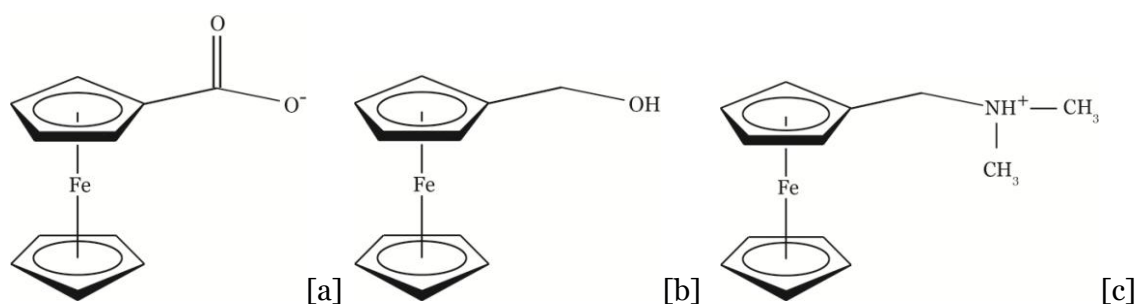


Figure 7.10; Structures of the Ferrocene derivatives; [a] deprotonated ferrocene carboxylic acid (FcCOO⁻), [b] ferrocene methanol (FcMeOH) and [c] protonated dimethylaminomethyl ferrocene (FcN⁺).

As the use of organic solvent for electrochemical measurements presents a source of potential error, through resistivity and ease of contamination, as well as introduces experimental challenges, the compounds selected were all soluble (albeit the FcN⁺ required the presence of acid) in aqueous solution allowing the study in H₂O and D₂O systems negating the usage requirement for the more costly and challenging THF and d₈-THF.

This shift away from the non-aqueous system provided the opportunity for the electrochemical measurements to be made in not only the non-deuterated analogous solvent, but also in an identical solution as the NMR measurements. Furthermore D₂O as a solvent has been shown to be much less prone to convection than d₈-THF which allowed the introduction of temperature

controlled experiments as the temperature could be raised slightly above room temperature. The NMR measurements used thermocoupling to the probe to set the experimental temperature with the electrochemical measurements carried out in a thermostatically controlled water bath. Adequate time was given to ensure the optimal sample temperature equilibration prior to measurement.

The electrochemical measurements to deduce the diffusion coefficients of the ferrocene derivatives in aqueous and deuterated or 'heavy water' systems were carried out via cyclic voltammetry at a variety of scan rates and by chronoamperometric double steps techniques. The supporting electrolyte, potassium chloride (KCl), avoided the incorporation of additional protons into the system, minimising the complexity of the DOSY spectra. The concentration of electrolyte and analyte were kept consistent with the THF experiments, 0.1 M and 0.5 mM respectively. Addition of sodium hydroxide (1.0 mM) to the ferrocene carboxylic acid [a] solution increased the pH of the solution to 11.29 so the complex, with a pK_a of 4.2^[215] was deprotonated ($FcCOO^-$). No acid or base was added to the ferrocene methanol [b] solution, pH 8.97 to leave this as a neutral molecule ($FcMeOH$)^[216].

Hydrochloric acid was added to the dimethylaminomethyl ferrocene [c] solution to lower the pH to allow protonation of the complex of $pK_a = 9.84$ (FcN^+).^[217] Initial experiments with the addition of ~10 mM HCl, resulting in a solution of pH 2.25, led to apparent D values orders of magnitude higher than those seen for $FcCOO^-$ and $FcMeOH$ despite the anticipated similarity.

This phenomenon was thoroughly investigated and was found consistently in a wide variety of experimental conditions including at a rotating disk electrode, at

varied electrode material and sizes, through variation of electrolyte concentration and showed a dependence upon analyte concentration in both voltammetric and chronoamperometric determination yet no evidence of adsorption, convection or anything other than the expected one electron reversible redox process.

The source of the overestimation was eventually identified as due to inadequate buffering of the acidic solution.

Despite the low bulk pH, the pH experienced in the solution near to the electrode surface may differ considerably.^{[53][141][218]} The potential of zero charge for a gold electrode in chloride ion solution under acidic conditions is -0.07 V vs. NHE^[219] which translates as -0.269 V vs. Ag/AgCl. This means that for the duration of the electrochemical experiments the working electrode is positively charged resulting in double layer effects.

The chloride ion distribution would be expected to be strongly affected in order to balance the electrode charge, becoming specifically adsorbed upon the positive gold surface to form the inner Helmholtz layer, an outer Helmholtz layer of non-specifically adsorbed solvated chloride ions, and diffuse layer where a higher proportion of anions are found attracted by the strong electrostatic forces compared to those of the bulk solution.

The protons in the vicinity of the electrode would be expected to experience electrostatic repulsion resulting in a localised pH increase.

This region is very small with the entire diffuse layer in standard electrolyte solutions less than $\sim 100 \text{ \AA}$,^[141] making up a tiny fraction of the diffusion layer (where the concentration of ions is different to the bulk solution), however any

electron transfer process with the electrode requires the analyte to traverse this region.

It was discovered that the use of the same electrolyte and acid in the H₂O system, but in a concentration ratio which allowed for more effective buffering of the pH of the solution, (1:4, HCl:KCl)^[220] the values obtained for the diffusion coefficient were found to be in the expected magnitude range. The exact reason for this alteration in behaviour is not immediately obvious however is attributed to the system having increased aptitude to compensate for localised pH changes. The addition of the amended electrolyte/acid concentration to the D₂O FcN⁺ system however did not show evidence of the same buffering ability as in H₂O with the electrochemical diffusion coefficient values showing a clear FcN⁺ concentration dependence as can be seen in figure 7.11.

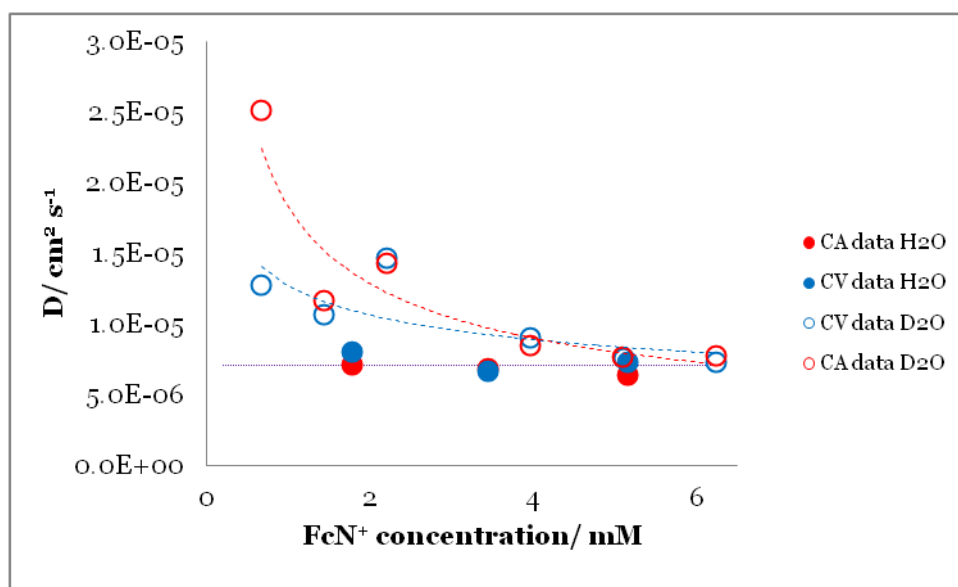


Figure 7.11; Diffusion coefficients obtained for FcN⁺ in the 'buffered' H₂O and D₂O systems.

The difference in intrinsic properties between H₂O and D₂O is rather pronounced with one of the best documented being the deviation in pH vs. pD and the lowered acidity of acids in D₂O compared with H₂O.

The stabilising effect on the diffusion coefficient seen by the buffering of the H₂O system, where consistent *D* values were obtained at all concentrations trialled, is not observed in the D₂O. Figure 7.11 shows that at low concentrations of FcN⁺ (< ~4 mM) the diffusion coefficient values obtained via CV and CA techniques are erratic and much higher than those found at higher FcN⁺ concentrations where the values appear to level out (> ~4 mM). The decision to include the higher concentration data for FcN⁺ in D₂O, where the *D* values are no longer changing dramatically, rather than attempting to better buffer the D₂O solution was made so as to obtain what appears to be more reliable, reproducible data than the low concentration without venturing further into the complex and often controversial area of pH/pH^{*}/pD measurement and interconversion.

7.4.1. Cyclic Voltammetry;

Cyclic voltammetry over the potential range corresponding to the first oxidation for each of the complexes was undertaken with scan rates varied from 10 mV s⁻¹ to 1000 mV s⁻¹ an example of which can be seen below in figure 7.12.

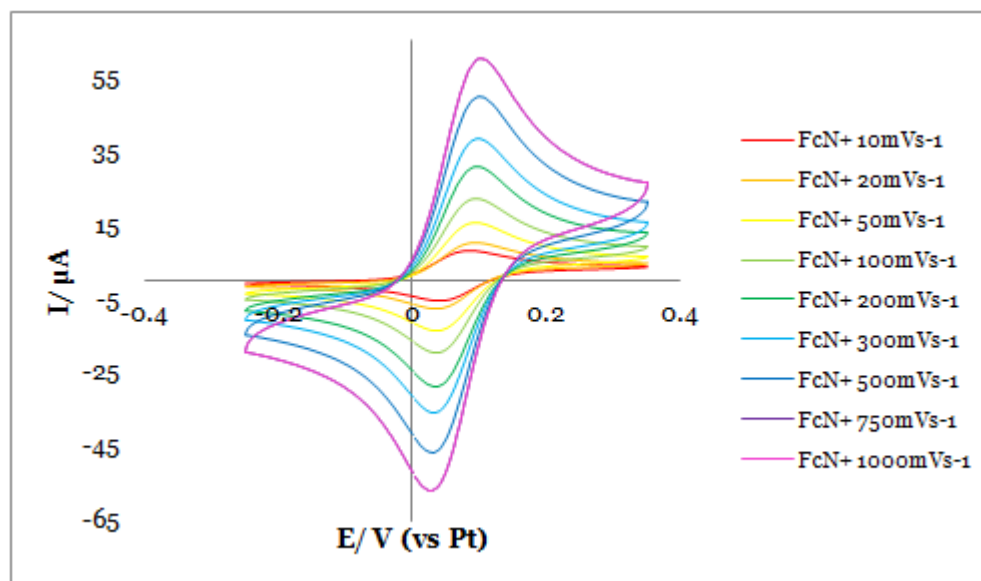


Figure 7.12; Cyclic Voltammogram of dimethylaminomethyl ferrocene, FcN^+ at various scan rates. (0.5 mM) at various scan rates in H_2O with KCl (0.16 M) and HCl (0.04 M) measured at 30°C . Gold WE (2 mm diameter), Pt pseudo reference electrode and counter.

Figure 7.12 is typical of all of the different ferrocenes' voltametric responses with FcCOO^- , FcMeOH and FcN^+ all giving seemingly ideal reversible diffusion limited voltammetry. Figure 7.13 (a) shows the ratio of the oxidative and reductive currents to be very close to one for all scan rates and (b) the peak separation remaining close to the ideal value of 59 mV for a one-electron transfer.

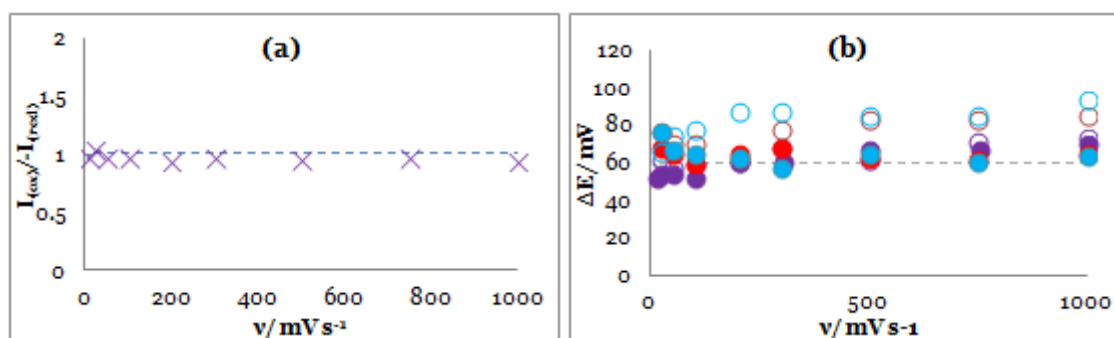


Figure 7.13; (a) Peak current ratio, $I_{(\text{ox})}/-I_{(\text{red})}$ and (b) Peak separation, ΔE , as a function of scan rate from the CV data for FcN^+ • seen in figure 7.11 and experimental data from analogous experiments with the stated conditions for FcMeOH • and FcCOO^- •. The solid circles represent the H_2O data, hollow ones the equivalent D_2O data.

From figure 7.13 (b) the peak separation for the measurements made in D₂O tends to be larger than for those made in H₂O for the same complex, particularly at higher scan rates as seen by the hollow data points dominating the higher ΔE region on the plot for everywhere except the slower 20-50 mV s⁻¹ scan rate data.

This larger peak separation is attributed to the difference in viscosity between the two solvents. D₂O has a viscosity ~20% higher than that of H₂O at room temperature due to dynamic isotope effect. Upon moving from H₂O ($M_r = 18.02$ g mol⁻¹) to D₂O ($M_r = 20.03$ g mol⁻¹), although the change in mass is proportionally quite considerable, this cannot fully explain the even larger viscosity deviation. The difference in viscosities is due also to the extent of hydrogen (or more accurately equivalent deuterium) bonding within D₂O. D-bond strength is greater within D₂O than the H-bond in H₂O as due to its restricted atomic vibrations the effect of the van der Waals repulsive core on overall hydrogen bonding is reduced, compared to that experienced in H₂O, resulting in stronger bond formation.^[221]

Other effects of deuteration observed through conducting the electrochemical measurements were lower solubility of the electrolyte and analyte compared with the water system with some of the solutions requiring slight sonication.

Deviation from the ideal peak to peak separation value of 59 mV per electron transferred is a fairly regular occurrence within measurements made in viscous or otherwise resistive solvents (or as a result of non-ideal electrode placement) for reversible systems particularly at high scan rate, as such the D₂O data seen in figure 7.13 (b) is in keeping with the expected, if not ideal, voltammetric response.^[141]

A linear relationship was observed between the peak current and the square root of the scan rate, as shown in figure 7.14, the linear regression of which allowed calculation of the diffusion coefficient, according to the Randles-Sevcik equation (2.6).

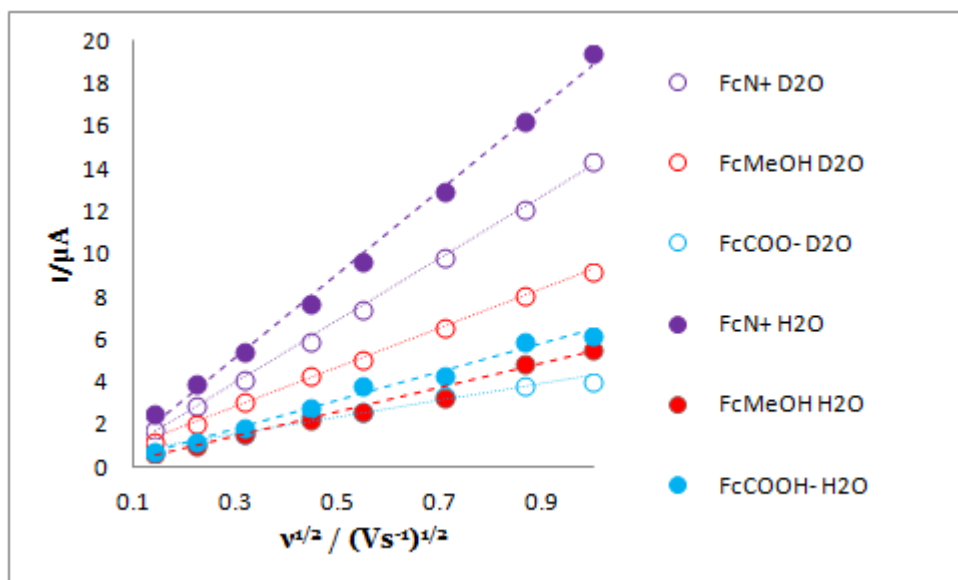


Figure 7.14; Randles-Sevcik plot for approximately 0.5 mM ferrocene derivatives (FcMeOH, FcCOO⁻, slightly higher 1.2 mM for FcN⁺) in H₂O (solid) and D₂O (hollow)

It can be seen from figure 7.14 that the data showed reasonably good linear correlation with R^2 values ranging from 0.9996 to 0.9713 (where R is the linear correlation coefficient).

Cyclic voltammetry is often better employed as a technique for qualitative studies of behaviour rather than for reliable quantitative assessment of the system which was reflected in the D values evaluated from this data given in table 7.3.

		D ($\times 10^{-6} \text{ cm}^2 \text{ s}^{-1}$)	R^2 value range [# of repeats]	σ ($\times 10^{-6} \text{ cm}^2 \text{ s}^{-1}$)
FcCOO⁻	H ₂ O	2.6 ± 0.04	0.9857-0.9980 [3]	0.10
	D ₂ O	5.3 ± 0.09	0.9713-0.9911 [2]	3.2
FcMeOH	H ₂ O	8.6 ± 0.1	0.9840-0.9984 [2]	4.8
	D ₂ O	4.1 ± 0.07	0.9984-0.9994 [2]	0.44
FcN⁺	H ₂ O	8.0 ± 0.01	0.9993 [1]	-
	D ₂ O	7.4 ± 0.02	0.9979 [1]	-

Table 7.3; Diffusion coefficients for ferrocene derivatives measured via cyclic voltammetry for both H₂O and D₂O systems. R^2 obtained from Randles-Sevcik plot analysis (where R is the correlation coefficient).

One of the most fundamental trends expected for this data is for the D values in the high viscosity D₂O to be below those found in the less viscous H₂O, which as seen in the above table 7.3, was not found to be the case for all three complexes. FcCOO⁻ showed an apparent D value in water of only half of that found in deuterium oxide.

As well as this deviation from expected behaviour the reproducibility of the data between repeat experiments was far from satisfactory, reflected in the values of standard deviation given which, for FcMeOH data set, the deviation is as high as 55% of the D value.

7.4.2. Chronoamperometry;

Double step chronoamperometric measurements of the set of ferrocene-derivatives in the two solvent systems were undertaken utilising the cyclic voltammograms to select appropriate ‘stepping’ potentials as shown in figure

7.15 (a). The oxidising potential E_{ox} , was held for 5 s then a potential where no redox processes occurred $E_{\text{ж}}$, (as evident from the CV) was held for 30 s to allow time not only for the oxidised species to be reduced but for fresh solution to reach the electrode before the oxidising potential step being repeated. This allowed for many repeats using the same solution to be acquired rapidly, the current response for which is plotted vs. time in figure 7.15 (b).

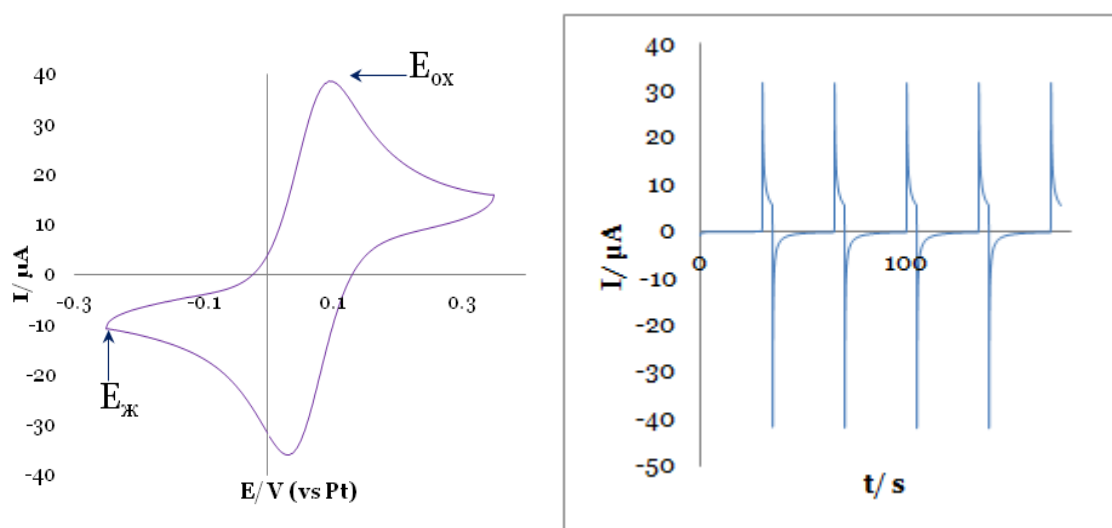


Figure 7.15; (a) CV depicting chosen E 's for potential steps. (b) Chronoamperogram for FcN^+ where $E_{ox}=0.1$ V and $E_{\text{ж}}=-0.15$ V

The overlay of the current transients for subsequent steps was consistently excellent, as illustrated by the overlay shown in figure 7.16 (a). Upon examination of the data utilising Cottrell plots of I vs $-t^{-1/2}$ for the region of the plot corresponding $0.5 \text{ s} > t > 3.0 \text{ s}$ (thus avoiding the initial charging currents and possible convection introduced at longer time scales influencing the diffusion coefficient determination), figure 7.16 (b) and employment of the Cottrell equation (2.15) values of diffusivity of the ferrocene species were obtained as given in table 7.4.

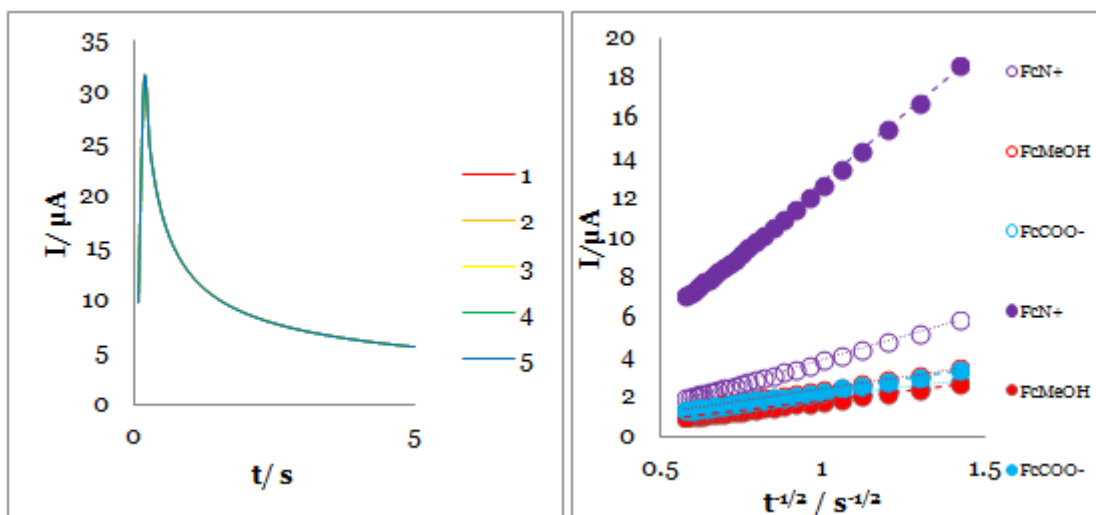


Figure 7.16; (a) transients for subsequent oxidising potential steps (0.1 V) for FcN^+ data from figure 14 (b) Cottrell plot for approximately 0.5 mM ferrocene derivatives (FcN^+ , FcMeOH , FcCOO^-) in H_2O (solid) and D_2O (hollow)

		$10^6 D / \text{cm}^2 \text{s}^{-1}$	R^2 value range	σ ($\times 10^{-6} \text{cm}^2 \text{s}^{-1}$)
		[# of repeats]		
FcCOO^-	H_2O	6.96 ± 0.002	0.9996-0.9997 [2]	0.21
	D_2O	6.93 ± 0.006	0.9991-0.9992 [2]	1.6
FcMeOH	H_2O	8.97 ± 0.003	0.9997-0.9998 [2]	1.9
	D_2O	7.99 ± 0.002	0.9997-0.9999 [2]	0.30
FcN^+	H_2O	7.14 ± 0.004	0.9995 [1]	-
	D_2O	7.78 ± 0.005	0.9994 [1]	-

Table 7.4; Diffusion coefficients for ferrocene derivatives measured via chronoamperometry for both H_2O and D_2O systems. R^2 obtained from Cottrell plot analysis (where R is the correlation coefficient).

The diffusion coefficients obtained via this method show R^2 values closer to one and much lower standard deviations than those obtained using cyclic voltammetry.

The difference between the D_2O and H_2O diffusion coefficient values determined for the Fc complexes investigated is much lower than via CV, particularly for the charged $FcCOO^-$ and FcN^+ reflecting either the enhanced consistency of results or perhaps the lesser significance of the higher viscosity solvent upon the current obtained during measurement. The diffusion coefficients measured in water using this technique are found to have a higher value than those measured in deuterium oxide solution as predicted, except for FcN^+ which shows a slightly higher D value in D_2O however the D_2O - FcN^+ value is of the correct order of magnitude.

The knowledge that the D_2O - FcN^+ solution is not being buffered as effectively as the H_2O - FcN^+ means that the value is perhaps not directly comparable as it is possible that the concentration of analyte is not homogeneous throughout the solution, in fact is likely not to be, and without knowledge of the exact concentration of analyte the diffusion coefficient calculations yield, at best, tenuous approximations. The inclusion of these values does make the table look nicer and give an idea of the possible trend.

The fact that the D_2O value is higher is suggestive of an enhanced FcN^+ concentration in the vicinity of the electrode, which is possible if the FcN^+ were to interact with the accumulated chloride ions in this region. The CV peak separations are, as discussed with respect to figure 7.13 b, fairly high therefore not suggestive of any direct adsorption.

The increase in accuracy and precision of the bulk of the data amassed via chronoamperometry compared with cyclic voltammetry could be rationalised through a number of different considerations. Foremost the timescale of the

experiments was somewhat different with the CA data taken over 5.0 s and only 2.5 s worth of this data used in the calculation of the D value, however the slow scan rate voltammetric measurements took up to 140 s to measure one cyclic voltammogram and much longer to collect the full data set for the array of scan rates sampled.

This means that any time dependent factors such as introduction of impurities or deactivation of the electrode or introduction of convection currents with time are likely to impact to a much higher degree in the voltammetry.

Another point is the number of data points used for the calculations; for CA even using just 2.5 s worth of the data for one step gave 25 data points at the acquisition frequency used, in contrast for each CV measured, unless convoluted through mathematical transformation, only one data point is gathered per experiment. The overall number of points used in the D determination is dependent upon the number of different scan rates investigated which, if more points are desired, increases the number of experiments and length of time spent gathering data.

Chronoamperometry employs a fixed potential, unlike the cyclic voltammetry where the potential is swept. The sweeping of the potential between the oxidative and reductive potentials over a range of up to ~ 1 V, although not moving into the region where solvent or electrolyte breakdown occurs, can be expected to alter the structure, bonding and behaviour of the solvent and electrolyte toward the analyte particularly near to the electrode, potentially resulting in differing degrees of bonding between the solvent and analyte.

The constantly changing potential in CV measurements may also impact upon the electrode surface environment in a manner not seen in the simple potential step experiment.

With chloride ions of the supporting electrolyte in solution and the implementation of a gold working electrode, as mentioned earlier, there is a likelihood of potential dependant adsorption of anions, which would be expected to result in deactivation of areas of the working electrode surface. This offers a viable rationalisation of any apparent drop in diffusion coefficient between CA and CV as techniques as only cyclic voltammetric analysis of the ferrocene derivatives required the application not only more extreme potentials, in excess of the relevant oxidation potential, but also constantly changing potential which would be expected to result in constantly adapting diffusion layer structure.

In CA the double layer charging can be easily separated from the analyte response as it is evident in the initial large spike however there is not such an easily accessible CV equivalent technique to compensate for the underlying non-faradaic current.^[141]

7.4.3. DOSY-NMR

For this set of experiments the DOSY were run with solutions of the same composition and concentrations as used in the initial electrochemical D₂O determination with electrolyte present in all measurements. The electrolyte employed was KCl which contains no protons and has a small ionic radius therefore could be expected to cause less obstruction effects than TBA(BF₄) used in the THF measurements as well as no ¹H-NMR signal. Temperature controlled measurements were made with the FcMeOH and FcCOO⁻ at 28°C and FcN⁺ at 30°C as stated. The difference in temperature of the measurements was due purely to difference in room temperature during measurement, with the higher ambient temperature precluding the stabilisation the thermocoupling device at 28°C without active cooling. The spectra recorded are given below in figure 7.17.

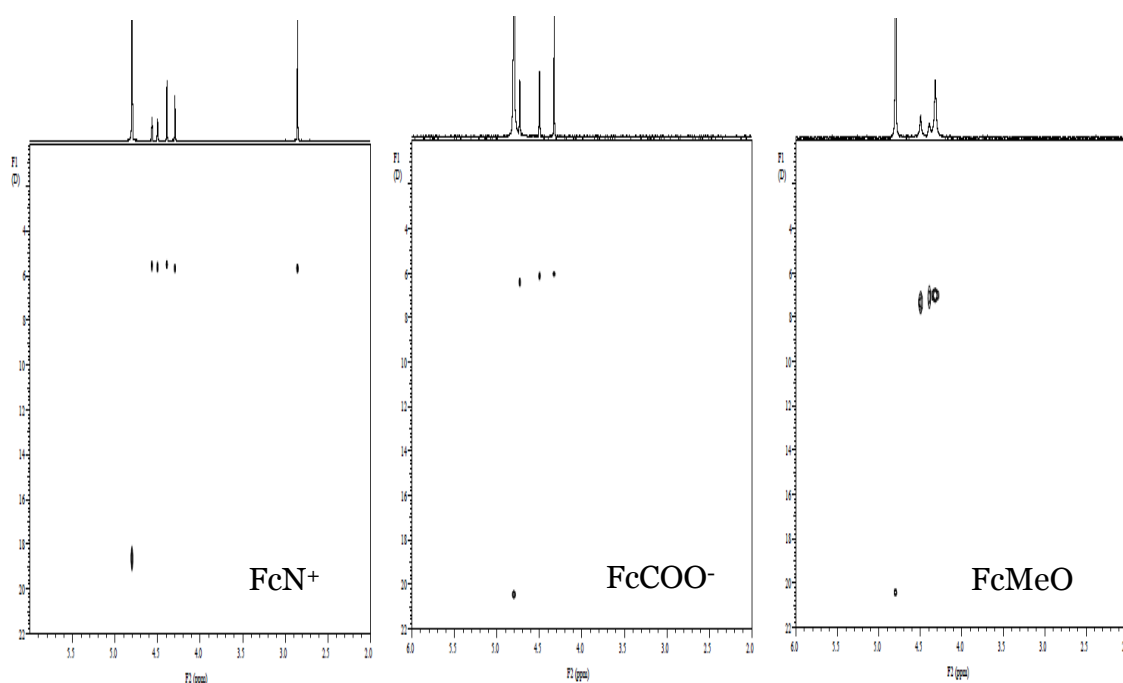


Figure 7.17; DOSY Spectra of dimethylaminomethyl ferrocene, FcN⁺(0.5 mM) in D₂O with KCl (0.1 M) and HCl (1.0 mM) measured at 30°C; ferrocene carboxylic acid, FcCOO⁻ (0.5 mM) in D₂O with KCl (0.1M) and NaOH (1.0 mM) measured at 28°C; ferrocene methanol, FcMeOH (0.5 mM) in D₂O with KCl (0.1 M) at 28°C.

The NMR signal multiplicity and chemical shift observed in the 1D spectra were as anticipated for the systems with the signal associated with the five protons of the unsubstituted cyclopentatrienyl ligand of the ferrocene derivatives found consistently at 4.49 ppm, as can be observed in figure 7.17. The peaks widths were low signifying accurate and reliable measurements. The 2D DOSY spectra for the ferrocene derivatives were fairly self consistent with the diffusion coefficient for water found as $2.04 \times 10^{-5} \text{ cm}^2 \text{ s}^{-1}$ and $2.05 \times 10^{-5} \text{ cm}^2 \text{ s}^{-1}$ for the FcMeOH and FcCOO⁻ systems respectively, however a degree of deviation was seen in the FcN⁺ system where the $D^*_{\text{H}_2\text{O}}$ dropped to $1.86 \times 10^{-5} \text{ cm}^2 \text{ s}^{-1}$. This could suggest the need to calibrate the data against this diffusion coefficient however the associated standard error in this value was found to have increased by over 450% when compared to the error associated with the water signal seen in the FcCOO⁻ and FcMeOH systems, and even more when compared against the error associated with the FcN⁺ signals within the same sample. This implies that the water molecules in solution did not behave ideally and interactions occur within the system which slowed the diffusion. This sample contained additional acid in order to ensure the protonation of the FcN⁺ species, which was not found in the other two ferrocene derivative systems. This acid could be expected to interact with the trace water present so this apparent ‘slowing’ and poor data fit may be as a result of H₂O, HDO, H₃O⁺, H₂DO⁺ and HD₂O⁺ species formation, proton exchange and subsequent signal overlap. The literature value for trace HDO diffusion in pure D₂O is given as $1.902 \times 10^{-5} \text{ cm}^2 \text{ s}^{-1}$, however this was measured over a slightly lower temperature range in a pure solvent so

although not in exact agreement, the experimental values obtained seem reasonable.^[222]

The determination of the diffusion coefficient uses the Stejskal-Tanner relationship (equation 7.1) so in order to see the data fit in a form comparable to that of the linear electrochemical Randles-Sevcik and Cottrell plots a graph of the natural log of the spin signal amplitude, $\ln(S/S_0)$ vs the gradient amplitude squared, G^2 was constructed, figure 7.18.

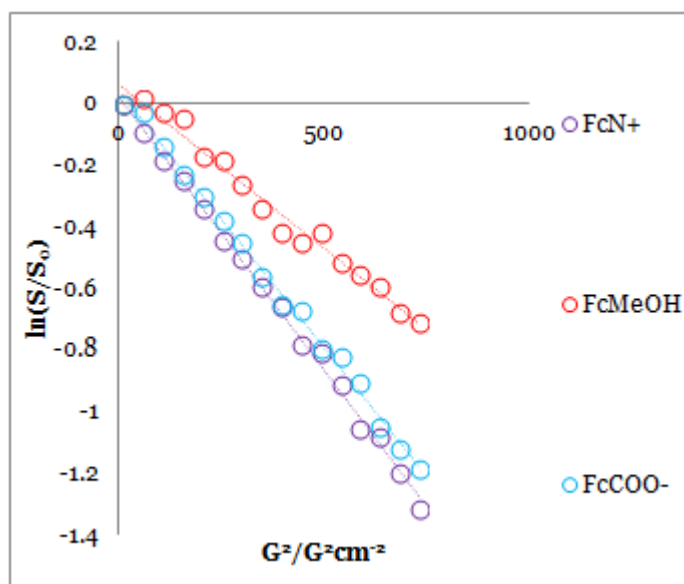


Figure 7.18; Logarithmic analysis of the normalised peak amplitude as a function of the squared magnetic field gradient for FcN^+ , FcMeOH and FcCOO^- data shown in figure 7.17.

From figure 7.18 it was possible to assess the correlation coefficients for the three systems analysed, the squared value of which is given in table 7.5 along with the diffusion coefficients determined from the gradients of these linear relationships, (presented in DOSY spectra in figure 7.17).

		$10^{-6} D^* / \text{cm}^2 \text{s}^{-1}$	R^2 value	σ ($\times 10^{-6} \text{cm}^2 \text{s}^{-1}$)
FcCOO⁻	D ₂ O	6.13 ± 0.07	0.9960	0.17
FcMeOH	D ₂ O	7.14 ± 0.35	0.9814	0.17
FcN⁺	D ₂ O	5.60 ± 0.016	0.9969	0.067

Table 7.5; Diffusion coefficients for ferrocene derivatives measured via DOSY in D₂O. R^2 obtained from $\ln(S/S_0)$ vs G^2 plot analysis (where R is the correlation coefficient). σ in this table is the standard deviation of D^* values of the individual proton signals of the complex which were averaged in order to find D^* not from distinct experimental runs as seen previously for the electrochemical values.

The diffusion coefficients gathered using NMR techniques are substantially less disperse than the electrochemical values, as would be expected for three molecules of similar size and shape. The values of D^* correlate very well with the Stokes-Einstein predicted relationship (equation 2.3), for which the hydrodynamic radius can be considered in terms of molecular weight according to equation 7.16.^[223]

The analyte hydrodynamic radius can be expressed as;^[223]

$$r = \sqrt[3]{\frac{3Pa MW}{4\pi\rho N_A}} \quad (7.16)$$

where Pa refers to the packing fraction of the material, which in the case of a liquid is taken as 0.64, MW being the molecular mass in g mol^{-1} and ρ the density of the bulk material in g cm^{-3} .

These equations describe quantitatively how as the molecular mass increases the radius is expected to increase and therefore the diffusion coefficient would be expected to decrease.

From the comparison of the molecular masses and diffusion coefficients found experimentally that this is indeed seen to be the case;

$$MW_{\text{FcMeOH}}=213.06 \text{ g mol}^{-1} < MW_{\text{FcCOOH}}=230.04 \text{ g mol}^{-1} < MW_{\text{FcN}}=243.13 \text{ g mol}^{-1}$$

$$D^*_{\text{FcMeOH}}=7.14 \times 10^{-6} \text{ cm}^2 \text{ s}^{-1} > D^*_{\text{FcCOO}^-}=6.13 \times 10^{-6} \text{ cm}^2 \text{ s}^{-1} > D^*_{\text{FcN}^+}=5.60 \times 10^{-6} \text{ cm}^2 \text{ s}^{-1}$$

The uncharged FcMeOH molecules with the lowest molecular mass, were observed to move the most readily through the solution with FcN⁺, the largest molecule present showing the slowest movement, as predicted.

What was unexpected was the lower linear correlation coefficient found in the DOSY data when compared to those seen for the electrochemical experiments, with none of the chronoamperometric plots yielding R² values so far from 1. This suggests that the electrochemical measurements showed a better fit to the expected relationship despite yielding such a large variation in actual values.

The Stejskal-Tanner relationship (equation 7.1) and the Stokes-Einstein equation (2.3) used in DOSY yield D^* directly, however the electrochemical Randles-Sevcik equation (2.6) and Cottrell equation (2.15) give $D^{1/2}$ which is squared to get D therefore any errors will be subject to magnification by the power of two. Also, as mentioned previously the electrochemical determination requires accurate knowledge of the concentration, electrode working area as well as the number of electron transferred in the process not only conveniently programmable computer parameters, which adds a further degree of uncertainty, presumably from the range of value seen the primary source of error.

The values of the diffusion coefficients obtained by CA and DOSY are assembled in table 7.6 for D₂O (a) and H₂O (b) along with literature values.

D₂O	C.A.	DOSY	Literature
	10⁶ × D /cm² s⁻¹	10⁶ × D* /cm² s⁻¹	10⁶ × D /cm² s⁻¹
FcCOO⁻	6.93 ± 0.006	6.13 ± 0.07	5.9 ^{Ja} , 5.2 ^{Jb}
FcMeOH	7.99 ± 0.002	7.14 ± 0.35	8.6 ^{Jc} , 8.3 ^{Jd}
FcN⁺	7.78 ± 0.005	5.60 ± 0.016	4.7 ^{Je}

H₂O	C.A.	DOSY	Literature
	10⁶ × D /cm² s⁻¹	10⁶ × D* /cm² s⁻¹	10⁶ × D /cm² s⁻¹
FcCOO⁻	6.96 ± 0.002	7.86^J	7.5 ^a , 6.6 ^b
FcMeOH	8.97 ± 0.003	9.15^J	11.0 ^c , 10.6 ^d
FcN⁺	7.14 ± 0.004	7.18^J	6.0 ^e

Table 7.6; Diffusion coefficients for the ferrocene derivatives from all methods trialled. ^J Values translated from alternate solvent. All shifted to match experimental T value using Stokes-Einstein ^a[224] 0.2M Na₂HPO₄, pH 9.2, 20 °C, Pt, 3.37 mM; ^b[225] 0.2M Na₂HPO₄, pH 9.2, 27 °C, GC, 3.37 mM; ^c[226] TMAP, 50 mM, Pt, 19.85 °C; ^d[227] 0.13 M KNO₃, 1.08 mM, Pt, 19.85 °C; ^e[228] evaluated using Stokes-Einstein. Values in keeping with [229][230].

The above data shows some of the expected trends; all of the measurements made in D₂O, except the already addressed possibly less than reliable FcN⁺-D₂O CA, show lower diffusion coefficient values than found in the corresponding H₂O experiments as expected from the anticipated viscosity difference between the solvents.

The trend predicted by the Stokes-Einstein equation and the change in molecular weights was followed well in the DOSY measurements with *D* for FcMeOH > FcCOO⁻ > FcN⁺. FcMeOH also tended to yield a higher *D* than FcCOO⁻ from the electrochemical measurements made, seen from the CA analysis in both solvents however FcN⁺, expected to show the lowest diffusion

coefficient of the trio of complexes, resulted in a slightly higher D value than FcCOO^- contrary to anticipated, resulting in deviation from the prospective sequence.

From the Stokes-Einstein equation (2.3) the ratio between the D found in D_2O to that found in H_2O would be expected to remain constant and proportional to the viscosity change, as seen in the ‘correction factor’ found in equation (7.12).

This manner of correcting the diffusion coefficient for viscosity change quite clearly does not hold true for the electrochemical data obtained;

From the viscosity data for the pure solvents;

$$\eta_{[\text{H}_2\text{O}]} / \eta_{[\text{D}_2\text{O}]} = 0.780$$

The ratio of D values obtained would be expected to yield the same value;

$$D_{[\text{FcMeOH}]\text{D}_2\text{O}} / D_{[\text{FcMeOH}]\text{H}_2\text{O}} = 0.891$$

$$D_{[\text{FcCOO}^-]\text{D}_2\text{O}} / D_{[\text{FcCOO}^-]\text{H}_2\text{O}} = 0.996$$

$$D_{[\text{FcN}^+]\text{D}_2\text{O}} / D_{[\text{FcN}^+]\text{H}_2\text{O}} = 1.090$$

All of the ratios obtained from the electrochemical data are higher suggesting that the viscosity change between the electrolyte solutions is not experienced to the same degree as between the pure solvents. The results suggest the D_2O -electrolyte solution is less viscous (or H_2O -electrolyte solution more viscous) than the viscosity ratio of the pure solvents implies. The former is in keeping with literature where the addition of KCl to H_2O and D_2O solution results in the destruction of the H-bonding lowering the associated viscosity for low to medium mole fractions, including the electrolyte concentrations

employed.^{[136][231]} As D₂O is more structured initially, the viscosity is affected to a greater extent than that of H₂O upon the addition of the same quantity of electrolyte.

The additional HCl for the FcN⁺ system, as another recognised structure breaker^[232] may contribute towards making this viscosity change even more pronounced, however the NaOH added to the FcCOO⁻ system is known as a structure maker and would be expected to enhance hydrogen bonding and therefore increase viscosity, however with the structure forming electrolytes this is expected to occur to the same extent both in H₂O and D₂O therefore would not be expected to influence the ratio.

The addition of the analyte itself may affect the bulk viscosity, particularly for the ferrocenes possessing charge, however with the relatively low concentration this effect would presumably be negligible.

As previously discussed the D₂O has a higher viscosity due to more and stronger hydrogen bond formation with itself compared with H₂O. Hydrogen bond formation with the analyte could also be different in D₂O than the corresponding bonding in H₂O leading to change in diffusivity not directly attributable or associated with the solvent viscosity change, with this bonding quite feasibly being influenced by the alteration of the charge on the analyte group during oxidation and reduction processes.

FcMeOH contains an alcohol group making it particularly adept at hydrogen bonding in aqueous solution, with the carboxylate group of FcCOO⁻ unable to donate, however it is in possession of two exposed electronegative oxygen atoms ergo could be expected to interact with the positive dipole of the H₂O or D₂O.

The FcN^+ H-bonding would be by far the weakest, even in its deprotonated state, due to the less electronegative nitrogen rather than oxygen atom found in the substituent and the additional steric hindrance provided by the two methyl groups on the tertiary amine centre. In its protonated state there would be a positive charge and proton which could partake in bonding however the presence of the methyl groups would be expected to hinder this making it less probable. This would suggest that the FcMeOH or FcCOO^- would be slowed by the greatest degree and FcN^+ by the least.

Aside from H-bonding the ferrocene analytes, particularly those possessing a charge, could be expected to undergo additional electrostatic interactions with the polar solvent molecules. D_2O has a higher polarity than H_2O therefore would presumably be more disposed toward greater degree of interaction and higher strength of bonding.^[233] This could help to explain the higher ratios obtained for the diffusion coefficients of FcN^+ and FcCOO^- when compared to that seen for FcMeOH .

The order of diffusion coefficient magnitude obtained via CA for both the D_2O and H_2O measurements is contrary to the order seen in DOSY and predicted through the investigation of molecular masses.

FcMeOH is the fastest diffusion molecule as expected for the smallest and being uncharged would be expected to undergo minimal electrostatic perturbation, however the largest FcN^+ is observed to diffuse faster than the FcCOO^- in both solvent systems.

This is also incongruous with the expected migratory or electrostatic effects, with the movement of the positive charge toward the positive electrode

seemingly enhanced when compared with the diffusion of the negatively charged species.

The deviation in values obtained via DOSY, where there is a lack of concentration gradient or potential dependant movement, and the electrochemical determination, appears to be limited to the diffusion of the charged species. The data suggests the FcN^+ diffuses faster than anticipated in D_2O or/and the FcCOO^- is slower than expected in H_2O upon application of the potential difference.

As already mentioned the ferrocenes can interact with the solvent to differing degrees therefore be expected to have differing solvation spheres. This solvation would be expected to be the same in the bulk solution of electrochemical measurements as in the DOSY experiments, however upon traversing the diffusion layer where the electrolyte structure and pH are significantly altered compared to that of the bulk the differences in both charge and solvation could impact significantly.

The more exposed charge of the FcCOO^- may lead to repulsive interaction between the chloride ions in the approach to the electrode where they are present in a very high concentration. Also solvent molecules not engaged in the solvation of ions would be expected to align themselves with the charge forming a well structured region with the additional hydroxide groups found in the FcCOO^- system enhancing this, forming a region which would act as an encumbrance for the analyte where solvating bonding interactions could be enhanced.

The opposite is true of the FcN^+ system where the addition of extra chloride leads to less solvent structure, the chloride ions would not be expected to impede the better shielded charge and the molecule is expected to experience a lower degree of solvent interaction therefore free to diffuse with less obstruction than FcCOO^- .

From the data gathered and the experimental difficulties faced in doing so it becomes apparent that diffusion coefficient elucidation via DOSY and electrochemical methods under the same experimental conditions do not necessarily result in the same diffusion coefficient values being obtained. The considerations needed in utilising the two as interchangeable techniques, particularly for the evaluation of diffusion of charges species are more complex than initially anticipated.

The choice of solvents employed although initially ascribed a positive contribution to the experimental design, so as to allow more comparable data, proved to incorporate additional sources of complicated, sometimes potential or surface specific interactions. Of all deuterated solvents D_2O possesses by far the most pronounced isotopic effects as the deuterons make up the highest proportion of the molecule and also as water and deuterium oxide possess such extensive intermolecular bonding networks which are affected by the substitution of protons.

The use of the H_2O - D_2O pair therefore may lead to the most emphasised difference in behaviour in an electrochemical environment compared to that in the absence of an applied potential. The solvent effects and the influence of potential would be expected to be substantially less significant in the distinction

between the techniques if a non-coordinating apolar solvent and its deuterated counterpart were employed in exchange.

7.5. Conclusion;

From the comparison of DOSY and electrochemical measurement of diffusion coefficients in the non-aqueous systems (d_8 -THF and THF) it was found that the addition of electrolyte to the system had a pronounced effect upon the D^* obtained via DOSY in contrast to the previously reported 'similar' values obtained (with the D^* lowered by almost a half in the case of $\text{Mo}(\text{CO})_4\text{bpy}$).

The incorporation of electrolyte gave more closely matching values than in its absence for both $\text{Mo}(\text{CO})_4\text{bpy}$ and Fc. This finding is attributed to a combination of the effect of electrolyte upon the solvent properties such as altering viscosity etc as well as the additional hindrance in diffusion through the incorporation of a high concentration of bulky ions and specific electrostatic interactions between the analyte and electrolyte ions.

The degree to which the addition of electrolyte affects the diffusion was varied, it is proposed to be linked to the polarity of the species under investigation with more polar components of the system being more greatly affected.

The experiments undertaken in D_2O allowed an even greater degree of direct comparison as the electrochemical and DOSY measurements were conducted in the same medium. The tentative conclusions drawn from the evaluation of FcCOO^- , FcMeOH and FcN^+ by electrochemical and DOSY measurements is that the two different methodologies do not provide access to the same

diffusivity values, as even with the conditions kept as consistent as possible, the quantitative analysis and trends observed in the values were not concurrent.

Further investigation with a wider array of analytes would be advantageous for understanding of the processes responsible for the deviation and to assess which situations, if any, would allow the techniques to be utilised interchangeably in future.

Having stated this, the degree of accuracy to which the diffusivity data is required should also be taken into consideration as both methods tended to yield values of similar magnitudes with the possibility that within the range of experimental errors encountered during measurement, the two may be similar enough for either to suffice.

8. Conclusion and Further Work;

8.1. Conclusion;

A study of electrochemical carbon dioxide reduction has been undertaken and the first molybdenum based molecular electrocatalyst for this process identified and characterised.

In order to understand the electrocatalytic process and system, the mechanism and kinetics were investigated through, predominantly voltammetry combined with an array of other electrochemical, spectroelectrochemical and spectroscopic techniques. A thorough and methodical investigation of the entire electrochemical system as well as the specific catalyst of interest and its chemical components through analogous species was conducted as, despite the vast quantities of research into the area of CO₂ reduction, particularly photo and electrocatalysis, the understanding of this complex process is lacking with the impact of seemingly subtle alterations in experimental parameters unpredictable.

Mo(CO)₄bpy was electrochemically characterised in the non-aqueous electrochemical system with previously unreported redox behaviour examined, including a third reduction and what is thought to be a tricarbonyl oxidative process. Evidence of its successful employment as a CO₂ reduction electrocatalyst is presented. The determination of the reduced radical anion as the active species was achieved through electrochemical methods as well as EPR spectroscopy and DFT calculation, however there was also significant evidence

of additional CO₂ current enhancement associated with the direduced species and the possibility of interaction of electrochemically inactive unidentified species, such as Mo(CO)₃bpy^{•-}.

The optimisation of the catalyst structure suggested that the tungsten analogue, W(CO)₄bpy, may offer additional lowering of the overpotentials associated with CO₂ reduction compared to the molybdenum centred complex, with bipyridyl and phenanthroline found to be the best ligands of those trialled.

The use of NMP, an industrially employed CO₂ scrubbing solvent, for the electrochemical reduction of CO₂ proved effective which may be noteworthy in itself, as the expenditure of energy is already required simply to remove the dissolved gas from the solvent without the prospect of transformation of CO₂ to a more valuable chemical.

From the experiments conducted, although pyridine, pyridinium and bipyridine showed no evidence of CO₂ current enhancement or catalysis as additives to the NMP system, the utilisation of pyridine as a solvent produced some promising voltammetry, perhaps offering a lower potential route to CO₂ reduction.

The effect of the working electrode material was most pronounced upon the system in both the presence and absence of CO₂ indicating that adsorption processes hold significant influence over the function and longevity of Mo(CO)₄bpy toward reduction and its interaction with CO₂. Gold was found to be the optimal working electrode material of those trialled.

The impact of electrolyte identity upon CO₂ reduction in NMP was explored, focussing specifically on the comparison of tetrabutylammonium and alkali metal cations. The voltammetry showed that M⁺ salts resulting in lower

associated currents and a significantly higher overpotential than observed with TBA⁺. This discovery, although seemingly supportive of the ‘catalytic’ interaction previously reported as associated with tetraalkylammonium cations, was further investigated and it was found that the presence of M⁺ in the system (even if not the sole electrolyte present) suppressed CO₂ reduction through deactivating film formation on the electrode surface. Film formation and underpotential deposition of alkali metals from their salts in non-protic solvents has been reported previously, however upon saturation of the solution with CO₂ different voltammetric processes were observed and the resultant film found to possess different properties. SERS investigation of the electrode surface confirmed that insoluble CO₂ derived species were responsible for the deactivation.

The comparison of DOSY and electrochemical determination of diffusion coefficients in d₈-THF clearly illustrated that the inclusion of electrolyte in DOSY measurements had a pronounced effect upon the D^* obtained, with this electrolyte-included value more close in value to that gleaned through electrochemical methods.

The further study of the interchangeability of DOSY and electrochemistry through a series of measurements, made in both H₂O and D₂O, of ferrocene derivatives possessing various charges led to the conclusion that the two distinct methodologies do not yield concurrent values.

8.2. Further work;

The most significant omission made (albeit unintentionally) within this research has been that of the quantitative product distribution. The detection, identification and quantification of the products of CO₂ reduction within this system is vital for the further analysis of the efficiency and turn-over rates. The product detection clearly requires careful consideration and further experiments. The use of C¹³O₂ as the starting material would allow for any solution phase products to be identified via NMR, whilst also providing an indication as to whether the CO₂ molecules bind on reduction with the metal centre of the catalyst species, as if so they are liable to interchange with existing carbonyl groups and C¹³ may be incorporated into the structure.

The use of on-line mass spectroscopy coupled to the reaction vessel has proven to be a valuable tool for product detection for other groups allowing an *in situ* detection as gaseous phase products are formed which may yield the quantitative data required.

The product adsorption at the electrode may also be worth further study also as if the potential were kept negative for the period prior to the detection attempt, electrochemical or SERS analysis may be able to provide additional insight possibly not obtained in previous attempts due to the prospective potential dependence.

Once the product distribution can be established the Faradaic efficiency and turnover number and other useful parameters for the comparison of catalytic activity can be found.

The optimisation of the catalyst structure showed that the most significant shifts in potential were found through the addition of substituents upon the bipyridyl ligand of the tetracarbonyl complex however in the two attempts made, neither resultant complex was suited to CO₂ electrocatalysis. If a more appropriate group could be incorporated into the bipyridyl structure it is conceivable that the reduction potential could be lowered considerably, yet the complex maintain its CO₂ catalytic ability.

Aside from this, the incorporation of Mo(CO)₄bpy into a photoelectrochemical system would be a logical next step in the development of this research as the overpotential required for catalyst activation is still considerable, however if the activation could be attained through the photosensitisation and excitement, the system would be a considerably less electrical energy intensive process.

During the brief investigation undertaken, the employment of pyridine as a solvent for CO₂ reduction yielded promising voltammetry. Further study and the addition of acid to this solvent system to see the effects upon CO₂ electroreduction would be of interest.

The DOSY vs. electrochemistry, as a means to evaluate *D*, chapter of this work would benefit immensely from further work to expand the solvents, analytes and electrolytes investigated in order to better understand the results gathered so far. The conclusions drawn from the study of just five solutes within two solvents is, at this stage, far from meaningful as it is based upon what may prove to be far from representative data.

References;

- [1] S. Arrhenius., *Philosophical Magazine and Journal of Science.*, 1896, **41**, 237-276.
- [2] K. St John, R. M. Leckie, K. Pound, M. Jones, L. Krissek., *Reconstructing Earth's Climate History*, John Wiley & Sons, 2012, p176.
- [3] Environmental and Energy Study Institute. "Timeline of EPA Action on Greenhouse Gases". Retrieved February 3, 2013.
- [4] *Carbon Capture And Its Storage: An Integrated Assessment.*, ed. S. Shackley, C. Gough, Ashgate Publishing Limited, 2008
- [5] P. Styring and D. Jansen, *Carbon Capture and Utilisation in the green economy*, 2011, ISBN 978-0-9572588-1-5.
- [6] M. Jitaru, D. A. Lowy, M. Toma, B. C. Toma, L. Omau., *J. Appl. Electrochem.*, 1997, **27**, 875-889.
- [7] E. E. Benson, C. P. Kubiak, A. J. Sathrum, J. M. Smieja., *Chem. Soc. Rev.*, 2009, **38**, 89-99
- [8] Y. Hori, in *Electrochemical CO₂ Reduction on Metal Electrodes, Modern aspects of Electrochemistry No.42*, ed. C. Vayenas et al., Springer, New York. pp 89-189.
- [9] R. P. S. Chaplin, A. A. Wragg., *J. Appl. Electrochem.*, 2003, **33**, 1107-1123.
- [10] K. Hara, A. Kudo, T. Sakata., *J. Electroanal. Chem.*, 1995, **391**, 141-147.
- [11] Y. Hori, K. Kikuchi, S. Suzuki., *Chem. Lett.*, 1985, **11**, 1695-1698.
- [12] M. Todoroki, K. Hara, A. Kudo, T. Sakata, *J. Electroanal. Chem.*, 1995, **394**, 199-203.
- [13] M. Gattrell, N. Gupta, A. Co., *J. Electroanal. Chem.*, 2006, **594**, 1-19.
- [14] A. Gennaro, A. A. Isse, M. G. Severin, E. Vianello, I. Bhugun, J. M. Saveant, *Journal of the Chemical Society-Faraday Transactions*, 1996, **92**, 3963-3968.
- [15] D. L. DuBois, in *Electrochemical Reactions of Carbon Dioxide, Encyclopedia of Electrochemistry Vol. 7a*, ed. F. Scholz, C. J. Pickett., Wiley-VCH, Weinheim. pp 202-224.
- [16] C. Costentin, M. Robert, J. M. Savéant., *Chem. Soc. Rev.*, 2013, **42**, 2423-2436.
- [17] M. R. M. Bruce, E. Megehee, B. P. Sullivan, H. Thorp, T. R. O'Toole, A. Downard, T. J. Meyer., *Organometallics*, 1988, **7**, 238-240.
- [18] K. Tanaka, *Bulletin of the Chemical Society of Japan*, 1998, **71**, 17-29.
- [19] P. Dube, G. M. Brisard., *J. Electroanal. Chem.*, 2005, **582**, 230-240.
- [20] K. W. Frese., *J. Electrochem. Soc.*, 1991, **138**, 3338-3344
- [21] K. J. P. Schouten, Y. Kwon, C. J. M. van der Ham, Z. Qin, M. T. M. Koper., *Chem. Sci.*, 2011, **2**, 1902-1909
- [22] Z. Chen, P. Kang, M. T. Zhang, B. R. Stoner, T. J. Meyer *Energy Environ. Sci.*, 2013, **6**, 813.
- [23] A. F. Sammels, R. L. Cook., "Electrocatalysis and Novel Electrodes for High Rate CO₂ Reduction under ambient conditions" in *Electrochemical and Electrocatalytic Reactions of Carbon Dioxide*, ed. B.P. Sullivan, K. Krist, H.E. Guard, Elsevier Science Publishers B.V., 1993. p245
- [24] Hara. K., Kudo A.SakataWatanabe., *M.J.Electroanal Chem.* 1995, **342** L57
- [25] Furuya N.Yamazaki T, Shibata., *M.J.Electroanal.Chem.* 1997, **431**, 39
- [26] D. P. Summers, S. Leach, K. W. Frese., *J. Electroanal. Chem.*, 1986, **205**, 219-232.
- [27] I. Taniguchi., in *Electrochemical and Electrocatalytic Reactions of Carbon Dioxide, Modern Aspects of Electrochemistry No.20*, ed. J. O'M. Bockris, R. E. White, B.E. Conway., Plenum Press, New York. pp 367-399.
- [28] S. Komatsu, M. Tanaka, A. Okumura, A. Kungi., *Electrochimica Acta*, 1995, **40**, 745- 753.
- [29] K. Hara, A. Tsuneto, A. Kudo, T. Sakata., *J. Electrochem. Soc.*, 1994, **141**, 2097-2103.
- [30] D. P. Summers, K. W. Frese., *ACS Symposium Series*, 1988, **378**, 518-527.
- [31] J. Lee, Y. Tak., *Electrochimica Acta*, 2001, **46**, 3015-3022.
- [32] R. M. Hernandez, J. Marques, O. P. Marques, M. Choy, C. Ovalles, J. J. Garcia, B. Scharifker., *J. Electrochem. Soc.*, 1999, **146**, 4131-4136.
- [33] M. N. Mahmood, D. Mashed, C.J. Harty., *J. Appl. Electrochem.*, 1987, **17**, 1159- 1170.
- [34] S. Wasmus, E. Cattaneo, W. Vielstich., *Electrochimica Acta*, 1990, **35**, 771-775.
- [35] K. Ohta, K. Suda, S. Kaneco, T. Mizuno., *J. Electrochem. Soc.*, 2000, **147**, 233-237.
- [36] D. W. DeWulf, T. Jin, A. J. Bard., *J. Electrochem. Soc.*, 1989, **136**, 1686-1691.
- [37] Y. Terunuma, A. Saitoh, Y. Momose., *J. Electroanal. Chem.*, 1997, **434**, 69-75.
- [38] N. Hoshi, S. Kawatani, M. Kudo, Y. Hori., *J. Electroanal. Chem.*, 1999, **467**, 67-73.

- [39] Y. Hori, A. Murata, R. Takahashi, S. Suzuki., *J. Electrochem. Soc.*, 1987, **134**, C498-C498.
- [40] P. Dubé, G. M. Brisard., *J. Electroanal. Chem.*, 2005, **582**, 230-240.
- [41] A. Schizodimou, G. Kyriacou., *Electrochimica Acta.*, 2012, **78**, 171-176.
- [42] Y. Hori, A. Murata, R. Takahashi., *J. Chem. Soc., Faraday Trans.*, 1989, **85**, 2309-2326.
- [43] G. Kyriacou, A. Anagnostopoulos., *J. Appl. Electrochem.*, 1993, **23**, 483-486.
- [44] Y. Hori, S. Suzuki., *Bull. Chem. Soc. Jpn.*, 1982, **55**, 660-665.
- [45] S. Kaneco, K. Iiba, N. Hiei, K. Ohta, T. Mizuno, T. Suzuki., *Electrochimica Acta*, 1999, **44**, 4701-4706.
- [46] T. Saeki, K. Hashimoto, N. Kimura, K. Omata, A. Fujishima., *J. Electroanal. Chem.*, 1995, **390**, 77-82.
- [47] S. Kaneco, H. Katsumata, T. Suzuki, K. Ohta., *Electrochimica Acta*, 2006, **51**, 3316-3321.
- [48] G. Hochgesand, *J. Ind. Eng. Chem*, 1970, **62**, 37-44; A. Kohl and R Nielsen, *Gas Purification*, 5th Ed. 1997, USA, Gulf Publishing Company, pp 1210-1215.
- [49] I. Taniguchi, B. Aurian-Blajeni, J O'M. Bockris., *J. Electroanal. Chem.*, 1984, **161**, 385-388.
- [50] J O'M. Bockris, J. C. Wass., *J. Electrochem. Soc.* 1989, **136**, 2521-2528.
- [51] T. Saeki, K. Hashimoto, N. Kimura, K. Umata, A. Fujishima., *Chem. Lett.*, 1995, **24**, 361-362.
- [52] A. Murata, Y. Hori., *Bulletin of the Chemical Society of Japan*, 1991, **64**, 123-127.
- [53] K. Izutsu in, *Electrochem. in Nonaqueous Solutions*, Wiley-VCH, Weinheim. pp 216-230.
- [54] D. Aurbach, M. Daroux, P. Faguy, E. Yeager., *J. Electroanal. Chem.*, 1991, **297**, 225-244.
- [55] H. Gerischer, D. Wagner., *Ber. Bunsenges. Phys. Chem.*, 1988, **92**, 1325-1330.
- [56] C. A. Paddon, R. g. Compton., *J. Phys. Chem. C.*, 2007, **111**, 9016-9018.
- [57] R. Bhattacharyya, B. Key, H. Chen, A. S. Best, A. F. Hollenkamp, C. P. Grey., *Nature Materials*, 2010, **9**, 504-510.
- [58] V. Sudha, M. V. Sangaranarayanan., *J. Phys. Chem. B.*, 2003, **107**, 3907-3913.
- [59] J. Lee, S. Pons., *Langmuir*, 1986, **2**, 297-301.
- [60] J. M. Savéant., *Chem. Rev.*, 2008, **108**, 2348- 2378.
- [61] C. M. Sánchez Sánchez, *Alternative uses of Carbon Dioxide Electrochemical Synthesis, Thesis (PhD)*, Universitat d'Alacant, 2004.
- [62] F. Gibanel, M. C. Lopez, F. M. Royo, J. Santafe, J. S. Urieta., *J. Solution Chem.*, 1993, **22**, 211-217.
- [63] G. Centi, S. Perathoner., *Catalysis Today*, 2009, **148**, 191-205.
- [64] K. Waugh, *Catalysis Today*, 1992, **15**, 51-75.
- [65] Z. Yang, V. R. Moure, D. R. Dean, L. C. Seefeldt., *PNAS*, 2012, **109**, 19644-19648.
- [66] T. Reda, C. M. Plugge, N. J. Abram, J. Hirst., *PNAS*, 2008, **105**, 10654-10658.
- [67] S. Kuwabata, R. Tsuda, H. Yoneyama., *J. Amer. Chem. Soc.*, 1994, **116**, 5437-5443.
- [68] B. A. Rosen, A. Salehi-Khojin, M. R. Thorson, W. Zhu, D. T. Whipple, P. A. Kenis, R. I. Masel., *Science*, 2011, **334**, 643-644.
- [69] R. D. Richardson, B. K. Carpenter., *J. Am. Chem. Soc.*, 2008, **130**, 3169-3180.
- [70] S. Meshitsuka, M. Ichikawa, K. Tamaru., *J. Chem. Soc., Chem. Commun.*, 1974, **5**, 158-159.
- [71] B. J. Fisher, R. J. Eisenberg., *Am. Chem. Soc.*, 1980, **102**, 7361-7321.
- [72] M. Beley, J. P. Collin, R. Ruppert, J. P. Sauvage, *Chem. Commun.*, 1984, **19**, 1315-1316.
- [73] E. Simon-Manso, C. P. Kubiak., *Organometallics*, 2005, **24**, 96-99.
- [74] D. J. Pearce, D. J. Pletcher., *Electroanal. Chem.*, 1986, **197**, 317-322.
- [75] M. Fujihira, Y. Hirata, K. J. Suga., *Electroanal. Chem.*, 1990, **292**, 199-203.
- [76] G.B. Balazs, F. C. Anson, *J. Electroanal. Chem.*, 1992, **322**, 325-327.
- [77] A. Jarzebinska, P. Rowinski, I. Zawisza, R. Bilewicz, L. Siegfried, T. Kaden., *Anal. Chim. Acta.*, 1999, **396**, 1
- [78] M. A. Mndez, P. Voyame, H. H. Girault, *Angew. Chem. Int. Ed.*, 2011, **50**, 7391-7394.
- [79] M. Hammouche, D. Lexa, J. M. Savéant, M. J. Mometeau., *Electroanal. Chem.*, 1988, **249**, 347.
- [80] L. Bhugun, D. Lexa, J. M. Savéant., *J. Am. Chem. Soc.*, 1996, **118**, 1769.
- [81] J. Grodkowski, P. Neta, E. Fujita, A. Mahammed, L. Simkhovich, Z. Gross., *J. Phys. Chem. A.*, 2002, **106**, 4772.

- [82] M. Hammouche, D. Lexa, M. Momenteau, J. M. Savéant., *J. Am. Chem. Soc.*, 1991, **113**, 8455.
- [83] T. Atoguchi, A. Aramata, A. Kazusaka, M. J. Enyo., *Electroanal. Chem.*, 1991, **318**, 309-312.
- [84] C. Costentin, S. Drouet, M. Robert, J. M. Savéant., *Science*, 2012, **338**, 90-94.
- [85] J. Hawecker, J. M. Lehn, R. Ziessel., *J. Chem. Soc., Chem. Commun.*, 1984, **328**, 328-330.
- [86] J. Hawecker, J. M. Lehn, R. Ziessel., *J. Chem. Soc., Chem. Commun.*, 1983, **9**, 536-538.
- [87] J. Hawecker, J. M. Lehn, R. Ziessel., *J. Chem. Soc.-Chem. Comms.*, 1985, **2**, 56-58.
- [88] J. Hawecker, J. M. Lehn, R. Ziessel., *Helvetica Chimica Acta*, 1986, **69**, 1990-2012.
- [89] M. Bourrez, F. Molton, S. Chardon-Noblat, A. Deronzier., *Angew. Chem. Int. Ed.*, 2011, **50**, 9903-9906.
- [90] K. A. Grice, N. X. Gu, M. D. Sampson, C. P. Kubiak, *Dalton trans.*, 2013, **42**, 8498-8503.
- [91] J. M. Smieja, C. P. Kubiak., *Inorgan. Chem.*, 2010, **49**, 9283-9289.
- [92] J. M. Smieja, E. E. Benson, B. Kumar, K. A. Grice, C. S. Seu, A. J. M. Miller, J. M. Mayer, C. P. Kubiak., *PNAS*, 2012, **109**, 15646-15650.
- [93] B. P. Sullivan, C. M. Bolinger, D. Conrad, W. J. Vining, T. J. Meyer, *J. Chem. Soc. Chem. Comms.*, 1985, **20**, 1414-1415.
- [94] J. R. Pugh, M. R. M. Bruce, B. P. Sullivan, T. J. Meyer., *Inorg. Chem*, 1991, **30**, 86-91.
- [95] I. Ishida, K. Tanaka, T. Tanaka, *Organometallics*, 1987, **6**, 181-183.
- [96] A. Begum, P. G. Pickup., *Electrochem. Comms.*, 2007, **9**, 2525-2528.
- [97] R. Angamuthu, P. Byers, M. Lutz, et al., *Science*, 2010, **327**, 313-315.
- [98] G. Seshadri, C. Lin, A.B. Bocarsly., *J. Electroanal. Chem.*, 1994, **372**, 145-150.
- [99] A. B. Bocarsly, Q. D. Gibson, A. J. Morris, R. P. L'Esperance, Z. M. Detweiler, P. S. Lakkaraju, E. L. Zeitler, T. W. Shaw., *ACS Catal.*, 2012, **2**, 1684-1692
- [100] E. E. Barton, D. M. Rampulla, A. B. Bocarsly., *J. Am. Chem. Soc.*, 2008, **130**, 6342.
- [101] C. E. Barton, P. S. Lakkaraju, D. M. Rampulla, A. J. Morris, E. Abelev, A. B. Bocarsly., *J. Am. Chem. Soc.*, 2010, **132**, 11539.
- [102] A. J. Morris, R. T. McGibbon, A. B. Bocarsly., *ChemSusChem.*, 2011, **4**, 191.
- [103] D. J. Darensbourg, A. Rokicki, M. Y. Darensbourg., *J. Am. Chem. Soc.*, 1981, **103**, 3223-3224.
- [104] T. W. Woolerton, S. Sheard, E. Reisner, E. Pierce, S. W. Ragsdale, F. A. Armstrong, *J. Am. Chem. Soc.*, 2010, **132**, 2132-2133.
- [105] M. Tezuka, T. Yajima, A. Tsuchiya, Y. Matsumoto, Y. Uchida, M. Hidai., *J. Am. Chem. Soc.*, 1982, **104**, 6834-6836.
- [106] E. W. Abel, M. A. Bennet, G. Wilkinson., *J. Chem. Soc.*, 1959, 2323.
- [107] D. J. Stufkens., *Coord. Chem. Rev.*, 1990, **104**, 39-112.
- [108] A. Vlcek., *Coord. Chem. Rev.*, 2002, **230**, 225-242.
- [109] S. S. Braga, A. C. Coelho, I. S. Gonçalves, F. A. Almeida Paz., *Acta Cryst.*, 2007, **E36**, m780-m782.
- [110] S. L. VanAtta, B. A. Dulcos, D. B. Green., *Organomet.*, 2000, **19**, 2397-2399.
- [111] Z. Petrovski, A. A. Valente, M. Pillinger, A. S. Dias, S. S. Rodrigues, C. C. Romão, I. S. Gonçalves., *J. Mol. Catal. A.*, 2006, **249**, 166-171.
- [112] S. Zalis, C. Daniel, A. Vlcek., *J. Chem. Soc. Dalton Trans.*, 1999, **3**, 3081.
- [113] S. Oishi., *Organomet.*, 1988, **7**, 1237-1240.
- [114] K. Kalyanansundaram., *J. Phys. Chem.*, 1988, **92**, 2219-2222.
- [115] M. J. Schadt, N. J. Gresalfi, A. J. Lees., *Inorg. Chem.*, 1986, **24**, 2942.
- [116] D. P. Drolet, L. Chan, A. J. Lees., *Organomet.*, 1988, **7**, 2502.
- [117] I. R. Farrell, F. Hartl, S. Zalis, T. Mahabiersing, A. Vlcek. Jr., *J. Chem. Soc. Dalton Trans.*, 2000, 4323.
- [118] Y. Kaizu, H. Kobayashi., *Bull. Chem. Soc. Jap.*, 1972, **45**, 470-477.
- [119] D. Miholova, A. A. Vlcek., *J. Organometallic Chem.*, 1985, **279**, 317-326.
- [120] R. W. Balk, T. Snoeck, D. J. Stufkens, A. Oskam., *Inorg. Chem.*, 1980, **19**, 3015-3021.
- [121] D. Miholova, B. Gas, S. Zalis, J. Klima, A. A. Vlcek., *J. Organometallic Chem.*, 1987, **330**, 75-84.
- [122] K. R. Thampy, J. Kiwi, M. Gratzel., *Nature*, 1987, **327**, 506-508.
- [123] A. Vlcek, F. Baumann, W. Kaim, et al., *J. Chem. Soc.- Dalton Trans.*, 1998, **2**, 215-220
- [124] R. E. Dessy, F. E. Stary, R. B. King, M. Waldrop., *J. Amer. Chem. Soc.*, 1966, **88**, 471-476
- [125] R. E. Dessy, L. Wiczore., *J. Amer. Chem. Soc.*, 1969, **91**, 4963-4969

- [126] S. Ernst, W. Kaim., *J. Amer. Chem. Soc.*, 1986, **108**, 3578-3586
[127] J. Hanzlik, L. Pospisil, A. Vlcek, et al., *J. Electroanal. Chem.*, 1992, **331**, 831-844
[128] R. Johnson, H. Madhani, J. P. Bullock., *Inorganica Chimica Acta*, 2007, **360**, 3414-3423
[129] I. Noviadri, K. N. Brown, D. S. Fleming, P. T. Gulyas, P. A. Lay, A. F. Masters, L. Phillips., *J. Phys. Chem. B.*, 1999, **103**, 6713-6722
[130] M. R. McDevitt, A. W. Addison., *Inorganica Chimica Acta*, 1993, **204**, 141-146
[131] V. Paylishchuk, A. W. Addison., *Inorganica Chimica Acta*, 2000, **298**, 97-102
[132] K. F. Morris, C. S. Johnson Jr., *J. Am. Chem. Soc.* 1992, **114**, 3139 – 3141
[133] J. Janisch, A. Ruff, B. Speiser, C. Wolff, J. Zigelli, S. Benthin, V. Feldmann, H. A. Mayer., *J. Solid State Electrochem.*, 2011, **15**, 2083-2094.
[134] A. Solangi, A. M. Bond, I. Burgar, A. F. Hollenkamp, M. D. Horne, T. Rüther, C. Zhao., *J. Phys. Chem. B.*, 2011, **115**, 6843-6852.
[135] C. André-Barrès, F. Najjar, M. P. Maether, C. Payraastre, P. Lavedon, T. Tzedakis., *J. Electroanal. Chem.*, 2012, **686**, 54-57.
[136] Y. Marcus, *J. Sol. Chem.*, 2006, **35**, 1271-1286.
[137] P. Atkins and J. de Paula., *Atkins' Physical Chemistry*. 8th ed. 2006. Oxford University Press.
[138] A. Einstein., *Ann. Phys.*, 1906, **19**, 289-306.
[139] C. R. Wilke, P. Chang., *AICHE Journal.*, 1955, **1**, 264-270.
[140] P. T. Kissinger, P. T. Heineman., *Laboratory techniques in electroanalytical chemistry*. 2nd ed. 1996, New York. Marcel Dekker Inc.
[141] A. J. Bard and L. R. Faulkner., *Electrochemical Methods: Fundamentals and Applications*. 2nd ed. 2001, USA, John Wiley and Sons Inc.
[142] A. C. Fisher., *Electrode Dynamics*, 1996, Oxford University Press.
[143] H. H. Girault., *Analytical and physical electrochemistry*. 2004. New York. Marcel Dekker Inc.
[144] P. Monk., *Fundamentals of Electroanalytical Chemistry*, Analytical Techniques in the Sciences (AnTS), ed. D. J. Ando, 2001, UK. John Wiley and Sons Ltd.
[145] J. A. Weil, J. R. Bolton, *Electron Paramagnetic Resonance: Elementary Theory and Practical Applications*, 2nd ed. 2007. New Jersey. John Wiley & Sons Inc.
[146] Y. C Liu., *J. Phys. Chem. B.*, 2004, **108**, 2948.
[147] K. Kneipp, Y. Wang, A. J. Berger, R. R. Dasari, M. S. Feld., *J. Raman Spec.*, 1995, **26**, 959-962.
[148] L. D. Burke, D. T. Buckley, J. A. Morrissey., *Analyst*, 1994, **119**, 841-845
[149] L. D. Burke, J. F. O'Sullivan., *Electro. Chima Acta*, 1992, **37**, 585-594
[150] M. Jeffrey, R. Woods., *J. Electrochem. Soc.*, 2001, **148**, E79-E84.
[151] R. Baron, N. M. Kershawb, T. J. Donohoeb, R. G. Compton., *J. Phys. Org. Chem.*, 2009, **22**, 1136–1141
[152] C. A. Paddon, R. G. Compton, *Electroanalysis* , 2005, **21**, 1919 – 1923
[153] G. Gritzner, J. Kuta, *Pure Appl. Chem.* 1984, **56**, 461–466.
[154] K. Izutsu, *Electrochem. in Nonaqueous Solutions*, 2002, Weinheim, Wiley-VCH.
[155] N. G. Tsierkezos., *J. Solutions Chem.*, 2007, **36**, 289-302.
[156] A. J. Zara, S. S. Machado, L. Otavio., *J. Electroanal.*, 1987, **221**, 165-174.
[157] M. Namizian, C. Y. Lin, M. L. Coote., *J. Chem. Theory Comput.*, 2010, **6**, 2721-2725.
[158] G. Gritzner., *Pure & Appl. Chem.*, 1990, **62**, 1839-1858.
[159] Z. Yang, V. R. Moure, D. R. Dean, L. C. Seefeldt., *PNAS*, 2012, **109**, 19644-19648.
[160] Gaussian 09, Revision B.01, M. J. Frisch, G. W. Trucks, H. B. Schlegel, G. E. Scuseria, M. A. Robb, J. R. Cheeseman, G. Scalmani, V. Barone, B. Mennucci, G. A. Petersson, H. Nakatsuji, M. Caricato, X. Li, H. P. Hratchian, A. F. Izmaylov, J. Bloino, G. Zheng, J. L. Sonnenberg, M. Hada, M. Ehara, K. Toyota, R. Fukuda, J. Hasegawa, M. Ishida, T. Nakajima, Y. Honda, O. Kitao, H. Nakai, T. Vreven, J. A. Montgomery, Jr., J. E. Peralta, F. Ogliaro, M. Bearpark, J. J. Heyd, E. Brothers, K. N. Kudin, V. N. Staroverov, T. Keith, R. Kobayashi, J. Normand, K. Raghavachari, A. Rendell, J. C. Burant, S. S. Iyengar, J. Tomasi, M. Cossi, N. Rega, J. M. Millam, M. Klene, J. E. Knox, J. B. Cross, V. Bakken, C. Adamo, J. Jaramillo, R. Gomperts, R. E. Stratmann, O. Yazyev, A. J. Austin, R. Cammi, C. Pomelli, J. W. Ochterski, R. L. Martin, K. Morokuma, V. G. Zakrzewski, G. A. Voth, P. Salvador, J. J. Dannenberg, S. Dapprich, A. D. Daniels, O. Farkas, J. B. Foresman, J. V. Ortiz, J. Cioslowski, and D. J. Fox, *Gaussian, Inc., Wallingford CT*, 2010.
[161] A.D. Becke, *J.Chem.Phys.*, 1993, **98**, 5648-5652; P.J. Stephens, F.J. Devlin, C.F. Chabalowski and M.J. Frisch, *J.Phys.Chem.* 1994, **98**, 11623-11627

- [162] F. Weigend and R. Ahlrichs, *Phys. Chem. Chem. Phys.*, 2005, **7**, 3297
- [163] D. Andrae, U. Haeussermann, M. Dolg, H. Stoll, H. Preuss, *Theor. Chim. Acta.*, 1990, **77**, 123.
- [164] M. Krejčík, A. A. Vlcek, *J. Electroanal. Chem.*, 1991, **313**, 243-257.
- [165] J. D. Wadhawan, P. J. Welford, E. Maisonhaute et al., *J. Phys. Chem. B.*, 2001, **105**, 10659-10668.
- [166] G. R. Pazuki, H. Pahlavanzadeh, *Theor. Found. Chem. Eng.*, 2005, **39**, 240-245.
- [167] F. Murrieta-Guevara, A. T. Rodriguez., *J. Chem. Eng. Data*, 1984, **29**, 456-460.
- [168] C. E. Housecroft and A. G. Sharpe, *Inorganic Chemistry.*, 2nd ed., 2005, Pearson Education Ltd, England. p215
- [169] J. N. Murrel, D. A. Jenkins, *Properties of Liquid and Solutions*, 2nd ed, 1994, Wiley, Chichester.
- [170] A. J. Parker., *Chem. Rev.*, 1969, **69**, 1-32
- [171] Th. Dretschkow, D. Lampner, Th. Wandlowski., *J. Electroanal. Chem.*, 1998, **458**, 121-138.
- [172] M. Hoon-Khosla, W. R. Fawcett, J. D. Goddard, W. Q. Tian, J. Lipowski., *Langmuir*, 2000, **16**, 2356-2362.
- [173] D. Yang, D. Bizzotto, J. Lipowski., *J. Phys. Chem.*, 1994, **98**, 7083-7089.
- [174] Th. Dretschkow, Th. Wandlowski., *J. Electroanal. Chem.*, 1999, **467**, 207-219.
- [175] S. H. Cadle, P. R. Tice, J. Q. Chambers., *J. Phys. Chem.*, 1967, **71**, 3517-3522.
- [176] M. Lyons, G. Keeley, *Int. J. Electrochem. Sci.*, 2009, **4**, 794 – 809.
- [177] K. Yasukouchi, I. Taniguchi, H. Yamaguchi, M. Shiraishi., *J. Electroanal. Chem.*, 1979, **105**, 794-809.
- [178] K. William., *Physical Review*, 1922, **19**, 512-524.
- [179] Ch. Wohlfarth., *Supplement to IV/18; Landolt-Börnstein - Group IV Physical Chemistry*, Volume 25, **2009**, 299.
- [180] P. H. Rieger., *J. of Mag. Res.*, 1997, **124**, 140-146.
- [181] R. Ahlrichs, K. May, *Phys. Chem. Chem. Phys.*, 2000, **2**, 943.
- [182] F. Neese, U. Becker, D. Ganyushin, S. Kossmann, A. Hansen, D. Liakos, T. Petrenko, C. Riplinger, and F. Wennmohs, *ORCA, an ab initio, density functional and semiempirical program package*, Max-Planck Institut für Bioanorganische Chemie, Mülheim an der Ruhr, Germany, 2011.
- [183] Simfonia EPR simulation software, Bruker.
- [184] S. Stoll, A. Schweiger, *J. Magn. Reson.* 2006, **178**, 42-55.
- [185] C. E. Dahm, D. G. Peters., *J. Electroanal. Chem.*, 1996, **402**, 91-96.
- [186] A. G. Davies, B. T. Golding, R. S. Hay-Motherwell, S. Mwesigye-Kibende, D. N. Ramakrishna Rao, M. C. R. Symons., *J. Chem. Soc. Chem. Comm.*, 1988, 378-381.
- [187] J. H. B. Chenier, H. A. Joly, J. A. Howard, B. Mile., *J. Chem. Soc. Faraday Trans.*, 1990, **86**, 3329-3335
- [188] K. Takeya, T. Sugahara, K. Ohgaki, A. Tani. *Radiation Measurements*, 2007, **42**, 1301 – 1306
- [189] H. Yang, J. F. Sanz, Y. Wang, J. L. Whitten., *J. Cluster Sci.*, 1999, **10**, 581-590.
- [190] J. Simonet, *Electrochem. Comm.*, 2012, **21**, 22-25.
- [191] S. Trasatti, O. A. Petrii, *J. Electroanal. Chem.*, 1992, **327**, 353-376.
- [192] P. Rodriguez, A. A. Koverga, M. T. M. Koper., *Angew. Chem. Int. Ed.*, 2010, **49**, 1241-1243.
- [193] N. M. Markovic, P. N. Ross, *Surf. Sci. Rep.*, 2002, **45**, 117.
- [194] R.L. McCreery in *Electroanalytical Chemistry 17*, 1991, A.J. Bard (Ed.), Marcel Dekker, New York, pp. 221-374.
- [195] A. B. Meneses, S. Antonello, M. C. Arévalo, F. Maran, *Electroanalysis*, 2006, **18**, 363-370.
- [196] A.J. Bard and H. Lund Eds., *The Encyclopedia of the Electrochemistry of the Elements*, 1973-1986, Marcel Dekker, New York.
- [197] R. W. Fawcett., *Liquids, Solutions and Interfaces; From classic Macroscopic description to Modern Microscopic Detail*, 2004, Oxford University Press. pp 189.
- [198] J. L. Roberts Jr., T. S. Calderwood, D. T. Sawyer., *J. Am. Chem. Soc.*, 1984, **106**, 4667-4670
- [199] M. A. Casadei, S. Cesa, F. M. Moracci, A. Inesi, M. Feroci., *J. Org. Chem.*, 1996, **61**, 380-383.
- [200] J. R. Lombardi, R. L. Birke., *J. Phys. Chem. C*, 2008, **112**, 5605-5617
- [201] H. J. Kim, A. E. Fouda, K. Jonasson, *J. App. Polymer Sci.*, 2000, **75**, 135-141

- [202] E. O. Stejskal, J. E. Tanner., *J. Chem. Phys.*, 1965, **42**, 288–292
- [203] D. Leaist, L. Hui, *J. Phys. Chem.*, 1990, **94**, 8741-8744
- [204] R. J. Bearman., *J. Phys. Chem.*, 1961, **65**, 1961
- [205] J. C. Bosma, J. A. Wesselingh., *Trans IChemE*, 1999, **77**, 325-328.
- [206] S. R. Ragsdale, H. S. White., *J. Electroanal. Chem.*, 1997, **432**, 199-203.
- [207] M. Holtz, X. Mao, D. Seiferling, A. Sacco., *J. Chem. Phys.*, 1996, **104**, 669-679
- [208] [http://ddbonline.ddbst.de/EE/159vis\(DynamicViscosity\).shtml](http://ddbonline.ddbst.de/EE/159vis(DynamicViscosity).shtml)
- [209] K. Kontturi, A.K. Kontturi, S. Mafé, J.A. Manzanares, L. Murtomäki., *Ber. Bunsenges. Phys. Chem.*, 1995, **99**, 1131-1136.
- [210] G. Canzi, A. A. Mrse, C. P. Kubiak., *J. Phys. Chem. C.*, 2011, **115**, 7972-7978.
- [211] A. M. Bond, K. B. Oldham, G. A. Snook., *Anal. Chem.*, 2000, **72**, 3492–3496
- [212] R. Baron, N. M. Kershawb, T. J. Donohoeb, R. G. Compton., *J. Phys. Org. Chem.*, 2009, **22**, 1136–1141
- [213] C. A. Paddon, R. G. Compton, *Electroanalysis* , 2005, **21**, 1919 – 1923
- [214] Private communication with Mister Adam Cooper
- [215] J. F. Cassidy, J. O’Gormon., *Electrochem. Comm.*, 1999, **2**, 69-71
- [216] W. Miao, Z. Ding, A. J. Bard., *J. Phys. Chem. B.*, 2002, **106**, 1393
- [217] R. Winter, G. Wolmerhäuser., *J. Organomet. Chem.*, 1998, **570**, 201-218
- [218] J. Matysik, J. Chmiel, M. Przegalinski, A. Cleszczyk-Chmiel., *Chem. Anal.*, 1994, **39**, 713-717.
- [219] D. D. Bode Jr., T. N. Andersen, H. Eyring., *J. Phys. Chem.*, 1967, **71**, 792–797
- [220] R. A. Robinson, R. H. Stokes, *Electrolyte solutions.*, 2nd ed., rev.1968. London, Butterworths.
- [221] A. D. Buckingham, L. Fan-Chen, *Int. Rev. Phys. Chem.* 1981, **1**, 253.
- [222] R. Mills, *J. Phys. Chem.*, 1973, **77**, 685–688.
- [223] R. Evans, Z. Deng, A. Rogerson, A. McLachlan, J. Richards, M. Nilsson, G. Morris., *Angew. Chem. Int. ed.*, 2013, **52**, 3199-3202.
- [224] T. Matsue, D. H. Evans, T. Osa, N. Kobayashi., *J. Am. Chem. Soc.*, 1985, **107**, 3411.
- [225] T. Carofiglio, F. Magno, I. Lavagnini., *J. Electroanalytical Chem.*, 1994, **373**, 11-17.
- [226] W. Miao, Z. Ding, A. J. Bard., *J. Phys. Chem. B.*, 2002, **106**, 1393
- [227] M. P. Longinotti, H. R. Cort., *Electrochem. Comm.*, 2007, **9**, 1444.
- [228] A. D. Modestov, J. Gun, A. Mudrov, O. Lev., *Electroanalyst.*, 2004, **16**, 367-378
- [229] A. Yamaguchi, M. M. Mekawy, Y. Chen, S. Suzuki, K. Morita, N. Teramae, *J. Phys. Chem. B*, 2008, **112**, 2024-2030.
- [230] B. T. T. Nguyen, C. Toh., *Electrochimica Acta.*, 2009, **54**, 5060-5064.
- [231] W. E. Waghorne., *Phil. Trans. R. Soc. Lond. A.*, 2001, **359**, 1529-1543.
- [232] K. D. Collins, *Methods*, 2004, **34**, 300-311.
- [233] K. E. Connors, *Chemical Kinetics: The Study of Reaction Rates in Solution*, 1990, Wiley-VCH